

Fatigue Crack Growth Prediction for generalized fiber metal laminates and hybrid materials

Gregory S. Wilson



Fatigue Crack Growth Prediction for generalized fiber metal laminates and hybrid materials

PROEFSCHRIFT

ter verkrijging van de graad van doctor
aan de Technische Universiteit Delft,
op gezag van de Rector Magnificus prof. ir. K.C.A.M. Luyben,
voorzitter van het College voor Promoties,
in het openbaar te verdedigen op donderdag 13 juni 2013 om
15.00 uur
door

Gregory Scott WILSON

Master of Science in Aeronautics and Astronautics
geboren te Santa Monica, California, Verenigde Staten.

Dit proefschrift is goedgekeurd door de promotor:

Prof. dr. ir. R. Benedictus

Copromotor: Dr. ir. R.C. Alderliesten

Samenstelling promotiecommissie:

Rector Magnificus	voorzitter
Prof. dr. ir. R. Benedictus	Technische Universiteit Delft, promotor
Dr. ir. R.C. Alderliesten	Technische Universiteit Delft, copromotor
Prof. dr. ir. S. van der Zwaag	Technische Universiteit Delft
Prof. dr. ir. R. Marissen	Technische Universiteit Delft
Prof. dr. ir. A. de Boer	Technische Universiteit Twente
Prof. S.M. Spearing	University of Southampton
Dr. E. Troiani	University of Bologna
Prof. dr. ir. L. J. Sluys	Technische Universiteit Delft, reservelid

Copyright © 2013 by G.S. Wilson

All rights reserved. No part of the material protected by this copyright notice may be reproduced or utilized in any form or by any means, electronic or mechanical, including photocopying, recording or by any information storage and retrieval system, without the prior permission of the author.

ISBN 978-9-08891-648-9

Published by: Uitgeverij BOXPress, 's-Hertogenbosch, Netherlands

Contents

List of Figures	v
List of Tables	xv
1 Introduction	1
Bibliography	2
2 Background	3
2.1 Fiber Metal Laminates	3
2.2 Development of FMLs	5
2.2.1 Arbitrary FMLs	12
2.3 Need for a generalized crack growth model	14
2.4 Goals of this work	15
2.5 Extant crack growth models	16
2.5.1 Empirical	16
2.5.2 Analytical	18
2.5.3 Other models	27
2.5.4 Summary	28
Bibliography	28
3 The model	33
3.1 Overview	33
3.2 Initialization and discretization	35
3.2.1 Material and laminate properties	35
3.2.2 Calculating stresses with CLT	36
3.2.3 Bar elements and nodes	37
3.3 Calculation loop	40
3.3.1 Calculating the bridging stress	40
3.3.2 Strain energy release rates	41

3.3.3	Crack and delamination growth	43
3.3.4	Updating the geometry	45
3.3.5	Exiting the calculation loop	50
3.3.6	Stability and convergence	50
3.3.7	Shortcomings of the present model	53
3.4	Summary	55
	Bibliography	56
4	Bridging load determination	59
4.0.1	Overview of Present Bridging Models	59
4.0.2	Limitations and motivation	62
4.1	Solution	64
4.1.1	Cracked Layer Displacement — $v_\infty(x)$ and $v_{br}(x)$	64
4.1.2	Prepreg Shear Deformation — $\delta_{pp}(x)$	66
4.1.3	Bridging Material Elongation — $\delta_{br}(x)$	68
4.1.4	Solving for the Bridging Stress	79
4.2	Verification	81
4.2.1	Approach	81
4.2.2	Results	84
4.3	Discussion	89
4.3.1	Residual stress	89
4.3.2	Saw cut	90
4.3.3	Number of layers	90
4.3.4	Bending	90
4.3.5	Differing crack lengths	91
4.3.6	Applicability of the model	92
4.3.7	Challenges for implementation	92
4.4	Conclusions	93
4.5	Notes on Accounting for Residual Stress	94
4.5.1	Effect on v_∞	95
4.5.2	Effect on v_{br}	95
4.5.3	Effect on δ_{br}	95
4.5.4	Effect on δ_{pp}	95
4.5.5	Conclusion	95
	Bibliography	96
5	Delamination strain energy release rate	99
5.1	Introduction	99
5.2	Generalized SERR calculation method	102
5.2.1	Assumptions	102

5.2.2	Derivation	107
5.3	Verifying approach with FEA	112
5.3.1	Calculations	112
5.3.2	Properties	113
5.3.3	Finite Element Analysis	113
5.3.4	Results	114
5.4	Discussion	130
5.5	Conclusion	133
	Bibliography	133
6	Testing	137
6.1	Methodology	137
6.1.1	Laminate manufacture	137
6.1.2	Test Matrix	138
6.1.3	Laminate crack growth testing	138
6.1.4	Post-test teardown inspection	142
6.1.5	Model input parameter testing	143
6.2	Test results	143
6.2.1	Destructive inspection results	152
6.2.2	Input parameter testing results	161
6.3	Summary	164
	Bibliography	164
7	Model validation	167
7.1	Introduction	167
7.1.1	Glare data of Alderliesten	168
7.1.2	Glare data in bending of Randell	168
7.2	Comparison to current test data	168
7.3	Comparison to legacy data	187
7.3.1	Glare 3 and 4B data of Alderliesten	187
7.3.2	Bending data of Randell	191
7.4	Alternate model assumptions	200
7.5	Summary	204
	Bibliography	208
8	Discussion	209
8.1	Introduction	209
8.2	Overview of the model	209
8.3	Lessons of validation	217
8.3.1	Lessons learned	219

8.4	Limits of validity	219
8.5	Practical uses	221
8.5.1	Considering the Glare 3 lay-up	221
8.5.2	Directed crack growth subject to combined tension-bending	223
8.6	Extensibility	229
8.6.1	Alternate geometries and structural configurations	229
8.6.2	Variable amplitude fatigue crack growth	230
8.6.3	Residual strength	231
8.7	Summary	233
	Bibliography	233
9	Conclusions	237
A	Delam. growth with added adhesive	239
A.1	Introduction	239
A.1.1	Theory	242
A.2	Material and Methods	243
A.2.1	Manufacturing	245
A.2.2	Testing	249
A.3	Results	250
A.4	Discussion	254
A.5	Conclusion	256
	Bibliography	257
B	Steady-state crack growth	261
B.1	Introduction	261
B.2	Property assessment, prediction, and validation	265
B.2.1	Testing of laminates with 2524 thick sheets	265
B.2.2	Tests to Evaluate Net Stress as the Driving Parameter	269
B.2.3	Evaluation of the SSCG Method for Predicting Crack Growth Through Stress Gradients	272
B.3	Conclusions	278
	Bibliography	281
	Summary	283
	Samenvatting	285
	Acknowledgments	287

List of Figures

2.1	Fatigue crack growth behavior for center cracked specimen under mini-TWIST fatigue loading ($\sigma_{mean} = 100$ MPa, $R_{GAG} = -0.1$, with peaks truncated to 1.15) [11]. The inset images illustrate the laminate stacking sequence. From left to right: monolithic aluminum, aluminum reinforced externally with Glare, aluminum with adhesively bonded internal Glare reinforcement, and internal Glare reinforcement with fibers in the bondline.	9
2.2	Comparison of delamination areas for adhesive (left) and bondpreg (right) CentrAl laminates [11]	10
2.3	Minor changes to the laminate such as multiple outer layers and symmetric Bondpreg resulted in large changes in crack growth performance [11]	11
2.4	Diagram of interrupted ply strip for strain energy release rate calculation from [6]	20
2.5	Bar element scheme for solving the compatibility equation for the bridging stress	23
3.1	Schematic of steps in the crack and delamination growth calculation method	34
3.2	Laminate with asymmetric delaminations, changing the length of b_2 while holding b_1 constant, laminate: [0.3 mm Al / 0.25 mm prepreg / 0.3 mm Al], $\sigma_{lam} = 100$ MPa, $\Delta T = -100^\circ\text{C}$, $b_1 = 8$ mm, $b_2 = x$ axis	42
3.3	Illustration of interpolation scheme for delamination length following crack and delamination extension. The delamination nearest the crack tip is interpolated by assuming a delamination length of zero at the tip.	46

3.4	Illustration of the “leapfrogging” issue that can arise in a bar element due to the discretization of delamination growth	49
3.5	Error with respect to the result with the smallest w_{max} of predicted crack growth lives.	51
3.6	Computational time, based on the model run on a single CPU, for model predictions with varying maximum tip bar element widths.	51
3.7	Predicted crack growth of Laminate 1-1 with different initial delamination heights, demonstrating stability of the model . . .	52
3.8	Predicted crack growth of Laminate 9-1 with different initial delamination heights, demonstrating stability of the model . . .	53
3.9	Predicted crack growth of Laminate 9-1 with different initial crack lengths, demonstrating stability of the model	54
4.1	Schematic of bridging scenario for a generalized laminate, showing one quarter of a center-cracked laminate subject to remote tension and bending loads. There is a delamination in each interface between a cracked and uncracked layer over which the bridging load is transferred, reducing the crack tip stress intensity.	60
4.2	Idealization of shear where bridging stress is transferred near a delamination tip	66
4.3	Illustration of the approach to calculating the elongation at each interface with a complex delamination configuration in a given bar element	69
4.4	Example of the region where the metal ahead of a short crack contributes to the bridging of a longer crack. The cracks of each metal layer are depicted, and the fiber layer between them is omitted for clarity.	71
4.5	Overview and breakdown approach for Example 1	73
4.6	The bridging load is introduced as a line load at z_{int}	74
4.7	Overview and breakdown approach for Example 2	76
4.8	Depiction of how the bridging loads are introduced in the CLT analysis of each segment	76
4.9	Mesh of the FEA model for the Glare2-3/2-0.3 laminate with a larger crack and delamination in the center.	83
4.10	Comparison of calculated bridging stress distributions with FEA results	84
4.11	Comparison of model and FEA results	85
4.12	2/1 Glare with different cracks and delaminations	86

4.13 2/1 Glare with different cracks and delaminations, with a 5 mm saw cut. 86

4.14 Comparison of model and FEA results for combined tension-bending loading, (a), and bending-only loading, (b) 87

4.15 Glare 2/1 with two unequal metal layer thicknesses 88

4.16 This 3 metal layer, 2 fiber layer laminate has a larger crack and delamination in the center. 88

5.1 Schematic of crack bridging scenario for a generalized laminate, showing one quarter of a center-cracked laminate subject to remote tension and bending loads. There is a delamination in each interface between a cracked and uncracked layer over which the bridging load is transferred, reducing the crack tip stress intensity. 101

5.2 Scheme for subdivision of delaminated bar element into sections to which classical laminate theory can be applied [2] 103

5.3 Definition of reference distances on a laminate segment 103

5.4 Secondary bending in a delaminated strip. (a) shows FEA results for the asymmetrically delaminated specimen of Figure 5.12 (with 10x deformation scaling). (b) shows a schematic representation of the neutral line location before and after loading. (c) shows the results of the extension of the top delamination: the bending shape around the delamination locations stay approximately the same, while the center portion of the newly lengthened segment straightens out somewhat. 106

5.5 Example FEA mesh with boundary conditions 115

5.6 Effect of adhesive layer thickness (t_{ad}) on SERR in 2/1 Glare with 0.3 mm metal sheets, laminate: [0.3 mm Al / t_{ad} adhesive / 0.25 mm prepreg / t_{ad} adhesive / 0.3 mm Al], $\sigma_{lam} = 100$ MPa, $\Delta T = -100^\circ\text{C}$ 116

5.7 Effect of adhesive layer thickness (t_{ad}) on SERR in 2/1 Glare with 1.6 mm metal sheets, laminate: [1.6 mm Al / t_{ad} adhesive / 0.25 mm prepreg / t_{ad} adhesive / 1.6 mm Al], $\sigma_{lam} = 100$ MPa, $\Delta T = -100^\circ\text{C}$ 117

5.8 Comparison of the mode mixity, and its change with increasing adhesive thickness, for finite element models with two different metal layer thicknesses 117

5.9 Effect of changing applied load on SERR, laminate: [1.6 mm Al / 0.12 mm t_{ad} / 0.25 mm prepreg / 0.12 mm t_{ad} / 1.6 mm Al], $\Delta T = -100^\circ\text{C}$ 118

5.10	Effect of changing applied temperature change on SERR, laminate: [1.6 mm Al / 0.12 mm t_{ad} / 0.25 mm prepreg / 0.12 mm t_{ad} / 1.6 mm Al], $\sigma_{lam} = 100$ MPa	119
5.11	When both delaminations are of equal length, changing the length does not affect the SERR. laminate: [1.6 mm Al / 0.12 mm t_{ad} / 0.25 mm prepreg / 0.12 mm t_{ad} / 1.6 mm Al], $\sigma_{lam} = 100$ MPa, $\Delta T = -100^\circ\text{C}$	120
5.12	Increasing load on an asymmetrically delaminated specimen, laminate: [0.3 mm Al / 0.25 mm prepreg / 0.3 mm Al], $\Delta T = -100^\circ\text{C}$, $b_1 = 8$ mm, $b_2 = 16$ mm	121
5.13	Laminate with asymmetric delaminations, changing the length of b_2 while holding b_1 constant, laminate: [0.3 mm Al / 0.25 mm prepreg / 0.3 mm Al], $\sigma_{lam} = 100$ MPa, $\Delta T = -100^\circ\text{C}$, $b_1 = 8$ mm, $b_2 = x$ axis	122
5.14	3/2 laminate with different delamination lengths and increasing load. Nonlinear FEA and modified calculation method results, laminate: [0.3 mm Al / 0.25 mm prepreg / 0.3 mm Al / 0.25 mm prepreg / 0.3 mm Al], $\sigma_{lam} = 100$ MPa, $\Delta T = -100^\circ\text{C}$, $b_1 = 10$ mm, $b_2 = 16$ mm, $b_3 = 14$ mm, $b_4 = 6$ mm	123
5.15	3/2 laminate with different delamination lengths and increasing load. Linear FEA results, laminate: [0.3 mm Al / 0.25 mm prepreg / 0.3 mm Al / 0.25 mm prepreg / 0.3 mm Al], $\sigma_{lam} = 100$ MPa, $\Delta T = -100^\circ\text{C}$, $b_1 = 10$ mm, $b_2 = 16$ mm, $b_3 = 14$ mm, $b_4 = 6$ mm	124
5.16	3/2 laminate with different and changing delamination lengths and increasing load. Nonlinear FEA and modified calculation method results, laminate: [0.3 mm Al / 0.25 mm prepreg / 0.3 mm Al / 0.25 mm prepreg / 0.3 mm Al], $\sigma_{lam} = 100$ MPa, $\Delta T = -100^\circ\text{C}$, $b_1 = 10$ mm, $b_2 = x$ axis, $b_3 = b_2 - 2$ mm, $b_4 = 6$ mm	125
5.17	3/2 laminate with different and changing delamination lengths and increasing load. Linear FEA results, laminate: [0.3 mm Al / 0.25 mm prepreg / 0.3 mm Al / 0.25 mm prepreg / 0.3 mm Al], $\sigma_{lam} = 100$ MPa, $\Delta T = -100^\circ\text{C}$, $b_1 = 10$ mm, $b_2 = x$ axis, $b_3 = b_2 - 2$ mm, $b_4 = 6$ mm	126
5.18	SERR of a 2/1 laminate with combined tension and bending loading, laminate: [0.3 mm Al / 0.25 mm prepreg / 0.3 mm Al], $\sigma_{lam} = 100$ MPa, $M = 40$ N mm/mm $\Delta T = -100^\circ\text{C}$, $b_1 = 8$ mm, $b_2 = x$ axis	127

5.19	Deformation of a 2/1 laminate with combined tension and bending loading, laminate: [0.3 mm Al / 0.25 mm prepreg / 0.3 mm Al], $\sigma_{lam} = 100$ MPa, $\Delta T = -100^\circ\text{C}$, $b_1 = 8$ mm, $b_2 = 23$ mm .	128
5.20	Very thick 3/2 laminate with only outer layers delaminated with changing b_4 and fixed b_1 , laminate: [1 mm Al / 0.25 mm prepreg / 3 mm Al / 0.25 mm prepreg / 1 mm Al], $\sigma_{lam} = 100$ MPa, $\Delta T = -100^\circ\text{C}$, $b_1 = 8$ mm, $b_2 = x$ axis	129
6.1	Typical crack growth specimen geometry. Lengths from 490 – 500 mm were used.	138
6.2	TU Delft’s 500 kN servo-hydraulic fatigue test machine with specimen installed.	141
6.3	Crack growth rates from visual measurement of external cracks in tests of CentrAl with 2024-T3 thick layers. The 100 MPa test was allowed to continue to look for evidence of edge effect. None was found	144
6.4	Crack growth rates from visual measurement of external cracks in tests of CentrAl with 2024-T3 thick layers tested at varying peak stress and stress ratio	145
6.5	Crack growth rates from visual measurement of external cracks in tests of CentrAl with 2524-T3 thick layers	146
6.6	Crack growth rates from visual measurement of external cracks in tests of CentrAl with 2524-T3 thick layers, showing the effects of changing the saw-cut starter notch length	147
6.7	Crack growth rates from visual measurement of external cracks in tests of Laminates 6 and 9	148
6.8	Crack growth rates from visual measurement of external cracks in tests of Laminates 6 and 9 with tension-compression loading	149
6.9	Crack growth rate results for 2/1 laminate with non-uniform metal layer thickness	150
6.10	Crack growth rate results for 2/1 laminate with asymmetric additional adhesive layers	151
6.11	Crack growth rate results for 3/2 laminates with additional adhesive layers on only one side of each fiber layer	152
6.12	Crack growth rate results for 2/1 laminates with mixed aluminum alloys	153
6.13	Delamination in the first interface of specimen 0-6.	154

6.14	Example from the first interface of specimen 0-6 showing all four delamination fronts from a given layer averaged into one representative front. “North” and “South” refer to the left and right cracks, respectively. “Top” and “bottom” are the delaminations above and below each crack, respectively.	155
6.15	Delamination shapes and internal crack lengths of specimen 0-6. Lines represent the averaged delamination shape from all four quadrants of the interface. Dots are the average half-crack length of the metal layer adjacent the delamination. Arrows indicate which interface is shown in the plot, and are color-coded with the data.	156
6.16	Delamination shapes and internal crack lengths of specimen 1-1.	157
6.17	Delamination shapes and internal crack lengths of specimens 6-1 and 6-2.	158
6.18	Delamination shapes and internal crack lengths of specimens 9-1 and 9-2.	158
6.19	Delamination shapes and internal crack lengths of specimen 8-1.	159
6.20	Delamination shapes and internal crack lengths of specimens 12-1 and 11-1.	160
6.21	Delamination shapes and internal crack lengths of specimen 7-1.	160
6.22	Delamination shapes and internal crack lengths of specimen 13-2.	161
6.23	Delamination shapes and internal crack lengths of specimen 14-1.	161
6.24	Crack growth results of 2524-T3 property tests, with power law fit	162
6.25	Effect of adhesive layer thickness on delamination growth rate .	163
7.1	MOHTB specimen design from [2]	170
7.2	Comparison of test results and model prediction for 2/1 laminate with extra bondline adhesive	172
7.3	Comparison of predicted and measured delamination shapes and internal crack lengths of specimens 6-1 and 6-2.	172
7.4	Comparison of test results and model prediction for 3/2 laminate with extra bondline adhesive	173
7.5	Comparison of predicted and measured delamination shapes and internal crack lengths of specimens 9-1 and 9-2.	174
7.6	Comparison of test results and model prediction for 3/2 laminates with asymmetric extra bondline adhesive	175
7.7	Comparison of predicted and measured delamination shapes and internal crack lengths of specimens 12-1 and 11-1.	176
7.8	Comparison of test results and model prediction for 2/1 laminate with non-uniform metal layer thickness	177

7.9	Comparison of predicted and measured delamination shapes and internal crack lengths of specimen 7-1.	178
7.10	Comparison of predicted and measured delamination shapes and internal crack lengths of specimen 8-1.	179
7.11	Comparison of test results and model prediction for 2/1 laminate with asymmetric extra bondline adhesive	179
7.12	Model predictions for CentrAl laminate 1 with different loading compared to test results	180
7.13	Comparison of predicted and measured delamination shapes and internal crack lengths of specimen 1-1.	182
7.14	Model predictions for CentrAl laminate 1 with different notch lengths compared to test results	183
7.15	Model predictions for CentrAl laminate 0 with different loading compared to test results	184
7.16	Model predictions for CentrAl laminate 1 with different stress ratios compared to test results	185
7.17	Comparison of predicted and measured delamination shapes and internal crack lengths of specimen 0-6.	186
7.18	Figure from [1] showing delamination growth between the 0° and 90° layers in Glare 4	187
7.19	Glare data from Alderliesten [1] with generalized model predictions	188
7.20	Glare data from Alderliesten [1] with generalized model predictions	189
7.21	Glare data from Alderliesten [1] with generalized model predictions	190
7.22	Glare data from Alderliesten [1] with generalized model predictions	190
7.23	Glare data from Alderliesten [1] with generalized model predictions	192
7.24	Glare data from Alderliesten [1] with generalized model predictions	193
7.25	Outer sheet crack growth data from MOHTB specimens of Randell [2] with generalized model predictions	194
7.26	Crack growth results from MOHTB specimen of Randell [2] with generalized model predictions for external and internal cracks .	195
7.27	Crack growth results from MOHTB specimen of Randell [2] with generalized model predictions for external and internal cracks .	196
7.28	Crack growth results from MOHTB specimen of Randell [2] with generalized model predictions for external and internal cracks .	197
7.29	Crack growth results from MOHTB specimen of Randell [2] with generalized model predictions for external and internal cracks .	198
7.30	Crack growth results from four-point bend specimen of Randell [2] with generalized model predictions for external and internal cracks	199

7.31	Comparison of model predictions for a CentAl specimen with and without the δ_K cracked bridging layer correction.	201
7.32	Comparison of model predictions for Laminate 9 specimen with and without the δ_K cracked bridging layer correction.	202
7.33	Comparison of model predictions for a CentAl specimen with and without the full neutral line model strain energy release rate calculation.	203
7.34	Delamination predictions of the model including the full neutral line model strain energy release rate calculation compared to the final measured delamination shapes from the test.	205
7.35	Comparison of model predictions for a laminate 8 specimen with and without the full neutral line model strain energy release rate calculation.	206
7.36	Comparison of model predictions for a Glare 2 modified open hole bending specimen with and without the full neutral line model strain energy release rate calculation.	207
8.1	Results of three different layups of Glare 3, comparing the opposite orientation of the glass fiber prepreg layers.	223
8.2	Crack growth prediction for a CentAl laminate with applied tension and bending moment.	225
8.3	Difference in crack lengths on opposite sides of a CentAl laminate subject to combined tension-bending loading due to varying the metal layer thicknesses. Positive values are preferred for inspection purposes.	226
8.4	Difference in crack lengths on opposite sides of a CentAl laminate subject to combined tension-bending loading due to varying the outside metal layer thicknesses. Positive values are preferred for inspection purposes.	227
8.5	Difference in crack lengths on opposite sides of a CentAl laminate subject to combined tension-bending loading due to varying the outside metal layer thicknesses. Positive values are preferred for inspection purposes.	228
A.1	Depiction of Bondpreg and definition of layup parameters	244
A.2	Lay-up process for Laminates G and H. Lay-up of Laminates A–F used full FM 94 sheets (with carrier) in place of strips . .	246
A.3	Specimen dimensions and delamination growth example	247

A.4 Post-test image of surface of metal layers of several specimens. The bottom 30 mm of each surface are the delamination surfaces created during testing. The rougher surfaces above are a result of manual disassembly of the specimens. 248

A.5 Test setup with specimen in hydraulic grips, showing camera location [9] 249

A.6 Test results of fiberglass-metal interfaces with different metal thickness and cure pressure 250

A.7 Specimens H1 and H2 ($t_{ad} = 0.03$ mm) showed inconsistent results. The two Laminate D specimens are shown to demonstrate the good agreement in results seen in the other laminates. Specimens H3–H6 were each tested at a single cyclic loading for the duration of the test. 251

A.8 Average delamination growth rates of specimens H3–H6, all with $t_{ad} = 0.03$ mm, plotted against the average delamination length. The rates are normalized by dividing the rate by the mean rate of each specimen in order to make the trends in growth rate with respect to delamination more directly comparable. 252

A.9 Effect of adhesive layer thickness on delamination growth rate . 253

A.10 Results from Figure A.9 replotted with error bars representing one standard deviation above and below the average growth rate based on a log normal fit of the growth rate of each of the four or eight delamination fronts measured for each SERR range. . . 253

A.11 Relative decrease in delamination growth rates with addition of adhesive in the bondline 255

B.1 a vs. N (left) and crack growth rate vs. crack length (right) plots representing the results of a typical fatigue crack growth rate test in a typical FML [2] 262

B.2 Test results from [2] showing constant crack growth rate for cracks up to 90% of specimen width. Loaded with $\sigma_{max} = 100$ MPa, $R = 0.05$ 263

B.3 Results from crack growth rate tests on CentraI with 2024-T3 thick sheets [2] 264

B.4 Results from crack growth rate tests on CentraI with 2024-T3 thick sheets [2] 264

B.5 Method for crack growth prediction using SSCG of FMLs . . . 265

B.6	Crack growth results from the FML with 2524-T3 thick sheets compared with the average results of the FML with 2024-T3 from [2]. The front and back terms refer to which face of the laminate the crack was located, while the North and South terms refer to the two ends of the central notch.	267
B.7	Crack growth rates of the tests with starter notch lengths of 5 mm	268
B.8	Steady-state crack growth rates plotted against applied cyclic stress range	269
B.9	Ultrasonic C-Scan images comparing delamination (red region) in the laminates from the current study with those from [2] . . .	270
B.10	Crack growth rates determined for the specimens with long starter notches, determined from 7-point polynomial method with average crack lengths	271
B.11	By changing the notch size, different net stresses were achieved. The data nearly coalesce into a power law function of net applied stress range. All tests used the laminate in Table 1 at a stress ratio of $R = 0.05$	272
B.12	4-hole specimen design. The second 4-hole specimen had holes placed 25 mm from the center, rather than 20 mm. All dimensions in mm	273
B.13	ABAQUS results for fiber-direction strain in 4-hole specimen. Line load equivalent to 100 MPa applied at top of specimen, cut off in image	274
B.14	Results of the 4-hole specimen with holes at 20 mm from the center, tested at $\sigma_{app,max} = 100$ MPa and $R = 0.05$	275
B.15	Results of the 4-hole specimen with holes at 25 mm from the center, tested at $\sigma_{app,max} = 100$ MPa and $R = 0.05$	276
B.16	Drawing of broken-stiffener specimen. Straps are 3mm and 6mm thick in the two different configurations, and are placed on both sides of the laminate. A starter notch of 5 mm was cut on each side of the central hole. All dimensions in mm	276
B.17	FEA output for broken strap model	277
B.18	Comparison of prediction with test results for the broken-stiffener tests. Both tests were conducted at $\sigma_{app,max} = 100$ MPa and $R = 0.05$	278
B.19	Comparison of predicted crack growth to the broken-stiffener tests data	279

List of Tables

2.1	Standard Glare grades [5]	7
3.1	Attributes of each layer used in laminate definition	36
3.2	Material properties defined for each layer (not all properties applicable to all layers)	36
4.1	Material properties used in FEA and model calculations	82
5.1	Material properties used in calculations and FEA	113
6.1	Test matrix	139
6.2	Laminate definitions	140
6.3	Power law fits for Equation (3.23) for each adhesive layer thickness. C_d and n_d terms are based on ΔG in units of $\sqrt{\text{MPa mm}}$ and $\frac{db}{dN}$ in units of mm/cycle.	163
7.1	Test parameter summary for data from [1] used in validation	169
7.2	Test parameter summary for data from [2] used in validation. The stress ratio of all tests was $R = 0.1$	169
8.1	Layups of Glare 3 used to explore the effect of changing the prepreg stacking sequence	222
A.1	Test Matrix	243
A.2	Power law fits for Equation (A.1) for each adhesive layer thickness	254
B.1	Laminate definitions	266

This page intentionally left blank.

Chapter 1

Introduction

Two ideal concepts bound the set of solutions for describing the universe and the matter it contains. The analytical extreme includes the search for a grand unified theory, a concise and elegant set of equations that describe all the units of matter and energy and the forces that govern their interactions [1, 2]. The numerical extreme is to simulate the universe directly, which would require a computer as complex as the entire universe, capable of performing 10^{120} operations on 10^{90} bits[3]. Both of these approaches fall far short of being useful for any practical application, but any practical approach to modeling must lie somewhere on the spectrum between clean, analytical equations and brute force numerical power.

In this thesis, one particular practical problem is modeled. That problem is predicting the growth of damage, specifically independent cracks and delaminations, in the newest class of fiber metal laminates, which may consist of any arbitrary configuration of fiber-reinforced composite laminae combined with metallic laminae. Insofar as it is possible, a solution to this problem toward the analytical end of the modeling spectrum will be sought. Where necessary, due to the limits of available analytical theories and the complex nature of the problem, concessions to the numerical aspect of modeling will be made.

This thesis describes the development of this solution in the following chapters:

Chapter 2 — Background This chapter will provide a brief history of fiber metal laminates, leading toward increasing tailorability and thus the need for a generalized model. Existing, less general models for crack and delamina-

tion growth in fiber metal laminates will be discussed. The specific objectives in developing the model will be laid out and explained.

Chapter 3 — The model This chapter will describe the model, first from an overview of its structure, then step-by-step through each component.

Chapter 4 — Bridging stress determination A detailed description of the bridging stress calculation, which is the fundamental component of the model.

Chapter 5 — Strain energy release rate A detailed description of the generalized strain energy release rate calculation used by the model to determine the driving parameter of delamination growth.

Chapter 6 — Testing A number of crack growth tests of differently-configured laminates were conducted to provide data against which to evaluate the unique aspects of the model.

Chapter 7 — Model validation By comparing predictions of the model to real test data from Chapter 6 and from the literature, the validity of the model for describing crack and delamination growth in arbitrary fiber metal laminates will be assessed.

Chapter 8 — Discussion The fulfillment of the model's objectives, as described in Chapter 2, will be evaluated. Areas where the model does and does not meet those objectives will be specifically addressed. Several ways in which the model can be further developed and its capabilities expanded will be described, and example applications of the model to specific engineering problems will be shown.

Chapter 9 — Conclusions The important conclusions from the entire work will be briefly noted in a concise summary.

Bibliography

- [1] Hawking, S. (1998) *A brief history of time*. Updated and expanded tenth anniversary edition, Bantam Books.
- [2] Kaku, M. (1995) *Hyperspace: a scientific odyssey through parallel universes, time warps, and the tenth dimension*. Anchor Books.
- [3] Lloyd, S. (2002) Computational capacity of the universe. *Physical Review Letters*, **88**.

Chapter 2

Background

This chapter includes a review of the history of fiber metal laminates, leading up to the development of laminates so complex that a generalized model is needed. The goals in developing a model are presented and justified. Several existing simpler models will be discussed for their usefulness as a starting point for the development of the generalized model.

2.1 Fiber Metal Laminates

Fiber metal laminates (FMLs) exemplify a juxtaposition common in aircraft materials. At once new materials are desired that push the boundaries of strength, durability, and light weight, while strict regulations and a safety-focused conservative attitude throughout the aviation industry lead to resistance to adopting new technologies. The strength of these opposing forces is in proportion to the degree of change.

A new aluminum alloy may offer incremental improvements of properties, while the process for acceptance and certification is clearly defined and straightforward. In contrast, the increasing adoption of fiber-reinforced composites has required the revision of design rules and inspection and repair protocols, a great deal of testing, and the very slow transition over more than 40 years from limited application to secondary structure in military vehicles to the complete high acreage components such as wings and fuselage skins. Despite these difficulties, progress was driven by the promise of lighter, more efficient structure with improved durability. Whether or not a new material is adopted depends

on the precise balance of its strengths versus the uncertainties and potential for challenges associated with it.

In the case of FMLs, the combination of two relatively well-understood materials has significant advantages for creating new structure, but this combination also raises problems that have not previously been addressed. The path through which FMLs have been developed has led to the demonstration and acknowledgment of their strengths, while the capabilities for their analysis have lagged. For use on the Airbus A380, Glare was certified as though it were a metal, based on experimentally measured properties [1]. While this approach eased introduction of the material, additional conservatism and limited material tailoring were employed. Only with analysis and certification that treat FMLs for what they are, a bonded laminate structure, can their full potential be realized in flying structure. The work in this thesis is intended to move the analytical capabilities available for FMLs forward and better enable the kind of tailorable, optimized design envisioned for FMLs from their conception.

Fatigue crack growth is only one of the suite of properties that must be analytically describable in order to fulfill this vision. It was selected as a topic for this study for several reasons. The overarching benefit of FMLs, and the reason they are targeted for such applications as the fuselage crown, tail plane leading edges, and the lower wing skin, is their damage tolerance. In order to maximize the benefit gained from this superior damage tolerance, it must be fully understood. Such a maximization could consist of simply achieving the greatest possible crack growth life, or it could come in the form of ensuring that the crack growth is just good enough to make some other property the constraining element of the design¹.

A second reason that crack growth became the subject of this dissertation is that this, along with the residual strength aspect of damage tolerance, seemed to be the property of generalized FMLs which required methods most different from those used for analyzing regular FMLs. Properties such as yield strength, open hole strength, stiffness, and even fatigue initiation, do not seem to require consideration of the particular stacking sequence of the laminate beyond that which is needed to describe the stress distribution through the laminate, which is already a well understood problem [2–4]. Such a laminate stress calculation is the starting point for a crack growth analysis, but other aspects of the stacking sequence that affect crack and delamination growth, particularly the load transfer between individual layers, had not been previously addressed, but were expected to have a significant influence on the resulting behavior of the lami-

¹After which, that property would be improved, while maintaining the damage tolerance at the required level

nate. This was thus a particular challenge for the development of non-regular FMLs.

Finally, at the initiation of this research, the results of several testing programs that had recently concluded indicated that subtle changes to the laminate design could have dramatic influence on the crack growth behavior of the laminate. Section 2.2 discusses some surprising results for thick FML structure that were seen in these programs and why the ability to predict crack growth behavior could mitigate the risk of unexpected or undesirable failure modes.

This chapter will briefly review the development of FMLs and provide some definitions of needed for the development of this model. The need for a generalized crack growth model will be discussed in the context of the increasing trend toward tailorability and non-standard configurations of FMLs. The goals of the model developed in this research will be outlined, so that its success can be assessed (see Chapter 8). The currently available crack growth models for FMLs will be reviewed and evaluated against these goals. Additionally, some background discussion of a number of techniques required in this model will be provided.

2.2 Development of FMLs

Fiber metal laminates, most broadly, are laminates constructed from one or more metallic sheets bonded to one or more fiber-reinforced polymer composite layers. They were originally conceived with the notion of adding reinforcing fibers to the bond line of metal laminates, thick metal sheets built up through adhesive bonding of thin metal sheets. Structures made of laminated metal sheets were already known to have improved crack growth properties compared with thicker monolithic metal [1, 5].

The first specific variant of FML created was ARALL [1, 5, 6]. ARALL was composed of 2XXX or 7XXX thin aluminum sheets interleaved with aramid-epoxy composite layers. The chief advantage of ARALL was that it overcame one of the major weaknesses of aluminum, the tendency for cracks to form and propagate over the service lifetime. Very slow crack growth in ARALL panels occurred because, while the metal layers cracked, the aramid composite layers did not. Load from the cracked aluminum layers was carried around the cracks by the intact fibers, reducing the crack driving force. This phenomenon was referred to as “crack bridging.” As part of the bridging phenomenon, the highly stressed bonds between metal and composite layers were broken in the

region around the crack. This additional form of damage is referred to as “delamination.”

The major drawbacks of ARALL, which limited its use in service to a small number of C-17 cargo doors [1], were the limitation on panel size and the need for laminate stretching after cure. The maximum dimensions of an ARALL panel were constrained by the dimensions of the largest metal sheet available. To build a larger structure, such as the C-17 cargo door, multiple ARALL sheets were joined with riveted titanium straps, adding extra manufacturing expense and weight to the structure. Since the difference in coefficients of thermal expansion between the aluminum and fiber layers led to a residual state of compression in the fibers and tension in the metal, it was necessary to stretch the laminate after curing. This post-stretching would plastically elongate the aluminum layers, reversing the residual stress state [1, p. 42]. Aramid fibers have a higher stiffness and strength when in tension compared to that when in compression, so the stress reversal improved fiber performance. Likewise the compressive residual stress in the post-stretched aluminum improved its fatigue behavior. Without the post-stretching, the material properties would be unsuitable for aircraft applications. The post-stretching requirement also limited the size of the ARALL panels, since the panel would have to be securely gripped at two ends and sufficient force applied.

Glass fibers were applied to FMLs as a means of obviating the need for post-stretching, since their stiffness is comparable in tension and compression, and their stability in compression was superior to that of aramid. The combination of S2 glass fibers and aluminum sheets in an FML is referred to as Glare (GLASS REinforced aluminum). Several standard grades of Glare, consisting of specific proportions of metal and composite layers of various orientations, have been established and are summarized in Table 2.1.

Glare enjoyed a second advantage over ARALL, in that at the time of its invention the splicing concept for FMLs was developed. Splicing entailed co-curing one large sheet of Glare by interleaving the smaller metal sheets at their boundaries. The overlap geometry was designed to ensure that the splice areas maintained structural properties equal to or greater than those of the base laminate.

Combined, the lack of post-stretching and the splicing technique allowed Glare to overcome the limitations of ARALL. Multi-orientation layups of fibers were now possible, as well. This made Glare particularly well suited to application as fuselage skin. Since the typical transport category aircraft fuselage is pressurized, a biaxial state of tension dominates in much of the structure. Laminates such as Glare 3 and Glare 4 orient fibers in the directions of hoop

Glare Grade	sub	Metal sheet thickness [mm] & alloy	Prepreg orientation	Main beneficial characteristics
Glare 1	-	0.3–0.4 7475-T761	0/0	fatigue, strength, yield stress
Glare 2	A	0.2–0.5 2024-T3	0/0	fatigue, strength
	B	0.2–0.5 2024-T3	90/90	fatigue, strength
Glare 3	-	0.2–0.5 2024-T3	0/90	fatigue, impact
Glare 4	A	0.2–0.5 2024-T3	0/90/0	fatigue, 0° strength
	B	0.2–0.5 2024-T3	90/0/90	fatigue, 90° strength
Glare 5	-	0.2–0.5 2024-T3	0/90/90/0	impact
Glare 6	A	0.2–0.5 2024-T3	±45	shear, off-axis properties
	B	0.2–0.5 2024-T3	∓45	shear, off-axis properties

Table 2.1 – *Standard Glare grades [5]*

stress and longitudinal stress.

Glare is currently used as skin material on the fore and aft fuselage crowns of the Airbus A380. Results from the full-scale fatigue test aircraft show very few crack initiation sites in the Glare skin and extremely slow crack growth where cracks did initiate [7]. A number of cracks arrested after periods of growth. Experience so far with the A380 supports the notion of Glare’s excellent durability, as well as demonstrating its manufacturability at the scale needed to support the production of a large commercial airliner.

Though Glare is now accepted as a mature technology for thin fuselage skin, can the FMLs be used to improve other, thicker structural components? There are, loosely, two classes of structural elements where a thickness greater than that of typical fuselage skin is required and where the damage tolerance advantages of FMLs could provide improved weight or longevity. One is internal, 3-dimensional “big bones,” such as ribs, frames, and bulkheads. The second is lower wing skins.

For both classes of structure, concepts employing FMLs as selective reinforcement have been developed. Selective reinforcement involves the strategic placement of a Glare or other FML strap, bonded to the metallic substrate

that makes up the bulk of the structural element, in order to provide effective crack retardation. This has the advantage of applying the FML only where additional crack growth resistance and residual strength are most needed.

One big bone structure where selective reinforcement with Glare is being implemented is the rear wing attachment frame of the A400M military transport aircraft [8]. Due to the high spectrum loads carried through a point attachment on the frame and the need to treat the frame as single load path structure, a design change was needed. Options considered included increasing the thickness of the inner flange, the location of high tensile stress in the frame, and bonding titanium or Glare straps to the flange. In preliminary testing, the slow crack growth of the Glare reinforced part and its low weight compared to both other options (the titanium strap was riveted, adding weight compared to the bonded Glare strap) won out.

Selective reinforcement of wing and fuselage skin with bonded Glare straps was explored by Heinemann et al. in a large panel crack growth and residual strength testing program [9, 10]. Glare straps were bonded in different configurations to the panels. Some panels had the straps bonded to the skin along the stringer center-lines, with the stringers fastened on top of the straps. Others, those panels with integral stringers, had straps in the stringer bays. In both cases, the straps led to longer crack growth lives at stresses 25% greater than the baseline.

The advantages of such straps, in addition to the direct benefit of improved crack growth resistance and residual strength of the structure, include their tailorability and manufacturability. The straps can be located only where additional damage tolerance is needed and manufactured separately from the substrate. This allows for post-cure stretching of the FML straps and easy application of the strap to a single- or double-curved substrate.

Bonded FML straps suffer from industry-wide skepticism regarding all bonded strap reinforcements resulting from historical difficulties. The bonded titanium straps on the Lockheed L-1011 had severe long-term stability issues due to poor bond quality and environmental degradation of the adhesive. Conservatism is required when certifying bonded straps in primary structure — the structure must be designed to withstand a complete delamination of the strap, undetected for some time. This scenario may be mitigated by adding fasteners to secure the strap to the skin, nullifying bonding's benefit of fewer holes and stress concentrations, or by placing the straps under mechanically fastened stringers, which limits the flexibility of designing with the straps.

The high load transfer from a cracked thick skin sheet into a strap can cause large delaminations in the strap-skin bondline. Though such delaminations

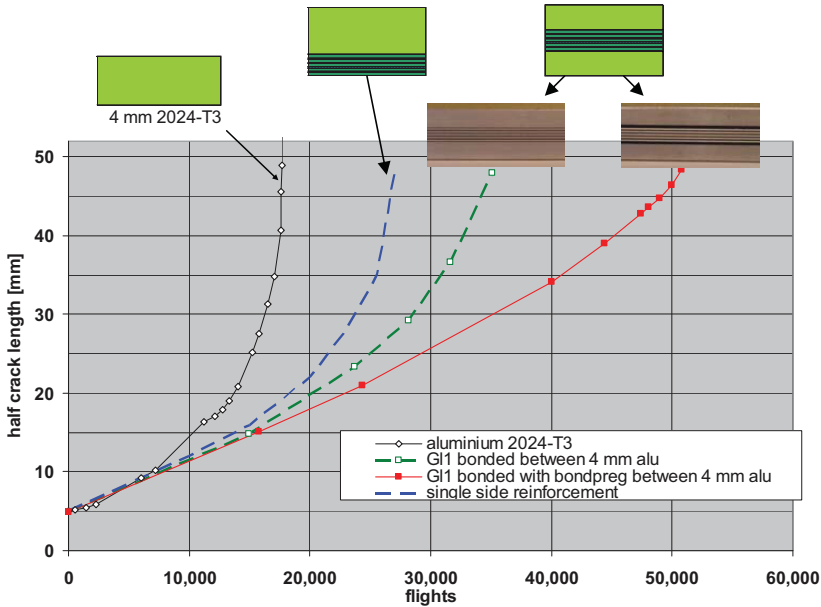


Figure 2.1 – Fatigue crack growth behavior for center cracked specimen under mini-TWIST fatigue loading ($\sigma_{mean} = 100$ MPa, $R_{GAG} = -0.1$, with peaks truncated to 1.15) [11]. The inset images illustrate the laminate stacking sequence. From left to right: monolithic aluminum, aluminum reinforced externally with Glare, aluminum with adhesively bonded internal Glare reinforcement, and internal Glare reinforcement with fibers in the bondline.

were found to grow stably in Alcoa’s large panel test program [9], their large size served as an ominous reminder of the kinds of whole-strap debonding troubles of which manufacturers were very wary. By moving the straps from the surface of the metal skin to the inside, the high crack bridging stresses were effectively cut in half, resulting in even more effective crack retardation and smaller delaminations than single-sided Glare strap reinforcement [11]. This laminate concept was referred to as CentrAl, for centrally reinforced aluminum.

Figure 2.1 shows the results of simple center-cracked test specimens with thick metal and various reinforcement concepts subject to spectrum loading. The single-sided reinforcement extended the crack growth life of the specimen by 50%, and the central reinforcement doubled the life.

One drawback of adhesively bonded external and central Glare reinforce-



Figure 2.2 – Comparison of delamination areas for adhesive (left) and bondpreg (right) CentrAl laminates [11]

ment that was observed in these and similar tests was that the adhesive bond was so tough, the thin metal layer of the reinforcement adjacent to the skin cracks right along with the thick skin. This metal layer thus makes no contribution to the crack bridging, and the delamination in the first fiber layer becomes quite large, as shown in the left side of Figure 2.2. The solution to this problem, the addition of fibers to the bond line to weaken the bond, allowing delamination to occur in that interface, was termed “bondpreg.” These fibers also created a physical barrier to crack growth directly through the adhesive. The furthest right crack growth curve in Figure 2.1 shows the dramatic improvement obtained with the inclusion of fibers in the bondline.

By further modifying the laminate, breaking the thick metal outer sheets into two or three thinner sheets on each side, a range of crack growth performances resulted. Altering the lay-up of bondpreg, from prepregged fibers with one adjacent adhesive layer to prepreg with a half-thickness adhesive layer on each side, additional improvement was obtained. The effects of these changes are shown in Figure 2.3. The range of crack growth results obtained by changing the laminate stacking sequence and composition demonstrates that crack growth performance is a tailorable property, just like stiffness and static strength!

By demonstrating that layer thickness is a viable design variable, manufacturability becomes a tailorable property as well. Fewer, thicker metal layers

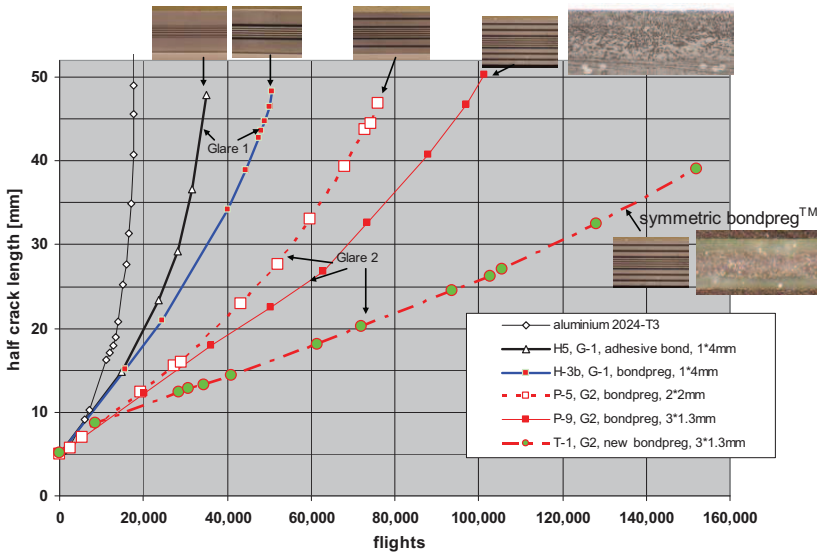


Figure 2.3 – Minor changes to the laminate such as multiple outer layers and symmetric Bondpreg resulted in large changes in crack growth performance [11]

results in fewer lay-up operations required in constructing the laminate. This improved manufacturability can be weighed against the damage tolerance improvement of more, thinner metal layers when making design decisions.

Similarly impressive results for CentAl laminates with the bondpreg improvement were obtained in Alcoa’s large, stiffened panel testing program [9, 10]. Under wing spectrum loading (with 25% higher stresses than the baseline spectrum) the CentAl panel’s cracks virtually arrested after just 25 mm of growth. The growth was so slow overall that it reached 25 mm of growth in as many cycles as the baseline monolithic metal panels in this program took to reach 100 mm.

In addition to its crack growth performance, the CentAl concept offers other advantages. Its thick outer layer prevents knife-edging. The increased thickness of the metal layers also allows for the use of additional alloys, such as aluminum-lithium, that cannot be easily manufactured in typical Glare metal thicknesses of 0.3-0.5 mm. The reinforcing is most important for span-wise stresses. The inner Glare layer can be manufactured separately in thin strips and butted together when manufacturing the CentAl laminate. This simplifies the manufacturing of the CentAl, since a separate dedicated Glare process can

be used, and since the Glare layers become one layer to add when manufacturing the final laminate, instead of 7 or more. The strips can be machined in advance with the appropriate contours for a double curved laminate. However, the implementation of this strap concept carries with it additional constraints. The effects of the straps' span-wise butt joints on fastener hole location, repairability, and chordwise stress concentrations must be analyzed and considered in design.

2.2.1 Arbitrary FMLs

While the CentrAl concept has already shown great promise, there is no compelling reason that its configuration, a Glare laminate inside some number of thicker aluminum layers bonded with prepreg and adhesive, is necessarily the ideal configuration for a thick FML. In fact, the need to reduce the thickness of a wing skin toward the tip means there must necessarily be “non-CentrAl” areas as ply drop-offs are used to transition between different laminate configurations, and as the Glare reinforcement would likely be dropped itself.

The sensitivity of laminate crack growth performance to subtle changes in the laminate demonstrated in Figures 2.1 and 2.3 suggest that a more arbitrary configuration of the laminate may indeed be advantageous if care is taken to understand the effects of design choices.

A more free, arbitrary laminate configuration allows many aspects of the laminate to be changed:

- Mixed thicknesses — There are a variety of reasons varying the thickness of the metal or composite layers in an FML. Thick metal layers are easier to machine, and can be strategically located in the outer layer of an FML skin sheet to allow countersunk fastener installation without knife-edging. Thin metal layers may be preferred in other locations to slow crack and delamination growth, since thinner layers will require lower bridging loads in adjacent fiber layers². Fiber layers may be manipulated with additional thickness to cope with the large bridging loads of thicker metal layers, to smooth thickness steps in the laminate, and add thickness to the laminate, improving bending stiffness.

²To a small extent, mixed-thickness Glare was been demonstrated in the Glare Megaliner Barrel program, with a Glare 3 laminate consisting of two external 0.4 mm metal sheets and three internal 0.3 mm metal sheets, as well as other similar combinations of thicknesses [5, p. 248].

- Mixed materials — In metals, there is typically a trade off between high strength and high toughness. In an FML, tough and strong alloys could be combined in one laminate to achieve an ideal balance. High toughness alloys could be employed in thicker layers, toward the outer layers of the laminate, while high strength alloys could be included as thin layers toward the middle of the laminate, to mitigate their poor crack growth. Laminate concepts employing entirely different metals have been proposed, as well. Fiberglass layers can also provide effective insulation between aluminum and steel layers in the same laminate [12]. Different fiber systems, with differing stiffnesses, may be located throughout the laminate to enable fine tailoring of bending and tensile properties.
- Asymmetry — The stress profile through the thickness of a wing skin is asymmetric. Since the bending moment is borne by the entire wing box, the lower wing skin sees tension, increasing toward the lower surface. An asymmetric layup may be better matched to such a loading than similar symmetric configurations. Tension-bending coupling of a laminate is often controlled in composite structures to achieve tailored structural performance. This technique could be exploited in FMLs through asymmetry. Asymmetry may also be useful for controlling crack growth. A damage tolerant philosophy of design relies on the use of inspections to ensure safe flight for a given interval. An asymmetric laminate could be designed to encourage crack growth in more inspectable layers — for example, the bottom layer of a lower wing skin can be inspected from outside the aircraft, while the top layer must be accessed through the fuel tank. If a cracked lower wing skin was certain to have longer cracks in the outside layer than in the inside layer, or any of the internal layers, difficult internal inspections would not be necessary.
- Orientations — Existing Glare variants have unidirectional fibers for applications with largely unidirectional stress, biaxial, $0^\circ/90^\circ$ fibers for biaxially stressed applications, and biaxial, $\pm 45^\circ$ fibers for applications where impact is a design driver. More free fiber orientation, including mixed orientations within a laminate, would improve the tailorability of FMLs. Techniques employed in composite structure, such as engineered tension-shear coupling, as used in the X-29 wing [13], could be employed in FMLs as well.

2.3 Need for a generalized crack growth model

The previous section made the case that designing generalized laminates may be beneficial. However, it does not necessarily follow that a generalized analysis method is needed for crack and delamination growth in such laminates. It is the results of testing some of the newest FML designs, as well as some unique tests on old Glare configurations, that highlight this need.

A prime example of a complex laminate with complex crack and delamination growth is the CentrAl configuration tested in a five-stringer crack growth and residual strength test by Heinimann *et al.* [9, 10]. A skin crack was initiated as a saw-cut in the center of the panel, and the center stringer was severed at this location. Loading cycles were applied — both constant amplitude and spectrum tests were conducted — until cracks in the skin grew just beyond the adjacent stringers. Further saw cuts were made to sever the fibers in the stringer bays, in the wake of the cracks, and the load was monotonically increased until the panels completely failed. The complex loading of the FML skin, with highly localized secondary bending due to the severed stringer, resulted in drastically different crack lengths across the thickness of the laminate. The stringer-side cracks grew much faster than the opposite side, becoming as much as four times as long. This same secondary bending moment resulted in much smaller through-the-thickness differences in panels with monolithic aluminum skin. No existing analytical model has the capability to model different-length cracks on opposite sides of the laminate growing while subject to a changing combined tension-bending load.

Teardown results of similar CentrAl panels [11] have shown drastic differences between the crack lengths in the outer thick layers and inner thin layers, as well. The inner layers tended to have crack lengths around 60% as long as the outer layers. The delaminations also differed through the thickness, with triangle-shaped delaminations in the inner prepreg-only interfaces, and shorter, more elliptical delaminations in the interfaces with additional adhesive. The internal cracks are short enough that modeling with the assumption that they grow together with the outer cracks is inappropriate, but not so short that the reduction in bridging effectiveness due to their growth can be ignored. No current model is suited to explicitly modeling their growth and the associated effects on the outer cracks.

Randell showed the capability to model non-uniform crack growth due to bending in Glare laminates by supplementing existing analytical models with finite element analysis (FEA) results [14]. However, the FEA results are laminate and loading specific. With the increased number of design options avail-

able thanks to the concepts outlined in the previous section, using this approach to develop a specialized laminate for structures with bending loads is impractical, though it is certainly suited to analyze a particular laminate in isolation. Replacing the FEA step with an analytical formulation would give vastly more power in the customization and optimization of FMLs.

Taken together, these examples illustrate the need for a more generalized model of cracks and delaminations in FMLs. Considering the wide range of possibilities for future laminates enabled by new design concepts, as listed in the previous section, only a fully generalized model will be capable of analyzing the unknown future FML laminate configurations subject to the wide variety of possible load cases.

2.4 Goals of this work

The goal of this work is to develop a crack growth model for fiber metal laminates that can account for the following:

- Arbitrary lay-up subject to arbitrary loading
- Independent crack lengths in each cracked layer
- Independent growth of delaminations at each interface

This model should predict crack and delamination growth as accurately as possible; be derived solely from first principles of mechanics; and take as input only material properties, laminate configuration and geometry, and loading conditions.

These goals are derived from the need to understand the experimental results and predict the performance of the potential new configurations described in the previous sections. The need for accuracy of the model's results is self evident. The requirement that the model tend toward the use of the physics of the problem, avoiding extraneous assumptions and inputs to fit the model to experimental results, is included to ensure that the model is useful not only for the current generation of advanced FMLs but is adaptable to any future FML concepts.

2.5 Extant crack growth models

This section will briefly discuss the FML fatigue crack growth models previously developed by other researchers. No attempt to assess the relative performance of these models against one another will be made, as all of these models share one major deficiency for use in this research: they are not applicable for non-regular FMLs. Alderliesten provides a review of these models and their appropriateness for modeling crack growth in regular FMLs [15], but the most relevant aspect of each model for this work is its utility as a basis for a generalized model. The existing models will be briefly described in the following sections, and the major reasons each is not suitable as a basis for a generalized model will be given.

2.5.1 Empirical

Several empirical methods have been proposed and refined for use in predicting crack growth in Glare. Such methods can be useful when performing basic design calculations on an already-existing, standardized laminate configuration. By dint of being based on empirical results of like laminates, these models are incapable of predicting the results of any change to a laminate, such as those described in Section 2.2.1. Therefore, all of the empirical models are ill suited to serving as a starting point for the development of a predictive, generalized model.

The existing empirical approaches can be broadly divided into two categories: those that attempt to shoehorn FML crack growth into models used for monolithic materials using correction factors and those that attempt to capture the unique phenomenological nature of crack growth in FMLs.

Those in the correction factor category, such as the models of Toi [16] and Takamatsu *et al.* [17] rely on the calculation of a stress intensity factor for the laminate as a whole, based on the crack length, loading, and geometry of the tested laminate. The crack growth rate is measured, and, since the relationship between the crack growth rate of the monolithic metal and its stress intensity factor is known, the stress intensity seen by the outer metal layers is calculated from the experimental growth rates. The ratio between the two stress intensity factors becomes a correction factor, β_{FML} multiplied along with the geometry correction factor to determine the laminate stress intensity factor to be used in crack growth prediction:

$$\Delta K_{FML} = \beta_{FML} \beta_{geom} \Delta \sigma \sqrt{\pi a} \quad (2.1)$$

Toi treated β_{FML} as a function of crack length, and Takamatsu *et al.* developed a β_{FML} that was a function of both crack length and maximum applied stress. Both of these correction factors leave out a number of other aspects of FMLs that influence the crack growth rate, such as starter notch length and geometry, cyclic stress ratio, and, of course, stacking sequence and composition of the laminate [15, 18, 19]. Acquiring sufficient empirical data to account for more of these parameters within one correction factor would be incredibly burdensome.

One special aspect of crack propagation in FMLs is the phenomenon of cracks growing at a nearly constant rate following some initial transient period. Cox [20] proposed that the stress amplitude could be used to predict the crack growth rate by multiplication with a function, f_s , that is characteristic of a given laminate:

$$\frac{da}{dN} = f_s \Delta\sigma \quad (2.2)$$

Wilson *et al.* [18, 19]³ explored this relationship for CentrAl and showed that Equation (2.2) could be replaced with a power law, in which the coefficient, C_{SS} depends on the stress ratio, and both the coefficient and the exponent are specific to a given laminate configuration. By basing the formula in Equation (2.3) on the net stress, rather than the gross applied stress, an attempt was made to account for the effects of different notch sizes.

$$\frac{da}{dN} = C_{SS} \Delta\sigma_{net}^{n_{SS}} \quad (2.3)$$

The equivalent crack length approach of Guo and Wu [21] incorporates the steady state aspect of FML crack growth into the concept of the laminate as a monolithic material. The crack length, a in the stress intensity factor equation is replaced with the equivalent crack length, l_0 . It also attempts to account for the transient period of crack growth by including a correction factor, β_{notch} , that is a function of crack length and approaches unity as the crack length increases:

$$\Delta K = \beta_{notch} \Delta\sigma \sqrt{\pi l_0} \quad (2.4)$$

³An adaptation of [18] is included in this thesis as Appendix B.

2.5.2 Analytical

A number of analytical approaches have been developed for FMLs, and most share two common assumptions: superposition of stress intensity factors in the metal layers and crack growth according to the stress intensity factors at the metal crack tips. As in Equation (2.5), the stress intensity factor seen by the metal sheets in an FML are considered the result of two factors. One, K_∞ is the stress intensity factor due to the farfield stress in the metal layers, and the other, K_{br} , represents the reduction in stress intensity factor due to the bridging load transfer from the metal sheets into the fiber layers.

$$K_{metal} = K_\infty - K_{br} \quad (2.5)$$

Once the K_{metal} is determined at the minimum and maximum of the loading cycle, conventional crack growth calculations, based on property data of monolithic metal sheets of the same alloy, are applied.

Model of Marissen

The crack and delamination growth model of Marissen was developed for ARALL FMLs [6]. This model employs the approach used by most subsequent models. Starting from an initial crack and delamination configuration, the bridging load is determined⁴. The bridging load is used to calculate the true metal stress intensity and the energy release rate of the delamination. These two parameters drive the growth of the crack and delamination, which are incremented. With the new damage geometries, the process repeats.

Based on physical examination of tested ARALL specimens, Marissen developed a number of assumptions that enabled translation of the bridging problem into explicit equations. These included a fixed elliptical delamination shape, with the major axis coinciding with the crack and terminating at the crack tip, and the minor axis on the panel centerline (or centered on the saw cut tip in saw cut panels).

The other significant assumption was that the bridging load is distributed equally along the delamination boundary. Marissen justified this assumption by noting the self-balancing nature of the delamination. Any portion with a higher bridging stress would tend to grow faster, and a longer bridging length would reduce the bridging stress in that portion of the delamination.

⁴Marissen referred to the bridging *stress* rather than load, which makes sense in the context of a laminate with fixed layer thickness and equally cracked metal layers.

The assumption of elliptical delamination shape has been shown to be inappropriate for other FMLs, based on experimental observation [11, 21, 22]. Further, a number of numerical calculations using subsequent models that treated the bridging stress distribution as an unknown found that the assumption of a constant bridging stress was unrealistic [22, 23]. These models found that the bridging stress tended to peak toward the crack tip, and that the nature of this peak was strongly dependent on the delamination shape. The resulting stress intensity factor was found to be very sensitive to this bridging stress peak. However, the ARALL modeled by Marissen differs from these later models, which focused on Glare, in the distribution of adhesive through the composite layers. Due to the production method of ARALL, in which the composite layers were manufactured as a filament wound fiber layer sandwiched within two adhesive sheets, an adhesive rich region existed at the interface between the composite layers and the metal layers. The shear deformation of this adhesive rich region, which Marissen took care to model, may have reduced the intensity of bridging stress peaks in ARALL.

The assumptions of constant bridging stress distribution and fixed elliptical delamination shape are contradictory in the context of a growing crack and delamination. Marissen approached the calculation of delamination growth by considering a two-dimensional strip of laminate, as shown in Figure 2.4, with cracked metal layers and intact fibers. The strain energy release rate was calculated using the change in strain energy and work with incremental growth of the delaminations. This resulted in a solution for the energy release rate that was a function of both the applied laminate stress and the bridging stress. This energy release rate determined the growth rate of the delamination at a single point — the minor axis of the ellipse, located on the specimen centerline or above the notch tip. However, if the bridging stress distribution was truly constant, the strain energy release rate should also be constant along the delamination front, and the delamination should grow at an equal rate at every point along the front. However, the delamination shape after a single iteration (or after an infinitesimal increment of growth) would no longer be an ellipse if the delamination at every point grew the same amount⁵!

The advantage of the assumptions used by Marissen is that they enabled a simple, direct solution for the value of the bridging stress based on the requirement of compatibility at the delamination front. The first component in the compatibility relation is the elongation of the bridging fibers over the delami-

⁵The energy release rate only calculated for damage growth parallel to the direction of loading. The bridging stress was also defined in this direction. Had the energy release rate for growth normal to the delamination front been calculated, and found to be equal along the entire front, then it would be possible for the delamination to remain an ellipse.

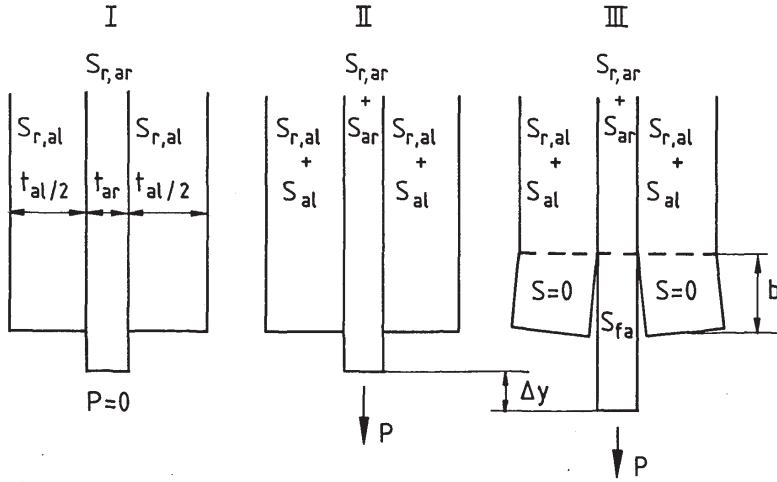


Figure 2.4 – Diagram of interrupted ply strip for strain energy release rate calculation from [6]

nation height. This is easily calculated by multiplying the strain of the fibers, a sum of the farfield strain in the fibers and the strain due to the bridging stress, by the delamination height, which was given by the equation of an ellipse⁶. The other component of the compatibility relationship was the displacement of the edge of the delaminated area. Marissen calculated this using a relation for the deformation of an infinite sheet with an elliptical hole with farfield tension and traction (equal to the bridging stress) on the hole edge. The laminate stiffness and thickness were used in this deformation calculation. This approach to the deformation underestimates the stiffness of the region which the delamination, since the metal layers, while cracked, will still provide some resistance to deformation. Further, by including the fibers in the stiffness of the material outside the delamination zone, it is inconsistent with the notion that the bridging stress represents load shed from the metal layers into the bridging fiber layers.

The model's internal inconsistencies, along with the fact that a number of assumptions used in the Marissen model are inconsistent with test results and would make the application of the model incompatible with laminates where multiple delamination shapes have been observed within the same lam-

⁶In further development of the model, the bridging fiber displacement was also modified to account for the effects of shear in the composite and residual stresses in the laminate.

inate, suggest that this model is inappropriate for adaptation as a generalized model. Fortunately, subsequent analytical models by Guo and Wu [21, 23] and Alderliesten [22, 24] have taken the original framework of Marissen’s approach and replaced these inappropriate assumptions with explicit calculations of the bridging load distribution along the delamination incorporating the effects on bridging and independent growth of arbitrary delamination shapes.

Model of Alderliesten

The model of Alderliesten employs the same iterative framework as the model of Marissen. The model is initialized with the input of material properties of each constituent and the number and thickness of the layers of each constituent. Because cross-ply laminates were common Glare configurations, prepreg layers with orientations of 0° and 90° are considered. Also input are the cure and test temperatures, the loading parameters, and the specimen and initial damage geometry. The Alderliesten model was developed specifically for center-cracked tension specimens, treated as quarter-symmetric.

The individual layer stresses, including thermal residual stresses, are calculated with classical laminate theory (CLT), and the iteration begins by solving the bridging problem.

Compatibility is employed as a means of calculating the bridging load. Since the metal and fiber layers are connected at the delamination boundary, the displacement there must be the same in each layer. The left side of Equation (2.6) gives the crack opening of the cracked metal layer, which Alderliesten assumes is nearly equivalent to the displacement at the delamination boundary. Here, superposition is employed to separate that due to the farfield stress, v_∞ , and that due to bridging, v_{br} . The right side of Equation (2.6) gives the displacement of the reinforcing fiber layers at the delamination boundary. The term, δ_f , represents that displacement due to the elongation of the fibers, and δ_{pp} accounts for shear deformation in the prepreg layer at the delamination boundary. All of the terms in Equation (2.6) are functions of x since the bridging stress, crack opening, and fiber elongation may vary along the boundary, and compatibility must hold at all x .

$$v_\infty(x) - v_{br}(x) = \delta_f(x) + \delta_{pp}(x) \quad (2.6)$$

The $v_{br}(x)$ and $\delta_f(x)$ terms are both functions of the bridging load, and Equation (2.6) can therefore be solved for the bridging load distribution. In

turn, K_{metal} can be determined from these results, and the growth of a crack in an FML can be predicted.

For the crack opening due to the farfield stress in the metal layers Alderliesten uses the following equation, from [25], in which $\sigma_{\infty,al}$ represents the farfield stress in the metal layers and E_{al} is the metal stiffness:

$$v_{infly} = 2 \frac{\sigma_{\infty,al}}{E_{al}} \sqrt{a^2 - x^2} \quad (2.7)$$

The crack opening due to the bridging load is expressed as an integral of the crack opening due to point loads along the delamination boundary:

$$v_{br}(x) = \int_s^a v(x, x_p) dx_p \quad (2.8)$$

In Equation (2.8), s is the width of the saw cut, where no fiber bridging force is present, and $v(x, x_p)$ is the crack opening displacement at horizontal location x due to a point load applied at location x_p . Alderliesten approximates $v(x, x_p)$ as

$$v(x, x_p) = \frac{4P(x_p)}{\pi E} \left(\tanh^{-1} \sqrt{\frac{a^2 - x^2}{a^2 - x^2 + b^2}} + \frac{\frac{1}{2}(1 + \nu)b^2}{x_p^2 - x^2 + b^2} \sqrt{\frac{a^2 - x_p^2}{a^2 - x^2 + b^2}} \right) \quad (2.9)$$

for $x < x_p$, and

$$v(x, x_p) = \frac{4P(x_p)}{\pi E} \left(\tanh^{-1} \sqrt{\frac{a^2 - x^2}{a^2 - x_p^2 + b^2}} + \frac{\frac{1}{2}(1 + \nu)b^2}{x^2 - x_p^2 + b^2} \sqrt{\frac{a^2 - x^2}{a^2 - x_p^2 + b^2}} \right) \quad (2.10)$$

for $x > x_p$. In Equations (2.9) and (2.10), $P(x_p)$ represents the bridging load along the delamination boundary, normalized to the metal layer thickness⁷. This approximation combines the solutions for crack opening displacement due to point loads above and below the crack plane on the centerline and point loads on the crack flanks to the left and right of the centerline from [25] in such a way that Equations (2.9) and (2.10) correspond exactly to those handbook solutions in the limits of $x \rightarrow 0$ and $b \rightarrow 0$, respectively.

⁷Alderliesten referred to the bridging load with the variable, S_{br} , which represents the stress in the fiber layers due to bridging. P is used in this description of the model for consistency with the direct use of the line load in the generalized model in subsequent chapters.

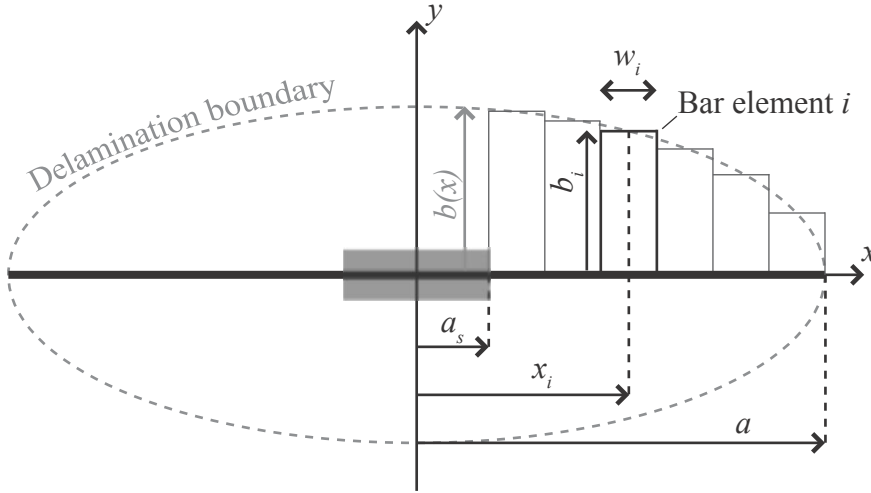


Figure 2.5 – Bar element scheme for solving the compatibility equation for the bridging stress

The stress intensity factor due to the bridging loads is similarly approximated by combining the solutions for the stress intensity factor due to point loads above the crack flanks along the centerline and due to point loads along the flanks, symmetric about the centerline.

$$K_{br}(x_p) = \frac{2P}{\sqrt{\pi a}} \frac{a}{\sqrt{a^2 - x_p^2 + b^2}} \left(1 + \frac{1}{2}(1 + \nu) \frac{b^2}{a^2 - x_p^2 + b^2} \right) \quad (2.11)$$

Because the integral in Equation (2.8) includes P , an unknown function of x_p , Equation (2.6) cannot be solved explicitly for the bridging stress distribution. Instead, it is solved numerically by treating the reinforcing stress material as a series of “bar elements” with width, w_i , height, b_i , and location at the center, x_i , as shown in Figure 2.5.

Under this scheme, the crack opening due to bridging at a given bar element, i , is given by:

$$v_{br}(x) = \sum_i v(x, x_i) w_i \quad (2.12)$$

Equation (2.6) can now be written as a series of linear equations - one equation for each bar element, in which its crack opening is a linear function of the bridging load at every bar element, as well as the farfield stresses - and solved with linear algebra.

The terms on the right side of Equation (2.6), when expressed per bar element, i , are:

$$\delta_{f,i} = \frac{\sigma_{\infty,f} + P_i \frac{t_m n_m}{t_f n_f} b_i}{E_f} \quad (2.13)$$

$$\delta_{pp} = C_b \sigma_{\infty,al} t_{al} \sqrt{\frac{t_f}{G_f} \left(\frac{1}{F_{al}} + \frac{1}{F_f} \right)} \quad (2.14)$$

In Equation (2.14), the prepreg shear is calculated for a unidirectional, fiber angle of 0° , laminate. For cross-ply laminates, an alternate formulation is given. The C_b term is a parameter limiting this deformation for short delamination lengths, and the F parameters are the effective stiffnesses of each constituent in the laminate, defined: $F = ntE$, where n and t represent the number of layers and thickness of a given constituent, respectively. This formulation is similar to the shear formulation used by Marissen, with the addition of the C_b parameter, not necessary in ARALL due to the presence of an adhesive-rich layer in the interface. Both the Alderliesten and Marissen shear formulas are functions of the farfield stress and not the bridging stress at the interface, which is physically unrealistic — the bridging load is transferred from metal layers to fiber layers as a shear stress. If there is no bridging, there should be no shear.

The overall stress intensity factor due to the distributed bridging stresses is given by summing the stress intensity due to the point bridging stresses at each bar element:

$$K_{br} = \sum_i K_{br}(x_i, P_i) w_i \quad (2.15)$$

The cyclic stress intensity factor range is determined by repeating the bridging stress calculation at the maximum and minimum applied cyclic loads, and $K_{max, metal}$ and $K_{min, metal}$ are determined with the relationship of Equation (2.5). The cyclic stress intensity factor range, ΔK_{metal} , and the stress ratio experienced by the metal layers crack tip, R_{metal} , which is not necessarily the same as the stress ratio of the applied loading, are determined from the crack tip stress intensities at the maximum and minimum loads. The crack growth

rate is calculated using a relationship between ΔK_{metal} and R_{metal} that is treated as a material property of the particular metal alloy of the laminate.

Delamination growth, in contrast to the fixed shape of Marissen's approach, is calculated separately in each bar element. The strain energy release rate is calculated by:

$$G_i = \frac{n_f t_f}{2j E_f} \left(\frac{n_{al} t_{al} E_{al}}{n_{al} t_{al} E_{al} + n_f t_f E_f} \right) \left(\sigma_{\infty, f} + P_i \frac{t_m n_m}{t_f n_f} \right)^2 \quad (2.16)$$

The maximum and minimum values, G_{max} and G_{min} , are used, with an interface-specific growth rate versus energy release rate property, to determine the cyclic growth rates of the delamination at each bar element.

The crack length was then extended by the width of one bar element, and the delaminations were grown according to the following equation. The process was repeated until a specified crack length was reached.

$$\Delta b_i = \frac{db}{dN} \Big|_i \frac{w}{\frac{da}{dN}} \quad (2.17)$$

This method was successful at predicting crack growth in a variety of Glare layups, in both cross-ply and unidirectional configurations. This method accurately captured the effects of changing notch sizes and applied loading. Alderliesten also validated the method by comparing crack opening displacements and delamination shapes *in situ* with those predicted by the model.

One disadvantage of this model in practice was instability of the delamination shape in the elements closest to the crack tip. Alderliesten attributed this to the high bridging loads in this area and mitigated the problem by applying a fixed shape to the four closest bar elements to the crack tip, interpolating between the height of the fifth bar element and zero at the crack tip⁸. Another difficulty of the Alderliesten model was convergence. Rensma [12] studied the effect of varying the bar element width on the predicted crack growth rates and found a strong influence on the resulting crack growth rate predictions, never actually identifying a converged result.

⁸It is possible that leaving the bridging stress out of the prepreg shear deformation formulation and using evenly-spaced bar elements played a significant role in this instability. The generalized model developed in this work, with its corrected shear formulation and biased bar element distribution, did not experience this instability. Another addition in the generalized model, incrementing the number of cycles per iteration based on limits on incremental crack *and* delamination growth may also help with stability in the crack tip region.

Model of Guo and Wu

The model developed by Guo and Wu [23, 26, 27] is similar in many ways to that of Alderliesten. The delamination is divided into a number of bar elements, and a separate bridging stress is calculated for each bar element. The bridging stress solution employs displacement compatibility, equating the crack opening displacement, due to the farfield and bridging stresses. The strain energy release rate of delamination is calculated in the same way as Marissen’s model.

One minor difference to the Alderliesten model is the use of a Green’s function crack opening formulation, rather than the approximated opening function of Alderliesten. The Green’s function used by Guo and Wu more exactly accounts for the effects of the bridging traction acting at the delamination boundary, some distance from the crack flanks. However, the use of the laminate stiffness in their Green’s function formulation, rather than the metal layer stiffness, may lead to overestimation of the crack closure due to bridging. Likewise, the crack opening due to farfield stress is calculated with the applied laminate stress and the laminate stiffness. It would be more physically realistic to use the metal layer stress and stiffness, since it is the metal layers, and not the laminate as a whole, that are cracked.

The use of the laminate stress in many parts of the model is problematic because it leaves out the effects of thermal residual stresses in the laminate. These stresses arise from the mismatch of coefficient of thermal expansion between the metal and fiber layers. Alderliesten’s model includes the thermal residual stress in the separate fiber and aluminum layer stresses calculated as the model is initialized. Wang and Smith [28] derived a correction to the Guo and Wu model, allowing residual stress to be taken into account, but it is somewhat cumbersome since it works around the original framework of a model that only considered laminate stress rather than individual layer stress.

The adhesive shear deformation formulation used by Guo and Wu, Equation 2.18, includes the bridging stress rather than the farfield stress used by Alderliesten. As noted in the previous section, this is more physically realistic.

$$\delta_{ad}(x_i) = \frac{2\sigma_{br}(x_i)}{E_{lam}} \sqrt{\frac{F_{la}F_{Al}}{jF_{ad}F_{fm}}} \quad (2.18)$$

The model of Guo and Wu was also developed with a variable bar element width, biasing the distribution of bar elements with more elements toward the crack tip and toward the sawcut. With such biased elements, good convergence

was demonstrated in the bridging stress solution [23]; however, no effort was made in the published articles to demonstrate convergence of the crack growth predictions of the model.

A major shortcoming of the model of Guo and Wu was the use of a fixed delamination shape. As in the model of Marissen, the energy release rate of the element at the sawcut or panel centerline is used to calculate the delamination growth rate. After the delamination height at that point is implemented, the rest of the delamination shape is interpolated from there to the crack tip. Guo and Wu used a triangular delamination shape in their predictions, but that does not truly match even the example experimental shape in their own paper [26], in which the delamination is rounded near the crack tip.

2.5.3 Other models

There are several models that try to use spring elements attached to the crack flanks in place of the bridging material [29–31]. As Alderliesten notes in [15], these models were developed with an eye toward bonded patch repairs, and are poorly suited to modeling FMLs, since the delamination shape, not accounted for in these models with the springs on the crack flanks, is an important aspect of FML crack growth.

Finite Element Analysis (FEA) techniques have also been used to model crack growth in FMLs [14, 32–36]. However, all such models to date rely on the tradeoff between high physical fidelity and low computational cost. These models either incorporate the assumptions of some analytical models, such as the use of spring elements to represent bridging material, or the models used are very complex, with many elements or complicated multi-scale modeling schemes. Some models, such as that in [34] rely on simplifying assumptions about uniformity of the damage state to reduce computational cost. A couple of these models have looked at the stress difference between different layers in Glare [33, 34], and one, that of Randell [14], even considers Glare in bending. However, none has been more generalized than that. The model of Randell used a FEA simulation of Glare in tension and bending to determine the bridging stress distribution in each cracked metal layer through the thickness. The FEA results were used as input to an analytical crack and delamination growth rate algorithm.

2.5.4 Summary

The model of Alderliesten is, of those examined, the most generalized, with its independent delamination growth rates along the delamination front. It is also the analytical model with the most direct connection to first principles of mechanics, free from such assumptions as spring elements or smeared laminate properties. Its modularity makes it highly adaptable to new geometries, loading regimes, and materials. For these reasons, it will be used as the basis for the generalized model developed in this thesis.

Bibliography

- [1] Vlot, A. (2001) *Glare: history of the development of a new aircraft material*. Kluwer Academic Publishers.
- [2] Jones, R. M. (1999) *Mechanics of Composite Materials*. Taylor and Francis, Inc., 2 edn.
- [3] Vinson, J. R. and Sierakowski, R. L. (2004) *The Behavior of Structures Composed of Composite Materials*. Kluwer Academic Publishers, 2 edn.
- [4] Gay, D. (2002) *Composite Materials: Design and Applications*. CRC Press.
- [5] Vlot, A. and Gunnink, J. (2001) *Fibre metal laminates: an introduction*. Kluwer Academic Publishers.
- [6] Marissen, R. (1988) *Fatigue crack growth in ARALL. A hybrid aluminium-aramid composite material: Crack growth mechanisms and quantitative predictions of the crack growth rates*. Ph.D. thesis, Delft University of Technology, Delft, The Netherlands.
- [7] Beumler, T. (2008) MoC for A380 hybrid structure. *ASIP 2008: the 2008 aircraft structural integrity program conference, Dec 2 – 4, 2008. San Antonio, Texas*.
- [8] Plokker, M., Daverschot, D., and Beumler, T. (2009) Hybrid structure solution for the a400m wing attachment frames. Bos, M. J. (ed.), *ICAF 2009, Bridging the Gap between Theory and Operational Practice: Proceedings of the 25th Symposium of the International Committee on Aeronautical Fatigue, 27-29 May 2009, Rotterdam, The Netherlands*, pp. 375–385.

- [9] Heinimann, M., Kulak, M., Bucci, R., James, M., Wilson, G., Brockenbrough, J., Zonker, H., and Sklyut, H. (2007) Validation of advanced metallic hybrid concept with improved damage tolerance capabilities for next generation lower wing and fuselage applications. Lazzeri, L. and Salvetti, A. (eds.), *Proceedings of the 24th ICAF Symposium*, Naples, Italy, May.
- [10] Heinimann, M. et al. (2007) Advanced hybrid structural concepts for care-free structures: Experimental validation and path forward. *ASIP 2007: the 2007 aircraft structural integrity program conference, Dec 5, 2007. Palm Springs, California*.
- [11] Roebroeks, G. H. J. J., Hooijmeijer, P. A., Kroon, E. J., and Heinimann, M. B. (2007) The development of CentrAl. *First International Conference on Damage Tolerance of Aircraft Structures*, Delft, The Netherlands.
- [12] Rensma, E. (2007) *Investigation of innovative concepts for hybrid structures*. Master's thesis, Delft University of Technology, Delft, The Netherlands.
- [13] Putnam, T. (1984) *X-29 flight-research program*. NASA technical report.
- [14] Randell, C. E. (2005) *Subsurface Fatigue Crack Growth in Glare Fibre Metal Laminates*. Ph.D. thesis, Delft University of Technology, Delft, The Netherlands.
- [15] Alderliesten, R. C. (2007) On the available relevant approaches for fatigue crack propagation prediction in glare. *International Journal of Fatigue*, **29**, 289–304.
- [16] Toi, R. (1995) An empirical crack growth model for fiber/metal laminates. *Proceedings of the 18th symposium of the international committee on aeronautical fatigue, Melbourne, Australia*, pp. 899–909.
- [17] Takamatsu, T., Matsumura, T., Ogura, N., Shimokawa, T., and Kakuta, Y. (1999) Fatigue crack growth of a glare3-5/4 fiber/metal laminate and validity of methods for analysing results. *Proceedings of the 20th symposium of the International Committee on Aeronautical Fatigue, Bellevue, Washington*, pp. 841–860.
- [18] Wilson, G. S., Alderliesten, R. C., and Benedictus, R. (2010) Steady-state crack growth in hybrid fiber metal laminates as a tool for design. *International SAMPE Symposium and Exhibition (Proceedings)*, May.

- [19] Wilson, G. and Alderliesten, R. (2009) Steady state crack growth prediction method for glare and advanced FMLs. *Proceedings of the 50th AIAA/ASME/ASCE/AHS/ASC Structures, Structural Dynamics, and Materials Conference*, May.
- [20] Cox, B. N. (1996) Life prediction for bridged fatigue cracks. Johnson, W. S., Larsen, J. M., and Cox, B. N. (eds.), *Life prediction methodology for titanium matrix composites. ASTM STP 1253*, pp. 552–572, ASTM.
- [21] Guo, Y. J. and Wu, X. R. (1999) A phenomenological model for predicting crack growth in fiber-reinforced metal laminates under constant-amplitude loading. *Composites Science and Technology*, **59**, 1825–1831.
- [22] Alderliesten, R. C. (2005) *Fatigue crack propagation and delamination growth in Glare*. Ph.D. thesis, Delft University of Technology, Delft, The Netherlands.
- [23] Guo, Y.-J. and Wu, X.-R. (1999) Bridging stress distribution in center-cracked fiber reinforced metal laminates: modeling and experiment. *Engineering Fracture Mechanics*, **63**, 147 – 163.
- [24] Alderliesten, R. C. (2007) Analytical prediction model for fatigue crack propagation and delamination growth in glare. *International Journal of Fatigue*, **29**, 628–646.
- [25] Tada, H., Paris, P., and Irwin, G. (1973) *The Stress Analysis of Cracks Handbook*. The American Society of Mechanical Engineers, 3 edn.
- [26] Guo, Y. J. and Wu, X. R. (1998) A theoretical model for predicting crack growth rates in fiber-reinforced metal laminates. *Fatigue & Fracture of Engineering Materials and Structures*, **21**, 1133–1145.
- [27] Guo, Y. J. and Wu, X. R. (2002) Fatigue behaviour and life prediction of fibre reinforced metal laminates under constant and variable amplitude loading. *Fatigue & Fracture of Engineering Materials and Structures*, **25**, 417–432.
- [28] Wang, J. T. and Smith, S. W. (2010) Residual strain effects on bridging stress of cracked and delaminated fiber metal laminates. *Journal of ASTM International*, **7**.
- [29] Kim, J. H. and Lee, S. B. (2000) Calculation of stress intensity factor using weight function method for a patched crack with a debonding region. *Engineering Fracture Mechanics*, **67**, 303–310.

- [30] Rose, L. R. F. (1987) Crack reinforcement by distributed springs. *Journal of Mechanics of Physical Solids*, **35**, 383–405.
- [31] Cox, B. N. and Rose, L. R. F. (1996) A self-consistent approximation for crack bridging by elastic/perfectly plastic ligaments. *Mechanics of Materials*, **22**, 249–263.
- [32] Yeh, J. R. (1995) Fatigue crack growth in fiber-metal laminates. *International Journal of Solids and Structures*, **32**, 2063–2075.
- [33] Burianek, D. A. (2001) *Mechanics of fatigue damage in titanium graphite hybrid laminates*. Ph.D. thesis, Massachusetts Institute of Technology.
- [34] Shim, D. J., Alderliesten, R. C., Spearing, S. M., and Burianek, D. A. (2003) Fatigue crack growth prediction in GLARE hybrid laminates. *Composites science and technology*, **63**, 1759–1767.
- [35] Miller, D. and Phelps, H. (2010) A finite element based stress intensity solution for cracks in fiber metal laminates. *ASIP 2010: the 2010 aircraft structural integrity program conference, Nov 30 – Dec 2, 2010. San Antonio, Texas*.
- [36] Saff, C., Heck, D., Forster, E., Flanagan, S., Fields, S., Gu, H., and Muntges, D. (2011) Advanced hybrid structures core technology development program: Program summary. *ASIP 2011: the 2011 aircraft structural integrity program conference, Nov 29 – Dec 1, 2011. San Antonio, Texas*.

This page intentionally left blank.

Chapter 3

The model

This chapter describes the structure of the generalized model, the way cracks and delaminations are dealt with numerically, and the underlying mechanics and mathematics of each step.

3.1 Overview

Overall, modeling the crack and delamination growth of an FML is an inherently iterative process — the damage configuration must be known in order to calculate its growth, and once it grows, the growth rates must be recalculated. Figure 3.1 gives an overview of the steps in this iterative process, and the main variables needed for and calculated in each step.

The laminate is initialized by inputting the layup of the laminate — the identity, orientation, and thickness of each layer in the laminate. The material properties relevant to each layer are input, including each material’s iso- or orthotropic elasticity properties, coefficients of thermal expansion, and properties relevant to the growth of damage in or adjacent to each layer. The loading and temperature parameters include the applied cyclic stresses to the laminate and the temperature range used in calculating thermal residual stresses. With all of these inputs, the stresses and strains in the farfield — the portion of the laminate remote from the damage location, denoted in this paper with the subscript, ∞ — can be calculated.

The damage is initialized by specifying the size of the panel’s sawcut, a_s , the length of each crack, \mathbf{a} , and the size and shape of each delamination in

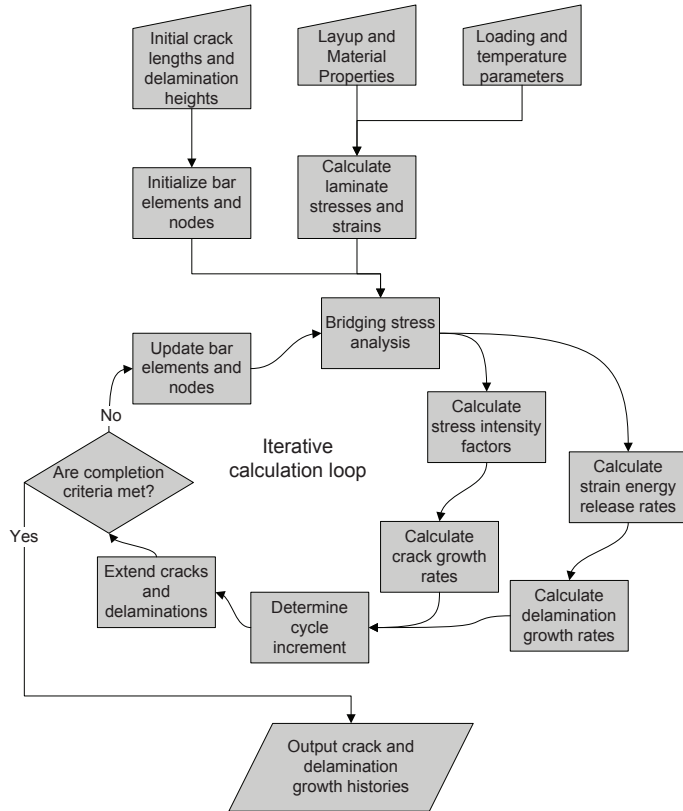


Figure 3.1 – Schematic of steps in the crack and delamination growth calculation method

the interfaces adjacent the cracked layers. For the purposes of performing the bridging calculation, the damage must be discretized, identifying specific locations along each delamination front where the bridging load is to be calculated.

The bridging load calculation takes the form of a displacement compatibility solution, solving simultaneously the set of equations describing the displacement of the cracked metal layers and the intact bridging material along the delamination fronts. With the bridging loads known, their effect on the stress intensity at the crack tips can be found, as well as the energy release rate of delamination growth. All of these calculations are performed twice — once at the maximum of the loading cycle and once at the minimum. Damage growth models that take as input the stress intensity factor and the strain energy release rate are used to calculate the rate of growth of the cracks and the delaminations, respectively.

The damage is grown based on the growth rate and an increment of applied cycles. This cycle increment is determined by a limit on the damage extension for each iteration. The discrete elements of the damage must be updated to accommodate the change in damage geometry. With the current damage, the calculation of bridging loads, growth drivers, and damage growth can repeat.

One or more parameters, such as a maximum crack length, maximum number of cycles, or maximum number of iterations, can be used as a limit, after which the calculation is stopped. Post processing, such as data output, graphing, and analysis then occurs.

3.2 Initialization and discretization

3.2.1 Material and laminate properties

A fiber metal laminate is composed of alternating layers of metal and fiber-reinforced composites. It may also contain additional adhesive to improve the delamination resistance of the interfaces. In the most general case, each layer may be of different composition, with respect to each other layer, and the thickness of each layer is independent. Additionally only some of the metal layers might be cracked, and those that are may start with cracks of different lengths.

A laminate is defined according to the attributes of each layer, listed below in Table 3.1. Table 3.2 lists the material properties required for the analysis. The delamination growth rate properties are needed only for composite or

Attribute	Description	Typical units
k	Layer number	
t_k	Thickness	mm
θ_k	Orientation	degrees
Cracked	Indicates this layer is cracked	Boolean
a_k	Initial crack length	mm
Adh	Indicates an adhesive only layer	Boolean
Material	Defines material properties (See Table 3.2)	

Table 3.1 – Attributes of each layer used in laminate definition

Property	Description	Typical units
E_1	Young's modulus in 0° direction	MPa
E_2	Young's modulus in 90° direction	MPa
ν_{12}	In-plane Poisson's ratio	
G_{12}	In-plane shear modulus	MPa
α_1	Coefficient of thermal expansion (0°)	$^\circ C^{-1}$
α_2	Coefficient of thermal expansion (90°)	$^\circ C^{-1}$
C_{cg}	Crack growth rate coefficient	$\text{mm} (\text{MPa}\sqrt{\text{mm}})^{-n_{cg}}$
n_{cg}	Crack growth rate exponent	
C_d	Delamination growth rate coefficient	$\text{mm} (\text{MPa}\sqrt{\text{mm}})^{-n_d}$
n_d	Delamination growth rate exponent	

Table 3.2 – Material properties defined for each layer (not all properties applicable to all layers)

adhesive layers, and the crack growth properties are needed only for cracked layers. Separating the geometric and material properties simplifies the definition of complex laminates. Multiple layers made of the same material can be identified with reference to that material, rather than repeating the same properties.

3.2.2 Calculating stresses with CLT

Classical laminated plate theory (CLT) is an oft-used method in the analysis of stress and strain in composite materials [1–3]. Its application to FMLs, when only elasticity is concerned, is no different from its application to conventional multi-material composite laminates, apart from the fact that some number of the constituent layers are isotropic. Recent work by Rickerd [4] has also

included plastic deformation of the metal layers in a CLT analysis.

The model takes as loading input a six-element vector, corresponding to the line load vector of CLT, divided by the thickness of the laminate. This puts the in-plane loads in stress format for easy comparison to test parameters. This vector corresponds to the cyclic maximum values of each of the six components of the line load. The stress ratio R is also input, such that the minimum of the load cycle is calculated by multiplying the maximum by R . This constrains the loads to be in phase and all have the same stress ratio. This is done for convenience, since this combination of inputs is sufficient to model all of the test specimens used to validate the model. However, the minimum and maximum loads could all be independently specified if desired.

CLT is used to calculate the stress at the midplane of each layer. The laminate strain, in-plane and curvature, is also derived. The stresses and strains are calculated including the effects of thermal residual stress. For some calculations, it is preferred to use only the stress or strain that is due to loading, ignoring the thermal component. These are also output from the CLT calculation, and the modules of the model in which they are used will be noted throughout this thesis.

3.2.3 Bar elements and nodes

The models of both Guo and Wu [5] and Alderliesten [6] discretize the cracked and delaminated FML by dividing it into bar elements along the x axis, from the notch tip to the crack tip. Bar element j , with its center located x_j from the laminate centerline, has width w_j and length $b(x_j)$, equal to the delamination height at that location.

The need for this discretization arose from the lack of a closed-form solution for a continuous bridging load distribution. Since the shape of the bridging load distribution along the delamination is unknown *a priori*, the integral of the crack opening displacement as a function of bridging loads (as in Equation (4.3), for example) is not indefinitely integrable. A discrete formulation of the integral as a sum allows the bridging problem to be solved with linear algebra.

The present generalized model has the added complexity of considering each interface separately. The method of solving for the bridging stress in this case is to apply compatibility along each delamination boundary, meaning that a separate integral must be written to relate bridging load along each delamination boundary to its displacement. Additionally, the bridging load along each delamination on an internal cracked metal layer also influences the

displacement at the delamination boundary on the opposite surface of that layer, meaning that an additional integral is required for each such delamination boundary. Again, since the shapes of the bridging load distribution along each boundary are unknown *a priori*, and since there is no set relationship between the distributions of different interfaces, discretization is necessary in order to solve the problem via linear algebra.

Let the points of intersection between bar element center-lines and delamination boundaries be referred to as nodes. It is at these locations that compatibility will be enforced in order to solve for the bridging load distribution (see Section 3.3.1). Node j, p refers to the point in the p th delaminated interface at the delamination boundary and at the centerline of bar element j . The bridging material elongation is considered separately within each bar element; thus, the bar element locations must be the same through the thickness of the laminate. So, node $j, 1$ and node $j, 5$ both have x -coordinate x_j and the associated width for both is w_j . They may differ in delamination height at that node. Node $j, 1$ has y -coordinate $b_{j,1}$, and node $j, 5$ has y -coordinate $b_{j,5}$.

In previous models, the bar elements have been distributed evenly [6] and biased toward both ends of the delamination [5]. The bridging stress results from these models has shown that the bridging load is stable over most of the length of the delamination, except toward the crack tip where the bridging load changes significantly over a short distance. It is therefore most logical to bias the bar elements only toward the crack tip. Higher resolution of bridging loads toward the notch or panel center is not needed.

In a generalized model, the bar elements and nodes must be biased toward each of the crack tips to allow accurate modeling of the bridging loads leading up to each crack tip. The Chebyshev nodes [7] are employed in this model in order to ensure stability and accuracy of the bridging loads approaching each delamination tip. The formula for the location of the Chebyshev nodes when only a single crack length is considered, rewritten with a sine in order to give only increasing values with increasing j , is:

$$x_j = a_s + (a - a_s) \sin\left(\frac{\pi}{4} \frac{2j - 1}{n}\right), \quad i = 1, 2, \dots, n \quad (3.1)$$

where a_s is the length of the notch, and n is the total number of nodes.

To adapt this distribution for multiple crack lengths, the crack lengths must first be sorted to increasing order, \tilde{a} . The redundant crack tips, two or more cracks with the same length, are dropped in sorting \tilde{a} . The bar element distribution is calculated over each interval between the crack lengths:

$$x_j = a_s + (\tilde{a}_1 - a_s) \sin\left(\frac{\pi}{4} \frac{2j-1}{n_1}\right), \quad j = 1, 2, \dots, n_1 \quad (3.2)$$

$$x_{j+\sum_{i=1}^q n_i} = \tilde{a}_q + (\tilde{a}_{q+1} - \tilde{a}_q) \sin\left(\frac{\pi}{4} \frac{2j-1}{n_{q+1}}\right), \quad (3.3)$$

$$j = 1, \dots, n_{q+1}, \quad q = 1, \dots, N_c - 1$$

where N_c is the number of cracks, minus the redundant crack tips, and n_q is the number of nodes in interval q .

The corresponding bar element widths come from the derivative of the node locations:

$$w_j = \left(\frac{dx}{dj}\right)_j = \frac{\pi}{2n_1} (\tilde{a}_1 - a_s) \cos\left(\frac{\pi}{4} \frac{2j-1}{n_1}\right), \quad (3.4)$$

$$j = 1, 2, \dots, n_1$$

$$w_{j+\sum_{i=1}^q n_i} = \left(\frac{dx}{dj}\right)_{j+\sum_{i=1}^q n_i} = \frac{\pi}{2n_{q+1}} (\tilde{a}_{q+1} - \tilde{a}_q) \cos\left(\frac{\pi}{4} \frac{2j-1}{n_{q+1}}\right) \quad (3.5)$$

$$j = 1, \dots, n_{q+1}, \quad q = 1, \dots, N_c - 1$$

To select values of n_q , a limit on the width of the tip bar element is used. This limit, w_{max} , is treated as a parameter of the computation. A smaller tip element means more bar elements are required, and computational accuracy and cost should both increase. The effects of using different sizes of w_{max} are explored in Section 3.3.6. The value of n for each segment q is increased until $w_{tip,q} \leq w_{max}$.

With the bar elements defined, the nodes must be initialized. The bridging calculation depends on the delamination shape, so an initial delamination must be chosen. Alderliesten [6] showed that the chosen initial delamination shape has a limited impact on the simulation, with the delaminations converging to the same shape within a small number of iterations. The initial size of the delamination must also be considered — too small, and a large number of iterations are required for the delamination to grow to a stable size; too large, and the bridging effectiveness of the intact layers is reduced.

The initial delaminations are defined in this model according to a ratio between the crack lengths and initial maximum delamination height, \mathbf{b}_0 . A typical ratio chosen is one half, i.e. $\mathbf{b}_0 = 1/2(\mathbf{a}_0 - a_s)$, element-wise, where \mathbf{a}_0 is a vector of initial crack lengths.

Based on experimental observation of final delamination shapes, an initially parabolic shape is used. The delamination in each interface, p , is thus:

$$B_{j,p} = b_{0,k} * \sqrt{1 - \frac{x_j - a_s}{a_k - a_s}} \quad (3.6)$$

Now every node j, p has a location defined by $(x_j, B_{j,p}, z_{int,p})$.

3.3 Calculation loop

3.3.1 Calculating the bridging stress

In [8], the compatibility between the displacement of the cracked metal layers and the bridging material was used to calculate the bridging loads. The cracked metal layer displacement combines the tendency of the cracks to open due to farfield stresses and close due to bridging loads. The bridging material displacement is a result of the elongation of the fiber layers and their shear deformation near delamination boundaries. A separate value of the bridging load was determined at each delamination boundary in each bar element. The bridging load was calculated as a line load, representing the load transferred per unit bar element width along the delamination boundary.

Chapter 4 is adapted from [8], and includes an in-depth description of the calculation of the bridging loads. The correction for bridging by cracked layers, the δ_K correction derived in that chapter, is not integrated into the generalized model. For comparison, some results of including it in the model are compared against the standard, correction-less model are compared in Section 7.4.

An addition to the prepreg shear deformation derived in Chapter 4 must be made to account for the presence of additional adhesive layers at the metal-prepreg interface. These adhesive layers crack along with the metal and do not have the constraint of zero shear deformation even when the delamination length is zero. It can be shown, following a similar derivation to that used for prepreg shear in Chapter 4, that the shear deformation of such a geometry is:

$$\delta_{pp} = F_{br} \frac{t_2}{G_2} \sqrt{\frac{1}{t_2/G_2 + C_b t_3/G_3} \left(\frac{1}{t_1 E_1} + \frac{1}{t_3 E_3} \right)} \quad (3.7)$$

$$+ F_{br} C_b \frac{t_3}{G_3} \sqrt{\frac{1}{t_2/G_2 + C_b t_3/G_3} \left(\frac{1}{t_1 E_1} + \frac{1}{t_3 E_3} \right)} \quad (3.8)$$

where the subscript 1 refers to the cracked metal layer, 2 refers to the adhesive layer, and 3 refers to the bridging fiber layer. All of the assumptions described in Section 4.1.2 hold for this expression, as well.

3.3.2 Strain energy release rates

An approach to calculating the strain energy release rates (SERR) in an arbitrary FML with non-uniform damage was developed in [9]. That method calculated the strain energy in cross-sections of bar elements above and below each delamination, in order to determine the difference in strain energy as the delamination grows. The change in work done by the load the laminate carries was also found by accounting for the added displacement that comes with a growing delamination.

A detailed derivation and description of this approach is given in Chapter 5. That approach includes the use of the neutral line model (NLM) to account for secondary bending in asymmetrically delaminated bar elements. Because the NLM approach requires additional computational effort, a simplified SERR calculation is presented here and is used in the model simulations, unless otherwise stated. The results of using the simplified and full NLM SERR calculations are compared in Section 7.4.

Figure 3.2, which is the same as Figure 5.13 in Chapter 5, shows the typical trend in SERR from finite element analysis and full NLM SERR model calculations. When two delaminations of unequal length in the same bar element are far apart, the shorter one has a high SERR and the longer one has a relatively low one. Both of these values approach constant limits as the distance between the delaminations is increased reducing the effects of localized secondary bending on the SERR at the delamination fronts¹. As the delamination lengths approach each other, which happens around 8 mm in Figure 3.2, the SERRs tend toward equilibrium at the average of the two constant limits. In some cases the secondary bending results in a small region of cross over, in which the shorter delamination actually has a lower SERR than the longer one.

Assume that two states of relative delamination growth between two delaminations will occur over multiple iterations. Either the delaminations will diverge, and continue to grow separately, or they will grow together. This corresponds to two states in which secondary bending has negligible influence on

¹When the delaminations are far apart, the change in length of one of them has a negligible effect on the secondary bending, while when they are close together, the effect of the change in length of one is evident in the stress distribution due to secondary bending.

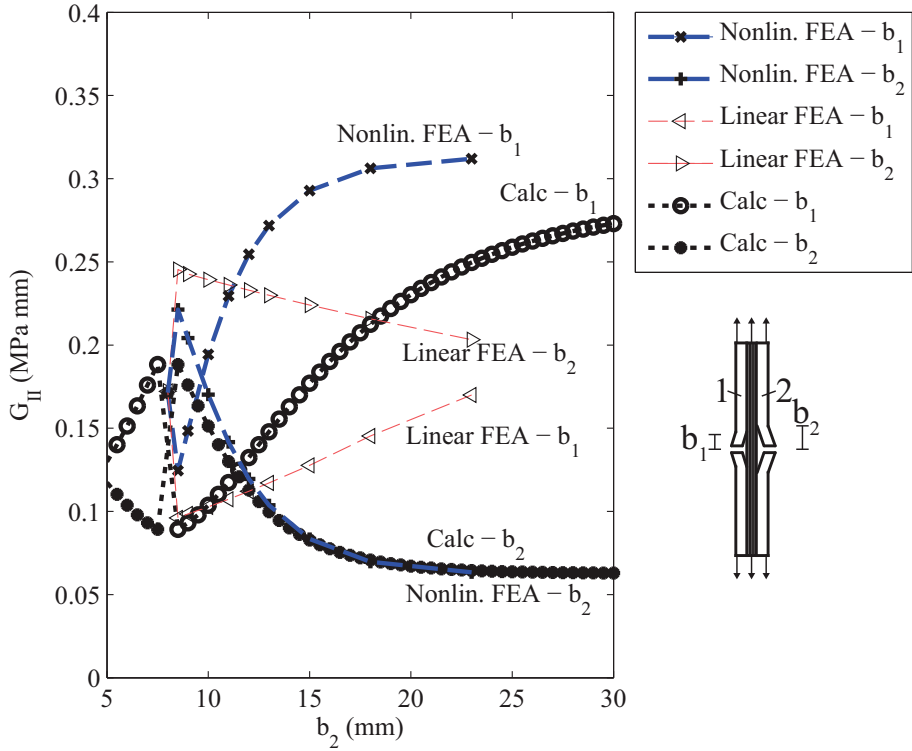


Figure 3.2 – Laminate with asymmetric delaminations, changing the length of b_2 while holding b_1 constant, laminate: $[0.3 \text{ mm Al} / 0.25 \text{ mm prepreg} / 0.3 \text{ mm Al}]$, $\sigma_{lam} = 100 \text{ MPa}$, $\Delta T = -100^\circ \text{C}$, $b_1 = 8 \text{ mm}$, $b_2 = x \text{ axis}$

the SERR. The SERR can therefore be estimated by removing the moment term from Equations (5.10) to (5.22) in Chapter 5, resulting in the following coefficients in the expressions for the components of SERR:

$$\psi_1 = \epsilon_{k\infty} + A_{11\ top}^* \sum_{n:b_n > b_i} F_{br_n} \quad (3.9)$$

$$\psi_2 = \kappa_\infty \quad (3.10)$$

$$\psi_3 = \epsilon_{k\infty} + A_{11\ bot}^* \sum_{n:b_n \geq b_i} F_{br_n} \quad (3.11)$$

$$\psi_4 = \kappa_\infty \quad (3.12)$$

Here, $A_{11\ top}^*$ refers to the (1, 1) term from the inverse of the A matrix from CLT, based on the “laminated” consisting of all the bridging material *above* the delamination of interest, with non-bridging layers treated as though they have zero stiffness. $A_{11\ bot}^*$ is similarly based on the intact material below the delamination.

3.3.3 Crack and delamination growth

The crack growth rate in each layer is determined based on a relation between the cyclic stress intensity factor, ΔK_k , of the crack in that layer and the crack growth properties of the material comprising layer k . The relevant stress intensity factor must account for the actual stress intensity around the crack tip in each layer, which is influenced by both the farfield stress in that layer and the bridging loads applied to that layer:

$$\Delta K_k = K_{max,k} - K_{min,k} = (K_{\infty,k,max} - K_{br,k,max}) - (K_{\infty,k,min} - K_{br,k,min}) \quad (3.13)$$

The $K_{\infty,k}$ terms come from the formula for stress intensity factor of a center-cracked infinite sheet:

$$K_{\infty,k,max} = \sigma_{k,max} \sqrt{\pi a_k} \quad (3.14)$$

where $\sigma_{k,max}$ is the farfield stress in layer k at the maximum applied load, including both that due to tension and bending loads and residual stress, and a_k is the length of the crack in layer k . $K_{\infty,k,min}$ uses the same formula, with $\sigma_{k,min}$ in place of $\sigma_{k,max}$.

The stress intensity reduction due to a point loading around a crack, from [10], can be used to calculate K_{br} by summing the effect of the bridging load at each node:

$$C_{K_{br}} = \frac{1}{\sqrt{\pi a_k}} \left[\frac{a_k}{\sqrt{a_k^2 - z_0^2}} + \frac{a_k}{\sqrt{a_k^2 - \bar{z}_0^2}} - \frac{1}{2} (1 + \nu_{12,k}) y_0 a_k i \left(z_0 (a_k^2 - z_0^2)^{-3/2} - \bar{z}_0 (a_k^2 - \bar{z}_0^2)^{-3/2} \right) \right] \quad (3.15)$$

$$K_{br,k,max} = \frac{1}{t_k} \sum_j C_{K_{br},j} w_j F_{max,k,j} \quad (3.16)$$

$$K_{br,k,min} = \frac{1}{t_k} \sum_j C_{K_{br},j} w_j F_{min,k,j} \quad (3.17)$$

For internal cracked layers, with delaminations, and therefore bridging loads, on both sides, the bridging stress intensity factor is the sum of the bridging K for both sets of bridging loads.

The effective stress ratio at the crack tip in layer k is given by

$$R_k = \frac{K_{min,k}}{K_{max,k}} \quad (3.18)$$

Note that the stress ratio seen by the cracks in the laminate is not necessarily the same as the stress ratio of the applied loading. Nor are the stress ratios seen by the cracks in each cracked layer necessarily the same.

With the stress intensity factor calculated, any applicable relation of ΔK to da/dN can be applied to calculate the crack growth rate. Because the actual stress ratio is not known *a priori*, it is preferred to use a relation that accounts for the changing R ratio. In this model, the correction for crack closure described by Schijve [11] for 2024-T3 was used. The stress intensity factor range at the tip is multiplied by a closure factor, U , which itself is a function of the stress ratio, to determine the effective ΔK .

$$U_k = 0.55 + 0.33R_k + 0.12R_k^2 \quad (3.19)$$

$$\Delta K_{k,eff} = U_k \Delta K_k \quad (3.20)$$

The crack growth rate is determined according to Equation (3.21), where $C_{cg} = 1.27 \times 10^{-11}$ and $n_{cg} = 2.94$, with da/dN in [mm/cycle] and ΔK_{eff} in [MPa $\sqrt{\text{mm}}$] [12, 13]:

$$\frac{da}{dN_k} = C_{cg,k} (\Delta K_{k,eff})^{n_{cg,k}} \quad (3.21)$$

In delamination growth, Rans et al. [14] has demonstrated that an appropriate definition of ΔG_{II} accounts for the stress ratio effect. ΔG_{II} of node j, p is based on the difference of the square roots of the energy release rates determined by Equation (5.23) of Chapter 5:

$$\Delta G_{II\ p,j} = \sqrt{G_{II\ max,p,j}} - \sqrt{G_{II\ min,p,j}} \quad (3.22)$$

And the delamination growth rate at each node can be found with the relation:

$$\frac{db}{dN_{p,j}} = C_{d,p} (\Delta G_{II\ p,j})^{n_{d,p}} \quad (3.23)$$

where the constant, material property terms have the p subscript to indicate that each interface may have different properties. For a typical Glare interface, with db/dN in [mm/cycle] and ΔG_{II} in [$\sqrt{\text{MPa} \cdot \text{mm}}$], $C_d = 0.05$ and $n_d = 7.5$ [6]. For an interface between aluminum and fiberglass/FM94 prepreg with a 0.12 mm thick layer of additional adhesive in between, $C_d = 5.646 \times 10^{-4}$ and $n_d = 7.166$ [15].

3.3.4 Updating the geometry

In each iteration, the crack lengths and delaminations must be extended in proportion to their growth rates. A small extension is desirable in order to better approximate the effects of changing crack and delaminations on the growth rates, while a large extension is desirable in order to speed computation. In Section 3.3.6, different limits on extension are explored.

The maximum allowed extension of crack lengths will be referred to as Δa_{max} , and the maximum allowed delamination extension will be referred to as Δb_{max} . To maintain proportionality of the growth, it is incremented in terms of an incremental number of cycles, ΔN , such that no crack front or node grows by more than Δa_{max} or Δb_{max} , respectively:

$$\Delta N \leq \min \left(\frac{\Delta a_{max}}{da/dN}; \frac{\Delta b_{max}}{db/dN} \right) \quad (3.24)$$

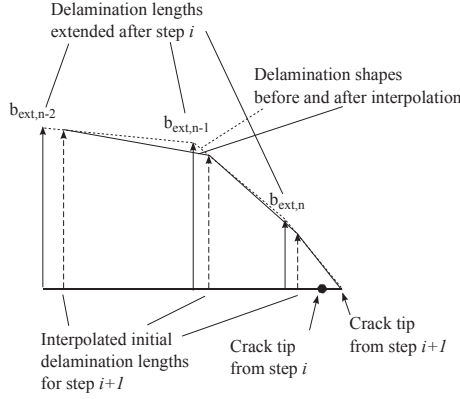


Figure 3.3 – Illustration of interpolation scheme for delamination length following crack and delamination extension. The delamination nearest the crack tip is interpolated by assuming a delamination length of zero at the tip.

where \mathbf{da}/dN and \mathbf{db}/dN represent the vectors of crack growth rates for all k and delamination growth rates for all nodes, p, j , respectively. The cycle count associated with the next iteration is $N_{i+1} = N_i + \Delta N$.

The crack lengths for use in the next iteration come from:

$$\mathbf{a}_{i+1} = \mathbf{a}_i + \Delta N \frac{d\mathbf{a}}{dN} \quad (3.25)$$

The delamination length of each of the nodes is increased in a similar manner, to \mathbf{b}_{ext} .

$$\mathbf{b}_{ext} = \mathbf{b}_i + \Delta N \frac{d\mathbf{b}}{dN} \quad (3.26)$$

However, since the crack lengths have increased, a new distribution of bar elements is required. First, new x and w vectors are calculated with \mathbf{a}_{i+1} according to the procedure described in Section 3.2.3. Then, for each delamination, new delamination length values, \mathbf{b}_{i+1} , are found by interpolating \mathbf{b}_{ext} at the locations of the new x vector between s and a_k . In this model, a linear interpolation was used, but other forms are possible. To account for the node near the crack tip, where the new node is located between the old node nearest the crack tip and the new crack tip, a zero is appended to \mathbf{b}_{ext} and $a_{k,i+1}$ is appended to x_k for the purposes of interpolation, as illustrated in Figure 3.3.

Leapfrogging

As a result of the drastically higher strain energy release rate for a short delamination, compared with a longer delamination within the same width-wise bar element, a leapfrogging phenomenon can occur in subsequent iterations. This means that after the first iteration, the shorter delamination grows quickly, becoming longer than the slower growing, initially longer delamination. On the next growth step, the growth rates are swapped, the delaminations once again change relative positions, and the cycle repeats. This computational phenomenon arises from the discretization of the delamination growths into finite steps per cycle, based on the initial delamination size. However, in a real delamination, the leapfrogging is mitigated by the immediate decrease in SERR as the faster-growing delamination begins extending.

Compared to determining the SERR of both delaminations growing together and extending them at that rate, this leapfrogging behavior leads to an overestimation of the delamination growth rate. Equations (3.27) and (3.28) show the effective crack growth rates occurring in the leapfrogging situation and the more realistic simultaneous extension situation, respectively. It can be shown that $da/dN|_{leapfrog} > da/dN|_{together}$ for all $n_d > 1$. This faster growth is merely a result of simulating the delamination extension in finite increments, and should be corrected in the model.

$$\frac{da}{dN}|_{leapfrog} = \frac{1}{2}C_d\Delta G_{long}^{n_d} + \frac{1}{2}C_d\Delta G_{short}^{n_d} = \frac{1}{2}C_d \left(\Delta G_{long}^{n_d} + \Delta G_{short}^{n_d} \right) \quad (3.27)$$

$$\frac{da}{dN}|_{together} = C_d \left(\frac{1}{2}\Delta G_{long} + \frac{1}{2}\Delta G_{short} \right)^{n_d} \quad (3.28)$$

A leapfrog mitigation scheme was included in the model. A potential instance of leapfrogging was identified when any two delamination fronts within the same bar element change rank in height relative to one another as a result of incremental delamination growth. The delamination that began as the largest, delamination “long,” is grown according to the average SERR of the two delaminations:

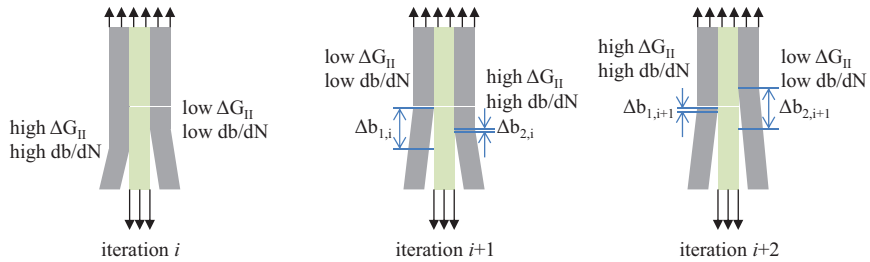
$$\begin{aligned}
B_{long, i+1} = & B_{long, i} + C_{d,long} \left[\sqrt{\frac{1}{2}(G_{long, max} + G_{short, max})} \right. \\
& \left. - \sqrt{\frac{1}{2}(G_{long, min} + G_{short, min})} \right]^{n_{d,long}} \quad (3.29)
\end{aligned}$$

The initially shorter delamination “short” must begin the second iteration longer than delamination “long.” This ensures that after the second iteration, either delamination “short” continues growing faster — meaning that it ought to remain longer — or the two delaminations switch places again — this indicates that leapfrogging is occurring and the two delaminations ought to continue to grow at rates based on the average SERR of the the two. The new length of the shorter delamination is calculated by adding an arbitrary and negligibly small amount to the new length of the initially longer delamination:

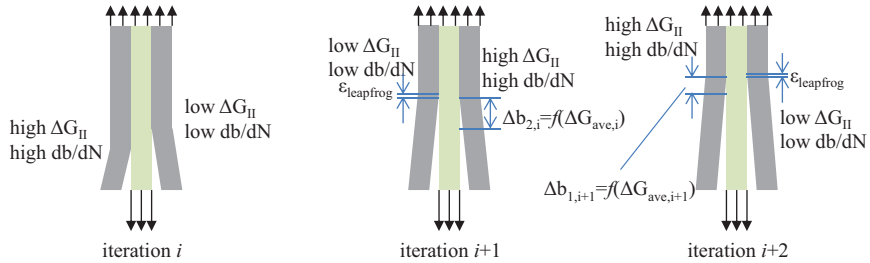
$$B_{short, i+1} = B_{long, i+1} + \epsilon_{leapfrog} \quad (3.30)$$

An example of leapfrogging behavior compared with the leapfrog mitigation approach of the model is show in Figure 3.4.

In laminates in which more than two delaminations grow in tandem, it would be most correct to calculate the SERR of simultaneous growth for all such delaminations together and apply it to them when calculating their growth rates. However, determining which delaminations to group for tandem growth becomes very complicated as the number of delaminations, and thus possible permutations, increases. As a simplifying assumption in the model, each node within a given bar element is compared against every other node in the same bar element. Where rank order changes occur, indicating the potential for leapfrogging, the growth of the two compared delaminations is recalculated according to Equations (3.29) and (3.30). When the same node is a member of more than one rank-swapping pair, the maximum of all the recalculated delamination heights for that node is taken as the result that is passed to the next iteration. While this assumption may yield less accurate iteration-to-iteration delamination growth, it should allow the overestimation of delamination growth due to leapfrogging to be avoided while sorting the nodes into the correct rank order or tandem sets over a large number of iterations.



(a) Example of leapfrogging delamination growth.



(b) Example of growth stabilization with the leapfrog mitigation scheme. Both delaminations grow at a rate equal to their average ΔG_{II} over a number of cycles.

Figure 3.4 – Illustration of the “leapfrogging” issue that can arise in a bar element due to the discretization of delamination growth

3.3.5 Exiting the calculation loop

Several criteria are available as options for ending iteration through the calculation loop. These include a maximum number of fatigue cycles, maximum number of iterations, or some measure of the damage, either based on the length of the longest crack, the external cracks (to match test results), or the average crack length. In the future, as predictions of laminate residual strength improve, periodic checks of residual strength could be used as a means of ending the simulation when the residual strength falls below a threshold value.

Once the calculation loop ends, minimal post-processing of the simulation results is necessary. All of the relevant variables of the model are already found in the process of iterating; they must merely be recorded at the end.

3.3.6 Stability and convergence

An aspect of model validity that must be addressed is the numerical and computational quality of the model. In this section, some results will be shown to demonstrate that the model is stable and to show the convergence behavior of the model.

The convergence behavior of the model was tested by performing predictions with the model for several different laminates using a range of w_{max} , the maximum allowed bar element width in the nearest element to the crack tip². Figure 3.5 shows the percent error calculated for each prediction, taking the result with the smallest w_{max} to have zero error. The predictions for the thicker laminates show excellent convergence behavior, remaining within 5% error even with the coarsest bar element distributions. On the other hand, the Glare prediction required a much finer bar element distribution to begin converging. The computational cost, based on CPU clock time with the predictions running on a single CPU, is plotted in Figure 3.6. Further refinement of the Glare prediction was infeasible due to the high computational cost.

Based on this convergence study, a w_{max} of 0.25 is appropriate for simulating the laminates with thick metal layers, and a w_{max} of 0.025 was selected as a compromise between accuracy and computational cost for all Glare simulations.

The numerical stability of the model can be assessed by performing predictions with slightly different initial conditions, and ensuring that this does not cause the results to diverge. Figures 3.7 and 3.8 show the crack growth

²See Chapter 6 for details about the laminates modeled.

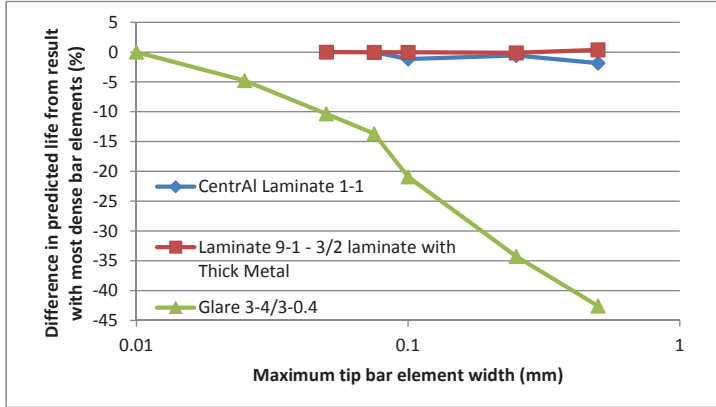


Figure 3.5 – Error with respect to the result with the smallest w_{max} of predicted crack growth lives.

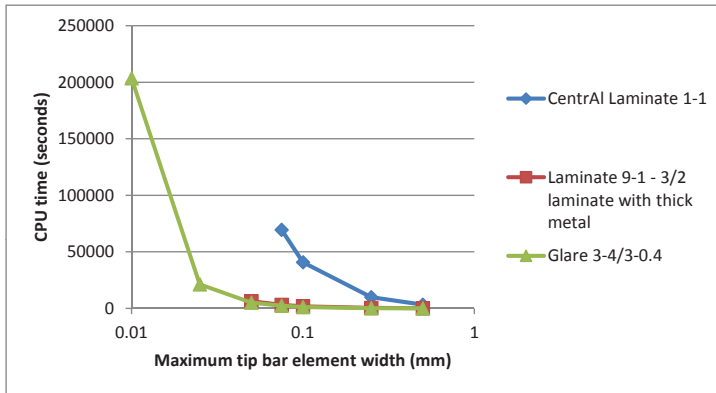


Figure 3.6 – Computational time, based on the model run on a single CPU, for model predictions with varying maximum tip bar element widths.

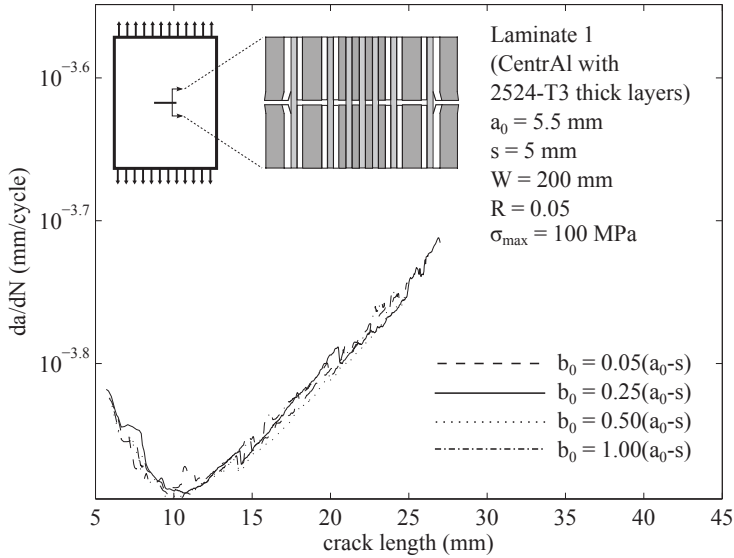


Figure 3.7 – Predicted crack growth of Laminate 1-1 with different initial delamination heights, demonstrating stability of the model

rates predicted for Laminates 1-1 and 9-1, respectively, beginning with different initial delamination heights, b_0 . These laminates are defined in Table 6.2 in Chapter 6. The crack growth rates are calculated with the methodology described in Chapter 7, including downsampling of the data by a factor of 10 to reduce noise. This may have the effect of removing the transient differences at the beginnings of the predictions. Some differences can be seen in the initial part of the curves. However, the different simulations quickly collapse into agreement.

Another possible variation of the initial conditions is changing the starting crack lengths. Figure 3.9 compares results for Laminate 9-1, a 3/2 laminate with thick metal layers, beginning from equal crack lengths, a longer internal crack, and longer external cracks. After initial transient periods, all of the simulations have the same crack growth rates and same slight difference in length between the internal and external cracks.

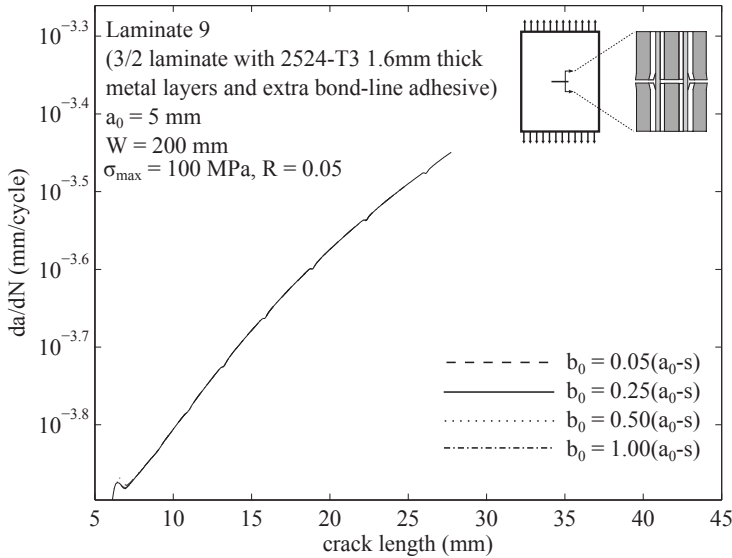


Figure 3.8 – Predicted crack growth of Laminate 9-1 with different initial delamination heights, demonstrating stability of the model

3.3.7 Shortcomings of the present model

Several simplifying assumptions of the model limit its applicability to the full range of loading conditions and crack geometries that might be encountered in a structural analysis. The effects of biaxial and shear loading applied to the laminate are accounted for in the laminate stress analysis; however, only the laminae stresses in the direction perpendicular to the cracks are used in many steps of the analysis thereafter. Most significantly, the crack opening, stress intensity factors, and strain energy release rates are only a functions of the stress in this y direction. Biaxial states of stress in the layers would have effects on all of these results. This shortcoming could be overcome by re-deriving the relations for crack opening, stress intensity factors, and strain energy release rates to account for biaxial stress states.

An additional effect of biaxial and shear loading is that crack turning may occur. As presently formulated, the model only accounts for cracks growing in straight lines in the x direction. Expressions for the displacement of metal layers with curved cracks would need to be derived to account for this, and a model for how the cracks would turn in response to mixed modes of stress

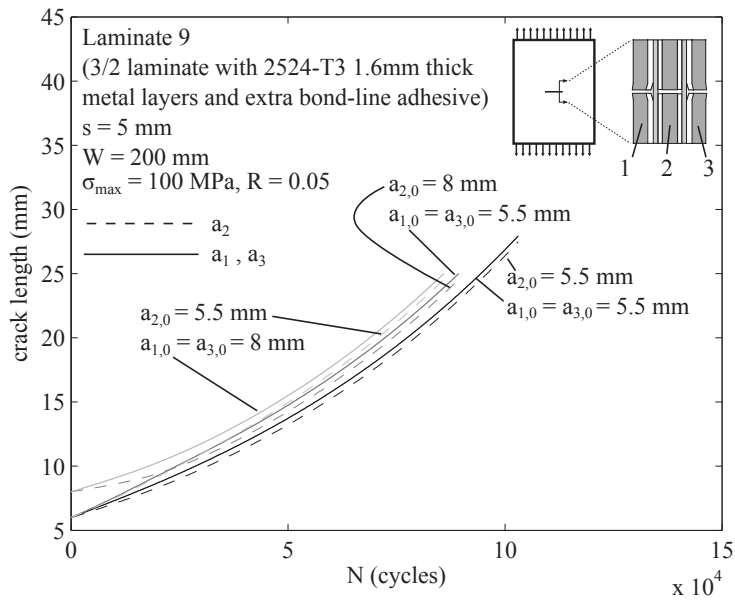


Figure 3.9 – Predicted crack growth of Laminate 9-1 with different initial crack lengths, demonstrating stability of the model

intensity would need to be included.

The model as presently formulated will not appropriately account for bridging fibers that are oriented at an angle other than 0° or 90° with respect to the loading axis. The bridging force borne by such fibers would be in the fiber direction, rather than perpendicular to the crack. A formulation for crack opening displacement that includes horizontal components of bridging force can be derived from [10]. The relationship between bridging, strain energy release rate, and delamination growth rates would have to be reconsidered, since the off-axis fibers would introduce a mode III component at the delamination boundaries.

The model ignores some aspects of bridging mechanics that may be important when the load cycle includes a compressive portion. With sufficient compressive load applied, the cracks would close, removing the stress intensity ahead of the crack tip and changing the load redistribution into the fibers. This closure is not presently included in the model. Additionally, if the fiber layers in the delaminated regions are put into sufficient compression, the fiber layers may buckle in this region, even at compressive loads that are less than the buckling load of the laminate. Whether the error introduced by ignoring these aspects of compressive load cycles is significant can be assessed through comparison of model predictions to the validation tests conducted with negative stress ratios.

3.4 Summary

The crack and delamination growth model for the general FML case has been laid out in this chapter with both analytical support and sufficient explanation of computational methods to render it reproducible. What remains, though, is the question of validity.

One necessary component of validity is that the model accurately describes the mechanics of crack and delamination growth in FMLs. In Chapters 4 and 5, the individual calculation methods used in this model were verified through comparison to finite element model results. The validity of the model overall will be tested through comparison to fatigue crack growth test results in Chapter 7.

Bibliography

- [1] Jones, R. M. (1999) *Mechanics of Composite Materials*. Taylor and Francis, Inc., 2 edn.
- [2] Vinson, J. R. and Sierakowski, R. L. (2004) *The Behavior of Structures Composed of Composite Materials*. Kluwer Academic Publishers, 2 edn.
- [3] Gay, D. (2002) *Composite Materials: Design and Applications*. CRC Press.
- [4] Rickerd, G. (2010) Considering fiber metal laminate aircraft wings — what should we know? *ASIP 2010: the 2010 aircraft structural integrity program conference, Nov 30 – Dec 2, 2010. San Antonio, Texas*.
- [5] Guo, Y.-J. and Wu, X.-R. (1999) Bridging stress distribution in center-cracked fiber reinforced metal laminates: modeling and experiment. *Engineering Fracture Mechanics*, **63**, 147 – 163.
- [6] Alderliesten, R. C. (2007) Analytical prediction model for fatigue crack propagation and delamination growth in glare. *International Journal of Fatigue*, **29**, 628–646.
- [7] Burden, R. and Faires, J. (2005) *Numerical analysis*. Thomson Brooks/Cole.
- [8] Wilson, G. S., Alderliesten, R. C., and Benedictus, R. (2013) A generalized solution to the crack bridging problem of fiber metal laminates. *Engineering Fracture Mechanics*, <http://dx.doi.org/10.1016/j.engfracmech.2013.03.008>.
- [9] Wilson, G. S., Delgrange, G., Alderliesten, R. C., and Benedictus, R. (2011) Generalized approach to calculating strain energy release rate in fiber metal laminates. *Engineering Fracture Mechanics*, submitted for publication June 2011.
- [10] Tada, H., Paris, P., and Irwin, G. (1973) *The Stress Analysis of Cracks Handbook*. Del Research Corporation, 1 edn.
- [11] Schijve, J. (1981) Some formulas for the crack opening stress level. *Engineering Fracture Mechanics*, **14**, 461–465.
- [12] Alderliesten, R. C. (2005) *Fatigue crack propagation and delamination growth in Glare*. Ph.D. thesis, Delft University of Technology, Delft, The Netherlands.

- [13] Homan, J. J. (2002) Crack growth properties of thin aluminium sheets, issue 2. Tech. Rep. B2V-01-16, Delft University of Technology, (restricted).
- [14] Rans, C., Alderliesten, R., and Benedictus, R. (2011) Misinterpreting the results: How similitude can improve our understanding of fatigue delamination growth. *Composites Science and Technology*, **71**, 230–238.
- [15] Wilson, G. S., Fassih, Y., Alderliesten, R. C., and Benedictus, R. (2011) Effect of adhesive layer thickness on fiber metal laminate delamination growth rate. Submitted for journal publication July 2011.

This page intentionally left blank.

Chapter 4

Bridging load determination

This chapter provides a detailed description of the bridging load calculation used in the generalized model. It is adapted from an article published in 2013 in *Engineering Fracture Mechanics* [1].

4.0.1 Overview of Present Bridging Models

Marissen [2] and Alderliesten [3] have developed crack growth models for FMLs using the linear-elastic fracture mechanics assumption of superposition to characterize the stress intensity factor seen by the cracks tips in metal layers, K_{tip} as

$$K_{tip} = K_{\infty} + K_{bridging} \quad (4.1)$$

where K_{∞} refers to the stress intensity factor due to the farfield stress in the metal sheet, including the portion of the applied load carried in the metal layers and the thermal residual stress of the metal layers, treated as a remotely applied load. $K_{bridging}$ is the stress intensity factor due to the bridging load acting on the cracked layers, which Alderliesten calculated by integrating the stress intensity factor due to point loads along the delamination boundary. These point loads correspond to the discretized bridging stress distribution for which Alderliesten solves with compatibility (this solution approach is discussed hereafter).

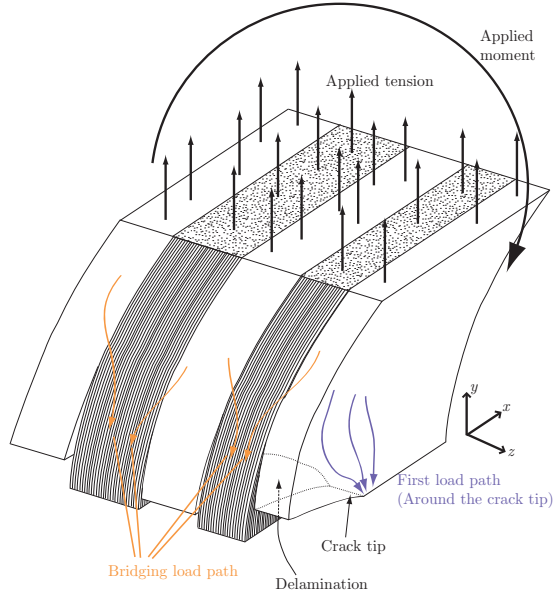


Figure 4.1 – Schematic of bridging scenario for a generalized laminate, showing one quarter of a center-cracked laminate subject to remote tension and bending loads. There is a delamination in each interface between a cracked and uncracked layer over which the bridging load is transferred, reducing the crack tip stress intensity.

The other component of damage tolerance for which fiber bridging is relevant is residual strength. Rodi [4] has measured the bridging stress distribution in cracked Glare FMLs tested for residual strength, and has shown that the size of the fiber bridging region has an effect on the crack tip opening angle of residual strength-tested FMLs. The ability to accurately predict the bridging stress distribution is key in developing an analytical framework for describing FML residual strength.

The method employed by Alderliesten is to calculate the bridging stress by imposing compatibility between the metal layers and fiber layers at the delamination boundary. As expressed in equation (4.2), the displacement of the metal layers at the delamination, in terms of the crack opening due to the farfield stresses, $v_{\infty}(x)$, and the crack closure due to the bridging forces, $-v_{br}(x)$, must equal the displacement of the bridging material, $\delta_f(x)$, and its deformation due to shear, $\delta_{pp}(x)$. Each term is a function of x because the deformations change along the length of the delamination. The coordinate

system used throughout this chapter is as defined in Figure 4.1, with x being the direction of crack growth, y the tension loading direction, and z through the thickness.

$$v_{\infty}(x) - v_{br}(x) = \delta_f(x) + \delta_{pp}(x) \quad (4.2)$$

The closure due to bridging, $v_{br}(x)$, is calculated by integrating the closure caused at location x due to the point load, $F_{br}(x_{br})$, applied at location x_{br} , over the entire delamination:

$$v_{br}(x) = \int_{a_s}^a v(x, x_{br}) dx_{br} \quad (4.3)$$

The opening due to the farfield stress in the cracked layers is calculated using the following relation from [5]:

$$v_{\infty}(x) = \frac{2\sigma_{\infty} al}{E_{al}} \sqrt{a^2 - x^2} \quad (4.4)$$

The bridging fiber elongation, $\delta_f(x)$, results from the elongation of the fiber layers due to the stress resulting from applied loading, $\sigma_{f\infty}$, and that due to the bridging stress in the fiber layers, $\sigma_{br}(x)$:

$$\delta_f(x) = b(x) \frac{\sigma_{f\infty} + \sigma_{br}(x)}{E_f} \quad (4.5)$$

where $b(x)$ describes the height of the delamination front above the crack plane, E_f is the modulus of the fiber prepreg layer in the loading direction, and the bridging stress of the fiber layers is defined by:

$$\sigma_{br}(x) = \frac{F_{br}(x)}{t_f}. \quad (4.6)$$

Note that Equation (4.5) merely multiplies the strain in the fibers over the length they are straining to obtain the elongation.

This assumes that the bridging load is not dispersed throughout the fiber layer in the transverse (x) direction, but rather that the bridging load stays in the fibers into which it was initially introduced. This assumption is reasonable for 0° and $0^\circ/90^\circ$ layouts considering the relatively low shear stiffness of the fiber prepreps.

The prepreg shear deformation was calculated by applying equilibrium and differential deformation according to the shear and tensile stiffnesses of the constituents, giving a total deformation of:

$$\delta_{pp}(x) = C_b \sigma_{al} t_{al} \sqrt{\frac{t_f}{G_f} \left(\frac{1}{F_{al}} + \frac{1}{F_f} \right)} \quad (4.7)$$

where the C_b term reflects the reduction in shear compatibility as the delamination length becomes small:

$$C_b = 1 - \left(\cosh \sqrt{\frac{G_f}{t_f^2 E_f}} b - \tanh \sqrt{\frac{G_f}{t_f^2 E_f}} b \sinh \sqrt{\frac{G_f}{t_f^2 E_f}} b \right) \quad (4.8)$$

In practice, Alderliesten solved Equation (4.2) for the bridging loads by discretizing the terms, effectively treating the delaminated region as a series of “bar elements,” and separating all of the coefficients of the bridging loads.

Guo and Wu [6, 7] used a similar compatibility approach, including bar elements, with the chief difference being that the crack opening, due to both farfield loads and applied bridging loads, was calculated based on the laminate — the thickness of the laminate, the overall laminate stiffness in the loading direction, the metal layer crack length, and the externally applied stress were used in weight function solutions for crack opening. Though the original model did not account for internal stresses resulting from thermal mismatch or plasticity, Wang [8] showed that it is possible to do so in the framework of this approach by adding additional displacement terms to the compatibility equation. In contrast, the model of Alderliesten incorporates the thermal residual stress in the farfield stress calculated for each layer.

4.0.2 Limitations and motivation

The models discussed above all rely on the following assumptions:

- Equal crack lengths in each metal layer
- Identical delamination size in each delaminated interface
- The bridging stress distribution is the same over each delamination

- Material properties and thicknesses are identical — i.e. each metal layer is the same alloy, thickness, and orientation, and each fiber layer is the same composition, thickness, and layup (and typically only 0° or $0^\circ/90^\circ$)
- Applied loads are only tension or compression - no bending

These assumptions stem from the key modeling simplification used in each of the models - treating the problem as 2-dimensional. The compatibility is solved over only one delamination, and the properties used in determining the deformations come from the properties of the constituent layers, ratioed according to their volume fraction in the laminate. The total amount of load transfer due to bridging is then divided over the number of interfaces.

Such assumptions have been shown to work reasonably well through experimental comparison to crack opening, as well as through the success of crack growth models using these assumptions in predicting experimental crack growth behavior of FMLs. Interestingly, these assumptions do have an inherent contradiction: if the bridging stress over each interface is the same, how can the displacement of each metal layer be the same if the external metal layers are bridged only by one interface and the internal metal layers are bridged by two? Despite this contradiction, crack growth predictions for laminates with internal and external metal layers still succeed in accurately matching experimental data.

There are cases, however, where these assumptions limit the ability of bridging models to properly characterize bridging in FMLs. One such example is combined tension-bending loading [9]. Randell's tests of Glare specimens subjected to combined tension and bending loads showed that cracks from an open hole grow at different rates in each cracked layer, with faster crack growth occurring towards the surface with the most tension. Delamination sizes also varied through the thickness.

Another example of the need for a more generalized model is the development of non-uniform laminates, consisting of metal and fiber layers of different thicknesses, such as CentrAl [10]. Teardown inspections of CentrAl after spectrum crack growth testing showed that the cracks in the thin inner layers grew to around 60% of the length of the cracks in the thicker outer metal layers. The delaminations also differed based on the thickness of the metal layer in the interface, and experiments showed that the delamination sizes could be reduced based on the inclusion of additional adhesive adjacent to the thick layers. To understand and take full advantage of the tailorability of FMLs, generalized analysis methods are required that can cope with the effects of this tailorability.

4.1 Solution

This model uses as its starting point the Glare bridging model of Alderliesten. The Alderliesten model was preferred over the model of Guo and Wu for this purpose because the latter bases its crack opening calculations on the laminate as a whole, whereas the former calculates the cracked layer deformations based on the application of the bridging loads to the cracked layers, separately from the bridging fiber layers. In this chapter's approach to the generalized model, it is desired to calculate the deformations of each cracked layer independently, so beginning from a model which already includes a distinction between the metal and fiber layers is a natural choice.

The following sections rederive where necessary the terms of Equation (4.2) to account for the through-the-thickness differences required of a generalized bridging model.

4.1.1 Cracked Layer Displacement — $v_{\infty}(x)$ and $v_{br}(x)$

Due to considering the delaminations on either face of an internal cracked layer independently, and the possibility of these delaminations having different shapes and sizes, it is necessary to distinguish the displacements at the two delamination fronts from one another. If, as was previously done by Alderliesten, the crack flank opening displacements are used to represent the cracked layer displacement, the compatibility solution would imply that the displacement and shear deformation of the bridging material at two different heights, b , would be equal, a physically unrealistic constraint.

By calculating the displacement due to farfield loading and bridging loads at the delamination boundary exactly, there can be as many equations (displacements at each delamination in each bar element) as unknowns (bridging loads). Such an exact solution, employing Westergaard stress functions, was discussed in detail by Wilson et al. in [11]. The resulting equations for $v_{\infty}(x)$ and $v_{br}(x)$ are as follows. Equation (4.9) includes the constant correction factor as described in [12].

$$v_{\infty}(x) = \frac{1 - \frac{\nu}{1+\nu}}{G} \text{Im} \bar{Z}_{I \infty} - \frac{y}{2G} \text{Re} Z_{I \infty} - \frac{1}{2G} \frac{\kappa - 3}{2} \frac{\sigma_{\infty_i}}{2} y \quad (4.9)$$

$$Z_{I \infty} = \frac{\sigma}{\sqrt{1 - \left(\frac{a}{z}\right)^2}}; \quad \bar{Z}_{I \infty} = \sigma \sqrt{z^2 - a^2}; \quad \kappa = \frac{3 - \nu}{1 + \nu} \quad (4.10)$$

$$v_{br}(x_i, b_i, S_{br}) = \sum_{j=1}^N \frac{v(x_i, b(x_i), x_j, b(x_j))}{F_{br}(x_j)} F_{br}(x_j) w_j \quad (4.11)$$

where:

$$v(x_i, b(x_i), x_j, b(x_j)) = \frac{1 - \frac{\nu}{1+\nu}}{G} \text{Im} \bar{Z}_{I \ br} - \frac{y}{2G} \text{Re} Z_{I \ br} \quad (4.12)$$

$$\begin{aligned} Z_{I \ br} = & \frac{P}{\pi} \left[\frac{\sqrt{a^2 - z_0^2}}{(z^2 - z_0^2)} + \frac{\sqrt{a^2 - \bar{z}_0^2}}{(z^2 - \bar{z}_0^2)} - \alpha y_0 \left(\frac{-iz_0}{(z^2 - z_0^2)\sqrt{a^2 - z_0^2}} \right. \right. \\ & + 2iz_0 \frac{\sqrt{a^2 - z_0^2}}{(z^2 - z_0^2)^2} + \frac{i\bar{z}_0}{(z^2 - \bar{z}_0^2)\sqrt{a^2 - \bar{z}_0^2}} \\ & \left. \left. - 2i\bar{z}_0 \frac{\sqrt{a^2 - \bar{z}_0^2}}{(z^2 - \bar{z}_0^2)^2} \right) \right] \frac{1}{\sqrt{1 - \left(\frac{a}{z}\right)^2}} \\ & + \frac{P}{\pi} \left[\frac{-y_0}{(z - x_0)^2 + y_0^2} - \frac{y_0}{(z + x_0)^2 + y_0^2} \right. \\ & \left. + \alpha y_0 \left(\frac{(z - x_0)^2 - y_0^2}{((z - x_0)^2 + y_0^2)^2} + \frac{(z + x_0)^2 - y_0^2}{((z + x_0)^2 + y_0^2)^2} \right) \right] \quad (4.13) \end{aligned}$$

$$\begin{aligned} \bar{Z}_{I \ br} = & \frac{P}{\pi} \left[\tan^{-1} \frac{\sqrt{z^2 - a^2}}{\sqrt{a^2 - z_0^2}} + \tan^{-1} \frac{\sqrt{z^2 - a^2}}{\sqrt{a^2 - \bar{z}_0^2}} \right. \\ & \left. - \alpha y_0 \left(\frac{iz_0}{z^2 - z_0^2} \frac{\sqrt{z^2 - a^2}}{\sqrt{a^2 - z_0^2}} - \frac{i\bar{z}_0}{z^2 - \bar{z}_0^2} \frac{\sqrt{z^2 - a^2}}{\sqrt{a^2 - \bar{z}_0^2}} \right) \right] \\ & + \frac{P}{\pi} \left[- \left(i \tanh^{-1} \frac{z}{z_0} - i \tanh^{-1} \frac{z}{\bar{z}_0} \right) \right. \\ & \left. + \alpha y_0 \left(\frac{z}{z_0^2 - z^2} + \frac{z}{\bar{z}_0^2 - z^2} \right) \right] \quad (4.14) \end{aligned}$$

In the above equations, P refers to a point load, which relates to the bridging line load by $P = F_{br \ j} w_j$, $z = x + iy$ gives the x and y coordinates at which displacement is calculated, and $z_0 = x_0 + iy_0$ gives the coordinates of point load application. For later use, let the compliance of cracked layer displacement at location (x_i, b_i) due to bridging loads at (x_j, b_j) be defined as in Equation (4.15). $C_{v, \ ij}$ can be computed directly with Equation (4.12) by using w_j in place of P in Equations (4.13) and (4.14).

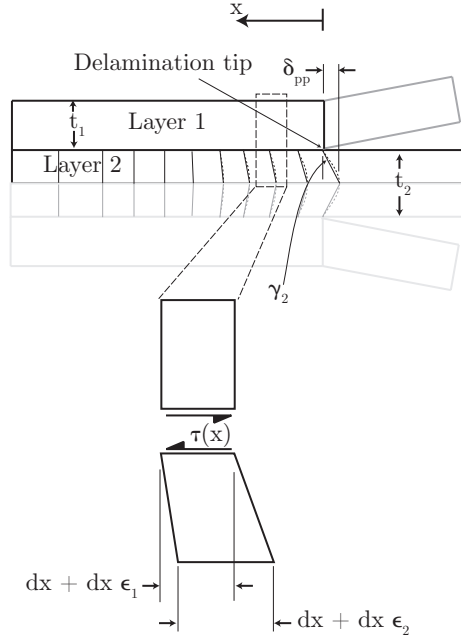


Figure 4.2 – Idealization of shear where bridging stress is transferred near a delamination tip

$$C_{v, ij} = \frac{v(x_i, b(x_i), x_j, b(x_j))}{F_{br, j}} \quad (4.15)$$

4.1.2 Prepreg Shear Deformation — $\delta_{pp}(x)$

The prepreg shear deformation is solved in a similar way to Alderliesten [3], with the main difference that instead of prescribing a load through the bar element based on the farfield stress of each lamina, the load transferred via shear stress over the interface is set equal to the bridging load of the bar element, F_{br} . Figure 4.2 represents a generic interface between a cracked layer, layer 1, and an uncracked layer, layer 2, and it defines the terms to be used in the derivation.

First, the increase in strain in the center of the intact layer as it carries additional load due to the shear is related to the strain in the cracked layer,

which is assumed to have negligible shear deformation compared to that of the intact layer, which decreases as load is transferred over the interface, through the definition of shear strain, assuming small angles:

$$\begin{aligned}
 \frac{d\gamma_2}{dx} t_2 &= \epsilon_2(x) - \epsilon_1(x) \\
 &= \left(\epsilon_2(L) + \frac{1}{t_2 E_2} \int_x^L \tau(x) dx \right) - \left(\epsilon_1(L) - \frac{1}{t_1 E_1} \int_x^L \tau(x) dx \right) \\
 &= \frac{1}{t_2 E_2} \int_x^L \tau(x) dx + \frac{1}{t_1 E_1} \int_x^L \tau(x) dx
 \end{aligned} \tag{4.16}$$

Since $\gamma_2(x) = \frac{\tau(x)}{G_2}$,

$$\frac{d\tau}{dx} = \frac{G_2}{t_2} \left(\frac{1}{t_1 E_1} + \frac{1}{t_2 E_2} \right) \int_x^L \tau(x) dx \tag{4.17}$$

Differentiating the above equation in terms of x gives:

$$\frac{d^2\tau}{dx^2} = \frac{G_2}{t_2} \left(\frac{1}{t_1 E_1} + \frac{1}{t_2 E_2} \right) \tau(x) \tag{4.18}$$

This second order differential equation has the general solution,

$$\tau(x) = c_1 e^{x\sqrt{\frac{G_2}{t_2} \left(\frac{1}{t_1 E_1} + \frac{1}{t_2 E_2} \right)}} + c_2 e^{-x\sqrt{\frac{G_2}{t_2} \left(\frac{1}{t_1 E_1} + \frac{1}{t_2 E_2} \right)}} \tag{4.19}$$

where c_1 and c_2 are unknown constant coefficients.

Two boundary conditions are applied. One is that the shear stress must be zero at distance L away from the delamination tip. The other is that the total load transferred over the interface must be equal to the bridging load.

$$\tau(L) = 0 \tag{4.20}$$

$$\int_0^L \tau(x) dx = F_{br} \tag{4.21}$$

By applying Equations (4.20) and (4.21), the constants in (4.19) can be solved. The formula for the shear stress along the interface is:

$$\tau(x) = F_{br} \sqrt{A} \left[\frac{e^{-\sqrt{A}L}}{2 - e^{\sqrt{A}L} - e^{-\sqrt{A}L}} e^{\sqrt{A}x} + \frac{1}{1 + e^{-2\sqrt{A}L} - 2e^{-\sqrt{A}L}} e^{-\sqrt{A}x} \right] \tag{4.22}$$

where

$$A = \frac{G_2}{t_2} \left(\frac{1}{t_1 E_1} + \frac{1}{t_2 E_2} \right) \quad (4.23)$$

Assuming that $L \gg 1$,

$$\tau(x) = F_{br} \sqrt{A} e^{-\sqrt{A}x} \quad (4.24)$$

Finally, the displacement due to shear seen at the delamination boundary, $x = 0$, is given for small γ as:

$$\delta_{pp} = F_{br} \frac{t_2}{G_2} \sqrt{\frac{G_2}{t_2} \left(\frac{1}{t_1 E_1} + \frac{1}{t_2 E_2} \right)} \quad (4.25)$$

For later convenience, define the prepreg shear compliance for an interface between material i and j , $C_{\tau_{ij}}$, as: $C_{\tau_{ij}} = \frac{t_j}{G_j} \sqrt{\frac{G_j}{t_j} \left(\frac{1}{t_i E_i} + \frac{1}{t_j E_j} \right)}$.

4.1.3 Bridging Material Elongation — $\delta_{br}(x)$

As part of the compatibility solution to the bridging problem in FMLs, it is necessary to describe the deformation of the bridging material - the material that is intact in the wake of the crack, bearing load that the cracked layers no longer carry. This is represented by the $\delta_f(x)$ term in the compatibility equation used by Alderliesten (4.2).

For the generalized model, it is necessary to solve the compatibility equation separately at each delamination boundary in each width-wise bar element. This must be possible for a scenario in which each interface has a different-sized delamination and each metal layer has a different length crack. Equation (4.26) expresses this need with the addition of the z_{int} term, implying that the relationship must hold at each interface through the thickness. z_{int} represents the location of the interface in the laminate thickness direction.

$$v_{\infty}(x, b(x)) - v_{br}(x, b(x))|_{z_{int}} = \delta_{br}(x)|_{z_{int}} + \delta_{pp}(x) \quad (4.26)$$

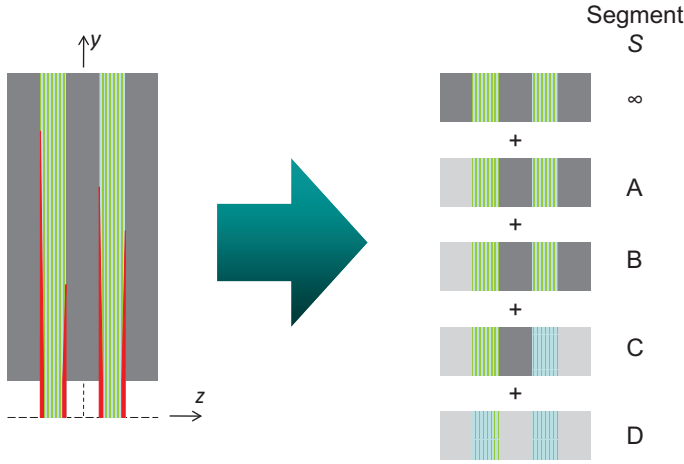


Figure 4.3 – Illustration of the approach to calculating the elongation at each interface with a complex delamination configuration in a given bar element

Approach

The general approach used to solve this problem is to assume that, at any given location in the height of a bar element, strain compatibility must hold through the thickness. This should be true within contiguous bridging material, as well as for bridging material that is separated by one or more delaminations, assuming small displacements.

The approach to calculating the elongation of the bridging material is to calculate the strain distribution, described by ϵ_0 , κ , and z , at each height in the bridging material, integrating the strain to obtain a displacement.

By splitting the laminate into vertical segments separated at the delamination boundaries, as shown in Figure 4.3, the laminate calculation need only be applied once to each segment, as the strain distribution should be the same throughout the height of each segment. The elongation at a point of interest, (x_i, y_j, z_k) , is then obtained by

$$\delta_f(x_i, y_j, z_k) = \sum_{l:0 \leq y_S \leq y_j} \Delta b_S \epsilon_S(z_k), \quad (4.27)$$

where Δb_S is the height of segment S , and $0 \leq y_S \leq y_j$ implies that only the elongation of segments below the point of interest is summed.

This approach amounts to a piecewise application of Classical Laminate Theory (CLT), where the strain in each segment is calculated separately. The use of CLT makes accounting for the bridging material straightforward. In the right side of Figure 4.3, the layers that are faded do not contribute to the bridging in that segment. In a CLT calculation, the stiffness matrices of these layers are simply not added to the laminate stiffness matrix to account for these layers not carrying any bridging load.

Since the entire compatibility solution (Equation (4.26)) is elastic, superposition of the far-field strain and the elongation due to the bridging loads is appropriate¹, which allows the strains to be separated, so that linear algebra can be used to solve the compatibility equation, as in the Alderliesten model.

Assumptions

No direct interaction between bar elements For the generalized model of FMLs, the assumption of the Alderliesten model that the elongation of adjacent bar elements is independent will be used, unless it is determined that doing so has a significantly negative impact on the accuracy of the model. This assumption may be worse for the generalized model than the Alderliesten model because the generalized model must account for the possibility of metal layers being among the bridging material. Since metal is more effective at transferring load via shear, the assumption may miss a significant portion of load that is transferred across the bar elements in this way.

What constitutes “bridging material”? It is necessary to establish a rule for whether or not a given layer carries any bridging load, and therefore contributes to the bridging stiffness. First, it is assumed that any layers which are uncracked in a given bar element, and therefore physically “bridge” the crack, carry some bridging load. This includes all fiber layers, as well as any uncracked metal layers, and any metal layer that has a crack that does not extend to the bar element of interest. Second, a cracked metal layer is considered part of the bridging material anywhere that it is bonded to a bridging layer. An internal

¹The far-field strain that is used in the superposition should be that of the full laminate, rather than that calculated with the remote load applied to the bridging material-only laminate of each segment. Remember that there are other load paths for the load carried by the cracked layers than through the bridging material; it can go through the intact portion of the metal layers or into the bridging material in another bar element. Solving the compatibility equation will tell how much of the far field stress from the metal layers in that bar element enter it via the bridging load.

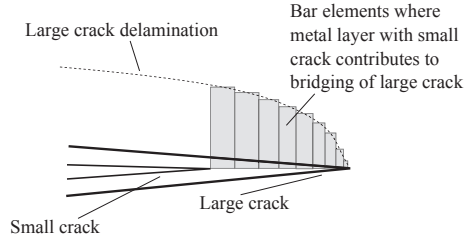


Figure 4.4 – Example of the region where the metal ahead of a short crack contributes to the bridging of a longer crack. The cracks of each metal layer are depicted, and the fiber layer between them is omitted for clarity.

cracked layer with delaminations of unequal size on either side contributes to the bridging where the bond is intact on at least one side.

In Figure 4.3, the center metal layer exemplifies this assumption. Although it is delaminated from the right fiber layer in segments B and C, it remains bonded to the left fiber layer, so it is considered to be part of the bridging material in these layers. In segment D, where it is delaminated on both sides, it is not considered to be part of the bridging material.

Including the cracked metal as bridging material, meaning that its stiffness contributes to the resistance of the bridging material to deformation when carrying bridging loads, may overestimate the bridging stiffness in the region around the bridging material’s own crack tip. Since the high stresses around the crack tip lead to high strains in the cracked layer, the bridging material itself must elongate along with the cracked layer for compatibility to be ensured wherever that layer is bonded to bridging material. This extra elongation (δ_{br}) reduces the bridging load necessary to achieve compatibility in Equation (4.26). The region where the short-cracked metal layer contributes to the bridging stiffness is highlighted in Figure 4.4. The δ_{br} may be important to modeling the stiffness of the bar elements closest to the short crack tip.

To account for this additional elongation, the following procedure is used:

Determine the elongation of the cracked aluminum layer over the height of the bar element where it is considered part of the bridging material by taking the difference of displacements due to the crack tip displacement field, $u_y(x, y)$ [13], at the top and bottom of this portion of the bar element:

$$u_y(x_i, y_{top}) - u_y(x_i, y_{bot}) \quad (4.28)$$

where

$$u_y = \frac{K_{tip}}{2G_k} \sqrt{r} \frac{r}{2\pi} \sin\left(\frac{\theta}{2}\right) \left[\kappa + 1 - 2\cos^2\left(\frac{\theta}{2}\right) \right] \quad (4.29)$$

in which $r = \sqrt{x^2 + y^2}$, $\kappa = (3 - \nu)/(1 + \nu)$ for plane stress, and

$$\theta = \begin{cases} \sin^{-1}(y/r) & : x \geq 0 \\ -\sin^{-1}(y/r) + \pi & : x < 0 \end{cases} \quad (4.30)$$

This elongation is multiplied by the ratio of the longitudinal compliance of the laminate made up of all the bridging material, $A'_{br_{11}}$ (described in Section 4.1.3), to the compliance of the cracked layer in the bar element, $1/(t_k E_{1,k})$:

$$\delta_K = t_k E_{1,k} A'_{br_{11}} [u_y(x_i, y_{top}) - u_y(x_i, y_{bot})] \quad (4.31)$$

The displacement due to the crack tip strain field in Equation (4.31) is added to the bridging material elongation term, $\delta_{br}(x)$, in Equation (4.26), on all interfaces bridged by that portion of the cracked layer. The K_{tip} term in Equation (4.29) is the stress intensity factor in the cracked layer in question, which is not known *a priori* in the bridging stress analysis, since it is a function of both the farfield load on the cracked layer and the bridging loads acting on it. It is therefore necessary to iterate the analysis, each time using the stress intensity factor calculated in the previous iteration, until the results converge.

To demonstrate the results of choosing to assume either that the cracked metal layers contribute their full stiffness or that the added displacement due to the crack tip stress field must be included in the bridging material elongation, results of this analysis with both assumptions will be compared to finite element data when verifying the bridging model.

Treat bridging as a line load instead of stress Because bending through the thickness is a concern, it is important to introduce the bridging load into the the material the right way. The assumption used here is to treat the bridging force as a line load acting exactly along the delamination boundary. This is consistent with the assumption used in the solution for displacement in the cracked metal layers due to the bridging load, in which the load transfer from metal layers to bridging layers occurred exactly at the height of the delamination boundary, neither above nor below it. However, this solution ignored the location through the thickness, assuming that the bridging load acts equally through the thickness and does not induce bending in the metal layer. This

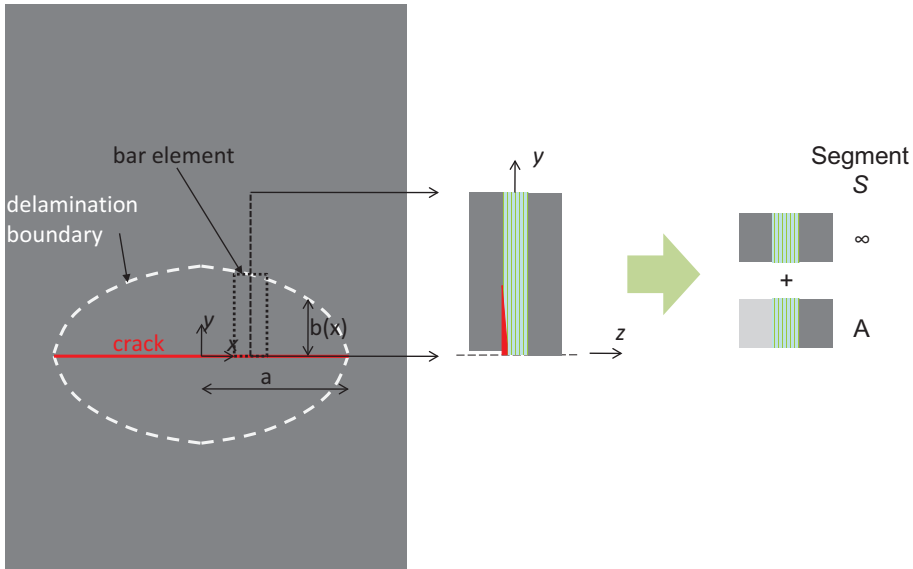


Figure 4.5 – Overview and breakdown approach for Example 1

bending, and non-uniformity through the thickness, is important to the distribution of bridging load in the intact bridging material.

For the purposes of calculating the elongation of the bridging material, the bridging load is treated as a line load acting at the delamination boundary in the height and thickness directions. It has dimensions [Force/Length].

Examples

Example 1: 2/1 FML with one cracked layer Figure 4.5 shows the problem schematically. The goal is to solve for $\delta_f(x)|_{z_{int}}$, the displacement of the bridging material at the delamination boundary. Let z_{int} refer to the location through the thickness of this interface (Figure 4.6), where $z = 0$ at the center of the laminate thickness, a common convention from CLT.

Since the strain at a given z in segment A does not vary with y , the deformation can be expressed as

$$\delta_f(x) = \epsilon(z_{int}) \cdot b(x), \tag{4.32}$$

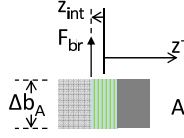


Figure 4.6 – The bridging load is introduced as a line load at z_{int}

where $\epsilon(z_{int})$ is the strain in segment A at the interface of interest, and $b(x)$ is the height of segment A and the height of the delamination expressed as a function of x .

By superposition, $\epsilon(z_{int})$ can be broken down into the far field strain calculated at location z_{int} through the thickness, $\epsilon_{\infty}(z_{int})$, and the strain in segment A at z_{int} due to the bridging load, $\epsilon_{br}(z_{int})$:

$$\epsilon(z_{int}) = \epsilon_{\infty}(z_{int}) + \epsilon_{br}(z_{int}). \quad (4.33)$$

It is easy to calculate $\epsilon_{\infty}(z_{int})$ as part of the initial CLT step in which the laminar stresses are calculated.

To calculate $\epsilon_{br}(z_{int})$, begin with the conditions depicted in Figure 4.6. The bridging load, transferring load from the cracked metal layer into the bridging material in this bar element, is represented by line load F_{br} applied at the location through the thickness, z_{int} . In this case, $z_{int} < 0$. To treat the bridging load as an applied load in CLT it must be split into a centerline load and a moment.

$$N_x = F_{br} \quad (4.34)$$

$$M_x = F_{br}z_{int} \quad (4.35)$$

This line load and moment are used to compute ϵ_{br} by employing CLT.

$$\begin{Bmatrix} N_x \\ N_y \\ N_{xy} \\ M_x \\ M_y \\ M_{xy} \end{Bmatrix} = \begin{bmatrix} A_{br} & B_{br} \\ B_{br} & D_{br} \end{bmatrix} \begin{Bmatrix} \epsilon_x \\ \epsilon_y \\ \epsilon_{xy} \\ \kappa_x \\ \kappa_y \\ \kappa_{xy} \end{Bmatrix} \quad (4.36)$$

In Equation (4.36), only ϵ_x and κ_x are of interest to the elongation², and all the applied forces and moments, apart from N_x and M_x are zero. The A_{br} , B_{br} , and D_{br} terms represent the 3×3 components of the laminate stiffness matrix, calculated by excluding the delaminated metal layer from the CLT method for constructing the stiffness matrix.

Inverting the stiffness matrix and solving for ϵ_x and κ_x gives

$$\epsilon_x = A'_{br_{11}} N_x + B'_{br_{11}} M_x \quad \text{and} \quad (4.37)$$

$$\kappa_x = B'_{br_{11}} N_x + D'_{br_{11}} M_x, \quad (4.38)$$

where $A'_{br_{11}}$, $B'_{br_{11}}$, and $D'_{br_{11}}$ represent the “1,1” terms from the A , B , and D portions of the inverted bridging stiffness matrix.

The strain at the interface of interest due to F_{br} can now be calculated, and put in terms of the bridging load by substituting Equations (4.34), (4.35), (4.37), and (4.38) into the definition of strain at a given height in the thickness of a laminate from CLT, $\epsilon(z) = \epsilon_0 + \kappa z$, where ϵ_0 is the midplane strain and κ is the curvature.

$$\begin{aligned} \epsilon_{br} &= \epsilon_x + \kappa_x z_{int} \\ &= A'_{br_{11}} N_x + B'_{br_{11}} M_x + z_{int} (B'_{br_{11}} N_x + D'_{br_{11}} M_x) \\ &= F_{br} (A'_{br_{11}} + 2B'_{br_{11}} z_{int} + D'_{br_{11}} z_{int}^2) \end{aligned} \quad (4.39)$$

Equation (4.39) gives the strain at the delaminated interface as a function of the bridging load and the laminate properties of the bridging material. Most significantly, Equation (4.39) shows that ϵ_{br} is a linear function of F_{br} . This means that the compatibility equation, Equation (4.26), can be solved simultaneously at each bar element with linear algebra, just as in the Alderliesten model.

Example 2: 2/1 FML with two different cracks and delaminations

The second example concerns the same laminate as the first example, but now both metal layers are cracked. The most general analysis must assume that both cracks are of different lengths and both delaminations are different. The scenario of interest is depicted in Figure 4.7. Since the elongation solution for a bar element located at $a_2 < x < a_1$ is the same as the solution for the first example, only the region $0 < x < a_2$ is considered here.

²The x direction for CLT corresponds to the laminate 0° direction, or the y direction in Figure 4.5

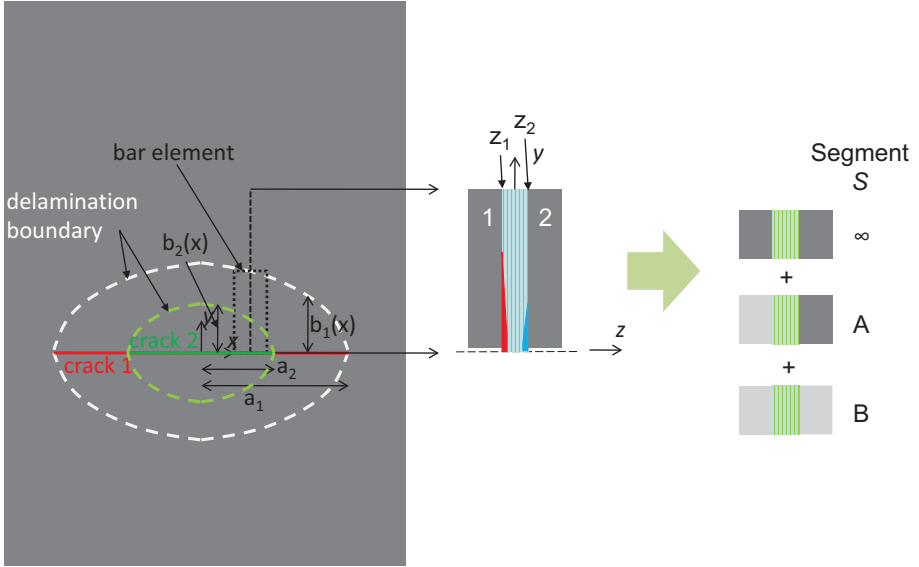


Figure 4.7 – Overview and breakdown approach for Example 2

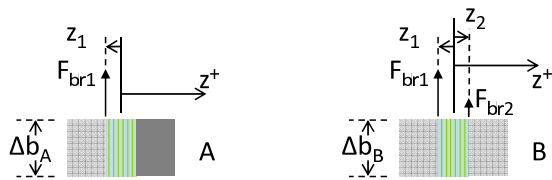


Figure 4.8 – Depiction of how the bridging loads are introduced in the CLT analysis of each segment

Because there are two delaminations, there must be two separate compatibility equations. It is therefore necessary to solve for δ_{br1} , the elongation at the boundary of delamination 1, located at the top of segment A at position z_1 through the thickness, as well as δ_{br2} , the elongation at the boundary of delamination 2, located at the top of segment B at position z_2 through the thickness.

First, consider δ_{br2} . The elongation here can be broken down by superposition into that due to the far-field stress, and each of the bridging loads.

$$\delta_{br2} = \Delta b_B (\epsilon_\infty(z_2) + \epsilon_{B21} + \epsilon_{B22}) \quad (4.40)$$

The notation ϵ_{Snm} is introduced to denote the strain in segment S at interface n due to bridging load F_{brm} . Δb_B refers to the height of segment B (Figure 4.8).

The way the bridging loads are introduced into each segment is depicted in Figure 4.8. From the solution to the first example, Equation (4.39), an equation for the strain at the same interface where the load is applied, that is appropriate for ϵ_{B22} is:

$$\epsilon_{B22} = F_{br2} \left(A'_{B_{br11}} + 2B'_{B_{br11}} z_2 + D'_{B_{br11}} z_2^2 \right). \quad (4.41)$$

To solve for ϵ_{B21} , in which the loaded interface and measured interface are different, start by altering Equation (4.35) by replacing z_{int} with z_1 , the location of the load:

$$M_x = F_{br1} z_1. \quad (4.42)$$

In the equation for ϵ_{B21} , the z_{int} is replaced with z_2 , the location where the strain is of interest, leading to the following derivation.

$$\begin{aligned} \epsilon_{B21} &= \epsilon_x + \kappa_x z_2 \\ &= A'_{B_{br11}} N_x + B'_{B_{br11}} M_x + z_2 \left(B'_{B_{br11}} N_x + D'_{B_{br11}} M_x \right) \\ &= A'_{B_{br11}} F_{br1} + B'_{B_{br11}} F_{br1} z_1 + z_2 \left(B'_{B_{br11}} F_{br1} + D'_{B_{br11}} F_{br1} z_1 \right) \\ &= F_{br1} \left(A'_{B_{br11}} + B'_{B_{br11}} (z_1 + z_2) + D'_{B_{br11}} z_1 z_2 \right) \end{aligned} \quad (4.43)$$

Note that in Equations (4.43) and (4.41), the inverted bridging stiffness matrix terms, such as $A'_{B_{br11}}$, are the same. Only one set of such terms is

required per segment, since it is the z terms that are altered to adjust for the position of the load and the interface of interest.

All the elements of Equation (4.40), which calculates δ_{br2} , are now known.

To calculate δ_{br1} , the elongation at the delamination boundary in interface 1, the elongation at the top of segment B at that interface is added to the elongation over the height of segment A at that interface.

$$\delta_{br1} = \Delta b_B (\epsilon_\infty(z_1) + \epsilon_{B11} + \epsilon_{B12}) + \Delta b_A (\epsilon_\infty(z_1) + \epsilon_{A11}) \quad (4.44)$$

The solutions for ϵ_{B11} and ϵ_{B12} can be obtained by swapping z_1 with z_2 and F_{br1} with F_{br2} , and *vice versa*, in Equations (4.41) and (4.43):

$$\epsilon_{B11} = F_{br1} \left(A'_{B_{br11}} + 2B'_{B_{br11}} z_1 + D'_{B_{br11}} z_1^2 \right). \quad (4.45)$$

$$\epsilon_{B12} = F_{br2} \left(A'_{B_{br11}} + B'_{B_{br11}} (z_1 + z_2) + D'_{B_{br11}} z_1 z_2 \right) \quad (4.46)$$

Solving for ϵ_{A11} is the same as for ϵ_{br} in the first example:

$$\epsilon_{A11} = F_{br1} \left(A'_{A_{br11}} + 2B'_{A_{br11}} z_1 + D'_{A_{br11}} z_1^2 \right). \quad (4.47)$$

The solution for the elongation at both delamination boundaries for Example 2 is now complete.

General solution

Based on the derivations used in the two examples, it is possible to state a general form for the elongation at a given delamination boundary.

Restating the solution derived in Equation (4.43) generally as the strain at interface n subject to a line load at interface m for segment S , gives:

$$\epsilon_{Snm} = F_{brm} \left(A'_{S_{br11}} + B'_{S_{br11}} (z_n + z_m) + D'_{S_{br11}} z_n z_m \right) = F_{brm} C_{br1} \quad (4.48)$$

This provides the strain, which is summed over the distance of all the segments below the interface of interest, superimposing the far field strain and the strains due to each bridging load.

$$\begin{aligned} \delta_{br_{int}}(x, b(x, n), z_n) &= \epsilon_\infty(z_n) \sum_{S:y(S) \leq b(x, n)} \Delta b_S & (4.49) \\ &+ \sum_{S:y(S) \leq b(x, n)} \Delta b_S \left(\sum_{m:b(x, m) \geq b(x, n)} \epsilon_{Snm} \right) \end{aligned}$$

Equation (4.50) can be simplified by noting that $\sum_{S:y(S) \leq b(x, n)} \Delta b_S = b(x, n)$ and that the second term can be rearranged to remove \bar{F}_{brm} from the innermost sum:

$$\delta_{br_{int}}(x, b(x, n), z_n) = \epsilon_\infty(z_n) b(x, n) + \sum_{m:b(x, m) \geq b(x, n)} F_{brm} C_{br2} \quad (4.50)$$

where

$$C_{br2} = \sum_{S:y(S) \leq b(x, n)} \Delta b_S C_{br1} \quad (4.51)$$

4.1.4 Solving for the Bridging Stress

Now that all the terms of Equation (4.26) have been derived in ways that are suitable for a generalized laminate it is necessary to put them together in a way that allows the unknown bridging loads to be solved.

In Equation (4.52), each of the terms of Equation (4.26) are written in terms of F .

$$\begin{aligned} v_{\infty, i, p} &- \sum_{j=1}^{N_k} [C_{v_{i, j, p}} F_{br_{j, p}} + C_{v_{i, j, op}} F_{br_{j, op}}] \\ &= \epsilon_{\infty_p} b_{i, p} + \sum_{m:b_{i, m} \geq b_{i, p}} F_{br_{i, m}} C_{br2} + F_{br_{i, p}} C_{\tau_p} \end{aligned} \quad (4.52)$$

The k subscripts refer to a particular cracked layer, which may have one (external layers) or two (internal layers) delaminations. The particular delamination of interest in Equation (4.52) is delamination p , with op representing the delamination on the opposite face of layer k , if k is an internal layer. If

layer k is an external layer, the op terms are excluded. The subscripts i and j refer to specific bar elements where the displacement is measured and where a bridging load is applied, respectively.

Rewriting Equation (4.52) to separate the unknown F_{br} terms from the known terms yields:

$$\sum_{j=1}^{N_k} [C_{v_{i,j,p}} F_{br_{j,p}} + C_{v_{i,j,q}} F_{br_{j,q}}] + \sum_{m: b_{i,m} \geq b_{i,p}} F_{br_{i,m}} C_{br2} + F_{br_{i,p}} C_{\tau_p} = v_{\infty, i, p} - \epsilon_{\infty_p} b_{i,p} \quad (4.53)$$

Define a $\sum_{p=1}^D N_p \times 1$ vector \mathbf{Q} (N_p is the number of bar elements of delamination p) of bridging-independent displacements from the right side of Equation (4.53):

$$\mathbf{Q} = v_{\infty, i, p} - \epsilon_{\infty_p} b_{i,p}; \quad i = 1, 2, \dots, N_p; \quad p = 1, 2, \dots, D \quad (4.54)$$

And define a $\sum_{p=1}^D N_p \times 1$ vector \mathbf{F} of the bridging loads:

$$\mathbf{F} = F_{br_{i,p}}; \quad i = 1, 2, \dots, N_p; \quad p = 1, 2, \dots, D \quad (4.55)$$

And define a $\sum_{p=1}^D N_p \times \sum_{p=1}^D N_p$ matrix \mathbf{H} that represents the compliance at the delamination boundaries with respect to the bridging loads in \mathbf{F} :

$$\mathbf{H}_{mn} = \delta_{pq} C_{v_{i,j,p}} + [\delta_{k_p k_q} - \delta_{pq}] C_{v_{i,j,q}} + \delta_{ij} C_{br2} + \delta_{mn} C_{\tau_p} \\ i, j = 1, 2, \dots, N_p; \quad p, q = 1, 2, \dots, D \quad (4.56)$$

The δ terms refer to the Kronecker delta, and have a value of one when the values of the two subscripts are equal and zero otherwise. The terms p and q refer to the delamination whose displacement is considered, and the delamination whose bridging loads are considered, respectively. The terms k_p and k_q refer to the cracked layers adjacent to delaminations p and q , respectively. The m and n subscripts of \mathbf{H}_{mn} relate to p and q by:

$$m = \sum_{l=1}^p N_l + i \quad (4.57)$$

$$n = \sum_{l=1}^q N_l + j \quad (4.58)$$

The equation

$$\mathbf{H}\mathbf{F} = \mathbf{Q} \quad (4.59)$$

satisfies the compatibility relationship of Equation (4.26) for all bar elements on all interfaces simultaneously.

The bridging loads can be found by inverting the compliance matrix:

$$\mathbf{F} = \mathbf{H}^{-1}\mathbf{Q} \quad (4.60)$$

4.2 Verification

For simple configurations, such as a 2/1 laminate with a center crack, having equal crack lengths and delaminations in all layers and interfaces, experimental measurements of crack opening have been used to infer bridging stress [6]. For more complex crack and delamination scenarios, with non-uniform crack lengths, delaminations, layer thicknesses, etc., which the newly proposed bridging solution is intended to address, direct experimental measurement of bridging forces — determining the load transfer distribution along any particular interface — is infeasible, and indirect measurement — such as comparing crack flank opening displacement — is insufficient to verify the detail of the model. For that reason, the verification for complex geometries has been done through finite element analysis (FEA). Simpler scenarios will also be modeled, for which this analytical approach has been verified through comparison to the bridging model of Alderliesten [11], to ensure the finite element approach yields valid results.

4.2.1 Approach

Laminates were modeled in ABAQUS using 3-D solid, quadratic C3D20 elements. Quarter-symmetry was employed, and only the upper right quadrant of the laminates was modeled, with symmetry constraints at the bottom and left edges. The symmetry constraints were removed on the crack faces. Tie constraints were applied between the surfaces of each adjoining layer in order to bond the laminate, except in the delaminated regions. A thermal step, with a temperature change of -100°C was used to introduce the thermal residual stresses, and the applied loading was introduced in a subsequent step. The material properties employed in the model are summarized in Table 4.1.

The bridging stresses were calculated from the FEA results through post-processing in which shear stresses — in the loading - thickness direction —

Table 4.1 – *Material properties used in FEA and model calculations*

Material	Aluminum	S2 Glass/FM94 Prepreg [14]
E_1 (MPa)	72400	48900
E_2 (MPa)	72400	5500
E_3 (MPa)	72400	5500
ν_{12}	0.33	0.33
ν_{23}	0.33	0.33
ν_{31}	0.33	0.0371
G_{12} (MPa)	N/A	5550
G_{13} (MPa)	N/A	5550
G_{23} (MPa)	N/A	5550

were extracted along a series of vertical paths on the interfaces between layers, covering an area surrounding and including the delaminated region. The shear stress along each of these paths was integrated to determine the load transfer along that path, in [N/mm], which should correspond to the bridging load of a bar element at the same x location in the bridging model described in this chapter.

The FEA calculations were performed with varying degrees of mesh density in order to ensure that the results were not skewed by a lack of convergence. Two elements through the thickness of each layer were always used — additional elements in the thickness did not affect results —, and typical element sizes ranged from 0.1–0.15 mm.

FEA calculations were performed using geometrically non-linear analyses. Non-linear effects, such as out-of-plane bending in asymmetrically delaminated laminates, may influence the bridging load distribution. Since the intent of this verification is to assess how well the model can be expected to describe the real behavior of FMLs, the less realistic geometrically linear FEA results are not included for comparison to the model in this paper. Only slight differences between linear and non-linear analyses were noted in preliminary investigations.

Figure 4.9 shows an example mesh from the verification simulations. This mesh is used to model the Glare 2-3/2-0.3 laminate with larger internal crack and delaminations, whose bridging stresses are shown in Figure 4.16.

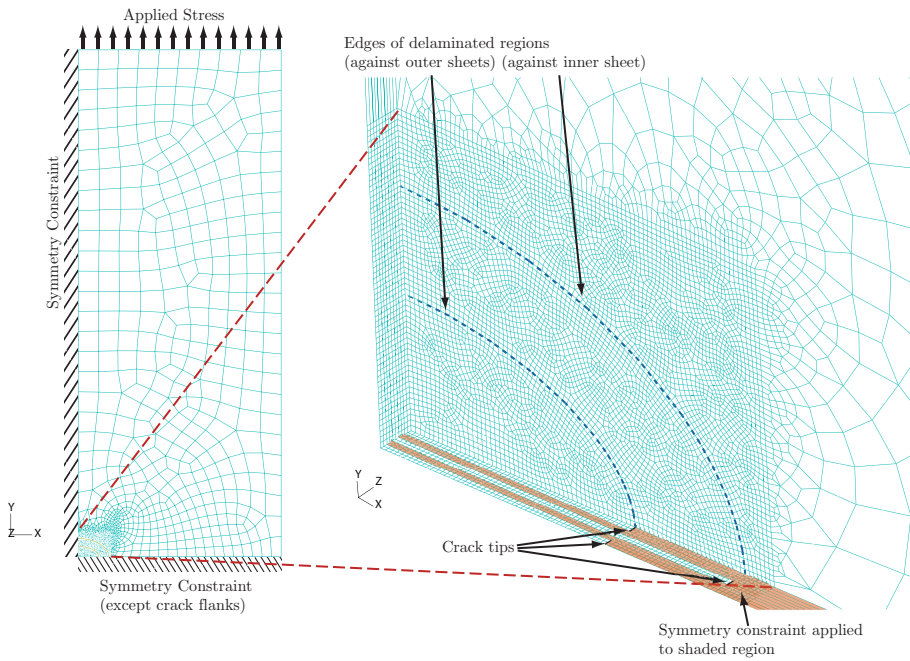


Figure 4.9 – Mesh of the FEA model for the Glare2-3/2-0.3 laminate with a larger crack and delamination in the center.

4.2.2 Results

Figure 4.10(a) shows the bridging stress distribution of a 2/1 layup of Glare with thermal residual stresses present and an applied tensile stress to the laminate of 100 MPa. In this case, there is good agreement between the model's calculated bridging stress and the FEA results along the entire extent of the delamination. Figure 4.10(b) shows the results for the same laminate with no thermal residual stresses present, but still with a remote applied stress on the laminate of 100 MPa. The lack of residual stress reduces the bridging load by approximately 4 N/mm over the length of the delamination, and this difference is reflected in both the FEA and the modeled bridging stress. This demonstrates that the bridging model handles thermal residual stresses in the laminate in a way consistent with the finite element code.

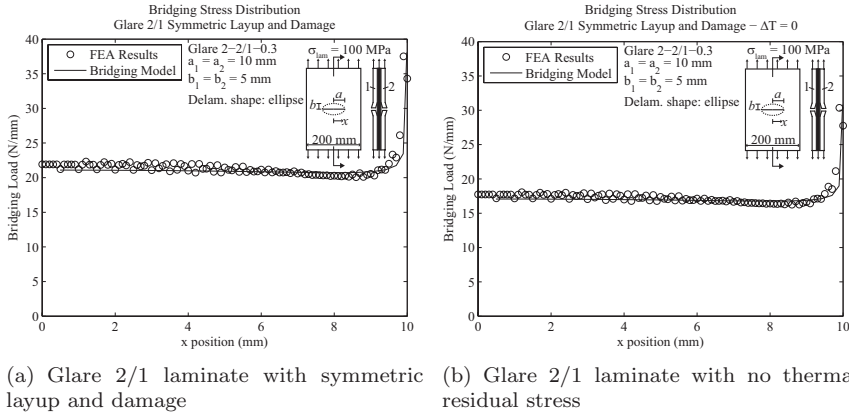


Figure 4.10 – Comparison of calculated bridging stress distributions with FEA results

The result of adding a saw cut to the center of the laminate is considered in Figure 4.11(a). Since there are no intact fibers over the length of the sawcut, $0mm < x < 5mm$, the model does not have any bridging stress results over this range. However, shear between the metal and fiber layers around the delamination boundary was still recorded in the FEA results, so the plot includes bridging stresses over the saw cut from the FEA. In the bridged region, the model overestimates the bridging load with respect to that measured in the FEA results. This may result from the model compensating for the ignored bridging in the saw cut region with additional bridging ahead of the saw cut.

Figure 4.11(b) shows the results for a laminate with two fiberglass composite

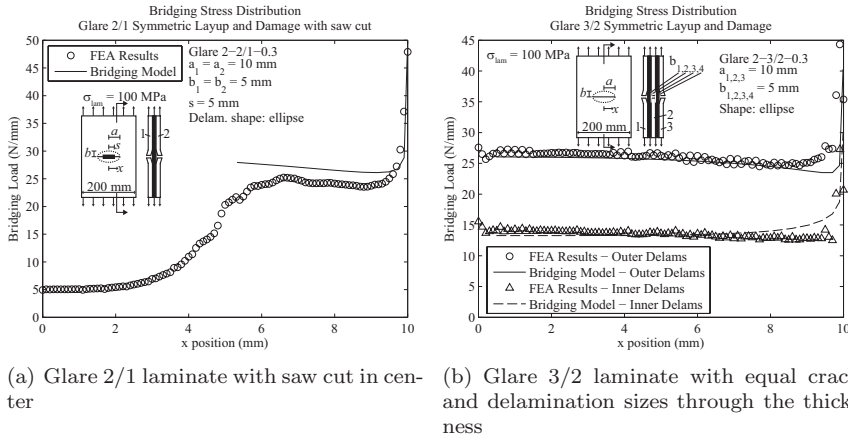


Figure 4.11 – Comparison of model and FEA results

layers and three cracked aluminum layers. The crack lengths and delaminations are equal through the thickness of the laminate.

In Figure 4.12 is a comparison of the FEA and analytically-modeled bridging loads for a 2/1 Glare laminate with different crack lengths in each of the two metal layers and different delamination sizes in each interface. The analytical model without the correction for reduced metal layer bridging stiffness (Figure 4.12(a)) accurately captures the bridging loads in the smaller delamination, but misses those of the larger one, overestimating the bridging load from $0mm < x < 10mm$ and underestimating the bridging load from $11mm < x < 15mm$. The additional inclusion of the δ_K correction, as in Section 4.1.3, for the cracked bridging material, depicted in Figure 4.12(b), worsens the comparison to the FEA results.

The addition of a 5 mm central notch to the asymmetric scenario of Figure 4.12 is considered in Figure 4.13. Since the analytical model only considers the bridging over bar elements with intact bridging material, it does not attempt to estimate the bridging that occurs over the delamination boundary in the notched region, $0mm < x < 5mm$. The additional discrepancy due to the notch — the bridging load varies in the FEA results where the calculation predicts a nearly constant load — matches that found for a symmetrically damaged laminate in Figure 4.11(a). It shows the same trends as the notched symmetrically damaged laminate, along with matching the small delamination’s bridging loads well while over- then underestimating the bridging loads

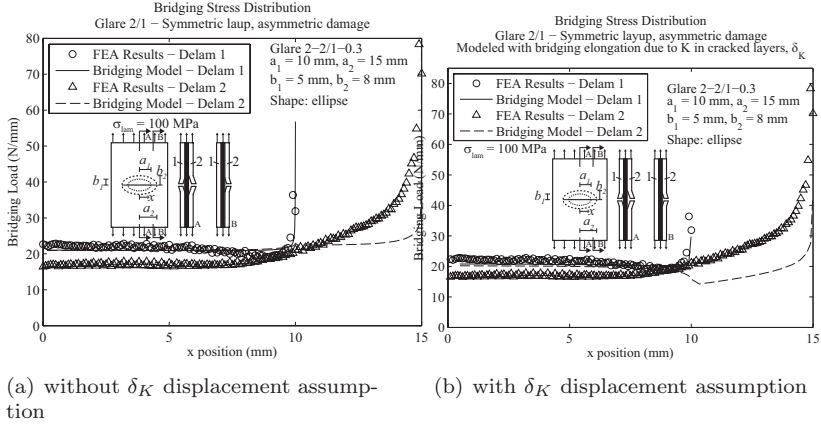


Figure 4.12 – 2/1 Glare with different cracks and delaminations

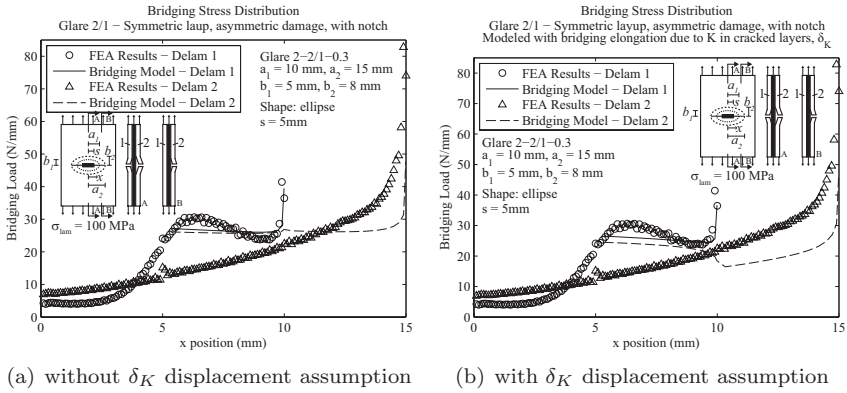


Figure 4.13 – 2/1 Glare with different cracks and delaminations, with a 5 mm saw cut.

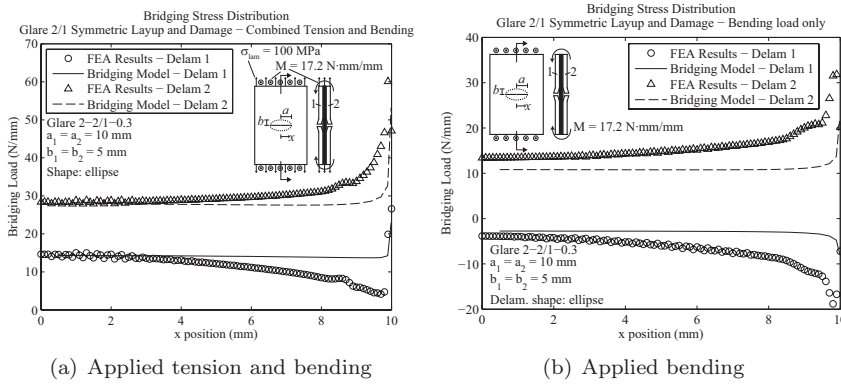


Figure 4.14 – Comparison of model and FEA results for combined tension-bending loading, (a), and bending-only loading, (b)

of the larger delamination before and after the smaller crack tip.

Figure 4.14(a) shows the analytical and FEA model results of bridging loads in a Glare 2 laminate with symmetric layup, crack lengths, and delaminations through the thickness, with applied tension and bending loads to the laminate. Bending was applied through a point moment applied to a reference point, to which the top surface of each layer of the laminate was constrained through a multi-point constraint. The analytical model matches the bridging stress of both delaminations near the center of the laminate, away from the crack tips, however the effects of the bending on the bridging stress near the crack tips are greater in the FEA model than expected according to the analytical model. Similar discrepancies exist in Figure 4.14(b), in which only a bending moment, M_x , is applied to the laminate. Note that the average of the two curves is not equal to zero due to the effects of residual stress, which leads to additional positive bridging on both delamination boundaries.

Figure 4.15 shows the results for a laminate with an asymmetric layup — one metal sheet is 0.3 mm thick, while the other has a thickness of 1.0 mm. The analytical model captures the trend seen in the FEA results, that the bridging load from the thick metal sheet is slightly higher than that from the thin sheet and that the bridging stresses are nearly constant over the lengths of the delaminations, up until they approach the crack tip. However, there is a small difference between the actual magnitudes of the bridging load between the analytical model and the FEA results.

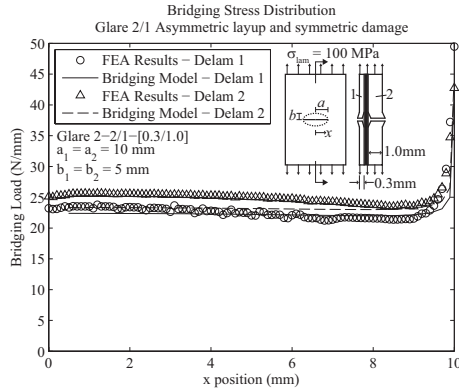


Figure 4.15 – Glare 2/1 with two unequal metal layer thicknesses

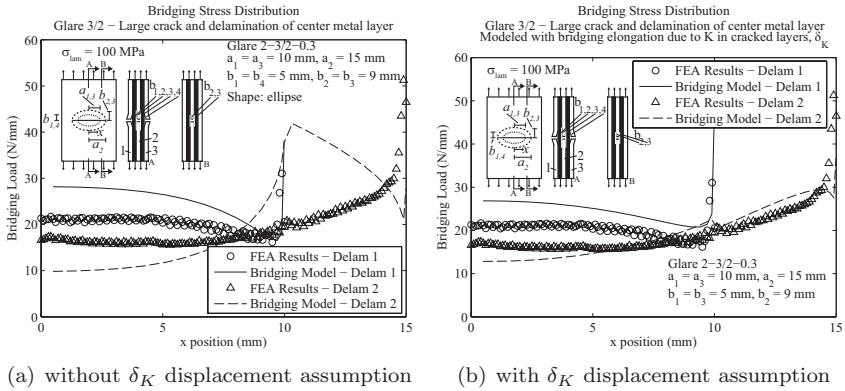


Figure 4.16 – This 3 metal layer, 2 fiber layer laminate has a larger crack and delamination in the center.

Figure 4.16 compares the results of the bridging model and FEA for a 3/2 laminate in which the center metal layer has a longer crack compared to the outer two layers and larger delaminations at its interfaces with the fiber layers. Computing the bridging stress with the assumption that the bridging layers contribute their full stiffness when cracked results in an overestimation of the bridging stiffness of the bar elements around the shorter, $a = 10mm$, crack tips, which in turn leads to an overestimation of the bridging stress acting on the central metal layer in this region, as can be seen in Figure 4.16(a). Figure 4.16(b) compares the results of the model, with the δ_K correction for extra displacement due to the crack tip stress field in the outer metal layers included, to the FEA results. The results with the δ_K correction have much improved agreement with the FEA results. The predicted bridging load for the inner, larger delaminations much more closely follows the FEA result, and the predicted bridging load for the outer, smaller delaminations moves closer to that from the FEA compared to that found in the non-corrected calculation.

4.3 Discussion

Overall, comparing the results of calculations with the proposed model to bridging loads from finite element simulations of laminates with different layup and damage configurations shows that the generalized bridging model presented in this chapter is capable of estimating the effects of a variety of complicating factors on the bridging stresses of cracked FMLs. The following sections discuss the performance of the model with regard to each complicating factor.

4.3.1 Residual stress

Comparing Figures 4.10(a) and 4.10(b) show that the effects of residual stress on the calculated thermal residual stress of the model match those from the FEA results. In this particular case, the effect was an increase of the bridging stress of about 4 N/mm over most of the length of the delamination. All of the other results given in Section 4.2.2 include the effects of residual stress. There is no error specifically attributable to thermal residual stress in any of these results.

4.3.2 Saw cut

In the cases where a saw cut was included in the analysis, the model performed poorly, missing the value of the bridging stress, and in the case with differing damage in each layer (Figure 4.13), missing even the qualitative trend of the bridging stress over the length of the delamination. This likely results from excluding the bridging in the saw cut region of the delamination from consideration in the model. The available bridging stress models for ungeneralized FMLs [3, 6, 8] also ignore any bridging effects occurring where the bridging material is not intact. Alderliesten found that observed crack opening displacement was less than predicted in the vicinity of the saw cut tip for large saw cuts; however, the resulting fatigue crack growth matched predictions well, indicating that bridging in the saw cut region may be safely ignored for such predictions.

4.3.3 Number of layers

The nearly exact match of the calculated bridging loads with the FEA results in Figure 4.11(b) shows that the proposed model is able to distinguish between the bridging of an external vs an internal cracked layer. The results in Figure 4.16(b) also show that varying damage size though the thickness can also be accounted for by the model for laminates with more than two metal layers.

4.3.4 Bending

In this generalized model, two types of bending are accounted for: applied bending loads on the laminate and localized bending due to asymmetry in the cracks and delaminations. The applied bending can be a result of an applied moment, as in the scenario depicted in Figure 4.14, or it can be a result of tension-bending coupling due to laminate asymmetry, as in Figure 4.15. In both of these cases, the model results approximate the FEA results with some amount of error, most significantly in Figure 4.14 the FEA results diverge from the model-calculated results towards the crack tips.

Localized bending is relevant in the cases depicted in Figures 4.12 and 4.13. In these figures, the model overestimates the bridging stress of the larger delamination to the left of the shorter crack tip, while underestimating the bridging stress of the larger delamination between the short crack tip and the longer one. In contrast, the bridging stress associated with the smaller

delamination is well predicted by the model in these cases, excepting the error due to the presence of the notch in Figure 4.13.

The errors in scenarios where bending is a factor may result from the use of CLT in determining the bending strain and stiffness of the bridging material. CLT linearizes strain through the thickness of a laminate, which has the effect of overestimating bending deformation for large moments and curvatures [15]. Incorporating a non-linear laminate theory, which can better approximate the true behavior of a laminate in bending, may improve the bridging model's performance where bending, both local and global, is present. Unfortunately, a non-linear laminate analysis will prove difficult to implement within the context of the linear algebra solution to the bridging problem used in this chapter.

It is also possible that the method of measuring the bridging stress in the FEA results, integrating the shear stress on the surface of the fiber layer, introduces error as there may be shear stress that is attributable to bending, not load transfer between the layers. Alternate methods of assessing the bridging stress with the finite element analysis, such as nodal contact forces, may clarify the true bridging stress.

4.3.5 Differing crack lengths

The ability of the model to estimate the bridging stress in laminates with differing crack lengths in the metal layers is demonstrated by Figures 4.12 and 4.16. Unfortunately, there is no clear answer as to whether the δ_K correction for bridging layer deformation due to crack tip stress fields is necessary or erroneous: the prediction for the 3/2 laminate with the longer crack in the center layer is much improved with the inclusion of δ_K , but the bridging stress calculated with δ_K for the 2/1 laminates with differing crack lengths matches the FEA results worse than that without δ_K . Generally, the inclusion of δ_k serves to reduce the bridging load transferred in regions where the bridging material is comprised of metal layers having shorter cracks than the cracked layer in question. Future work should include comparing crack growth and residual strength predictions based on the bridging model with and without this correction to test data, to determine which assumption provides the best agreement with experimental data in the widest variety of circumstances. Alternative assumptions about the contributions of cracked metal layers to bridging that better match the FEA results should also be explored.

4.3.6 Applicability of the model

Determining the bridging stress in a cracked FML is not an end in itself; rather, it is a means to determining the damage tolerance of the FML through simulation of cyclic and static damage growth. What kind of indication of the applicability of the model for this purpose can be derived from the verification results? Ideally, the model would perfectly calculate the bridging stress for any laminate-crack-delamination combination, thereby providing perfect input for a calculation of delamination growth and crack extension.

This model does not exactly match the FEA results in all cases; however the self-balancing nature of damage growth in FMLs is such that slight errors in bridging stress may have only small effects on the outcome of residual strength and crack growth predictions. In regions where the bridging load is overestimated, the predicted static or cyclic delamination growth will be greater, leading to a larger predicted delamination and subsequent reduction in predicted bridging load. Likewise, where bridging load is underestimated, the reduction in predicted delamination growth will lead to subsequent increases in predicted bridging. An important capability of the bridging model, when used to make such predictions, will be to distinguish the effects of changes in the laminate composition or load scenario. This would make these predictions useful in improving the design of new FMLs. The good comparisons between this model's predictions and the FEA results presented in this chapter for a variety of laminate and load scenarios suggest that the proposed bridging model should be sufficiently capable of discerning the effects of changes to laminate composition and loading.

4.3.7 Challenges for implementation

Additional work is necessary to enable the inclusion of this generalized bridging model into existing schemes for crack growth prediction of FMLs. The Alderliesten model [3] utilizes an iterative approach, wherein the bridging load is found at the minimum and maximum applied loads, then the delamination front and crack lengths are extended by an increment proportional to their growth rates. These growth rates are a function of the Mode II strain energy release rate range for delamination and a function of the cyclic change in stress intensity factor for the fatigue cracks. With the new delamination and crack configuration, the bridging calculation and damage extension are repeated. The results of this analysis are a prediction of crack length and delamination shape linked to the number of load cycles applied to the FML.

For a generalized laminate, once the bridging loads are known, the calculation of stress intensity factors of each crack tip is straightforward. Taking the view of each metal sheet as interacting with the laminate through its farfield stress and through the bridging load along the delamination front, superposition of the stress intensity factors due to each of these loadings yields the stress intensity factor of that metal layer in the laminate.

Calculating the strain energy release rate (SERR) of delamination growth, however, is less straight forward. Methods of determining SERR in non-generalized FMLs [2, 3, 6] are based on a simple representation of each bar element in which all delaminations are the same height and grow at equal rates, and all of the layers are of equal thickness and material (one thickness for metals and one for fibers). These models further make no effort to include the effects of bending. A generalized approach to the SERR is needed before a complete, generalized model of FML crack growth or residual strength can be developed.

To apply the model of this chapter to residual strength predictions would require, in addition to a new SERR calculation method, a means of calculating the plastic deformation around each crack tip and including this deformation in the bridging analysis. This could possibly be done in a way similar to the way the singular crack tip deformation field was addressed in Section 4.1.3.

4.4 Conclusions

A generalized model for crack bridging load distribution in FMLs, no longer constrained to simple laminates, loading scenarios, and damage configurations, has been developed. It relies on the same delamination front compatibility requirement that serves as the foundation for previous, simpler FML bridging models. The necessary changes to each component of the displacement at the delamination fronts in order to generalize the model have been described through the various derivations in this chapter.

Calculation results from the generalized bridging model were compared to bridging stresses from 3D solid element finite element simulations of cracked and delaminated FMLs with several laminate, damage, and load configurations. Overall good agreement is found between the model and the FEA results, though improvements could be made in situations where global or local bending occur. The results are also ambiguous with regard to whether or not the crack tip strain field must be taken into account when cracked layers act as bridging layers.

The ability of the proposed generalized model to discern the effects of a variety of changes to the laminate and damage configurations shows its great potential to serve as the foundation of generalized models for FML crack growth and residual strength.

4.5 Notes on Accounting for Residual Stress

It is important when performing the bridging analysis that residual stress, specifically thermal residual stress resulting from mismatched coefficients of thermal expansion between the layers, is accounted for in a physically realistic and self-consistent manner. This can be assured by zeroing the displacements of the laminate in an appropriate way:

1. Each layer, considered to be a separate piece, has a remote stress applied to it equal to the thermal residual stress calculated with CLT. This stress is exerted on each layer to maintain compatibility of the layers while reducing the temperature after curing to the testing or analysis temperature. At this point there are no cracks and no delaminations in the laminate.
2. The displacement of all points within the laminate is now considered to be zero.
3. Any new changes in displacement are measured relative to this initial state.
4. The cracked layers are then considered cracked, so the cracks open (or close) due to the already-present residual stress. Delaminations are also now considered present; however, since the delaminations are represented in the model via load passed between the layers to maintain compatibility at the delamination boundary, the delaminations themselves have no *direct* effect on the displacement of the bridging layers³.
5. The stress due to loading in each layer, calculated with CLT, is treated as a remote load acting on that layer.

³Consider an uncracked FML with an internal delamination. As long as the delamination is small relative to the size of the laminate, the presence of the delamination does not change the strain of the delaminated material, despite residual stresses, since it is still constrained by the surrounding material.

4.5.1 Effect on v_∞

The displacement of the cracked layer due to residual stress, before the crack is present, must be subtracted from v_∞ since this displacement occurs before point 2, above.

$$v_{\infty_i}(x, y) = \frac{1}{2G} \left[\frac{\kappa + 1}{2} \text{Im}\bar{Z} - y \text{Re}Z - \frac{\kappa - 3}{2} \frac{\sigma_{\infty_i}}{2} y \right] - \frac{\sigma_{resi}}{E_{11i}} b_{z_{int}}(x) \quad (4.61)$$

4.5.2 Effect on v_{br}

Since v_{br} is determined only by the bridging stress, there is no special consideration required for residual stress.

4.5.3 Effect on δ_{br}

The term for the farfield strain in Equation (4.50), $\epsilon_\infty(z_n)$, must represent only that strain due to applied loads, and not include that due to residual stress or thermal expansion.

4.5.4 Effect on δ_{pp}

The displacement at the delamination boundary was derived as a function of only the bridging stress in Equation (4.25). Since the farfield stresses of neither layer play a role in this displacement, no special consideration is required to incorporate residual stress into the bridging model.

4.5.5 Conclusion

The treatment of bridging stress as the transfer of load between otherwise independent layers along the delamination boundaries necessitates application of residual stresses and stresses due to load application to the laminate as farfield loads (or displacements) applied to separate layers. At some point where the stresses and strains are known, the displacement must be zeroed, since displacement is always relative. Given this framework, the above approach picks a reasonable situation against which to measure the displacement.

Bibliography

- [1] Wilson, G. S., Alderliesten, R. C., and Benedictus, R. (2013) A generalized solution to the crack bridging problem of fiber metal laminates. *Engineering Fracture Mechanics*, <http://dx.doi.org/10.1016/j.engfracmech.2013.03.008>.
- [2] Marissen, R. (1988) *Fatigue crack growth in ARALL. A hybrid aluminium-aramid composite material: Crack growth mechanisms and quantitative predictions of the crack growth rates*. Ph.D. thesis, Delft University of Technology, Delft, The Netherlands.
- [3] Alderliesten, R. C. (2007) Analytical prediction model for fatigue crack propagation and delamination growth in glare. *International Journal of Fatigue*, **29**, 628–646.
- [4] Rodi, R., Wilson, G. S., Alderliesten, R. C., and Benedictus, R. (2009) The effect of bridging fibres on the entire strain field in fibre metal laminates. *17th ICCM International Conference on Composite Materials*, Edinburgh, UK.
- [5] Tada, H., Paris, P., and Irwin, G. (1973) *The Stress Analysis of Cracks Handbook*. Del Research Corporation, 1 edn.
- [6] Guo, Y.-J. and Wu, X.-R. (1999) Bridging stress distribution in center-cracked fiber reinforced metal laminates: modeling and experiment. *Engineering Fracture Mechanics*, **63**, 147 – 163.
- [7] Guo, Y. J. and Wu, X. R. (1998) A theoretical model for predicting crack growth rates in fiber-reinforced metal laminates. *Fatigue & Fracture of Engineering Materials and Structures*, **21**, 1133–1145.
- [8] Wang, J. T. and Smith, S. W. (2010) Residual strain effects on bridging stress of cracked and delaminated fiber metal laminates. *Journal of ASTM International*, **7**.
- [9] Randell, C. E. (2005) *Subsurface Fatigue Crack Growth in Glare Fibre Metal Laminates*. Ph.D. thesis, Delft University of Technology, Delft, The Netherlands.
- [10] Roebroeks, G. H. J. J., Hooijmeijer, P. A., Kroon, E. J., and Heinimann, M. B. (2007) The development of Central. *First International Conference on Damage Tolerance of Aircraft Structures*, Delft, The Netherlands.

- [11] Wilson, G. S., Alderliesten, R. C., Rodi, R., and Lemmen, H. J. K. (2009) Practical applications of improvements in fnl crack bridging theory. Bos, M. J. (ed.), *ICAF 2009, Bridging the Gap between Theory and Operational Practice: Proceedings of the 25th Symposium of the International Committee on Aeronautical Fatigue, 27-29 May 2009, Rotterdam, The Netherlands*, pp. 539–558.
- [12] Sun, C. T. and Farris, T. N. (1989) On the completeness of the Westergaard stress functions. *International Journal of Fracture*, **40**, 73–77.
- [13] Anderson, T. (1991) *Fracture mechanics: fundamentals and applications*. CRC Press, 2 edn.
- [14] Alderliesten, R. C. (2005) *Fatigue crack propagation and delamination growth in Glare*. Ph.D. thesis, Delft University of Technology, Delft, The Netherlands.
- [15] Sun, C. T. and Chin, H. (1988) On Large Deflection Effects in Unsymmetric Cross-Ply Composite Laminates. *Journal of Composite Materials*, **22**, 1045–1059.

This page intentionally left blank.

Chapter 5

Delamination strain energy release rate

This chapter provides a detailed description of the strain energy release rate calculation used in the generalized model. It is adapted from an article submitted in December 2011 to *Engineering Fracture Mechanics* [1].

5.1 Introduction

Laminated structures offer numerous advantages, such as property tailorability, low scrap production, and inherent multiple load paths. Fiber metal laminates (FMLs) have the added advantage of combining the best features of metals and composites in one laminate. However, a major disadvantage of laminates is that each interface between laminae is a potential failure location. Delamination initiation, growth, and residual strength are therefore important considerations in the design and analysis of laminated structures. In the case of FMLs, delamination growth plays an important role in the bridging of cracks propagating in the metal layers [2–5]. Anywhere a metal layer crack is present in an FML, delamination between the cracked layers and intact fiber layers is found to occur.

Any analytical model of FML behavior must therefore accurately take into account the effects of the delamination shape on the bridging load distribution and the effects of the loading on the growth of the delamination. In the case

of cyclic fatigue crack growth of FMLs, the incremental growth and change in shape of the delamination due to cyclic loading must be considered. In the case of residual strength modeling, the static delamination growth as the load in the FML is increased must be accurately described.

Cyclic delamination growth rates have been shown to be a function of the cyclic change in strain energy release rate (SERR). As a specific example, Alderliesten [6, 7] has proposed

$$\frac{db}{dN} = C \left(\sqrt{G_{max}} - \sqrt{G_{min}} \right)^n \quad (5.1)$$

where C and n are constants, and $\frac{db}{dN}$ is the amount of crack extension in a single load cycle. The square roots in Equation (5.1) are important for maintaining similitude under different loading conditions [8].

Likewise, static delamination can be characterized by SERR, typically with a critical SERR, G_c , criterion.

In testing several configurations of FML specimens for delamination growth rate, mode II has been shown to be dominant in the growth of internal delaminations [3, 9, 10], and thus only mode II is considered in this work. In more complex geometries, mode I delamination growth and mode mixity may come into play. However, a good understanding of mode II will still be needed in those cases.

Previous analytical methods of calculating SERR in FMLs, such as those in [5] and [6] have been derived based on assumptions of through-the-thickness similarity of the laminate — that all the metal layers have the same properties and thickness, all the composite fiber layers have the same composition and thickness, and all the crack lengths and delamination sizes and shapes are the same at every metal layer and internal interface. These assumptions hold for most variants of previous-generation FMLs, such as Glare and ARALL, subject to in plane tensile and compressive cyclic loading, but newer, thicker FMLs are now in development in which metal and fiber layers of different composition and varying thickness are laminated together [11, 12]. Additionally in such cases, crack lengths are found to vary through the thickness, and delaminations may have different sizes at each interface (Figure 5.1).

In order to model such laminates well, a generalized method of calculating the SERR of each individual delamination in an FML is necessary. This chapter presents such a method, and compares the SERRs calculated therewith to SERRs calculated with finite element analysis to confirm the results.

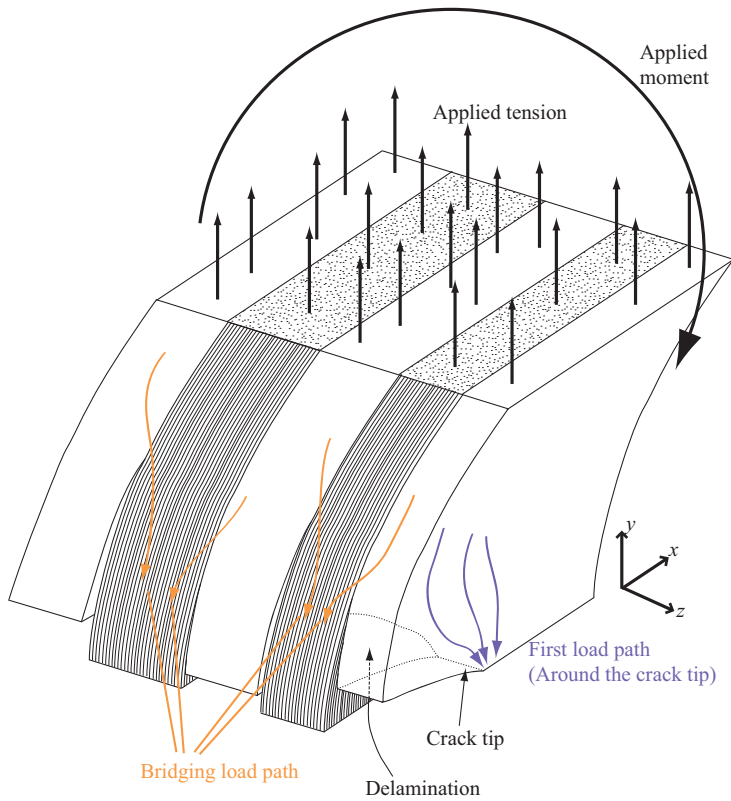


Figure 5.1 – Schematic of crack bridging scenario for a generalized laminate, showing one quarter of a center-cracked laminate subject to remote tension and bending loads. There is a delamination in each interface between a cracked and uncracked layer over which the bridging load is transferred, reducing the crack tip stress intensity.

5.2 Generalized SERR calculation method

The strain energy release rate of an individual delamination in the laminate can be found by considering the energy balance given in Equation (5.2).

$$G = -\frac{dW}{db} = \frac{d}{db} [F - U_{bot} + U_{top}] \quad (5.2)$$

F is the work associated with the load passing through the laminate causing the additional elongation of the laminate as the delamination extends. The U terms refer to the strain energy in a cross section below and above the delamination of interest. The change in strain energy for a given extension db is the difference between these strain energies, since there is an increase in the amount of laminate below the delamination and a decrease of that above the delamination as it extends. All other components of the laminate strain energy do not vary with b , assuming a small delamination growth, and can be ignored. Classical laminate theory is used to calculate the work and these energies.

5.2.1 Assumptions

The calculation method derived below can account for the SERR at one delamination front in a single bar element. A bar element is a finite-width strip of the laminate in which the delamination front is assumed to be horizontal — perpendicular to the applied tensile load — and the bridging loads evenly distributed. Such bar elements are used to enable discretization for the numerical solution of the crack bridging problem in FMLs [2, 7, 13].

The bar elements are further subdivided into vertical segments of laminate, between each delamination front, as in Figure 5.2. The assumptions of classical laminate theory (CLT), such as continuity of strain through the thickness hold for each segment. This segmented CLT approach has been used to determine the compliance of a cracked and delaminated FML in [2]. Each segment only includes the intact fiber layers and those layers bonded to one or more fiber layers — the “bridging material.” The far field strain of the laminate is applied to each segment, as well as the bridging load from all delamination fronts above a given segment. This is illustrated with the placement of the bridging force over segment A in Figure 5.3.

The strain energy associated with the near-tip stress field of the delamination is ignored. This is done because, assuming that the incremental delamination is small and it occurs while the applied load is held constant, the localized peak stresses around the delamination will move up the laminate along with

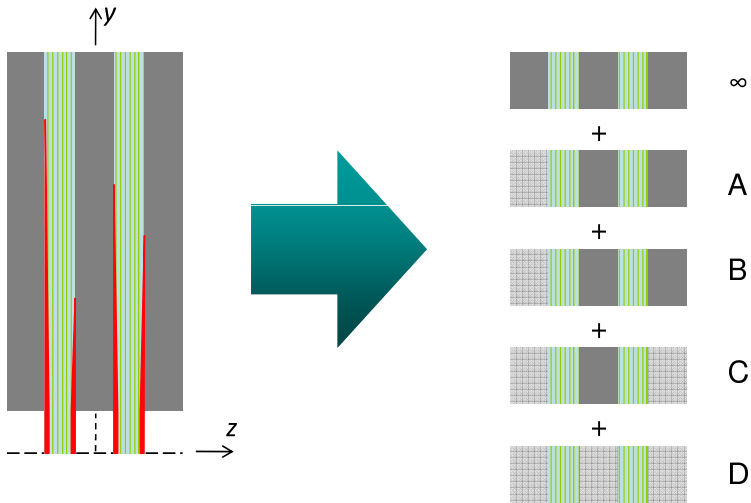


Figure 5.2 – Scheme for subdivision of delaminated bar element into sections to which classical laminate theory can be applied [2]

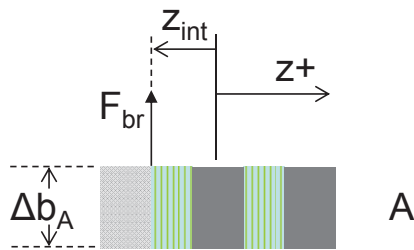


Figure 5.3 – Definition of reference distances on a laminate segment

the delamination front, and the relative difference in these localized stress fields before and after delamination will be negligible.

Residual stress is dealt with by including it in the stress of each lamina. Care must be taken to consistently treat the residual stress throughout the analysis in order to properly account for its effects. For instance, the release of residual stress from fully delaminated metal layers must be treated through the bridging stress mechanism¹, it does not simply disappear by virtue of the metal layer contracting in the absence of constraining fiber layers. It is convenient to treat the residual stress in this way in the model, because it simplifies accounting for the crack opening effect of releasing the residual stress where the metal layer is cracked. The laminate must be thought of as a system - the release of residual stress may occur along multiple load paths, just as the release of stress due to loading.

A cautionary note regarding including residual stress is that when calculations are based on the strain in a given layer (such as with the segmented classical laminate theory approach to determining the compliance of the bridging material) the strain used cannot be merely the laminate strain calculated with CLT. The strain from CLT includes the effect of loading the laminate and the effect of the temperature change between curing and testing. To account for the residual stress in the individual layers, the strain of an individual lamina, separate from its laminate, due to the same ΔT must be subtracted from the laminate strain from CLT:

$$\epsilon_{CLT} = \epsilon_{load} + \epsilon_{\Delta T} \quad (5.3)$$

$$\epsilon_{k\infty} = \epsilon_{CLT} - \epsilon_{lamina\Delta T} = \epsilon_{load} + (\epsilon_{laminate\Delta T} - \epsilon_{lamina\Delta T}) \quad (5.4)$$

Now ϵ_{lamina} is directly proportional to the lamina stress, including the contributions of both applied loading and the thermal residual stress of the laminate, including no offset from the origin - if $\epsilon_{lamina} = 0$, then $\sigma_{lamina} = 0$, and vice versa. If this correction is not made, there is an offset in the relationship between stress and strain, and they are not directly interchangeable.

Another assumption of this approach is that the segmented CLT approach, which assumes a linear strain distribution through the thickness of the laminate, and ignores interlaminar shear due to localized load introduction, sufficiently captures the distribution of stress in a given laminate cross-section due to the bridging stresses above that cross-section (see Figure 5.3). This assumption

¹Or in the case of the full laminate, it is released from a cracked metal layer through both bridging stress and via the first load path. The first load path is that through the metal layer itself, flowing around the crack tip, thereby increasing the stress intensity factor.

is acceptable in the compatibility solution of the bridging stresses, where the change in deformation of the laminate over a distance due to a localized load is considered, but for calculating strain energies and work, the localized stress may become important.

Secondary bending

Along the length of the laminate, as delaminated layers are removed from the load-carrying material, any asymmetry results in a shift in the neutral axis of the material. Under a tensile load, the neutral axis tends to displace out of the plane of the laminate toward the axis of loading, a phenomenon referred to as secondary bending. Schijve [14] derived the Neutral Line Model (NLM), based on beam theory, to describe the out of plane displacement and the associated bending stress when eccentricity of loading or of the neutral line occurs.

The NLM is used in this chapter to account for the effects of asymmetry of the laminate or of portions of the laminate where the intact, undelaminated material is asymmetric. The strains used in calculation of the strain energy and work in the laminate will be composed of two components: that due to the load carried in the laminate, and that due to the bending of the laminate. For purposes of calculating the farfield stress in each layer, any applied moment is left out of the CLT calculations. The stress due to the moment is re-included in the local strain energy calculations (e.g. Equation (5.7), below).

To simplify the calculation, only the strain energy across the middle, vertically, of a segment of laminate will be considered. Consider Figure 5.4, which shows a laminate with two different-length delaminations and a representation of its secondary bending. As long as any two delaminations are separated by some distance, any differential growth of one delamination will leave the stress fields in the neighborhood of each delamination unchanged, so that the only change in strain energy comes from an increase in the amount of laminate subject to the bending stress in the middle region of the segment below the delamination and a decrease in laminate subject to the bending in the middle region above the delamination. In this study, the point of load application is taken to be the middle of that segment, when no external bending is applied, and the plane of symmetry in the center of the laminate is taken to be the middle of that segment.

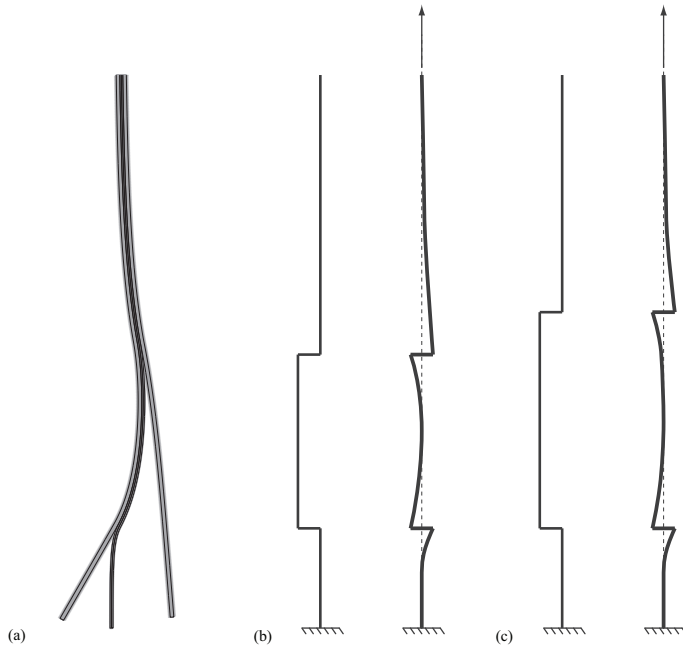


Figure 5.4 – Secondary bending in a delaminated strip. (a) shows FEA results for the asymmetrically delaminated specimen of Figure 5.12 (with 10x deformation scaling). (b) shows a schematic representation of the neutral line location before and after loading. (c) shows the results of the extension of the top delamination: the bending shape around the delamination locations stay approximately the same, while the center portion of the newly lengthened segment straightens out somewhat.

5.2.2 Derivation

Starting with $U_{top\ i}$, the strain energy in a cross-section of the laminate above the delamination of interest, i , the general form for strain energy is:

$$U_{top\ i}^d = \int_V \frac{\sigma^2}{2E} dV \quad (5.5)$$

The superscript d in Equation (5.5) denotes that the derivative with respect to the height of the delamination of interest, b_i , has already been taken. This allows the components of the laminate strain energy that are not functions of b to be ignored.

Splitting the integral in Equation (5.5) to account for each lamina, and the strain distribution in the z direction due to bending yields:

$$U_{top\ i}^d = \sum_{k:k \in \mathbf{B}_{top}} \int_{\bar{z}_k - t_k/2}^{\bar{z}_k + t_k/2} \frac{E_{11\ k} \epsilon_{k\ top}(z)^2}{2} dz \quad (5.6)$$

where summation in k includes only those laminae that are considered bridging material in the cross-section of interest. Bridging material refers to material that is not cracked in a given bar element or material that is directly bonded to uncracked material in the segment of interest. This is the same definition as in [2].

And $\epsilon_k(z)$ can be calculated:

$$\epsilon_{k\ top}(z) = \epsilon_{k\infty} + z\kappa_\infty + M_{top} (B_{11\ top}^* + zD_{11\ top}^*) + A_{11\ top}^* \sum_{n:b_n > b_i} F_{br_n} \quad (5.7)$$

where n refers to bridging loads due to delaminations located above the cross-section of interest. $A_{11\ top}^*$ refers to the (1,1) term from the inverse of the A matrix from CLT, based on the ‘‘laminate’’ consisting of all the bridging material *above* the delamination of interest, with non-bridging layers treated as though they have zero stiffness. $B_{11\ top}^*$ and $D_{11\ top}^*$ come from the inverse of the full CLT ‘‘ABD’’ matrix. A similar derivation for this expression for strain due to a bridging load is described in [2].

The strain, $\epsilon_k(z)$, can be factored into terms that are and are not linear coefficients of z :

$$\begin{aligned} \epsilon_k(z) &= [\epsilon_{k\infty} + A_{11\ top}^* \sum_{n:b_n > b_i} F_{br_n} + M_{top} B_{11\ top}^*] \\ &\quad + z[\kappa_\infty + M_{top} D_{11\ top}^*] \\ &= \psi_1 + z\psi_2 \end{aligned} \quad (5.8)$$

U_{top}^d is thus:

$$U_{top}^d = \sum_{k:k \in \mathbf{B}_{top}} \int_{\bar{z}_k - t_k/2}^{\bar{z}_k + t_k/2} \frac{E_{11} k (\psi_1 + z\psi_2)^2}{2} dz \quad (5.9)$$

$$= \sum_{k:k \in \mathbf{B}_{top}} \frac{E_{11} k t_k}{2} \left[\psi_1^2 + 2\psi_1 \psi_2 \bar{z}_k + \psi_2^2 \bar{z}_k^2 + \frac{1}{12} \psi_2^2 t_k^2 \right] \quad (5.10)$$

where ψ_1 and ψ_2 are defined:

$$\psi_1 = \epsilon_{k\infty} + A_{11}^*{}_{top} \sum_{n:b_n > b_i} F_{br_n} + M_{top} B_{11}^*{}_{top} \quad (5.11)$$

$$\psi_2 = \kappa_{\infty} + M_{top} D_{11}^*{}_{top} \quad (5.12)$$

Similarly, the strain energy in a cross-section of the laminate below the delamination of interest, U_{bot}^d can be shown to be:

$$U_{bot}^d = \sum_{k:k \in \mathbf{B}_{bot}} \int_{\bar{z}_k - t_k/2}^{\bar{z}_k + t_k/2} \frac{E_{11} k (\psi_3 + z\psi_4)^2}{2} dz \quad (5.13)$$

$$= \sum_{k:k \in \mathbf{B}_{bot}} \frac{E_{11} k t_k}{2} \left[\psi_3^2 + 2\psi_3 \psi_4 \bar{z}_k + \psi_4^2 \bar{z}_k^2 + \frac{1}{12} \psi_4^2 t_k^2 \right] \quad (5.14)$$

where ψ_3 and ψ_4 are defined:

$$\psi_3 = \epsilon_{k\infty} + A_{11}^*{}_{bot} \sum_{n:b_n \geq b_i} F_{br_n} + M_{bot} B_{11}^*{}_{bot} \quad (5.15)$$

$$\psi_4 = \kappa_{\infty} + M_{bot} D_{11}^*{}_{bot} \quad (5.16)$$

There are two key differences between U_{top}^d and U_{bot}^d . The first is the difference between the terms for the laminate compliance above and below the delamination, for instance $A_{11}^*{}_{top}$ vs. $A_{11}^*{}_{bot}$. These compliance terms depend on what laminae are considered to be bridging material above and below the delamination of interest. It is possible that they are identical, for instance an internal metal layer with differing delamination heights on either side may still be considered bridging material in the height between the two delaminations, since it still must be compatible with one of its adjacent fiber layers. It is also possible that these terms can be different.

The other key difference between the above- and below-delamination strain energies is the particular bridging forces which are included. Note that in

Equations (5.11) and (5.12) the summation is performed for all bridging forces above the delamination of interest ($>$), while in Equations (5.15) and (5.16) the bridging forces at the delamination of interest (and those of equal height) are also included in the summation (\geq).²

The final component of the strain energy release rate is that portion due to the work done via the load in the laminate acting through the additional deformation due to delamination extension, F^d , again with the superscript d to denote that this work is considered while having already been differentiated by b .

Stated most generally, this work is the product of the load, P , and the additional displacement due to delamination extension, $\Delta\epsilon \times b$. Differentiating in terms of b means that F^d is the product of the force and $\Delta\epsilon$. Because both the load going through the laminate and the strain in the laminate vary through the thickness, the work must be found by integrating the stress, $\sigma(z)$, and the strain difference:

$$F^d = \int_k \sigma(z) \Delta\epsilon(z) dz \quad (5.17)$$

Rewriting the stress in terms of the strain, expanding the strain difference, and recognizing that the integral can be broken into the sum of the integrals for each lamina gives:

$$F^d = \sum_{k:k \in \mathbf{B}_{bot}} \int_{\bar{z}_k - t_k/2}^{\bar{z}_k + t_k/2} E_{x,k} \epsilon_{k bot}(z) (\epsilon_{k bot}(z) - \epsilon_{k top}(z)) dz \quad (5.18)$$

Recognizing that

$$\epsilon_{k top}(z) = \psi_1 + z\psi_2 \quad (5.19)$$

and

$$\epsilon_{k bot}(z) = \psi_3 + z\psi_4, \quad (5.20)$$

²If the equal-height delaminations are expected to grow together at the same rate, it may make sense to include the bridging stresses from both together in $U_{bot i}^d$, then dividing the resulting strain energy release rate, G , by the number of equal delaminations. If they may grow at different rates it is more appropriate to consider them separately in terms of which bridging stresses are included and in calculating the compliance terms, assuming that one or the other extending some small increment means that there is an intermediate laminate cross-section in between the two delaminations, for which the bottom strain energy (and hence compliances) is calculated.

F^d can be written as:

$$F^d = \sum_{k:k \in \mathbf{B}_{bot}} E_{x,k} \int_{\bar{z}_k - t_k/2}^{\bar{z}_k + t_k/2} (\psi_3 + z\psi_4)(\psi_3 + z\psi_4 - \psi_1 - z\psi_2) dz \quad (5.21)$$

Solving the definite integral gives:

$$F^d = \sum_{k:k \in \mathbf{B}_{bot}} E_{x,k} t_k \left[\psi_3^2 - \psi_3\psi_1 + \frac{1}{12}(\psi_4^2 - \psi_4\psi_2)t_k^2 + \bar{z}_k (2\psi_3\psi_4 - \psi_4\psi_1 - \psi_3\psi_2) + \bar{z}_k^2 (\psi_4^2 - \psi_4\psi_2) \right] \quad (5.22)$$

Equations (5.10), (5.14), and (5.22) are combined to give the strain energy release rate of delamination i :

$$G_i = F_i^d - U_{bot\ i}^d + U_{top\ i}^d \quad (5.23)$$

Determining the bending moment with NLM

Generally, the Neutral Line Model relies on the beam-theory equation of a moment:

$$M_x = M_a + Pw - Tx = E^* I \left(\frac{d^2 w}{dx^2} \right) \quad (5.24)$$

where M_a is the applied moment, T is the applied lateral force, P is the longitudinal force, w is the out-of-plane displacement, E^* is the Young's modulus corrected for plane bending, $E^* = E/(1 - \nu^2)$, and I is the bending moment of inertia.

For Laminates, $E_{lam}^* I$ is computed by

$$(E_{lam}^* I)_i = \sum_{k:k \in \mathbf{B}_i} \frac{E_{x,k}}{1 - \nu_{xy,k}^2} \left[t_k (\bar{z}_k - \tilde{z}_i)^2 + \frac{1}{12} t_k^3 \right] \quad (5.25)$$

where \tilde{z}_i is the z -coordinate of the neutral axis of the bridging material in segment i . This is found with CLT by noting that the neutral axis is the vertical location in the laminate where the strain in the x direction is zero when only a moment, M_x is applied.

$$\begin{aligned}
\epsilon &= \epsilon_0 + \kappa z \\
0 &= B_{11\ i}^* M_x + D_{11\ i}^* M_x \tilde{z}_i \\
\tilde{z}_i &= \frac{B_{11\ i}^*}{D_{11\ i}^*}
\end{aligned} \tag{5.26}$$

When there is no misalignment in loading, an assumption appropriate for the FMLs considered in this chapter since the undamaged laminate in the grip area will be the same at both ends, M_a and T are related, for equilibrium of the model, by:

$$2M_a - TL = 0, \tag{5.27}$$

where L is the total length of the specimen.

Equation (5.24) is solved for w for each vertical segment of the laminate:

$$w_i(x) = A_i \sinh \alpha_i x + B_i \cosh \alpha_i x - \frac{M_a}{P_i} + \frac{T}{P_i} x_1 \tag{5.28}$$

where $\alpha_i = P_i / (E_{lam}^* I)_i$. Note that T/P_i is multiplied by x_1 , rather than x_i , since the moment due to T is a function of the distance from the end of the specimen. For the purposes of this model, in contrast to prior descriptions of the NLM, P is considered to be changeable in each section. It is now defined as the total of the remote load carried in the intact layers and the bridging stress borne by those layers:

$$P_i = \sum_{k:k \in \mathbf{B}_i} \sigma_k \infty t_k + \sum_{n:b_n > b_i} F_{br_n} \tag{5.29}$$

In full laminates with cracked layers, P_i is not necessarily equal to the applied load since some load from the cracked layers goes through the first load path, around the crack tip, rather than through the intact bridging material.

The constants A_i and B_i in Equation (5.28) are determined by applying boundary conditions for the out of plane displacement of the neutral line, and its slope, for each segment of the laminate. At $x_1 = 0$, the load is applied, so $w_1(0) = 0$. At $x_n = l_n$, there is a plane of symmetry, so $\frac{dw_n}{dx}(l_n) = 0$. At each delamination location, the boundaries between segments, continuity is preserved by:

$$w_i(l_i) + e_i = w_{i+1}(0) \tag{5.30}$$

$$\left(\frac{dw}{dx} \right)_i = \left(\frac{dw}{dx} \right)_{i+1} \tag{5.31}$$

Material	E_1 [MPa]	E_2 [MPa]	ν_{12} [-]	G_{12} [MPa]	α_1 [$\epsilon/^\circ C$]	α_2 [$\epsilon/^\circ C$]
Aluminum	72400	72400	.33	26900	22.0×10^{-6}	22.0×10^{-6}
Adhesive	5500	5500	.33	5550	26.2×10^{-6}	26.2×10^{-6}
Prepreg	48900	5500	.33	5550	6.1×10^{-6}	26.2×10^{-6}

Table 5.1 – *Material properties used in calculations and FEA*

the problem is solved here in two dimensions. A given external load is applied in the form of a line load (or line moment) as in classical laminate theory. The scenarios are analogous to ply-interrupt delamination testing specimens, such as those described in [6].

The bridging loads at each delamination are assumed to be equal to the force born by the adjacent severed layer, for external severed layers. For internal severed layers, the bridging forces are the load born by the layer divided by two when the delaminations are of equal height. It is assumed that the entire bridging load is transferred at the shorter delamination, since compatibility must be maintained where the severed layer is still bonded on one side.

5.3.2 Properties

The material properties presented in Table 5.1 were used in all calculations and in the finite element analysis.

5.3.3 Finite Element Analysis

Parametric modeling of the various scenarios considered in this analysis was done using 2D simulations in ABAQUS. Plain strain continuum CPE4I elements, with incompatible modes included to improve bending and shear behavior, were used to construct each lamina. Typical elements were in the range of 0.03 to 0.075 mm on a side. Several of the models were run with smaller elements as a check that the models were sufficiently converged. The layers were bonded via contact interactions, applied everywhere on the interface except where delaminations were present. Models were quarter-symmetric, where applicable, but most were half-symmetric, including the entire top half of a specimen, when delaminations were not of equal length, or other asymmetries were present. Loads and moments were applied through a reference node, which was kinematically coupled to the top surface of the model. A typical meshed model is

shown in Figure 5.5.

The analysis occurred in two steps. The first was a thermal step, in which the temperature reduction of cure temperature to room temperature, $\Delta T = -100^\circ\text{C}$, was applied. In the second step, the applied load or moment was ramped. The SERR of the delamination tips in the model was calculated with ABAQUS's built-in VCCT functionality.

5.3.4 Results

Figures 5.6 and 5.7 shows the results of two analyses of 2/1 Glare laminates with additional adhesive in the bondline. As the adhesive thickness, t_{ad} , is increased, the energy release rate increases. Since the adhesive increases the laminate thickness without adding much stiffness, applying the same stress to the laminate means that the stress of the aluminum layers, and the load transfer over the interface, increases with t_{ad} . This is reflected in both the FEA results and the model calculations. However, for the thin laminate, the model calculates a somewhat higher rate of increase in G_{II} with respect to adhesive thickness than the FEA results. That this happened for the thin metal laminate in Figure 5.6, and not for the thick metal scenario of Figure 5.7, suggests that out-of-plane bending of the thin metal layers accounts for this discrepancy. Figure 5.8 compares the mode mixity derived from the nonlinear finite element models of the two laminates. Mode I SERR is a higher proportion of the total SERR for the laminate with thin metal layers, and this proportion increases rapidly with increasing t_{ad} for the thin metal FML, but not the thick metal FML. The low stiffness of the adhesive allows the thin metal layers more freedom to displace out-of-plane as the adhesive becomes thicker. This in turn alleviates some of the Mode II SERR, accounting for the discrepancy of Figure 5.6.

In Figure 5.9, the load is increased on an FML with a fixed adhesive thickness. The model is in close agreement with the results of the linear FEA and has somewhat higher SERR than the geometrically nonlinear FEA. Figure 5.10 shows the effects of changing the temperature drop between cure and test (ΔT). Greater temperature drops increase the thermal residual stresses of the laminate, leading to greater SERR's. Here, the model agrees with the linear FEA results, and is still close to the nonlinear results.

A series of analyses were made of a symmetrically delaminated laminate with changing delamination lengths, and the results are shown in Figure 5.11. Apart from a slight difference when the delaminations are extremely short (0.5 mm or less), there is no effect of the delamination length on the SERR.

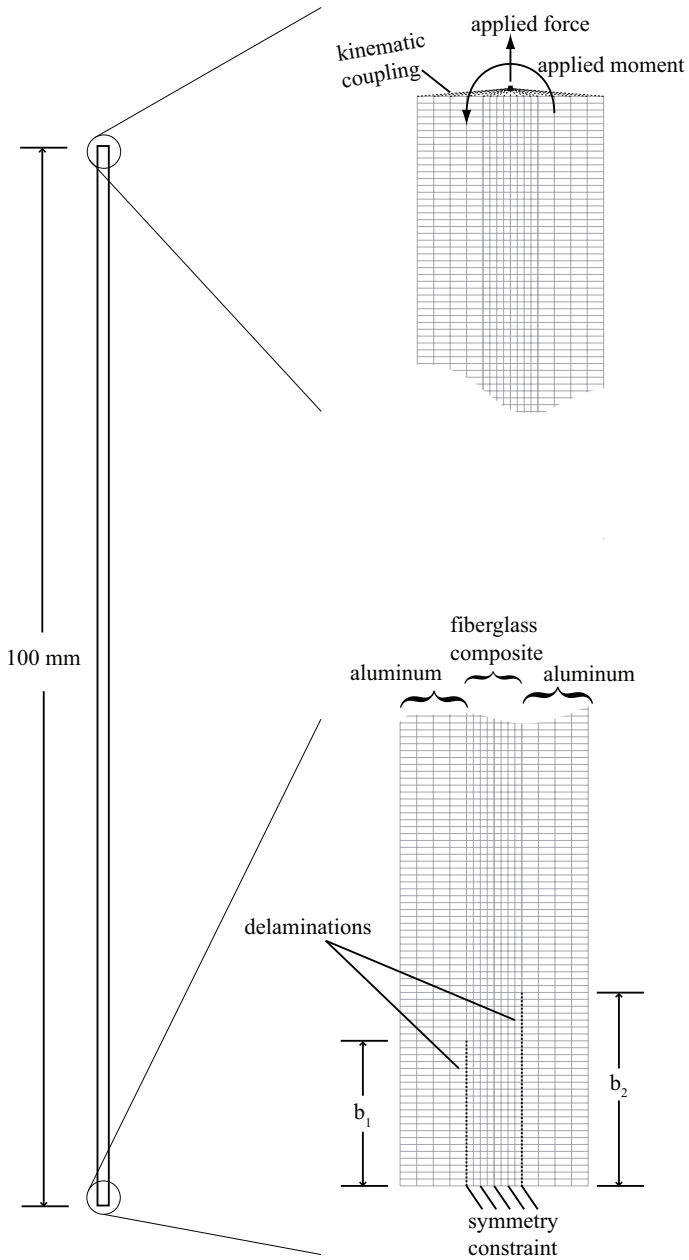


Figure 5.5 – Example FEA mesh with boundary conditions

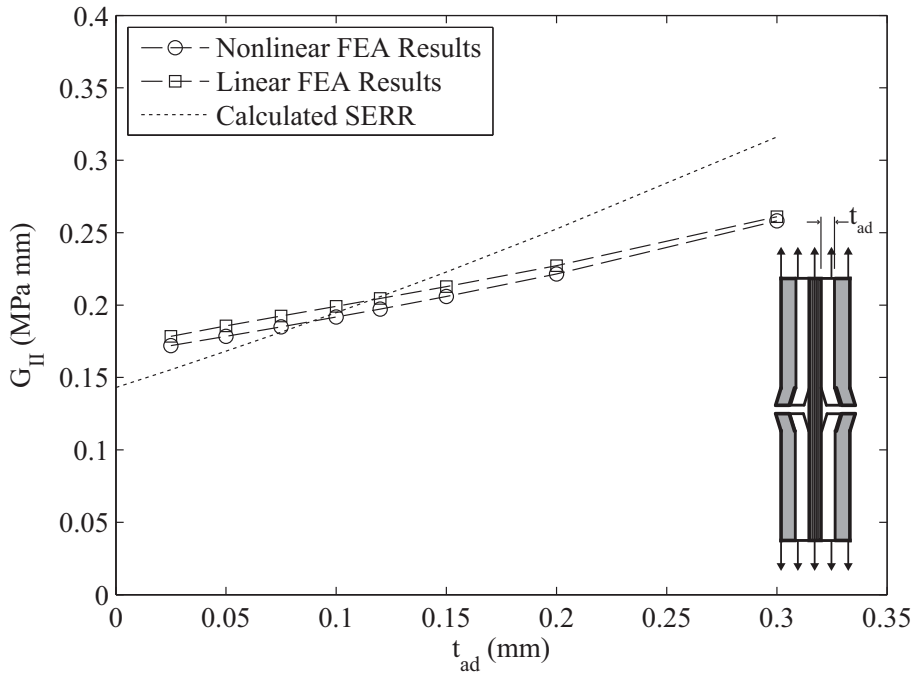


Figure 5.6 – Effect of adhesive layer thickness (t_{ad}) on SERR in 2/1 Glare with 0.3 mm metal sheets, laminate: [0.3 mm Al / t_{ad} adhesive / 0.25 mm prepreg / t_{ad} adhesive / 0.3 mm Al], $\sigma_{lam} = 100$ MPa, $\Delta T = -100^\circ C$

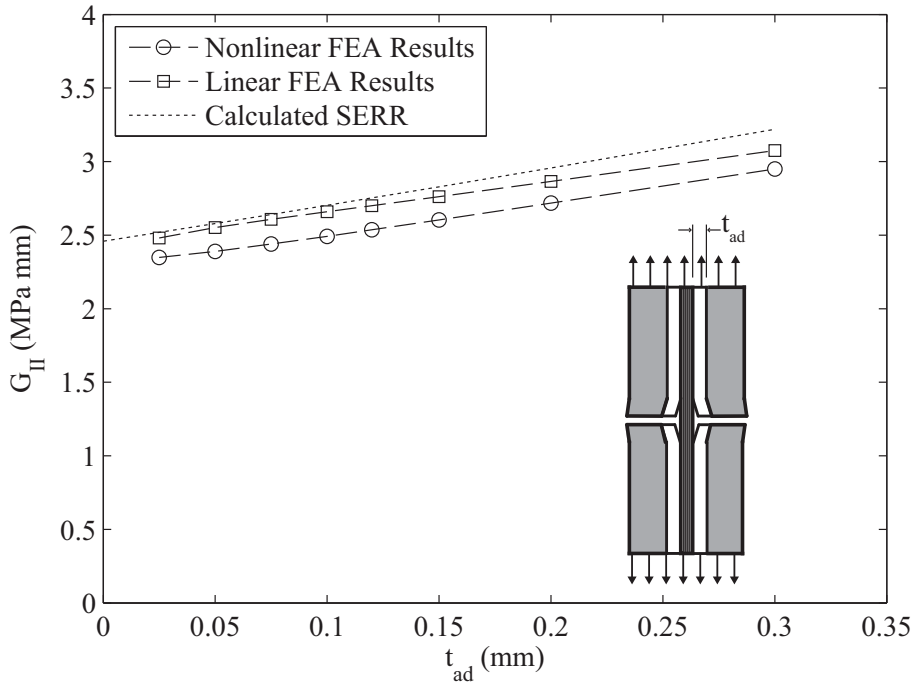


Figure 5.7 – Effect of adhesive layer thickness (t_{ad}) on SERR in 2/1 Glare with 1.6 mm metal sheets, laminate: [1.6 mm Al / t_{ad} adhesive / 0.25 mm prepreg / t_{ad} adhesive / 1.6 mm Al], $\sigma_{lam} = 100$ MPa, $\Delta T = -100^\circ C$

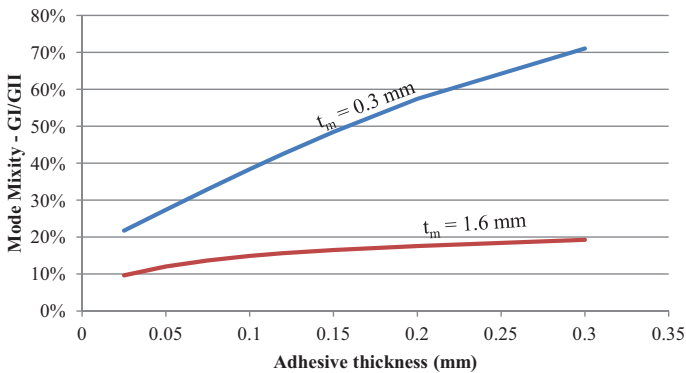


Figure 5.8 – Comparison of the mode mixity, and its change with increasing adhesive thickness, for finite element models with two different metal layer thicknesses

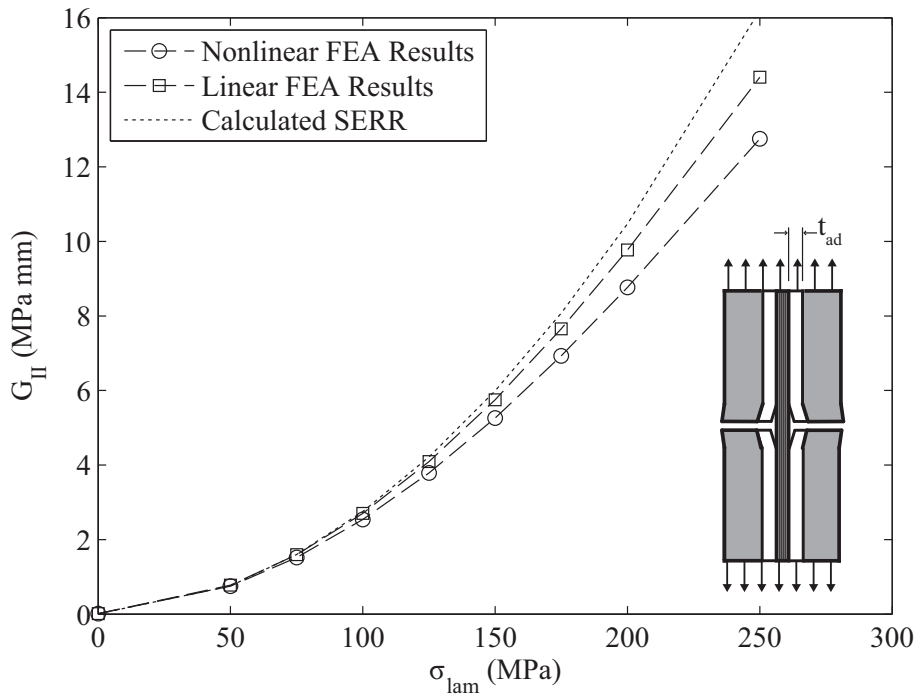


Figure 5.9 – Effect of changing applied load on SERR, laminate: [1.6 mm Al / 0.12 mm t_{ad} / 0.25 mm prepreg / 0.12 mm t_{ad} / 1.6 mm Al], $\Delta T = -100^\circ C$

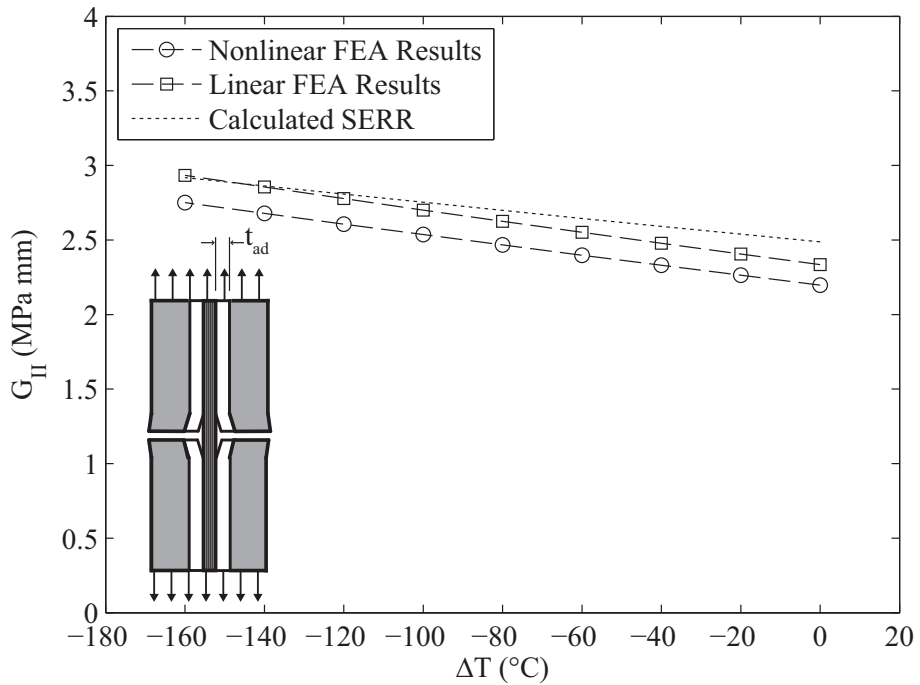


Figure 5.10 – Effect of changing applied temperature change on SERR, laminate: $[1.6 \text{ mm Al} / 0.12 \text{ mm } t_{ad} / 0.25 \text{ mm prepreg} / 0.12 \text{ mm } t_{ad} / 1.6 \text{ mm Al}]$, $\sigma_{lam} = 100 \text{ MPa}$

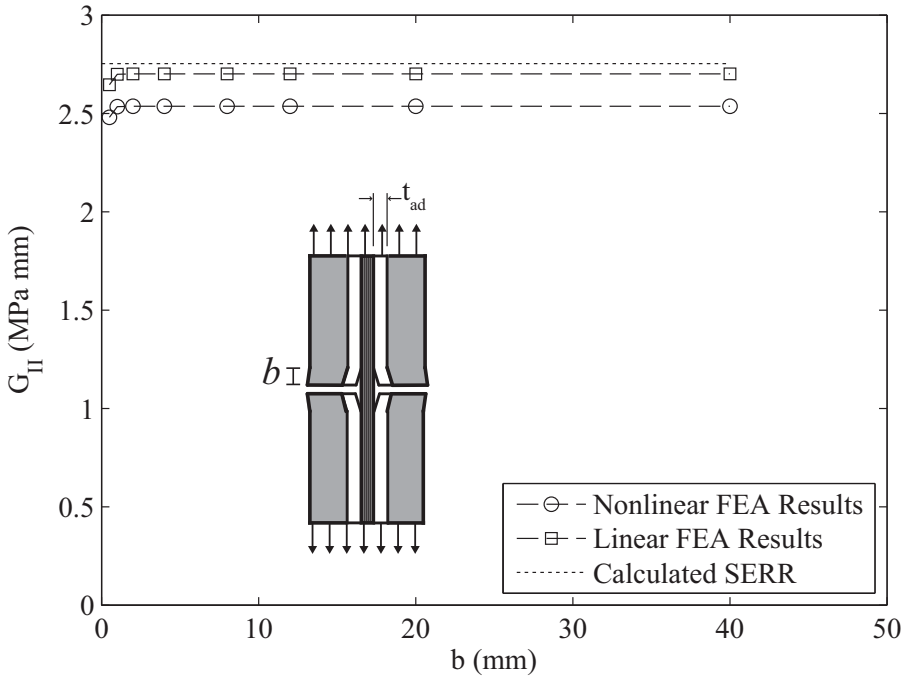


Figure 5.11 – When both delaminations are of equal length, changing the length does not affect the SERR. laminate: [1.6 mm Al / 0.12 mm t_{ad} / 0.25 mm prepreg / 0.12 mm t_{ad} / 1.6 mm Al], $\sigma_{lam} = 100$ MPa, $\Delta T = -100^\circ C$

This is consistent with previously derived calculation methods for SERR of symmetrically delaminated laminates, such as those in [5] and [6], which do not include the delamination length as a variable.

Figure 5.12 shows the results of FEA and model analyses of a 2/1 Glare laminate with different delamination lengths on either side. As the applied stress increases, the SERR increases for both delaminations, but not equally. In this case, there are dramatic differences between the linear and nonlinear FEA results. The nonlinear FEA results and the calculation model both show b_1 , the shorter delamination, with higher energy release rates than b_2 , while the linear FEA shows the opposite. The nonlinear FEA and the model are in good agreement with respect to values of G_{II} , with the values for the longer delamination, b_2 , closely matching, and with the model underestimating the G_{II} of the shorter delamination compared to the nonlinear FEA results.

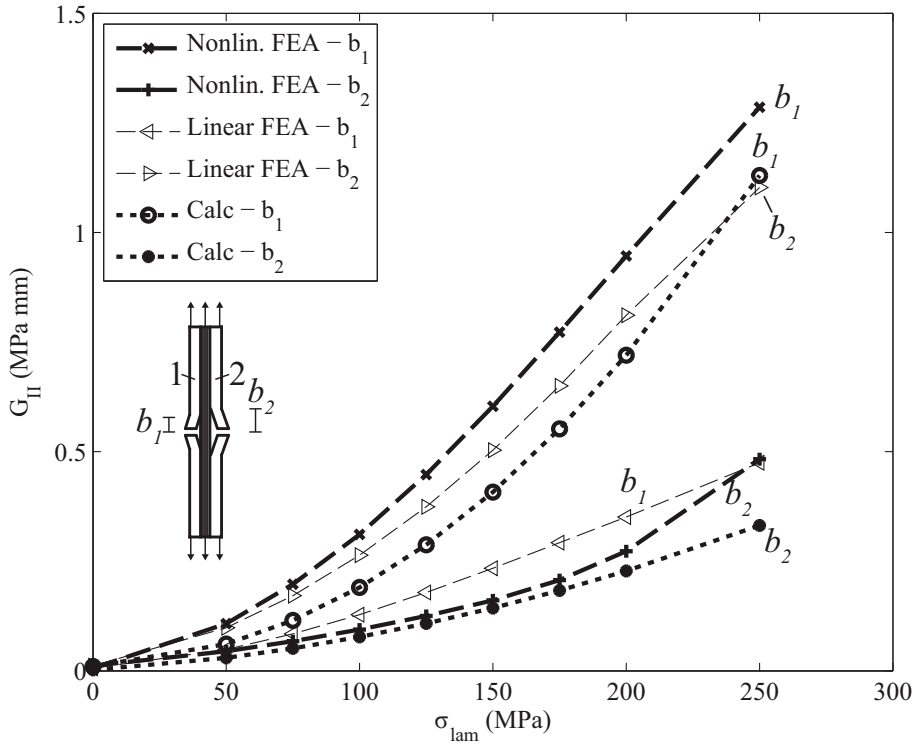


Figure 5.12 – Increasing load on an asymmetrically delaminated specimen, laminate: $[0.3 \text{ mm Al} / 0.25 \text{ mm prepreg} / 0.3 \text{ mm Al}]$, $\Delta T = -100^\circ \text{C}$, $b_1 = 8 \text{ mm}$, $b_2 = 16 \text{ mm}$

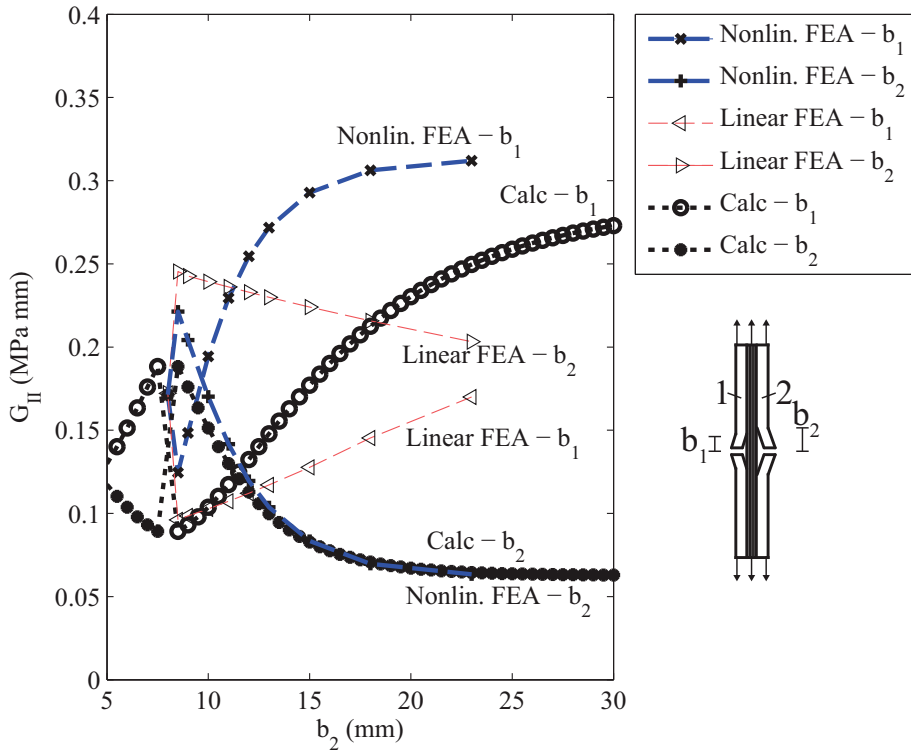


Figure 5.13 – Laminate with asymmetric delaminations, changing the length of b_2 while holding b_1 constant, laminate: $[0.3 \text{ mm Al} / 0.25 \text{ mm prepreg} / 0.3 \text{ mm Al}]$, $\sigma_{lam} = 100 \text{ MPa}$, $\Delta T = -100^\circ \text{ C}$, $b_1 = 8 \text{ mm}$, $b_2 = x \text{ axis}$

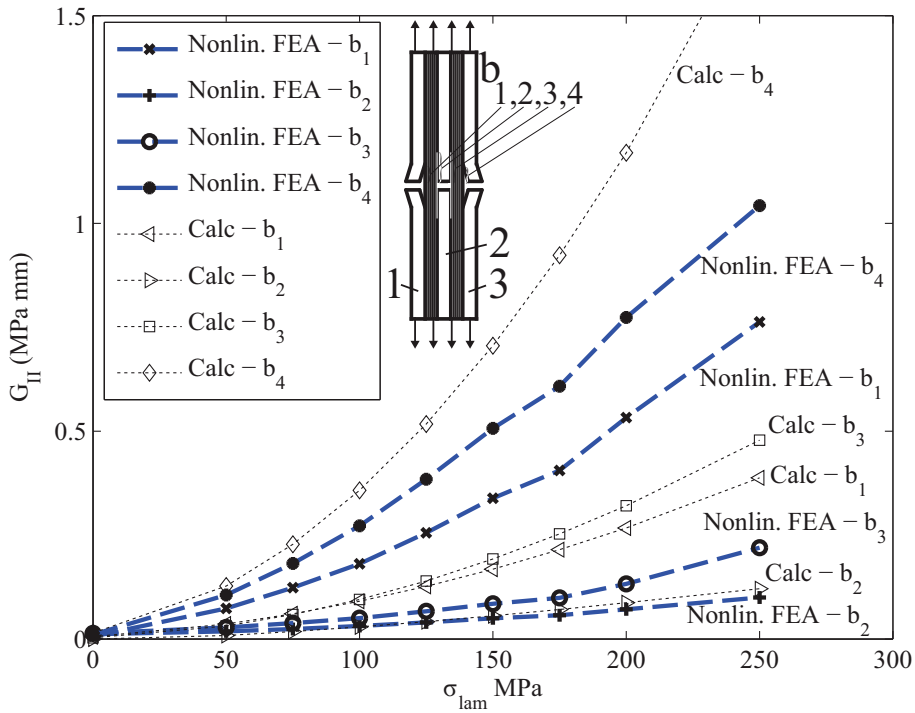


Figure 5.14 – 3/2 laminate with different delamination lengths and increasing load. Nonlinear FEA and modified calculation method results, laminate: [0.3 mm Al / 0.25 mm prepreg / 0.3 mm Al / 0.25 mm prepreg / 0.3 mm Al], $\sigma_{lam} = 100$ MPa, $\Delta T = -100^\circ C$, $b_1 = 10$ mm, $b_2 = 16$ mm, $b_3 = 14$ mm, $b_4 = 6$ mm

Figure 5.13 shows the effect of changing one of the delamination lengths while holding the other constant. One interesting feature of both the nonlinear FEA results and the calculation model is the region of the graph where b_2 is close to 8 mm. Here, where the delamination lengths are similar, the longer delamination actually has a higher value of G_{II} . As the distance between the delamination lengths grows, this reverses, and the shorter delamination has a greater G_{II} . The model matches the FEA values of G_{II} of the longer delamination, but tends to give lower G_{II} values for the shorter delamination, consistent with the error seen in Figure 5.12.

As the number of layers in the laminate increases, the model still captures the trends seen in the nonlinear FEA, but the error in the SERR values in-

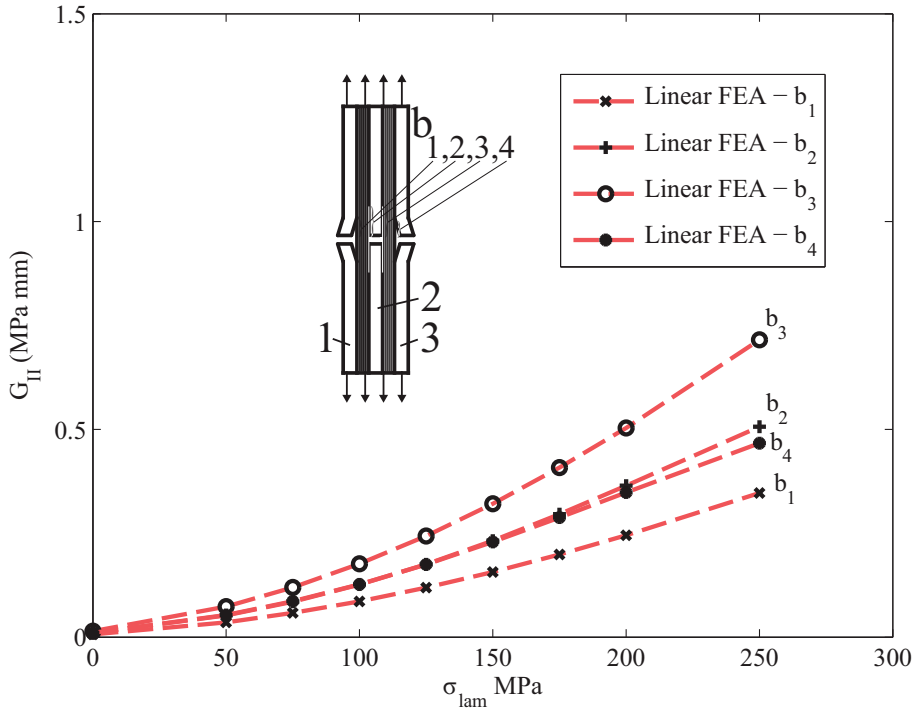


Figure 5.15 – 3/2 laminate with different delamination lengths and increasing load. Linear FEA results, laminate: [0.3 mm Al / 0.25 mm prepreg / 0.3 mm Al / 0.25 mm prepreg / 0.3 mm Al], $\sigma_{lam} = 100$ MPa, $\Delta T = -100^\circ C$, $b_1 = 10$ mm, $b_2 = 16$ mm, $b_3 = 14$ mm, $b_4 = 6$ mm

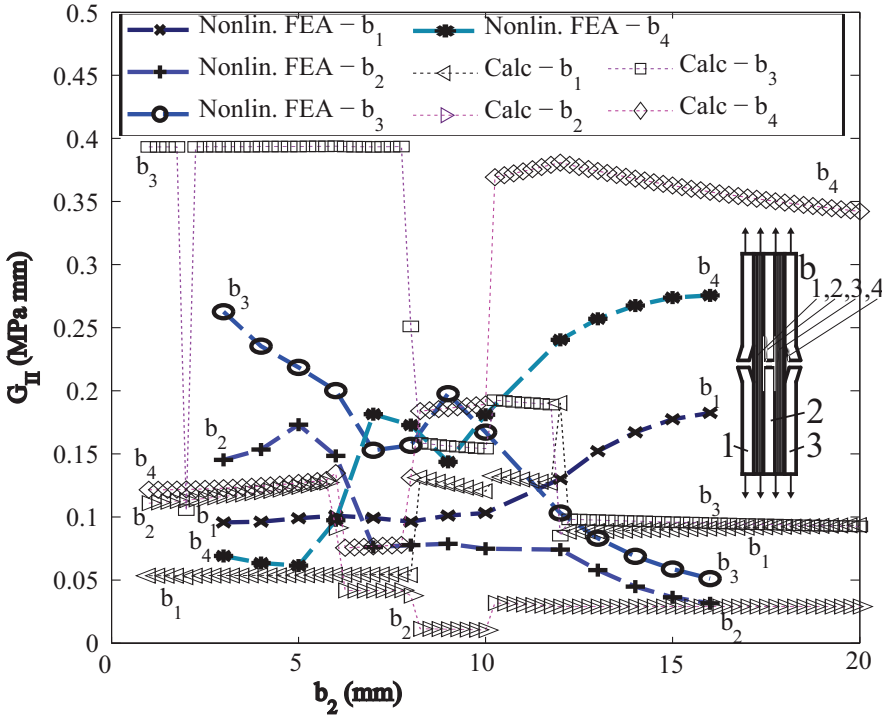


Figure 5.16 – 3/2 laminate with different and changing delamination lengths and increasing load. Nonlinear FEA and modified calculation method results, laminate: [0.3 mm Al / 0.25 mm prepreg / 0.3 mm Al / 0.25 mm prepreg / 0.3 mm Al], $\sigma_{lam} = 100$ MPa, $\Delta T = -100^\circ C$, $b_1 = 10$ mm, $b_2 = x$ axis, $b_3 = b_2 - 2$ mm, $b_4 = 6$ mm

creases. These results are shown in Figure 5.14. The rank order of the FEA results is nearly captured by the model, and the values are similar. The exception is the order of b_1 and b_3 , which the FEA results have close together. In contrast, the linear FEA results in Figure 5.15 are substantially different from the nonlinear FEA results in both order and value.

Figures 5.16 and 5.17 show the results of a scenario in which a 3/2 laminate has 4 different delamination lengths, and the center two delaminations, b_2 and b_3 , are varied. The x axis of the plot gives the length of b_2 , and b_3 was kept 2 mm shorter than the length of b_2 in each analysis. The nonlinear FEA and calculation method results shown in Figure 5.16 have much in common. At the

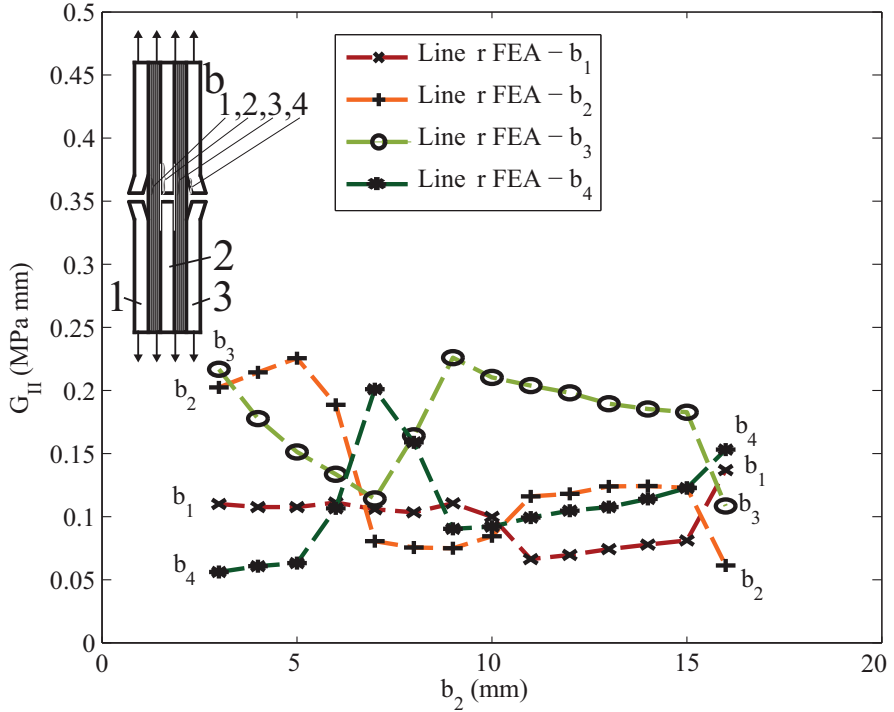


Figure 5.17 – 3/2 laminate with different and changing delamination lengths and increasing load. Linear FEA results, laminate: $[0.3 \text{ mm Al} / 0.25 \text{ mm prepreg} / 0.3 \text{ mm Al} / 0.25 \text{ mm prepreg} / 0.3 \text{ mm Al}]$, $\sigma_{lam} = 100 \text{ MPa}$, $\Delta T = -100^\circ \text{C}$, $b_1 = 10 \text{ mm}$, $b_2 = x \text{ axis}$, $b_3 = b_2 - 2 \text{ mm}$, $b_4 = 6 \text{ mm}$

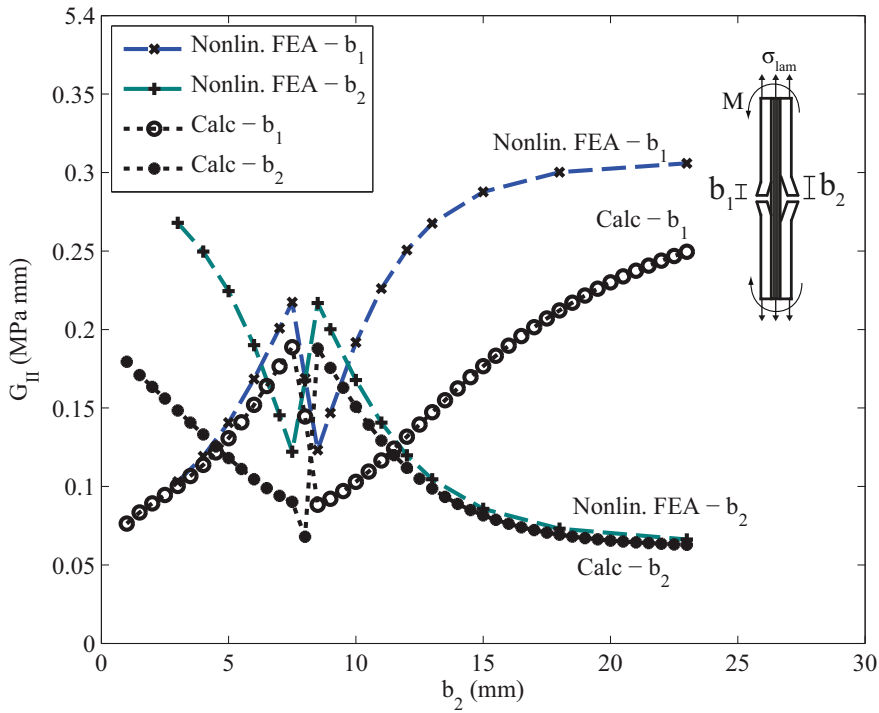


Figure 5.18 – SERR of a 2/1 laminate with combined tension and bending loading, laminate: [0.3 mm Al / 0.25 mm prepreg / 0.3 mm Al], $\sigma_{lam} = 100$ MPa, $M = 40$ N mm/mm $\Delta T = -100^\circ$ C, $b_1 = 8$ mm, $b_2 = x$ axis

right of the chart, as b_2 and b_3 become longer than the other two delaminations, the calculation results tend toward better agreement with the FEA results as the two delamination lengths increase. When the two internal delaminations are small, the model correctly determines that delamination 3 has the highest SERR but overestimates the value of G_{II} . There is some error in the order and value of the other delaminations. When all four delaminations are close to each other, in the center of the figure, the calculation picks up some of the changes in order, but not all, and matches some of the actual values, but not all. The linear FEA results depicted in Figure 5.17 are significantly different from the nonlinear FEA results in 5.16.

The addition of a bending moment to the applied loading has little effect on the strain energy release rates, as shown in Figure 5.18. Comparing these

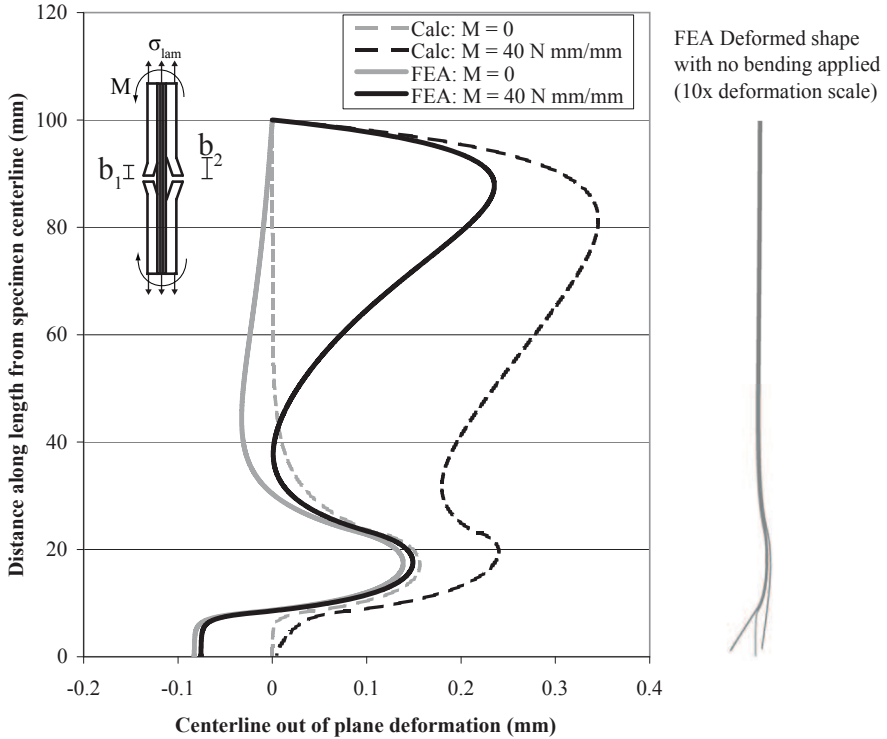


Figure 5.19 – Deformation of a 2/1 laminate with combined tension and bending loading, laminate: [0.3 mm Al / 0.25 mm prepreg / 0.3 mm Al], $\sigma_{lam} = 100$ MPa, $\Delta T = -100^\circ C$, $b_1 = 8$ mm, $b_2 = 23$ mm

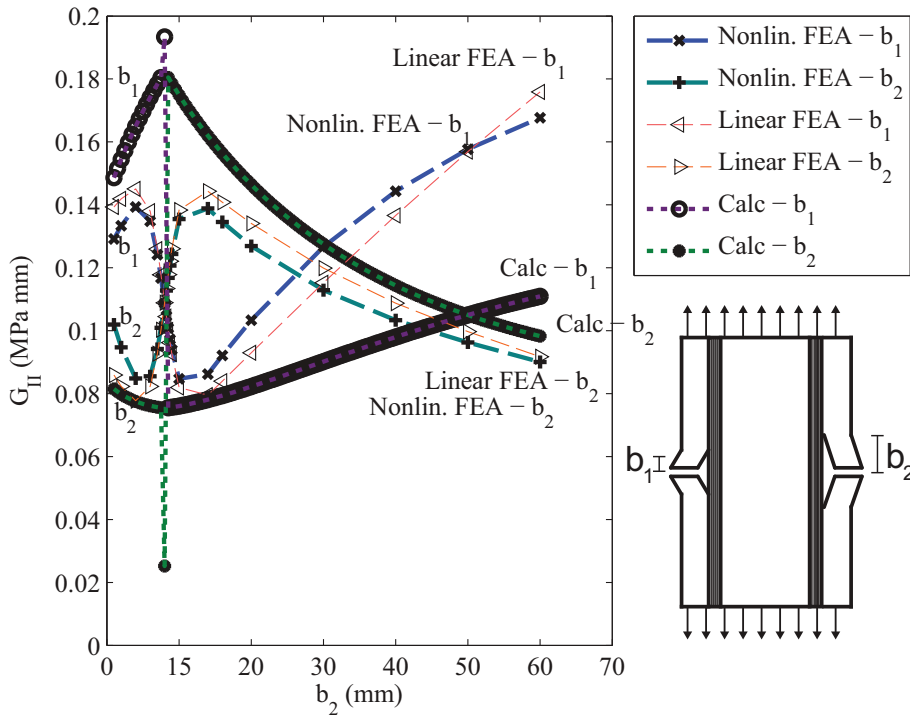


Figure 5.20 – Very thick 3/2 laminate with only outer layers delaminated with changing b_4 and fixed b_1 , laminate: $[1 \text{ mm Al} / 0.25 \text{ mm prepreg} / 3 \text{ mm Al} / 0.25 \text{ mm prepreg} / 1 \text{ mm Al}]$, $\sigma_{lam} = 100 \text{ MPa}$, $\Delta T = -100^\circ \text{C}$, $b_1 = 8 \text{ mm}$, $b_2 = x \text{ axis}$

results with those of Figure 5.13 shows that no difference is evident with both the nonlinear FEA results and the calculation model results. This is explained by the deformation shapes shown in Figure 5.19. When a moment is applied, both the FEA shape and the predicted secondary bending shape of the model show that the greatest effects of the moment on the laminate occur near the point of load application. The bending shape in the area of the delaminations changes little between the shapes with no applied moment and with a substantial moment applied.

In Figure 5.20, the SERR in a very thick laminate is considered. The laminate in question is a 3/2 laminate with thick metal layers (1, 3, and 1 mm). The two outer metal sheets have delaminations, while the bonds between the fiber layers and the inner, 3 mm thick, metal sheet are left intact. In these

results, the same cross-over of SERRs is observed as in Figure 5.13 — when the delaminations are close, the longer delamination has a higher G_{II} , and this relationship reverses as they grow apart. The thick laminate shown has the values cross over when b_1 is 8 mm and b_2 is 30 mm, while the thinner laminate of Figure 5.13 has the SERRs cross when b_2 is just 10 mm. The model captures this increase in the length of delamination growth before crossover, going from 12 mm to 49 mm in the thick and thin laminates, respectively. The thicker the laminate, the longer the length of the laminate over which the secondary bending around a given delamination is felt thanks to the increased bending stiffness.

5.4 Discussion

The analytical model described in this chapter uses the conventional approach to calculating SERR in a cracked and delaminated FML, determining the strain energy in cross sections above and below the delamination and calculating the work done in delamination extension. But rather than deriving a single equation for a specific case, the approach is laid out as generally as possible. The development of this approach is driven by the latest generations of laminates and the desire to fully analyze them and explore the potential of property tailoring. Additionally, the need exists for analysis of both new and old laminates in different loading regimes, such as compression and bending [15].

Laminates are divided into segments along the length, the boundaries of which are the delamination tips. The strains in each segment are found by accounting for the effects of remote loading on each layer and the addition of the bridging load from the delaminated layers. Up to this point, it is consistent with the approach used to calculate bridging stresses in a generalized cracked FML in [2]; however, the present model must go a step further, since, as the FEA results make clear, the secondary bending due to the shifting neutral axis when asymmetric delaminations are present plays a significant role in the strain energy release rates. The present model uses the neutral line model to account for this secondary bending. The bridging stress model should be reconsidered in light of the efficacy of the NLM in this chapter. It is possible that inaccuracies in its bridging stress predictions could be reduced by incorporating the out of plane effects in the same manner as in this model. Since a complete generalized model of fatigue crack growth in FMLs will require the use of both this SERR model and the bridging model of [2], it is also important that the two models be as consistent as possible.

Comparison of calculations made with this model to FEA results reveal that the model is able to characterize the effects of many changes to the laminate, such as adhesive layer thickness, metal layer thickness, temperature change, increasing load, and changing delamination length. The trends associated with changing asymmetric delamination lengths are picked up by the model, but there remain some errors in the exact values which warrant further investigation of improvements to the model. In particular, the way the neutral line model is applied to asymmetrically delaminated specimens with more than two metal layers could be improved by treating portions of the laminate, separated by delamination, as independent beams.

The FEA results demonstrate an enormous difference between the nonlinear and linear geometry analyses for cases in which secondary bending is important, such as in Figure 5.13. This is to be expected, since secondary bending is nonlinear with respect to increasing load. It shows that a model of the bending behavior of the laminate cannot be accurate with a conventional linear approach, and some inclusion of secondary bending in an analytical model is necessary.

A complication to assessing the appropriateness of a particular approach to analyzing SERR based on analysis of ply-interrupt type specimens is the lack of constraint from adjacent material. In a cracked FML with delaminations, a given bar element in the wake of a crack matches a ply-interrupt specimen geometry, but the adjacent bar elements may limit the out-of-plane deformation of the element. Even the cracked metal layers are attached to the rest of the metal layer on either side, and continuity must be preserved. One bar element is adjacent to the crack tip, where the delamination length goes to zero and the bending is limited by the stiffness of the full laminate. For all other bar elements, the adjacent bar elements on both sides have similar delamination sizes. For sufficiently thin bar elements, the constraint due to adjacent bar elements will be negligible, and treating them as independent ply-interrupt specimens for the purposes of calculating SERR may be an acceptable approximation.

Ultimately, the appropriateness of the model proposed in this chapter depends on the application for which it is used. One is unlikely to encounter a real structure where multiple delaminations emanate from a number of interrupted layers in isolation of some other damage. To align so many ply interruptions in a structure would be poor design practice. Two scenarios where this model would be applicable, and which are more likely to be encountered in the design and analysis of a real structure, are the delamination of a bonded stiffener, reinforcing strap, or patch and the scenario discussed in the introduction of this chapter, that of multiple delaminations growing transverse to cracks in a

complex (non-uniform) FML. In the first case, the verification results of the model show that it models such simple scenarios well, and adequately takes into account the effects of secondary bending, which can be important for a disbanded strap or patch.

In the case of the crack and delamination growth problem of complex FMLs, this model provides an estimate of individual SERRs of each delamination. There is presently no analytical alternative available. Although there is some disagreement between the model results and the nonlinear FEA results for the more complex cases studied, the simplicity of this approach makes it attractive for use in a full FML crack growth model. Such a model operates iteratively, meaning that the computational cost of any individual step may be multiplied several thousand fold. Some error is therefore acceptable, if the SERR model can give reasonably close estimates with straightforward, simple calculations. Further small errors in SERR are mitigated by the self-balancing nature of crack and delamination growth in FMLs [16]. Comparison of a full crack and delamination growth prediction model incorporating this SERR calculation method with experimental crack and delamination growth results will serve to test whether or not this model is sufficient to characterize the behavior of the laminates.

Future effort on improving this model could focus on the assumptions dealing with the use of the neutral line model in analyzing secondary bending. Particularly, using the mid-segment bending moment as a representative of the strain energy gained (lost) in extension (reduction) in the length of that segment could obscure the effect of the interaction between nearby delaminations, since the secondary bending changes more drastically with an incremental change in delamination length when the delaminations are close versus when there is greater separation between them. An approach that integrates the energy along the full length of each segment may prove more accurate. Also, the additional moment due to the bridging load being introduced into the bridging layers along the interface with the delamination could be included.

The finite element analysis used to verify the model in asymmetric conditions could also be improved. The discrepancy between the mode mixity of thick and thin metal sheet laminates, demonstrated in Figure 5.8, suggests that less error between the analytical and finite element models may have occurred if thicker metal layers were used in the asymmetric analyses. Having thicker metal layers would mean that mode II dominates, and the model is only set up to calculate mode II. This suggests that the model, as currently defined is more appropriate for laminates in which the outer sheets are thicker, and that the model could be modified to incorporate mode mixity effects to better

calculate the mode II SERR for delamination of thinner metal sheets bonded with additional adhesive.

5.5 Conclusion

A generalized method of calculating the strain energy release rate in FMLs was derived and demonstrated in this chapter. It enables the calculation of SERR for an FML of arbitrary layout, with arbitrary damage size, and subject to tension or combined tension-bending. The accuracy of this model was verified through comparison to FEA-modeled laminates. The proposed method was able to capture the effects of changing many of these arbitrary parameters, though as complexity increased the accuracy of the SERR values was reduced. The model was not appropriate for applied moment only scenarios. The result is a method suitable for use in combination with generalized bridging analysis for simulating the fatigue crack and delamination growth of fiber metal laminates.

Bibliography

- [1] Wilson, G. S., Delgrange, G., Alderliesten, R. C., and Benedictus, R. (2011) Generalized approach to calculating strain energy release rate in fiber metal laminates. *Engineering Fracture Mechanics*, submitted for publication June 2011.
- [2] Wilson, G. S., Alderliesten, R. C., and Benedictus, R. (2013) A generalized solution to the crack bridging problem of fiber metal laminates. *Engineering Fracture Mechanics*, <http://dx.doi.org/10.1016/j.engfracmech.2013.03.008>.
- [3] Alderliesten, R. C. (2007) Analytical prediction model for fatigue crack propagation and delamination growth in glare. *International Journal of Fatigue*, **29**, 628–646.
- [4] Rodi, R., Wilson, G. S., Alderliesten, R. C., and Benedictus, R. (2009) The effect of bridging fibres on the entire strain field in fibre metal laminates. *17th ICCM International Conference on Composite Materials*, Edinburgh, UK.
- [5] Marissen, R. (1988) *Fatigue crack growth in ARALL. A hybrid aluminium-aramid composite material: Crack growth mechanisms and quantitative*

- predictions of the crack growth rates*. Ph.D. thesis, Delft University of Technology, Delft, The Netherlands.
- [6] Alderliesten, R. C., Schijve, J., and van der Zwaag, S. (2006) Application of the energy release rate approach for delamination growth in glare. *Engineering Fracture Mechanics*, **73**, 697–709.
- [7] Alderliesten, R. C. (2009) Damage tolerance of bonded aircraft structures. *International Journal of Fatigue*, **31**, 1024–1030.
- [8] Rans, C., Alderliesten, R., and Benedictus, R. (2011) Misinterpreting the results: How similitude can improve our understanding of fatigue delamination growth. *Composites Science and Technology*, **71**, 230–238.
- [9] Alderliesten, R. C. (2005) *Fatigue crack propagation and delamination growth in Glare*. Ph.D. thesis, Delft University of Technology, Delft, The Netherlands.
- [10] Wang, J. T. (2009) Calculation of stress intensity factors for interfacial cracks in fiber metal laminates. *Proceedings of the 50th AIAA/ASME/ASCE/AHS/ASC Structures, Structural Dynamics, and Materials Conference*, May.
- [11] Roebroeks, G. H. J. J., Hooijmeijer, P. A., Kroon, E. J., and Heinimann, M. B. (2007) The development of CentrAl. *First International Conference on Damage Tolerance of Aircraft Structures*, Delft, The Netherlands.
- [12] Heinimann, M., Kulak, M., Bucci, R., James, M., Wilson, G., Brockenbrough, J., Zonker, H., and Sklyut, H. (2007) Validation of advanced metallic hybrid concept with improved damage tolerance capabilities for next generation lower wing and fuselage applications. Lazzeri, L. and Salvetti, A. (eds.), *Proceedings of the 24th ICAF Symposium*, Naples, Italy, May.
- [13] Guo, Y.-J. and Wu, X.-R. (1999) Bridging stress distribution in center-cracked fiber reinforced metal laminates: modeling and experiment. *Engineering Fracture Mechanics*, **63**, 147 – 163.
- [14] Schijve, J., Campoli, G., and Monaco, A. (2009) Fatigue of structures and secondary bending in structural elements. *International Journal of Fatigue*, **31**, 1111–1123.
- [15] Randell, C. E. (2005) *Subsurface Fatigue Crack Growth in Glare Fibre Metal Laminates*. Ph.D. thesis, Delft University of Technology, Delft, The Netherlands.

- [16] Guo, Y. J. and Wu, X. R. (1999) A phenomenological model for predicting crack growth in fiber-reinforced metal laminates under constant-amplitude loading. *Composites Science and Technology*, **59**, 1825–1831.

This page intentionally left blank.

Chapter 6

Testing

A number of crack growth tests of FMLs with varied layup were carried out to produce data to be compared against the crack and delamination growth predictions of the generalized model. This chapter describes the methodology and results of these tests, as well as several tests that were carried out to generate input data for the model.

6.1 Methodology

6.1.1 Laminate manufacture

The FMLs produced for this study were manufactured using similar techniques to the standard Glare preparation and lamination procedure [1]. The aluminum sheets were prepared through chromic-acid anodizing followed by the application of BR127 primer.

The laminates were laid up by hand on a flat, thick aluminum tool, vacuum-bagged, and cured in an autoclave. The cure cycle consisted of roughly three hours at the cure temperature of 120° C. Laminates containing additional adhesive layers were cured at a pressure of 4 bar, whereas Glare is normally cured at 6 bar. The internal Glare portions of “CentrAl” laminates (such as laminates 0 and 1 in Table 6.2) were first cured at 6 bar then added as a single layer when laying up the thicker laminate.

After cure, specimens were cut from the panels, leaving at least two cm scrap around the edges, and machined to the geometry shown in Figure 6.1.

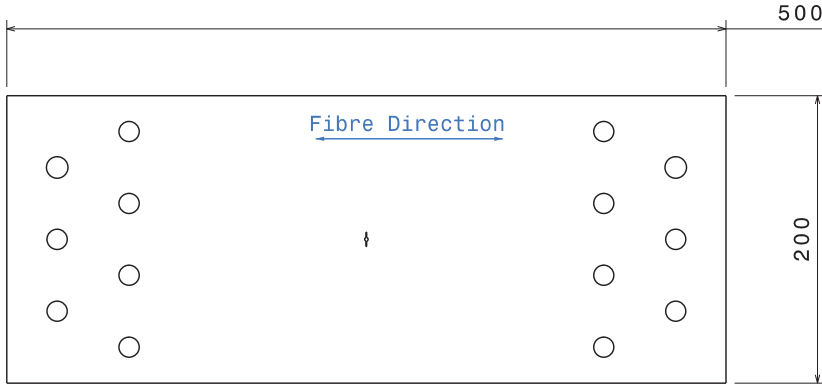


Figure 6.1 – *Typical crack growth specimen geometry. Lengths from 490 – 500 mm were used.*

A small (2–3 mm) hole was drilled in the center of each specimen, and two notches were cut by hand saw, one on each side of the hole.

No reinforcement was applied to the gripping region, since the purpose of the tests was only fatigue crack growth, and not residual strength measurement.

6.1.2 Test Matrix

Table 6.1 summarizes the test parameters for each laminate crack growth test whose results appear in this chapter. The laminate column refers to the stacking sequences presented in Table 6.2. Test results presented later refer to the specific tests by listing the laminate number, followed by the specimen number, e.g. 1-7.

6.1.3 Laminate crack growth testing

Crack growth tests were carried out in accordance with ASTM Standard E647 [2]. The specimens were installed in a servo-hydraulic fatigue test machine, including the 500 kN machine shown in Figure 6.2 and a 100 MN machine, bolted into the steel grips with sufficient torque to ensure good clamping of the specimens. Constant amplitude loading was applied with a frequency of 10 Hz. The tests occurred in a laboratory air environment.

Table 6.1 – *Test matrix*

Laminate	Specimen	σ_{max} (MPa)	R	a_0 (mm)
0	1	100	0.05	5
	2	120	0.05	5
	3	80	0.05	5
	4	120	0.5	5
	5	160	0.5	5
	6	140	0.05	5
	7	100	-0.3	5
	8	80	-0.3	5
	9	100	0.05	5
1	1	100	0.05	5
	2	120	0.05	5
	3	100	0.05	20.7
	4	100	0.05	13
	7	140	0.05	5
	10	91.5	0.05	13
6	1	100	0.05	5
	2	100	-0.1	5
7	1	100	0.05	5
8	1	100	0.05	5
9	1	100	0.05	5
	2	80	-0.3	5
11	1	100	0.05	5
12	1	100	0.05	5
13	2	100	0.05	5
14	1	100	0.05	5

Table 6.2 – *Laminate definitions*

Laminate	Layup (layer thickness in mm)
0	2024-T3 (1.6) / adh (.12) / prepreg 0° (.26) / adh (.12) / 2024-T3 (1.6) / adh (.12) / prepreg 0° (.26) / adh (.12) / 2024-T3 (.4) / prepreg 0° (.26) / 2024-T3 (.4) / prepreg 0° (.26) / 2024-T3 (.4) / prepreg 0° (.26) / 2024-T3 (.4) / adh (.12) / prepreg 0° (.26) / adh (.12) / 2024-T3 (1.6) / adh (.12) / prepreg 0° (.26) / adh (.12) / 2024-T3 (1.6)
1	2524-T3 (1.6) / adh (.12) / prepreg 0° (.26) / adh (.12) / 2524-T3 (1.6) / adh (.12) / prepreg 0° (.26) / adh (.12) / 2024-T3 (.4) / prepreg 0° (.26) / 2024-T3 (.4) / prepreg 0° (.26) / 2024-T3 (.4) / prepreg 0° (.26) / 2024-T3 (.4) / adh (.12) / prepreg 0° (.26) / adh (.12) / 2524-T3 (1.6) / adh (.12) / prepreg 0° (.26) / adh (.12) / 2524-T3 (1.6)
6	2524-T3 (1.6) / adh (.12) / prepreg 0° (.26) / adh (.12) / 2524-T3 (1.6)
7	2524-T3 (1.3) / adh (.12) / prepreg 0° (.26) / adh (.12) / 2524-T3 (1.6)
8	2524-T3 (1.6) / prepreg 0° (.26) / adh (.24) / 2524-T3 (1.6)
9	2524-T3 (1.6) / adh (.12) / prepreg 0° (.26) / adh (.12) / 2524-T3 (1.6) / adh (.12) / prepreg 0° (.26) / adh (.12) / 2524-T3 (1.6)
11	2524-T3 (1.6) / adh (.24) / prepreg 0° (.26) / 2524-T3 (1.6) / prepreg 0° (.26) / adh (.24) / 2524-T3 (1.6)
12	2524-T3 (1.6) / prepreg 0° (.26) / adh (.24) / 2524-T3 (1.6) / adh (.24) / prepreg 0° (.26) / 2524-T3 (1.6)
13	7055-T76 (1.6) / adh (.12) / prepreg 0° (.26) / adh (.12) / 2524-T3 (1.6)
14	Al-Li Alloy (1.6) / adh (.12) / prepreg 0° (.26) / adh (.12) / 2524-T3 (1.6)



Figure 6.2 – *TU Delft's 500 kN servo-hydraulic fatigue test machine with specimen installed.*

The load was periodically held at the maximum cyclic load to allow for crack length measurements. The reduced crack opening due to the bridging mechanism of FMLs, makes measuring at the maximum load particularly important for FMLs. Measurements were made visually using a graduated loupe with 10x magnification and hand-held lighting. The horizontal distance from the specimen centerline to each of the four visible crack tips (front and back, left and right) was recorded to the nearest 0.1 mm. Cyclic loading continued until the average of these visible crack lengths reached approximately 45 mm.

6.1.4 Post-test teardown inspection

The lengths of the cracks in each of the inner layers and the sizes and shapes of the delaminations throughout the laminate were of interest. After testing, a number of the specimens were inspected destructively to characterize the internal damage.

The ends of the specimens were sawn off, leaving approximately the middle 15 cm. A hole was drilled in one corner of each piece, so that the orientation of each layer relative to the intact laminate could be preserved after teardown.

Teardown was performed by clamping the specimen in a vice grip and driving a sharp, 25 mm-wide chisel between a surface layer and the remainder of the laminate with a rubber-tipped mallet. Care was taken to avoid directly chiseling the region around the cracks where delaminations were expected to be. Once a sufficient portion of the bond had been broken, prying by hand or with pliers was used to separate the layers. This process was repeated for each layer of the laminate until it was completely torn down. Often, fibers would remain bonded to one or both surfaces of each interface, necessitating their removal by working a tool under the fibers until they could be grasped and pulled off, along the fiber direction.

The hole drilled in a corner was used to string together the individual layers, preserving the stacking sequence of the laminate. Each surface was labeled with its identity and a reference grid. The interfaces were photographed so that the delamination shapes could be digitized, with the grid used for scale. Four points at the corners of a 10 mm grid square were used to determine the ratio of pixels to millimeters in the image. The angle of a line fit to the two crack tips and the hole center was used to apply a rotational transformation to the delamination data. The delamination shapes were recorded by manually selecting at least ten points at intervals along the edge of each quadrant of the delamination.

6.1.5 Model input parameter testing

Two additional sets of tests were performed to generate input properties for the model that were not already available.

2524 crack growth rate testing

Since 2524-T3 aluminum sheet was used in a number of laminates in this study, crack growth tests were performed on several 2524-T3 specimens. Several stress ratios were used in order to calibrate the crack growth of the alloy for an arbitrary stress ratio, since the ratio of $K_{tip\ min}/K_{tip\ max}$ is not necessarily the same as the applied stress ratio. The same specimen geometry and methods described in Section 6.1.3 were used. Crack growth rates were determined with the 7-point polynomial method [2]. By applying the correction factor for closure from [3], crack growth curves from each specimen were plotted together in terms of ΔK_{eff} , and a power-law fit was made to determine the crack growth properties of the material.

Adhesive layer delamination growth rate testing

Because a number of the tested laminates contain additional adhesive layers in the interfaces, a series of tests was performed to characterize the effects of the extra adhesive on the delamination growth rate. This testing is described in detail in [4] and Appendix A. Properties were obtained in the form of relations between the delamination growth rate and the mode II strain energy release rate based on adhesive layer thickness.

6.2 Test results

Figures 6.3 and 6.4 show the results of testing laminate 0, a Central configuration with 2024-T3 outer sheets. The test results are shown as average crack growth rate, as observed in the outer metal sheets, versus the average crack length. Figure 6.3 includes the results of tests with a stress ratio of $R = 0.05$, and different maximum applied stresses. Specimen 0-1 was tested until the average crack length reached 93.8 mm, such that $2a/W = 93.8\%$, and yet the crack growth rate remained relatively constant. The expected trend of increasing crack growth rate with increasing stress is observed. Figure 6.4 shows the effects of changing the stress ratio. For the same maximum stress, decreasing R

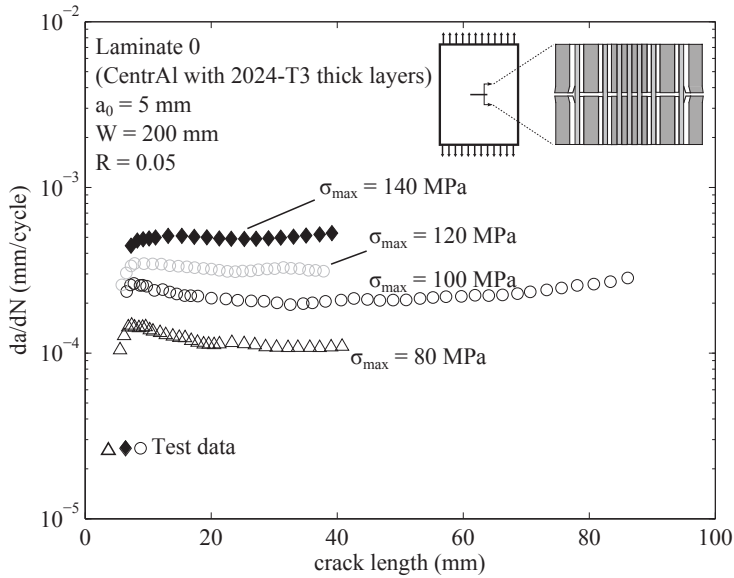


Figure 6.3 – Crack growth rates from visual measurement of external cracks in tests of Centra1 with 2024-T3 thick layers. The 100 MPa test was allowed to continue to look for evidence of edge effect. None was found

increases the stress range, speeding crack growth. Increasing R reduces crack growth rates.

Figure 6.5 shows the results of tests of laminate 1, which is identical to laminate 0, but with 2524-T3 in the thick metal layers in place of 2024-T3. Considering comparable test results, the use of 2524-T3 resulted in a reduction of crack growth rates of approximately 10% compared to laminate 0.

Several of the laminate 1 specimens were tested with varying saw-cut length. The results of these tests are plotted in Figure 6.6. Specimen 1-10 had a long saw-cut of 13 mm, but the applied stress was reduced to make the net stress in the plane of the saw-cut equal to that of specimen 1-1. Longer saw-cuts resulted in faster crack growth rates, which is expected since there is less intact material in the wake of the crack to provide bridging. Though specimen 1-10 showed an initially higher growth rate, as the crack length increased it tended towards the same steady-state rate as specimen 1-1, with the same net-section stress. This suggests that the crack growth rate reduction due to bridging is driven more by the stress and the load distribution near the crack tip, and

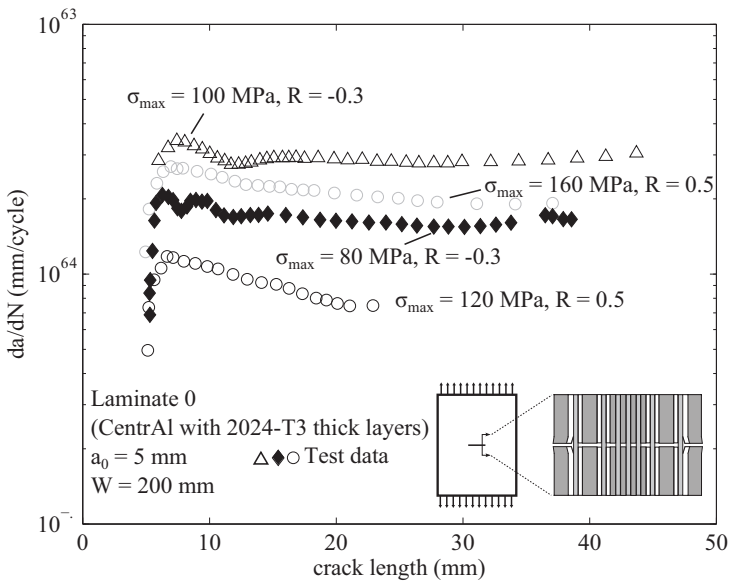


Figure 6.4 – Crack growth rates from visual measurement of external cracks in tests of CentrAl with 2024-T3 thick layers tested at varying peak stress and stress ratio

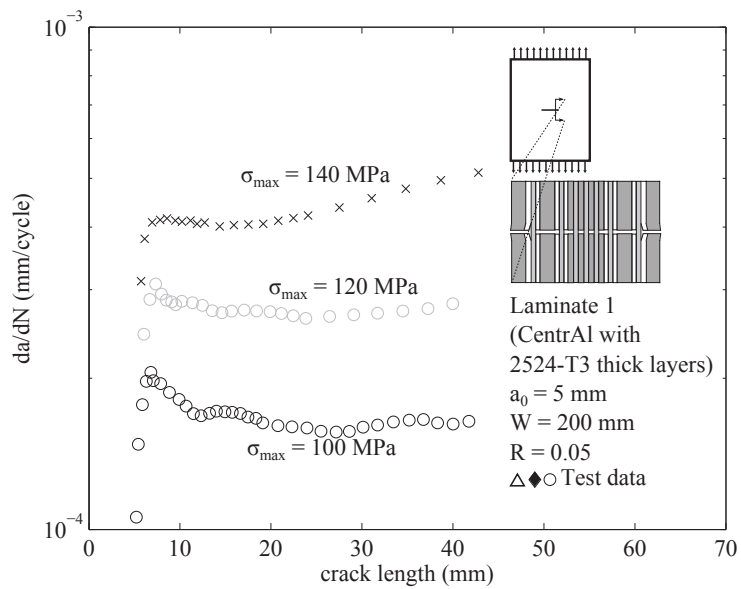


Figure 6.5 – Crack growth rates from visual measurement of external cracks in tests of CentrAl with 2524-T3 thick layers

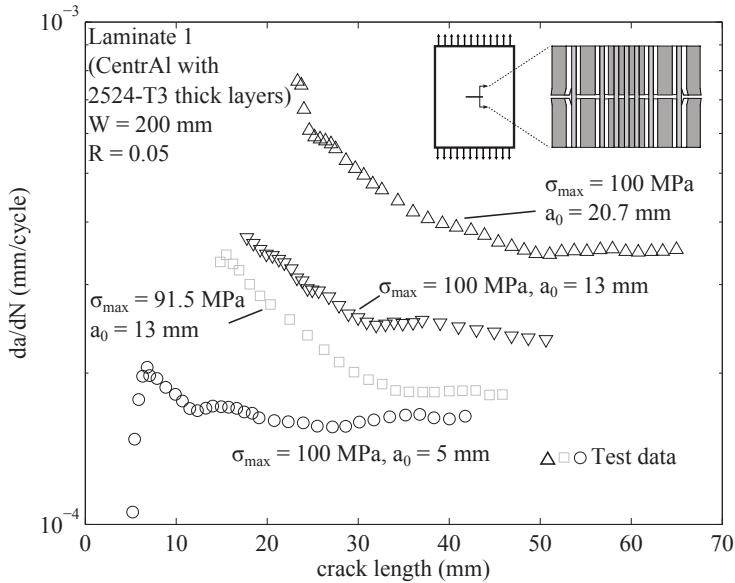


Figure 6.6 – Crack growth rates from visual measurement of external cracks in tests of CentraI with 2524-T3 thick layers, showing the effects of changing the saw-cut starter notch length

differences in the bridging material far from the crack tip have small effects on growth rate. This notion is addressed in more detail in Appendix B.

Figure 6.7 includes crack growth rate data from a 2/1 and a 3/2 layup of thick 2524-T3 sheets, glass fiber prepreg, and extra adhesive in the interfaces. Test 9-1, with its 3/2 layup, had slower crack growth than the 2/1 layup of test 6-1. Additionally, 6-1 exhibits a much greater effect of crack length on the crack growth rate - as the cracks in 6-1 grew longer they grew even faster compared with 9-1. These laminates were also tested in tension-compression loading. The results of these tests are shown in Figure 6.8. The observation that increasing the number of layers decreases crack growth rate is consistent with prior work in thin-metal Glare and ARALL [5, 6].

Specimen 7-1 tested an asymmetric layup, with a 1.6 mm thick metal sheet on one side, and a 1.3 mm sheet on the other. The crack growth rate curves of this test are shown in Figure 6.9, respectively. The crack lengths on opposite faces of the specimen differed by 4 mm by the end of the test. Initially, cracks in both layers grew at the same rates, since little bridging occurs while the cracks

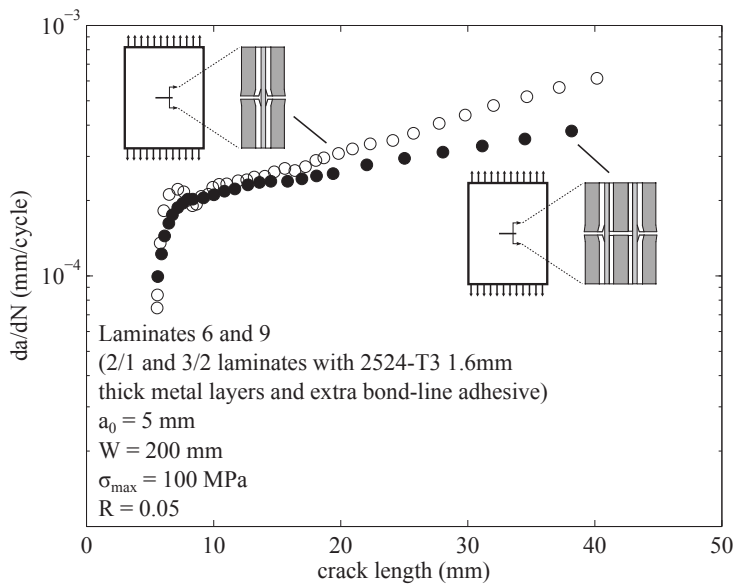


Figure 6.7 – Crack growth rates from visual measurement of external cracks in tests of Laminates 6 and 9

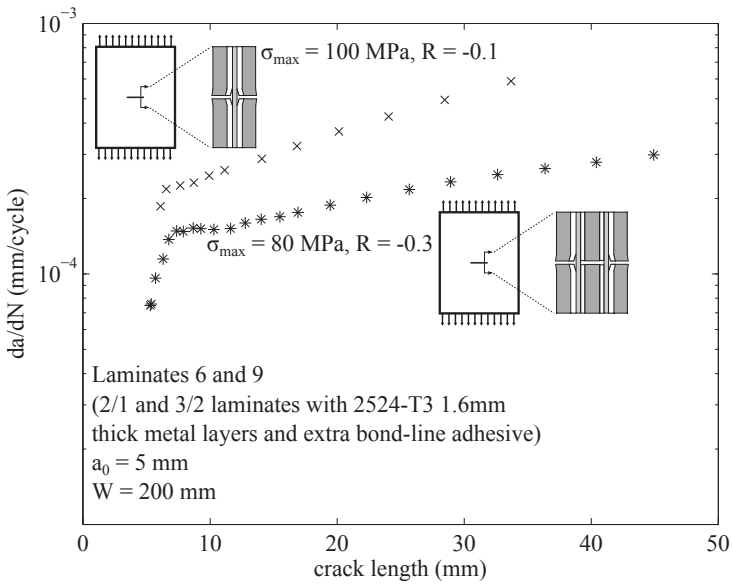


Figure 6.8 – Crack growth rates from visual measurement of external cracks in tests of Laminates 6 and 9 with tension-compression loading

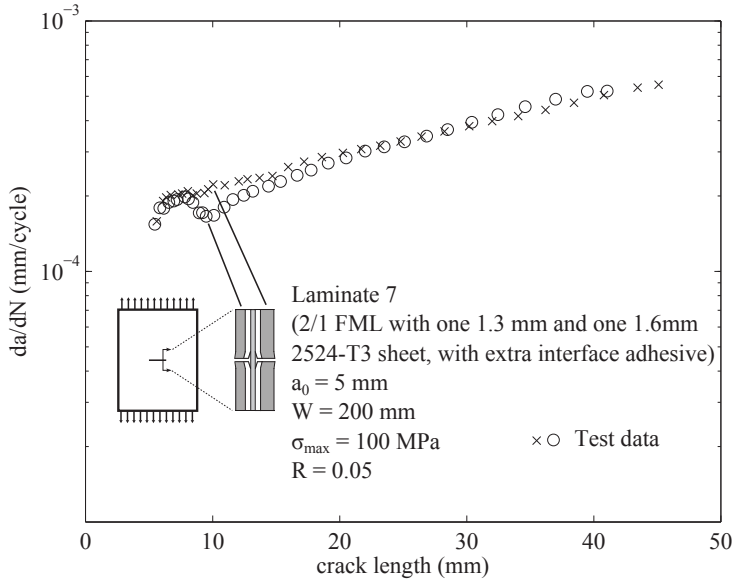


Figure 6.9 – Crack growth rate results for 2/1 laminate with non-uniform metal layer thickness

first grow from the saw-cut. After about 4 mm of growth, the growth rate of the thin sheet slowed, indicating that it was being more effectively bridged than the thick sheet. As the cracks in the thick sheet increased in length, the additional load shed from the thick sheet through bridging increased the growth rate of the thin sheet cracks, and for the duration of the test, the growth rates were nearly the same with respect to crack length.

Another asymmetric laminate was laminate 8. The asymmetry in this case was in the additional adhesive layer, with no additional adhesive between the glass fibers and the front aluminum sheet and double adhesive thickness between the fibers and the back sheet. There was negligible difference between the crack lengths and crack growth rates on opposite sides of the laminate, as shown in Figure 6.10.

Laminates 11 and 12 employ the same single-side extra adhesive configuration as laminate 8, but in a 3/2 configuration, resulting in a symmetric laminate. In laminate 11 the extra adhesive was adjacent to the outer metal sheets, and in laminate 12 the extra adhesive was between the prepreg layers and the inner metal sheet. Figure 6.11 includes the crack growth rates results

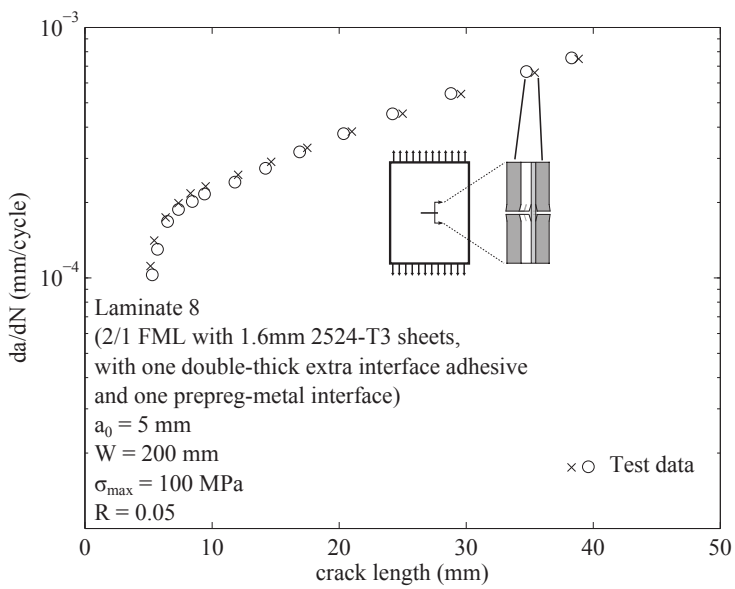


Figure 6.10 – Crack growth rate results for 2/1 laminate with asymmetric additional adhesive layers

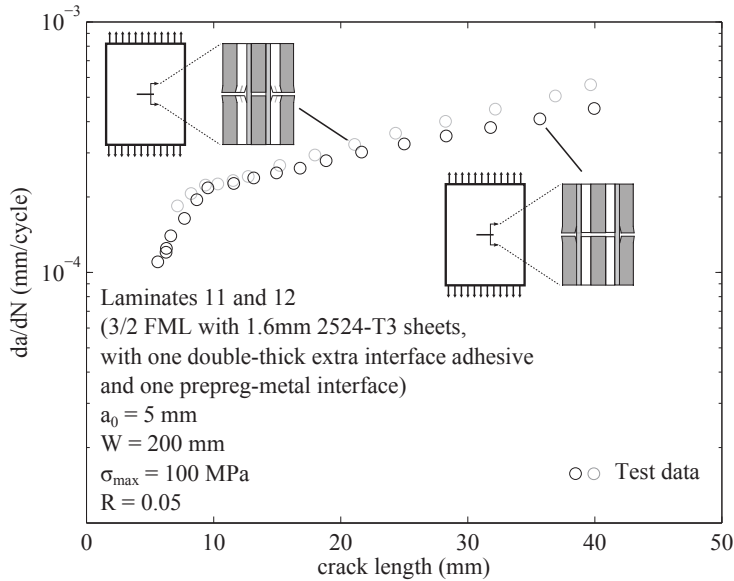


Figure 6.11 – Crack growth rate results for 3/2 laminates with additional adhesive layers on only one side of each fiber layer

from test 11-1 and 12-1. Laminate 11 had slightly faster crack growth than laminate 12.

Two 2/1 laminates with mixed aluminum alloys were tested. Laminate 13 had one layer of 2524-T3 and one layer of an aluminum-lithium alloy, and laminate 14 had one layer of 2524-T3 and one of 7055-T76. Figure 6.12 shows the crack growth rate curves from tests of these laminates, with the data from opposite sides of the specimens separated. There was no difference in the crack growth of the lithium alloy and its companion 2524-T3 sheet, but in laminate 14 the cracks in the 7055 layer grew significantly faster.

6.2.1 Destructive inspection results

A sample image of an internal delamination is given in Figure 6.13. The tapered, somewhat rounded shape of the delamination around the cracks is readily apparent.

The four delamination fronts (top right, bottom right, bottom left, and top left) were digitized, and are plotted, after mirroring about the x and y

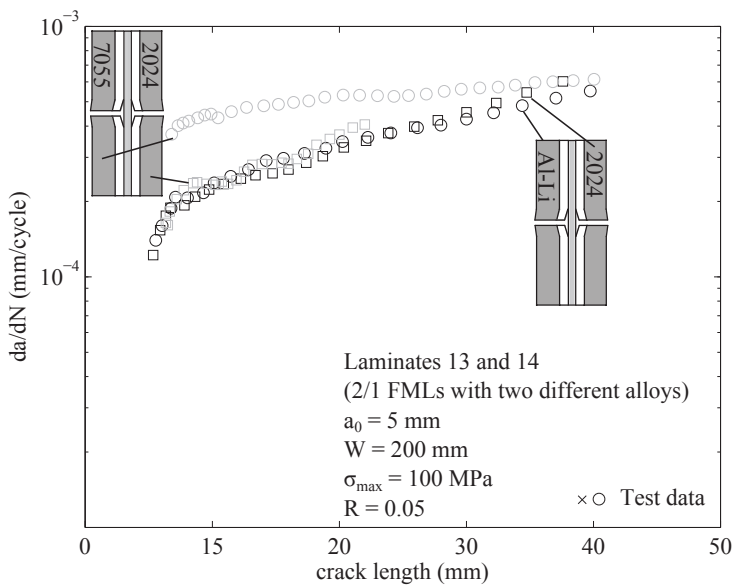


Figure 6.12 – Crack growth rate results for 2/1 laminates with mixed aluminum alloys

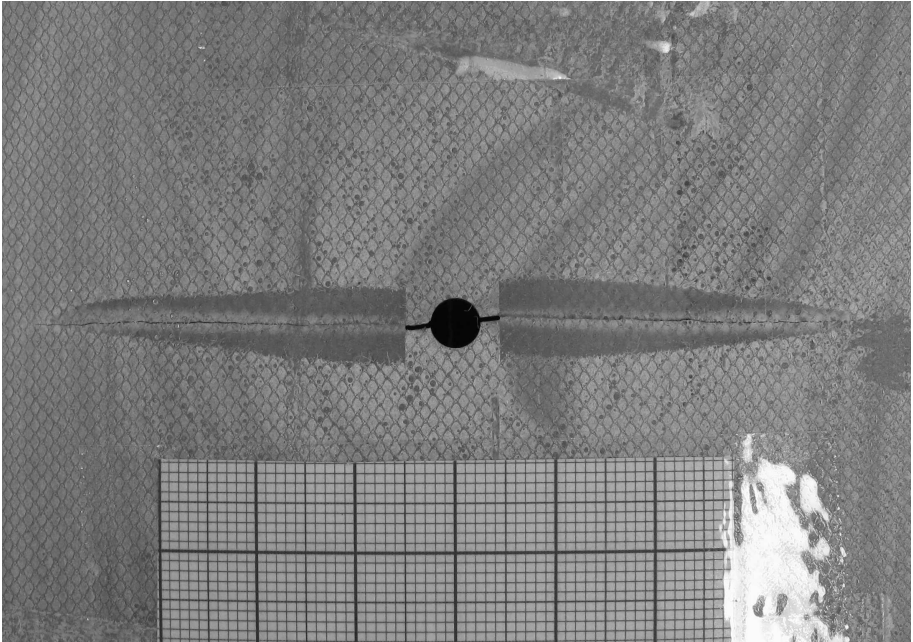


Figure 6.13 – *Delamination in the first interface of specimen 0-6.*

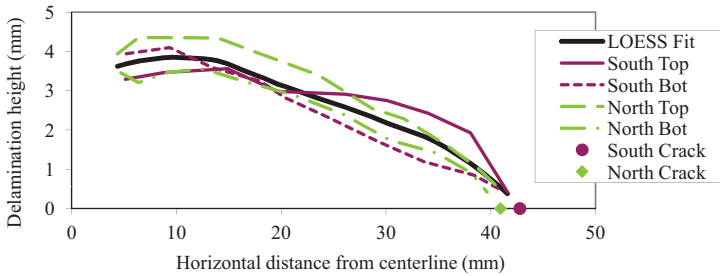


Figure 6.14 – Example from the first interface of specimen 0-6 showing all four delamination fronts from a given layer averaged into one representative front. “North” and “South” refer to the left and right cracks, respectively. “Top” and “bottom” are the delaminations above and below each crack, respectively.

axes such that they are all in the 1st quadrant, in Figure 6.14. These data are then averaged with LOESS smoothing [7] in order to produce an average delamination shape for that interface, appropriate for model comparison and for comparing the results from each measured interface.

The complete set of averaged delamination shapes for test 0-6 is compiled in Figure 6.15. Since the laminate is symmetric, delaminations from equivalent interfaces are plotted together (e.g. interfaces 1 and 14 are both adjacent to the outer layers, and interfaces 4 and 11 are outside the outermost thin metal sheets of the inner Glare). The crack tip locations for each metal layer are plotted along with the delamination shapes. Each shape corresponds to two crack tips, the left and the right.

The measurements in Figure 6.15 show that even though the laminate is symmetric, the delamination shapes and crack lengths in equivalent interfaces are not identical. Crack lengths are longest on the outside of the laminate in the thicker layers, with lengths in the 40–45 mm range, and the cracks in the thin layers of the internal Glare measured 20–25 mm.

Test specimen 1-1 was also destructively tested. Its delamination shapes are plotted in Figure 6.16. The ratios in crack length between the inner and outer layers in specimens 1-1 and 0-6 are very close. Specimen 1-1, loaded to a maximum stress of 100 MPa, has smaller delaminations compared with specimen 0-6, with $\sigma_{max} = 140\text{MPa}$. This is expected considering the magnitude of bridging load transfer would be much higher in the specimen with greater load applied if the cracks and delaminations were the same size. The delaminations in 0-6 should have grown large to relieve the high bridging loads.

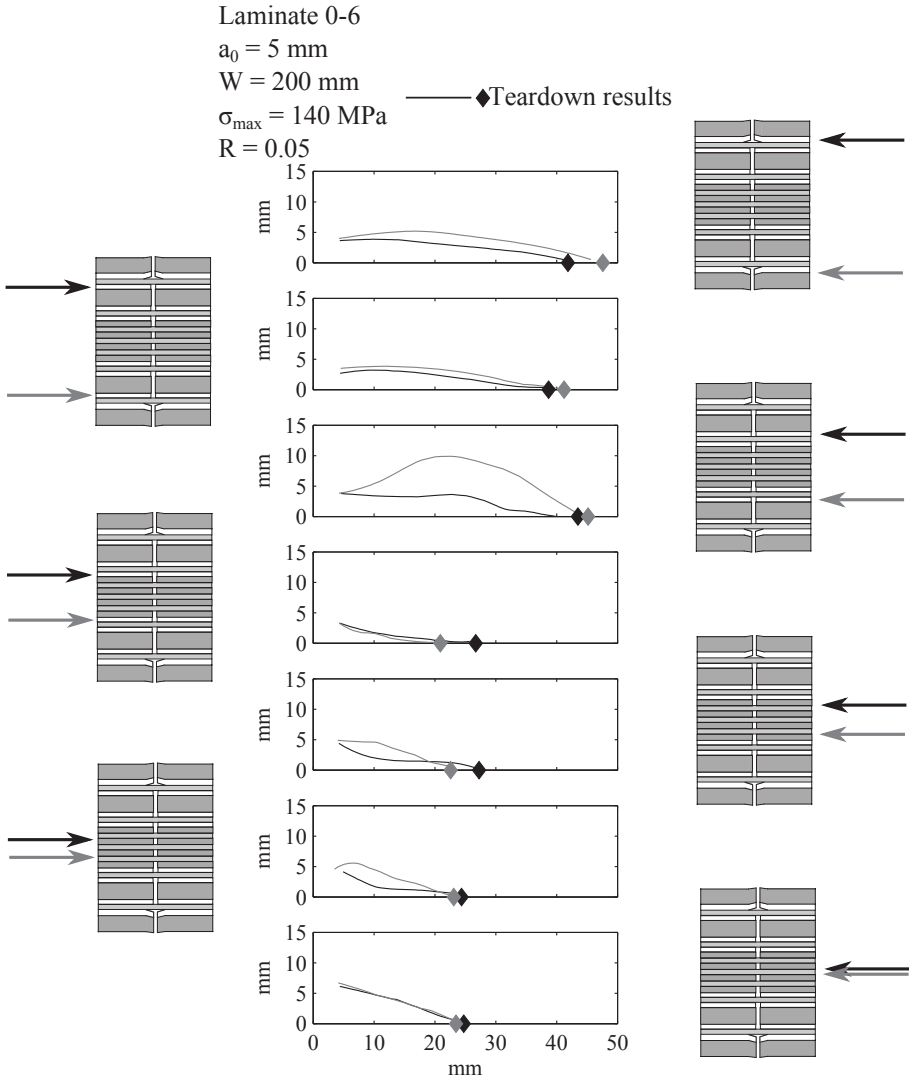


Figure 6.15 – Delamination shapes and internal crack lengths of specimen 0-6. Lines represent the averaged delamination shape from all four quadrants of the interface. Dots are the average half-crack length of the metal layer adjacent the delamination. Arrows indicate which interface is shown in the plot, and are color-coded with the data.

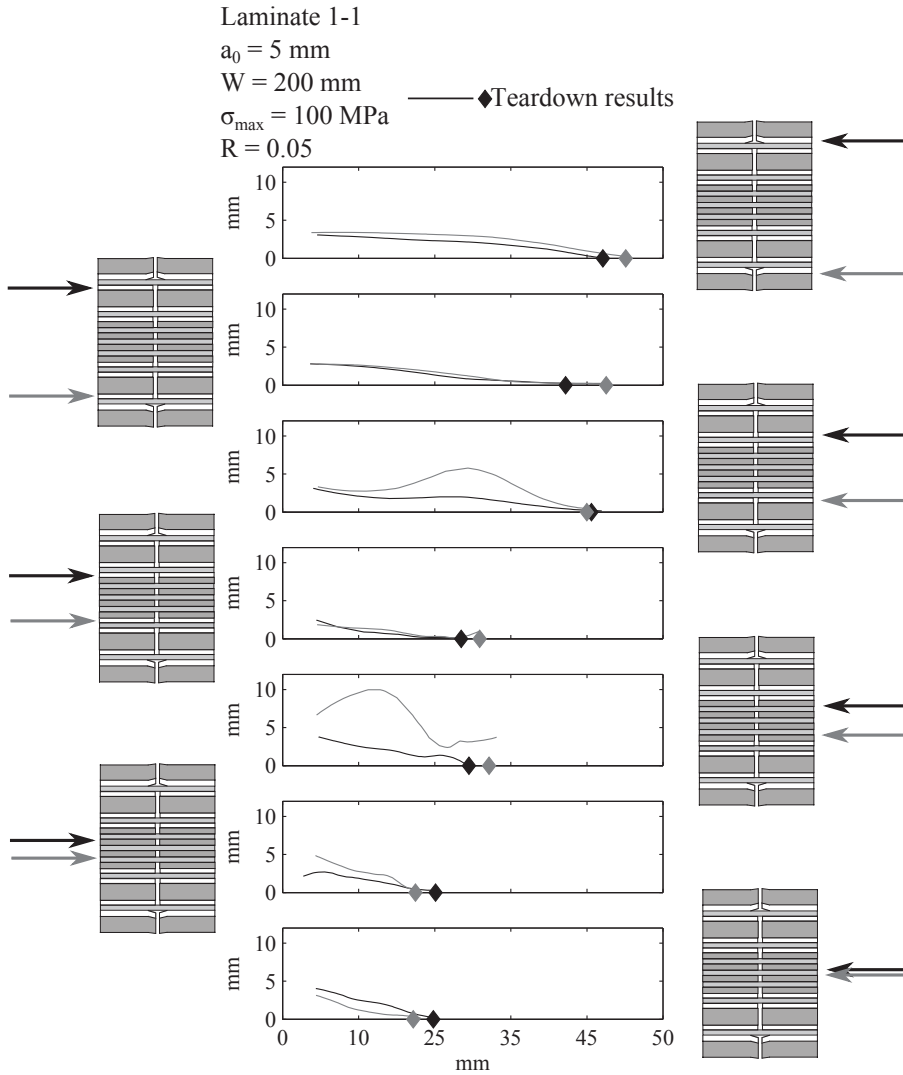


Figure 6.16 – Delamination shapes and internal crack lengths of specimen 1-1.

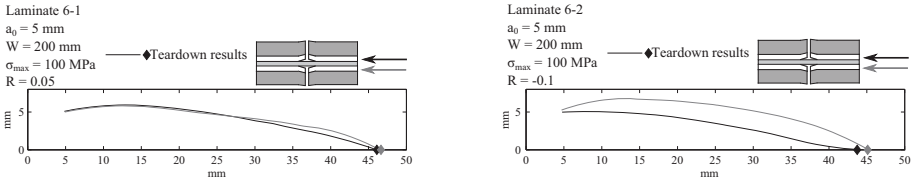


Figure 6.17 – Delamination shapes and internal crack lengths of specimens 6-1 and 6-2.

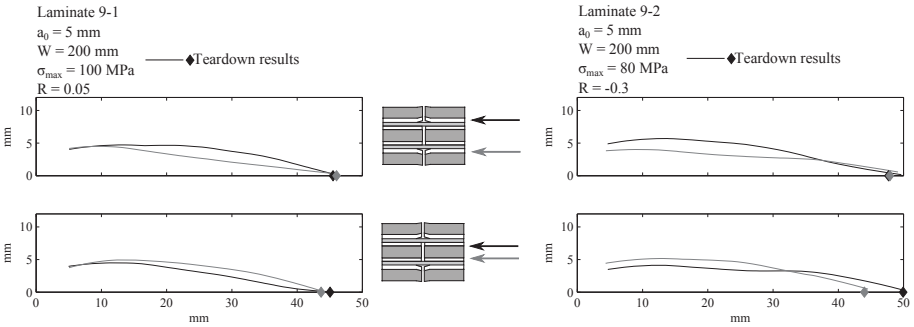


Figure 6.18 – Delamination shapes and internal crack lengths of specimens 9-1 and 9-2.

Figure 6.17 shows the delaminations from specimens 6-1 and 6-2, the 2/1 laminates with thick 2524-T3 and additional bondline adhesive. Specimen 6-2, which was tested in tension-compression loading at $R = -0.1$, exhibits more through-thickness difference between delaminations, whereas specimen 6-1, tested in tension-tension loading, has symmetric delamination through the thickness. Figure 6.18, in which the delaminations of specimens 9-1 and 9-2 are plotted, does not show an obvious through-thickness asymmetry as a result of the different loading in these specimens. The lower thickness of laminate 6 could have led to the presence of local buckling in the delaminated area in compression, whereas the thicker laminate 9 could have constrained such asymmetric behavior. Additionally, the delaminations in the inner and outer interfaces of specimens 9-1 and 9-2 are of similar size. Though the bridging load transferred over the interfaces with the outer sheets should have been twice that of the inner metal sheet, the equal delamination sizes indicate a self-balancing behavior of the delamination growth through the thickness.

Laminate 8 was laid up asymmetrically, with the additional adhesive placed

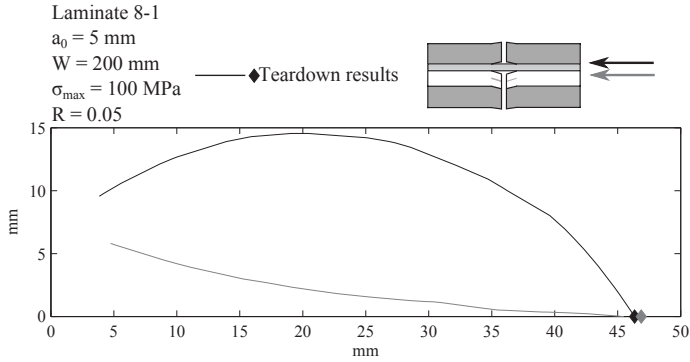


Figure 6.19 – Delamination shapes and internal crack lengths of specimen 8-1.

only in one fiber-metal interface. Its measured delamination shapes are plotted in Figure 6.19. This difference had a dramatic effect on the delamination shape. The interface with additional adhesive had a small delamination — even smaller than the delamination in specimen 6-1. The prepreg-metal interface had a large delamination — over 14 mm at its peak. The shapes are also different, with the adhesive interface having a narrow triangular shape, and the prepreg-metal interface having a rounded shape. Two mechanisms can be considered to have some role in the asymmetric delamination behavior. The toughness of the interfaces is different, with the thick adhesive interface being much tougher than the adhesive-free interface. Also, the asymmetric placement of the fibers in the laminate will make the laminate stiffer towards the adhesive free interface, resulting in somewhat more load being carried by the metal sheet on that side.

In Figure 6.20, including the delamination shapes from 3/2 laminates 12-1 and 11-1, the results are similar to test 8-1. Interfaces with additional adhesive have small, triangular delaminations, while those without have large, rounded delaminations. No significant effect of the location of the delamination, whether the interface was adjacent to the outer metal layer or the internal one, was observed. This suggests that the driving factor in the different delamination size in each interface of specimen 8-1 was the interface resistance to delamination, rather than the asymmetry of the laminate, since the symmetric laminates 11 and 12 showed the same behavior.

Laminates 7, 13, and 14 explored asymmetry of the metal layers of the FML. The delamination results of test 7-1 are shown in Figure 6.21. The thicker metal sheet had larger adjacent delaminations and a slightly larger crack length. Larger delaminations were expected at this interface, since the thicker

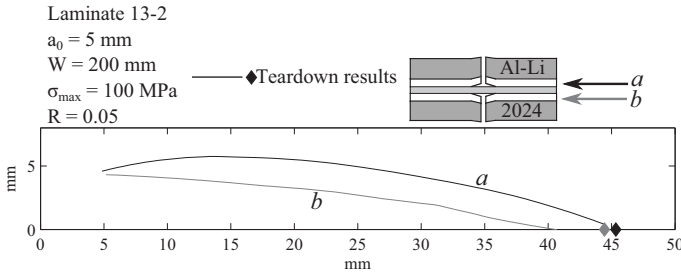


Figure 6.22 – Delamination shapes and internal crack lengths of specimen 13-2.

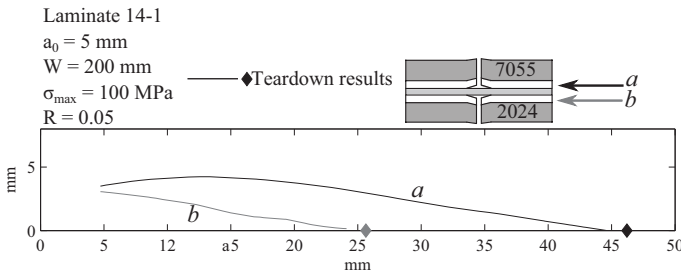


Figure 6.23 – Delamination shapes and internal crack lengths of specimen 14-1.

Laminate 14’s 7055-T76 sheet had much faster crack growth than the 2524-T3 sheet. Correspondingly, the delamination is larger. However, the 7055-adjacent delamination of test 14-1 is somewhat smaller than the 2524-T3-adjacent delamination of test 6-1. Since the crack in the 7055 metal layer grew so much faster, the ratio of delamination height to crack length was expected to be smaller.

6.2.2 Input parameter testing results

2524-T3 crack growth rate

The data from crack growth testing sheets of 1.6 mm thick 2524-T3, having been processed with the 7-point polynomial method [2], are shown in Figure 6.24. ΔK_{app} in this chart was calculated according to:

$$\Delta K_{app} = \Delta \sigma_{app} \sqrt{\pi a} \sqrt{\sec\left(\frac{2a}{W}\right)} \quad (6.1)$$

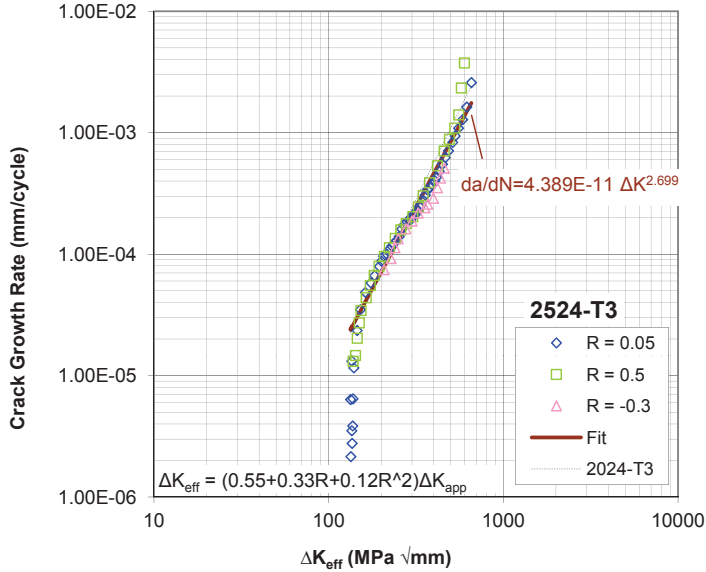


Figure 6.24 – Crack growth results of 2524-T3 property tests, with power law fit

By using the closure correction by Schijve [3], $\Delta K_{eff} = (0.55 + 0.33R + 0.12R^2)(1 - R)K_{max}$, the ΔK_{eff} curves from each sample line up over most of the tested ΔK range in Figure 6.24. Fitting a power law function to these plots provides an estimate of the crack growth in 2524-T3 as a function of ΔK_{eff} to be used in the crack growth model:

$$\frac{da}{dN} = 4.389 \times 10^{-11} \Delta K_{eff}^{2.6989} \quad (6.2)$$

where $\frac{da}{dN}$ is in mm/cycle and ΔK_{eff} is in units of $\text{MPa}\sqrt{\text{mm}}$.

The power law fit for 2024-T3 used in previous FML models is plotted in Figure 6.24 for comparison. It is slightly higher than the 2524-T3 data, particularly for higher values of ΔK_{eff} .

Delamination growth with extra bondline adhesive

The delamination growth rate results from ply-interrupt specimens with varying additional adhesive thickness are plotted against cyclic strain energy release

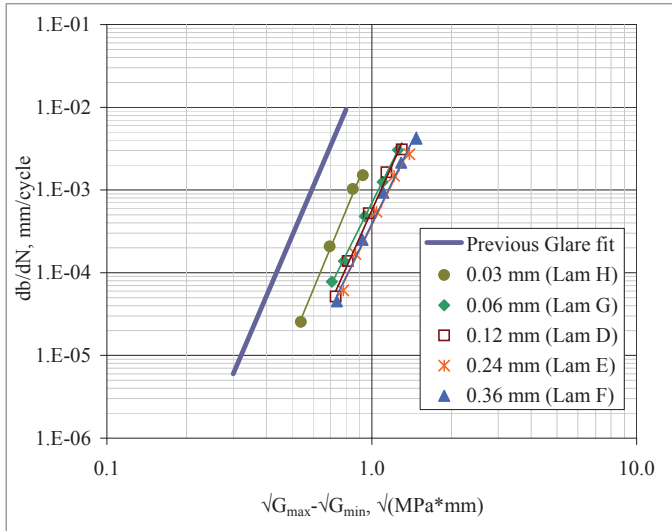


Figure 6.25 – Effect of adhesive layer thickness on delamination growth rate

rate in Figure 6.25. The previous Glare curve in this figure is derived from tests with no additional adhesive in the bondline [8].

The coefficients to be used in the model for delamination growth in Equation (3.23) are given in Table 6.3. The C_d and n_d terms are based on ΔG in units of $\sqrt{\text{MPa mm}}$ and $\frac{db}{dN}$ in units of mm/cycle.

For more detail on the test procedure and interpreting the results, see Appendix A.

Table 6.3 – Power law fits for Equation (3.23) for each adhesive layer thickness. C_d and n_d terms are based on ΔG in units of $\sqrt{\text{MPa mm}}$ and $\frac{db}{dN}$ in units of mm/cycle.

t_{ad} (mm)	C_d	n_d
0.03	3.196×10^{-3}	7.731
0.06	6.941×10^{-4}	6.422
0.12	5.646×10^{-4}	7.166
0.24	3.742×10^{-4}	6.541
0.36	3.875×10^{-4}	6.565

6.3 Summary

The test results presented in this chapter show that, by rearranging the same or slightly different constituents in an FML, a wide variety of crack growth and delamination performance can result. Explanations for all of the observed trends were provided, where possible. In some cases, such as crack growth rates increasing with stress or with saw-cut length, it was possible to relate the results to prior FML crack growth results from the literature. In cases where novel configurations were tested, such as the asymmetric lay-ups, explanations in line with a conceptual understanding of the material were offered. In the following chapter, the question of whether the generalized model of this thesis can capture the observed variations in behavior of each test, and thus whether conceptual understanding of this material system developed throughout this thesis is sufficient to explain its damage growth behavior, will be addressed.

Bibliography

- [1] Vlot, A. and Gunnink, J. (2001) *Fibre metal laminates: an introduction*. Kluwer Academic Publishers.
- [2] ASTM Standard E647, 2008e1 (2008), Standard test method for measurement of fatigue crack growth rates. ASTM International.
- [3] Schijve, J. (1981) Some formulas for the crack opening stress level. *Engineering Fracture Mechanics*, **14**, 461–465.
- [4] Wilson, G. S., Fassih, Y., Alderliesten, R. C., and Benedictus, R. (2011) Effect of adhesive layer thickness on fiber metal laminate delamination growth rate. *International Journal of Fatigue*, submitted for publication July 2011.
- [5] Marissen, R. (1988) *Fatigue crack growth in ARALL. A hybrid aluminium-aramid composite material: Crack growth mechanisms and quantitative predictions of the crack growth rates*. Ph.D. thesis, Delft University of Technology, Delft, The Netherlands.
- [6] Alderliesten, R. C. (2005) *Fatigue crack propagation and delamination growth in Glare*. Ph.D. thesis, Delft University of Technology, Delft, The Netherlands.
- [7] Mathworks *MATLAB Documentation*.

- [8] Alderliesten, R. C. (2007) Analytical prediction model for fatigue crack propagation and delamination growth in glare. *International Journal of Fatigue*, **29**, 628–646.

This page intentionally left blank.

Chapter 7

Model validation

7.1 Introduction

The purpose of this chapter is to evaluate the generalized FML crack growth model, described in Chapter 3, against its goals. The model was intended to accurately predict the growth of cracks and delaminations in various non-uniform FMLs subject to fatigue loading.

The validation of the model will consider both its absolute accuracy — how closely do the predicted crack growth lifetimes, crack growth rates, and delamination sizes match the test results? — and its relative performance — does the effect of changes to the laminate or test conditions observed in testing correspond to the modeled difference due to changes in the same parameters? By making these assessments for a variety of different laminates, initial conditions, and applied loadings, an overall assessment of the model can be made, its limitations explored, and needs for improvement identified.

Model calculations have been made for each of the FML tests described in Chapter 6. Additionally, calculations have been performed for a number of test results taken from [1] and [2]. Where any special pre-processing or assumptions have been applied to the model inputs in order to accommodate a unique test scenario, the additional accommodations will be described along with the presentation of that model and test data.

7.1.1 Glare data of Alderliesten

A number of different Glare configurations were tested for crack growth by Alderliesten [1], mostly cross-ply laminates. The specimen configuration used is a center-cracked tension specimen. Cracks were initiated from two saw-cuts of varying length, a_s , spaced vertically. The lay-up, saw-cut length, stress, and stress ratio of the specimens tested by Alderliesten whose data are included in this chapter for validation purposes are summarized in Table 7.1.

7.1.2 Glare data in bending of Randell

Randell performed tests on Glare 2 and Glare 3 laminates in bending and combined tension-bending [2]. Bending moments in the bending-only specimens were introduced via a 4-point bend apparatus, and tension-bending tests were conducted using a milled open-hole tension bending (MOHTB) specimen, as shown in Figure 7.1. With tensile loading applied along an axis offset from the laminate center line, secondary bending occurs, leading to a state of combined tension and bending at the location of a hole. For both types of test, cracks were allowed to initiate naturally from the edges of the holes, rather than being induced with artificial saw-cuts, allowing both crack initiation and crack growth data to be obtained.

The lay-ups and loadings tested by Randell are summarized in Table 7.2. The MOHTB specimens were characterized by their bending ratio, k_b , which gives the ratio of the surface stress to the stress at the neutral line in the test section of the specimens.

7.2 Comparison to current test data

The simplest laminate constructed and tested for this work was laminate 6¹, with two outer 2524-T3 aluminum layers reinforced with a central prepreg layer with additional adhesive in the bondline.

The tests were modeled with a saw-cut length matching those measured on the test specimens and initial crack lengths 0.5 mm longer than the saw-cut. The initial delamination height, at the saw-cut tip, was 25% of the initial crack length less the saw-cut length. Sufficient bar elements were added to limit the bar element width at the delamination tip to $w_{max} = 0.25$ mm, based

¹Refer to Table 6.2 for full lay-up details of laminates discussed in this section.

ID	Laminate	σ_{max} (Mpa)	R	a_s	a_{final}
A1	G13 4/3 .4	120	0.05	2.5	20
A2	G14B 4/3 .4	120	0.05	2.5	20
A3	G14B 4/3 .4 T-L	120	0.05	2.5	20
A4	G13 4/3 .4	100	0.05	5	20
A5	G13 6/5 .4				
A6	G13 8/7 .4				
A7	G13 6/5 .4	100	0.05	1.5	17
A8	G13 6/5 .5	100	0.05	1.5	17
A9	G13 6/5 .4	100	0.05	10	28
A10	G13 4/3 .4	100	0.05	2.5	10
A11	G13 4/3 .4	120	0.5	2.5	8
A12	G13 4/3 .4	100	0.5	2.5	6
A13	G13 4/3 .4	120	0.05	15	45
A14		100	0.05		45
A15		120	0.5		30
A16		100	0.5		25
A17	G1 4B 4/3 .5	120	0.05	2.5	22
A18		100	0.05		12
A19		120	0.5		8
A20		100	0.5		6

Table 7.1 – Test parameter summary for data from [1] used in validation

Configuration	Laminate	σ_{max} (Mpa)	kb	a_s (mm)	a_{final} (mm)
MOHTB	G2-5/4-.4	80	2.77	2.8	29
MOHTB	G2-5/4-.4	100	2.5	2.8	29
MOHTB	G2-6/5-.4	100	2	2.8	18
4-pt bend	G2-11/10-.4	200 (bending)	N/A	2.8	15
MOHTB	G3-7/6-.3	100	2.3	2.8	30

Table 7.2 – Test parameter summary for data from [2] used in validation. The stress ratio of all tests was $R = 0.1$

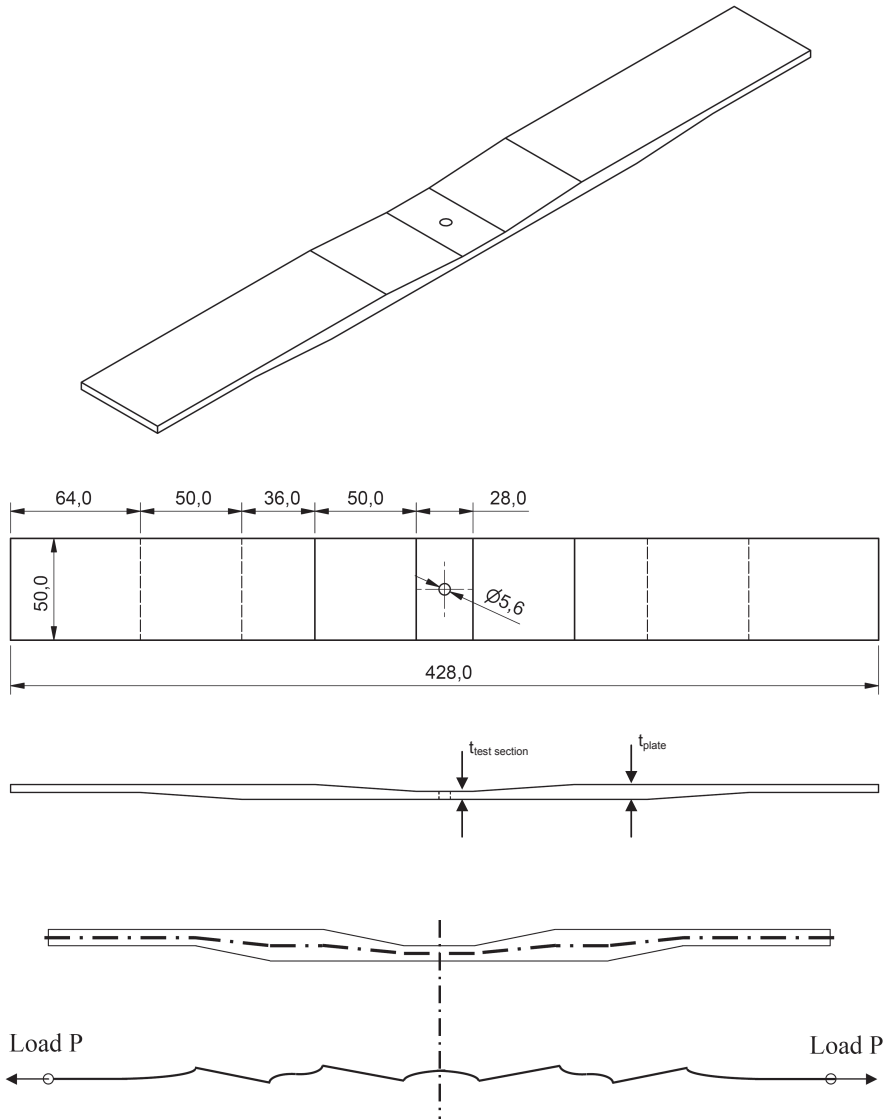


Figure 7.1 – MOHTB specimen design from [2]

on the convergence study discussed in Section 3.3.6 of Chapter 3. The model results are smoothed by taking the crack lengths from every tenth iteration, then applying the seven-point polynomial method to calculate the crack growth rate [3].

The temperature differential used in the CLT portion of the model was $120^{\circ}\text{C} - 20^{\circ}\text{C} = -100^{\circ}\text{C}$. Applied stresses and moments were zero in all directions, except the applied stress parallel to the fibers and perpendicular to the saw-cut and crack. Specimen 6-1 had an applied maximum gross stress of 100 MPa with a stress ratio of $R = 0.05$, and specimen 6-2 had an applied maximum cyclic stress of 100 MPa with a stress ratio of $R = -0.1$, for tension-compression stress cycles.

The test results of both specimens 6-1 and 6-2, plotted in Figure 7.2, showed crack growth rates beginning around 2×10^{-4} mm/cycle and increasing steadily to around 6×10^{-4} mm/cycle at final lengths of 37-45 mm. The model predictions, plotted in the same figure, show the same qualitative behavior — a slow but steady increase over the crack growth period. Additionally, the model prediction has specimen 6-2 growing slightly faster than specimen 6-1. The crack growth rates predicted by the model for specimen 6-2 are within 5×10^{-5} mm/cycle of the test data, while the model-predicted growth rates of specimen 6-1 are between 5×10^{-5} to 2×10^{-4} mm/cycle less than the growth rates from the test. In underpredicting the specimen 6-1 growth rate, the model slightly overestimates the difference in growth rate as an effect of the differing loading schemes applied to the two specimens.

The predicted final delamination shapes of the two laminate 6 tests are plotted along with the measured delamination shapes in Figure 7.3. The model-predicted delamination shape of 6-1 matches the test result over most of the delamination front, apart from the down-turn of the test delamination shape close to the saw-cut. The prediction for 6-2 matches the larger shape observed in the second interface of the test in the region of the delamination toward the crack tip, but overestimates the delamination size toward the notch. The overprediction of delamination height near the notch tip is consistent with the overprediction of bridging load in this area, discussed in Section 4.3.2. The model did not predict the difference in shapes that were observed between the two interfaces. This difference likely results from some out-of-plane buckling occurring in the compression portion of the load cycle, which would cause a stress gradient through the thickness of the otherwise symmetrical (and symmetrically loaded) laminate. Such buckling behavior in compression is not accounted for in the model.

Specimens 9-1 and 9-2 represent an increase of complexity, with three metal

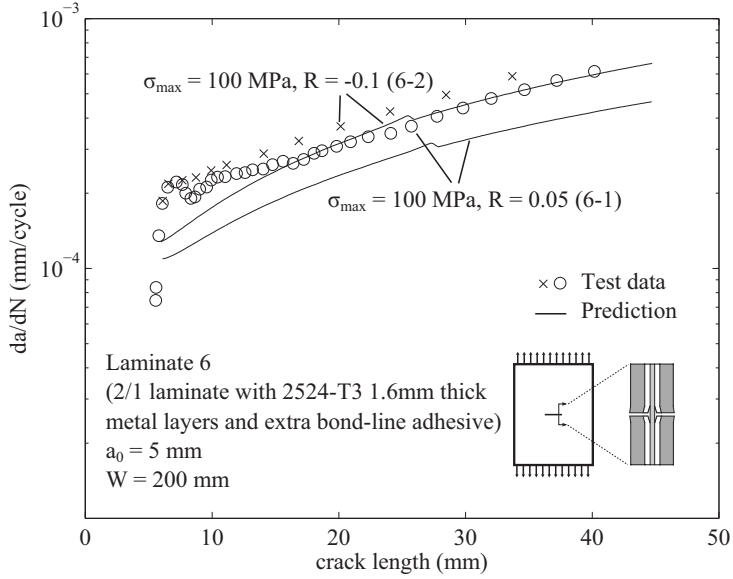


Figure 7.2 – Comparison of test results and model prediction for 2/1 laminate with extra bondline adhesive

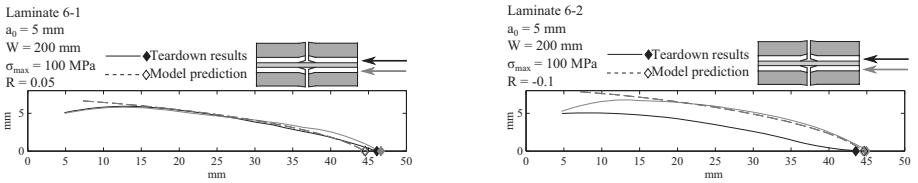


Figure 7.3 – Comparison of predicted and measured delamination shapes and internal crack lengths of specimens 6-1 and 6-2.

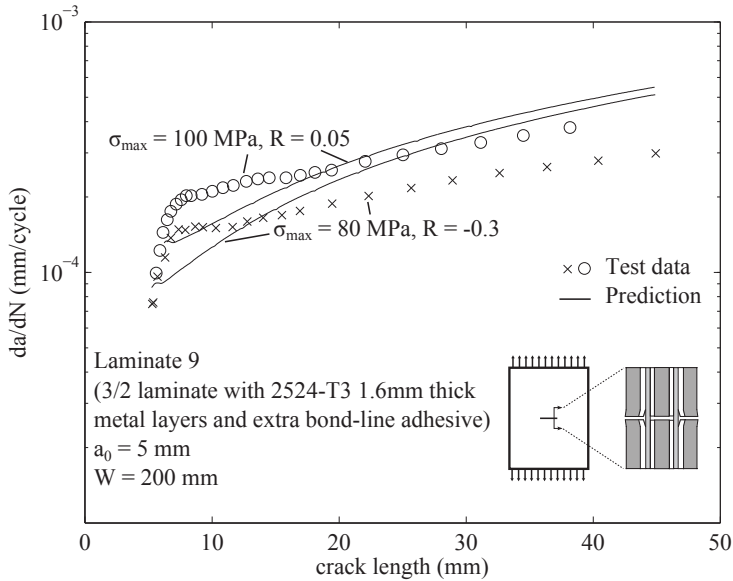


Figure 7.4 – Comparison of test results and model prediction for 3/2 laminate with extra bondline adhesive

layers and two reinforcing layers with additional adhesive. These tests were modeled using the same approach as for specimens 6-1 and 6-2. Specimen-specific parameters of the modeling are included in Figure 7.4, in which the outer-sheet crack growth rates from the simulation results are plotted against the test data for these two specimens. The simulation results for specimen 9-1 are in good agreement with the test data over most of the test, except the early crack growth period, in which the model slightly underpredicts the crack growth rates. The rate of growth of specimen 9-2 is overpredicted by the model, except while the crack is short. For shorter crack lengths, the modeled growth rate matches the test result. Qualitatively, both the model and the test results are increasing steadily over the length of the test, and the model correctly predicts that specimen 9-2 grows slower than specimen 9-1, though the actual difference between the two specimens' growth rates was larger than predicted.

The model predicted that the crack length of the inner metal sheet would lag behind the outer crack lengths by approximately 0.7 mm and 0.3 mm in specimens 9-1 and 9-2, respectively. The average of the outer sheet crack

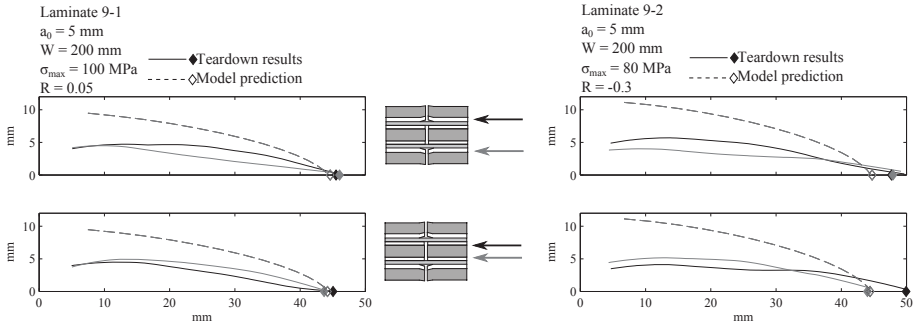


Figure 7.5 – Comparison of predicted and measured delamination shapes and internal crack lengths of specimens 9-1 and 9-2.

lengths was 1.4 mm longer than the measured final inner crack lengths of specimen 9-1 and 0.8 mm longer for specimen 9-2. The measured and predicted final delamination sizes are plotted together in Figure 7.5. For both specimens, the model-predicted delaminations are larger than the experimental results, especially so for specimen 9-2, explaining the overprediction of growth rates. The model does agree with the experimental observation that the delamination sizes are similar through the laminate thickness for both specimens.

The destructive inspection results of Laminates 11 and 12 (see Figure 6.20) showed that the asymmetric application of additional adhesive in the reinforcing layers affected the size of the delamination in those layers; however, both laminates had nearly identical crack growth curves (Figure 7.6). The simulation results also have nearly identical crack growth curves, and the predicted growth rates match the test results closely in the initial crack growth period and overestimate the growth rates with respect to the test results by approximately 2×10^{-4} mm/cycle as the cracks grow. In testing, specimen 12-1 grew at a rate 1×10^{-4} mm/cycle faster than specimen 11-1 when the outer sheet cracks were 25 mm and longer, while the simulation results predict that specimen 12-1 will grow approximately 1.5×10^{-4} to 2×10^{-4} mm/cycle faster than specimen 11-1.

The delamination test results and model results for specimens 11-1 and 12-1 are compared in Figure 7.7. When tested, specimen 11-1 had large delaminations in the inner, prepreg-metal interface, and small delaminations in the outer interface, where the additional adhesive was located. Further, the outer sheet crack lengths averaged 1.8 mm shorter than the inner crack lengths. The model results have the inner delaminations slightly larger than the outer de-

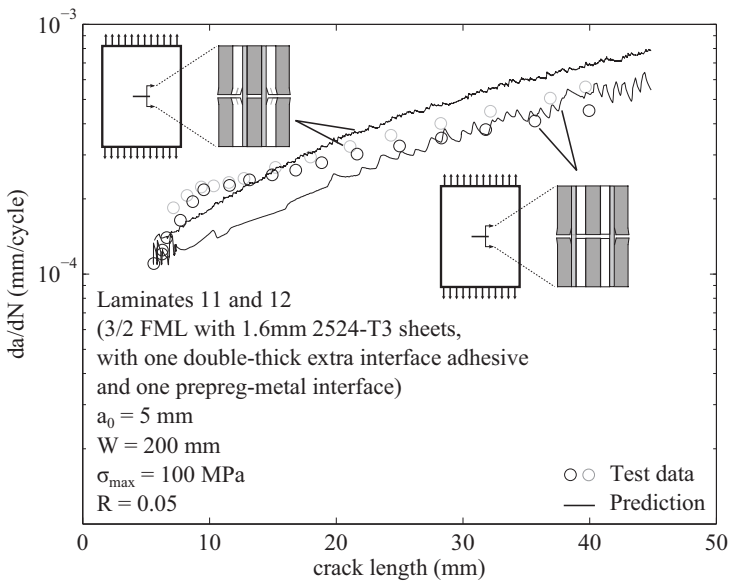


Figure 7.6 – Comparison of test results and model prediction for 3/2 laminates with asymmetric extra bondline adhesive

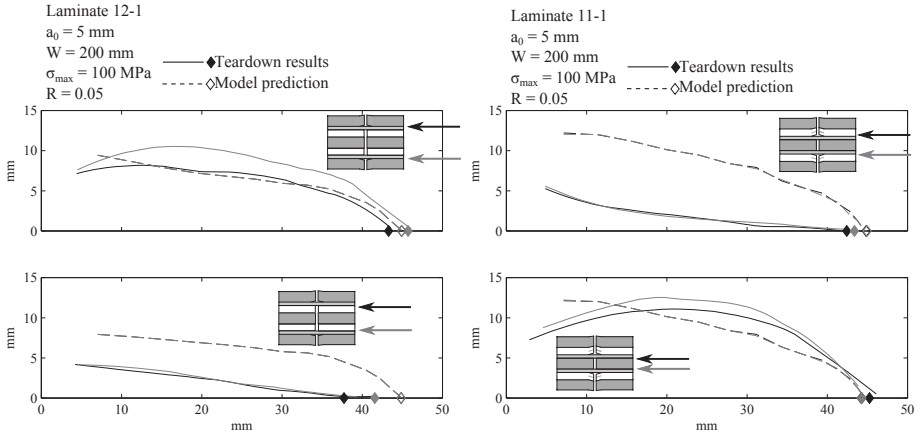


Figure 7.7 – Comparison of predicted and measured delamination shapes and internal crack lengths of specimens 12-1 and 11-1.

laminations, and the overall size of both is similar to the size of the inner delaminations from the test. The model predicts that the outer crack lengths are approximately 0.6 mm longer than the inner crack.

Specimen 12-1 had opposite delaminations after testing compared with specimen 11-1. The outer interfaces were the weaker prepreg-metal interface, and these had large delaminations, while the inner, adhesively strengthened interfaces had smaller delaminations. Likewise, the outer crack lengths were longer by an average 2.9 mm. The model predicted a much larger delamination in the outer interfaces than the inner interfaces; however, the final delamination prediction was much larger than the test result. The length of the internal crack was significantly underpredicted.

The model and test results of specimen 7-1, a 2/1 laminate with one 1.6 mm sheet and one 1.3 mm sheet, are shown in Figure 7.8. The growth rates of the thick and thin sheets are plotted together. The model and test results are in agreement about the qualitative behavior of the laminate, with both cracks growing at the same rate with respect to their lengths over most of the test, but with the crack in the thicker sheet growing faster for a period early on. This results in a final crack length difference of 4.3 mm in the test and 1.5 mm in the model simulation. The crack growth rates are underpredicted by the model, being 1×10^{-4} mm/cycle off over the entire range of crack lengths.

The delamination test and model results are shown in Figure 7.9. While

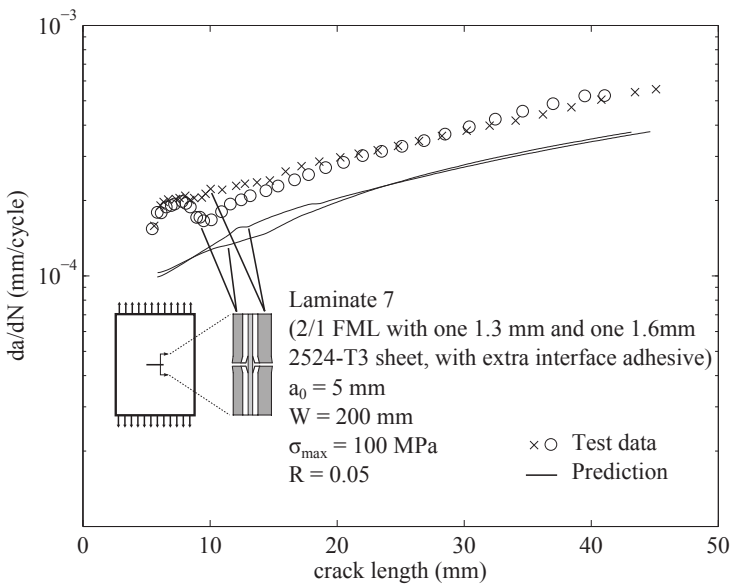


Figure 7.8 – Comparison of test results and model prediction for 2/1 laminate with non-uniform metal layer thickness

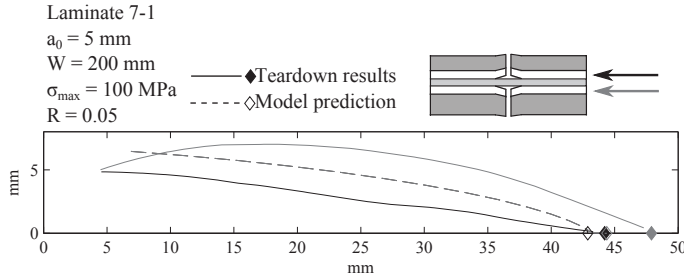


Figure 7.9 – Comparison of predicted and measured delamination shapes and internal crack lengths of specimen 7-1.

the delaminations in the tested specimen showed a difference, with the delamination larger in the interface with the thicker metal layer, the model did not predict a difference in the delamination sizes. The tendency of two or more delaminations through the thickness to remain identical sizes was observed in a number of results, which follow, and will be addressed in detail in Section 8.3 of the Discussion chapter. The model’s delaminations end up between the two delaminations from the test.

Specimen 8-1 was most dramatically characterized by the larger difference in the delamination sizes between the two interfaces. The delamination shape results of the model, meanwhile, failed to show any difference in delamination sizes, as shown in the comparison in Figure 7.10. The size predicted by the model is similar to that of the large delamination seen in the test. The crack growth rates predicted by the model are only slightly short of those seen in the test, as shown in Figure 7.11.

In Figure 7.12 test data and simulation results from three of the CentrAl laminates with 2524-T3 thick layers are plotted. Specimens 1-1, 1-2, and 1-7 were all tested at a stress ratio of $R = 0.05$, with maximum stresses of 100 MPa, 120 MPa, and 140 MPa, respectively. All three of the simulations match the test results in the early growth periods then overestimate the crack growth rates as the cracks grow longer. The degree of overestimation of growth rates increases with increasing stress. However, the model did correctly capture the effects of increasing stress in the initial 5 to 15 mm of growth. Not that, as with all of the comparisons with the test data, the initial increase over the first two or three data points is not considered. That test data results from a seven-point fit that includes crack lengths shorter than the initial crack length of the model.

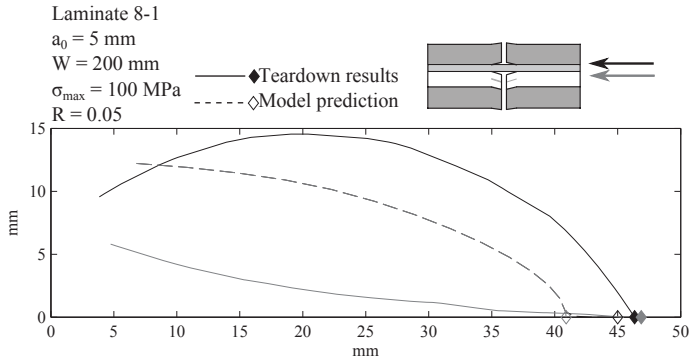


Figure 7.10 – Comparison of predicted and measured delamination shapes and internal crack lengths of specimen 8-1.

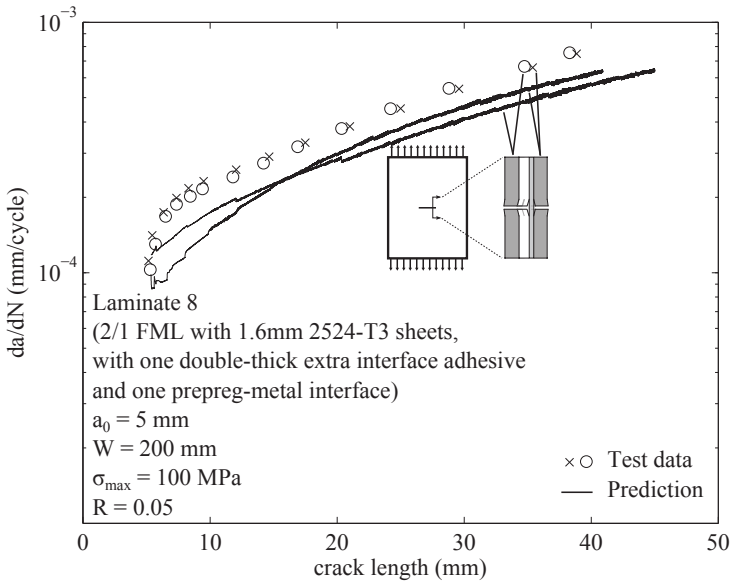


Figure 7.11 – Comparison of test results and model prediction for 2/1 laminate with asymmetric extra bondline adhesive

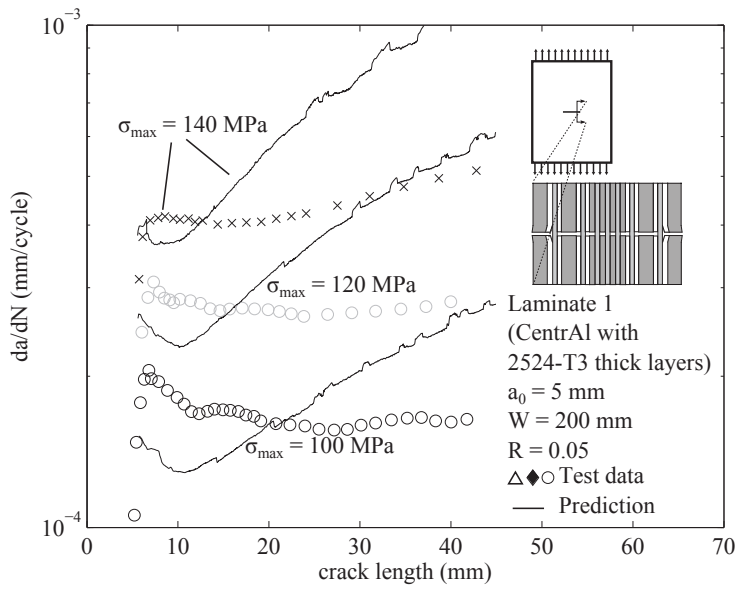


Figure 7.12 – Model predictions for Centra1 laminate 1 with different loading compared to test results

The reason for the model failing to capture the roughly constant growth rate over the length of the tests is illustrated in the comparison of delamination predictions for specimen 1-1 with the measured delamination shapes, shown in Figure 7.13. The model-predicted delamination is larger than all of the delaminations through the thickness in the tested specimen. The delaminations of all the interfaces through the thickness of the simulation grew together, rather than growing at their own individual rates, as is evident in the test results. With large delaminations, the simulated cracks in the internal metal layers grew as fast as the outer metal layer cracks. In turn, with less intact internal metal to act as bridging material, the cracks in the thick, outer sheets were less effectively bridged, and they grew at a faster rate, compared to the well bridged outer sheets in the tested laminate.

The model accounts for changing saw-cut length as well as it accounts for different applied loads. Figure 7.14 shows a comparison of test results and model predictions for laminate 1 with different starter notch sizes. The model is excellent at predicting the growth rates initially, but overpredicts the growth rates for longer crack lengths. This is consistent with overpredicting the growth of the internal delaminations and missing the beneficial bridging effects of smaller internal cracked aluminum layers.

In the CentrAl laminates with 2024-T3 metal sheets, similar trends were observed. Figure 7.15 shows the test and model results for crack growth rates at different stress levels, and Figure 7.16 compares the results for laminates with different stress ratios. The model captures the difference in test results due to changing stress and stress ratios, but the same errors as seen in Laminate 1 are present. The reason is the same. Figure 7.17 shows a comparison of predicted and measured final delamination shapes for specimen 0-6, and the internal delaminations stuck to the outer delaminations, growing too large.

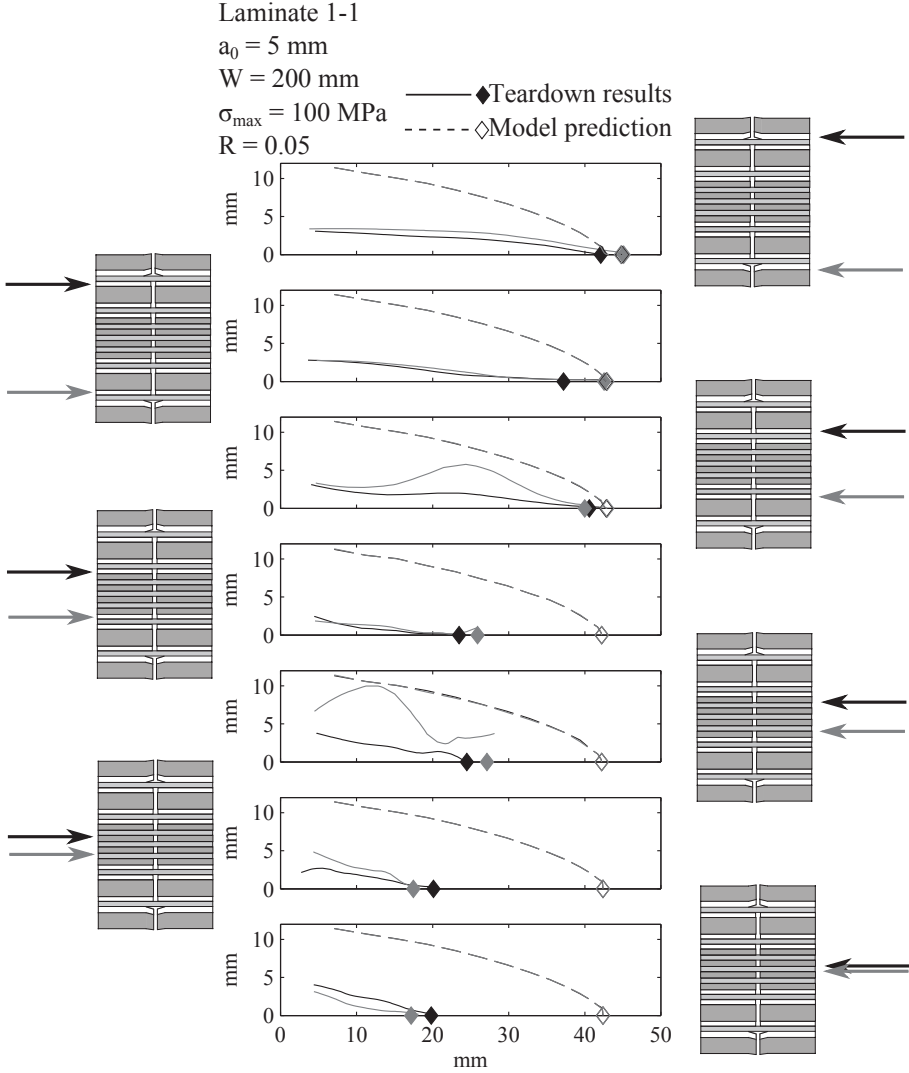


Figure 7.13 – Comparison of predicted and measured delamination shapes and internal crack lengths of specimen 1-1.

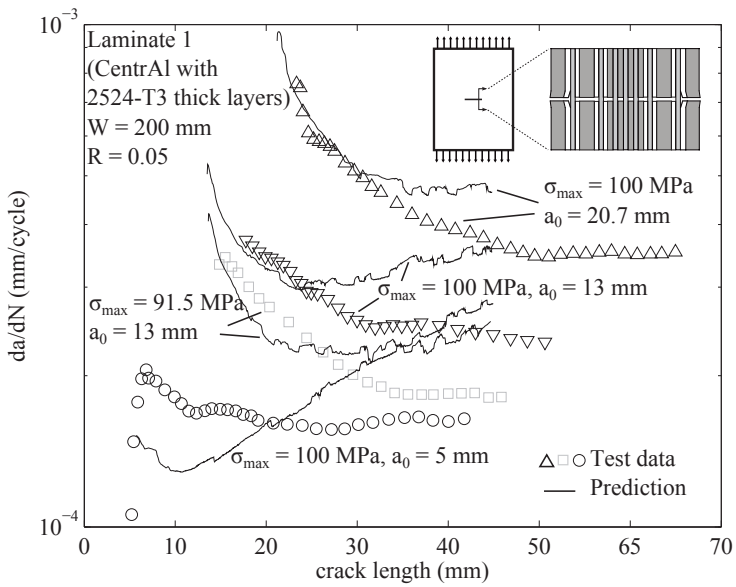


Figure 7.14 – Model predictions for Central laminate 1 with different notch lengths compared to test results

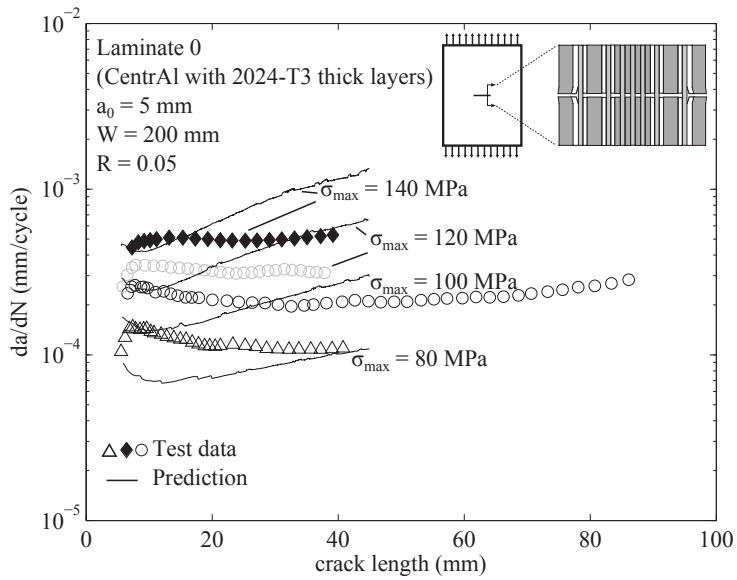


Figure 7.15 – Model predictions for Centra1 laminate 0 with different loading compared to test results

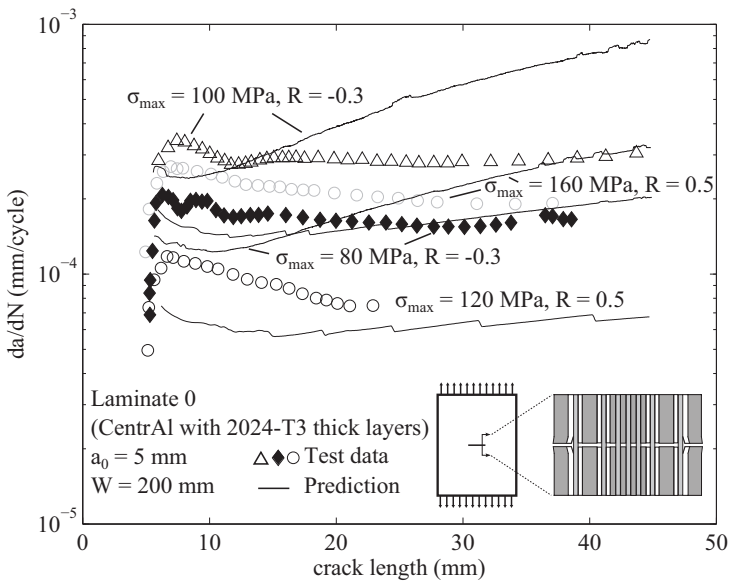


Figure 7.16 – Model predictions for Centra1 laminate 1 with different stress ratios compared to test results

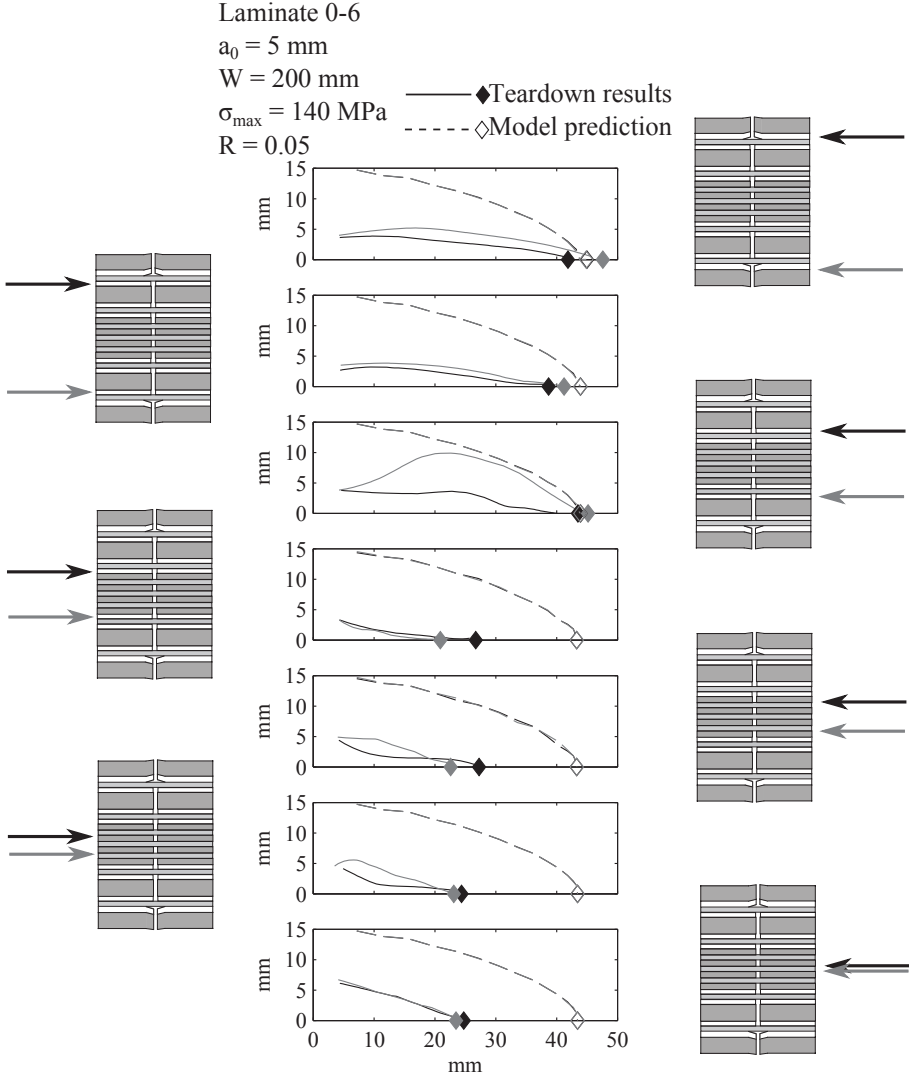


Figure 7.17 – Comparison of predicted and measured delamination shapes and internal crack lengths of specimen 0-6.

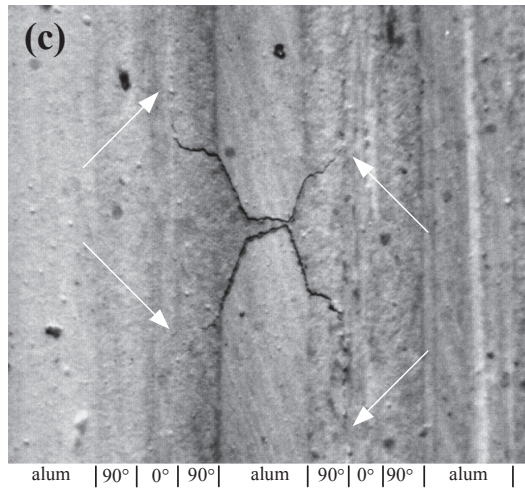


Figure 7.18 – Figure from [1] showing delamination growth between the 0° and 90° layers in Glare 4

7.3 Comparison to legacy data

7.3.1 Glare 3 and 4B data of Alderliesten

The Glare 3 and 4 tested by Alderliesten differs from the laminates tested in this study with the presence of glass fiber prepregs oriented at 90° with respect to the loading direction. It has been observed in delamination growth rate testing of cross-ply laminates that the 90° fiber layers crack along with the adjacent metal layers, and the delaminations propagate in the loading direction between the 90° and 90° layers, as in Figure 7.18. This behavior corresponds to the cracking and delamination behavior of additional adhesive in the prepreg-metal interface, observed in Appendix A. The 90° fiber layers were treated the same as additional adhesive layers in the model. Chiefly, this entailed using the modified adhesive shear deformation formulation of Equation (3.8) and keeping the 90° prepreg layers out of the bridging material array (discussed in Section 4.1.3). The properties used for the 90° prepreg layers are the same as the 0° layers with transposed x - and y -direction properties. The Poisson's ratio ν_{xy} is changed from 0.33 to 0.037.

All simulations of these Glare 3 and 4B laminates were performed with identical parameters to the tests, including saw-cut length, loading, and final

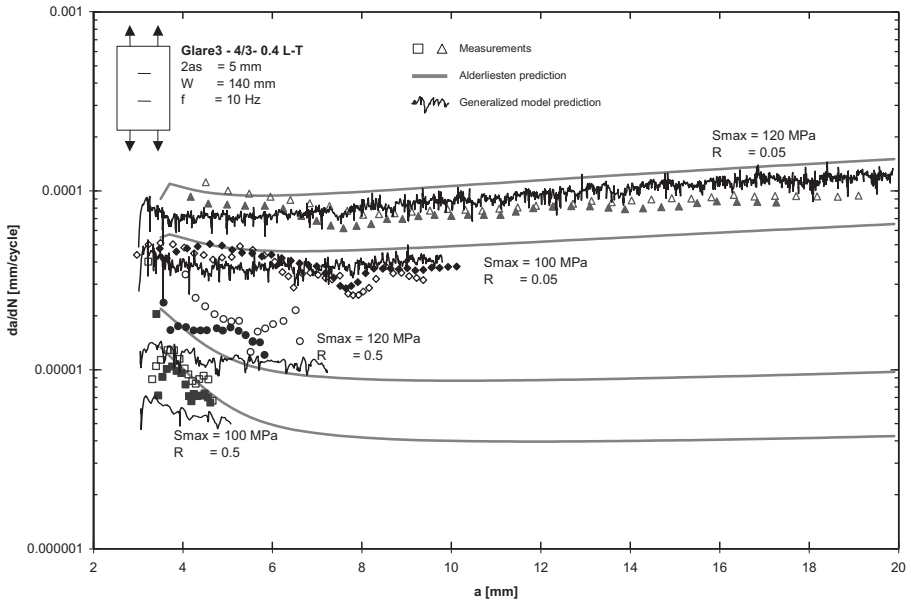


Figure 7.19 – Glare data from Alderliesten [1] with generalized model predictions

crack length. The simulation data were processed in the same manner as the data in Section 7.2. A more dense distribution of nodes was used, with $w_{max} = 0.025$ mm, since the convergence of the model Glare 3 requires denser bar elements.

Figure 7.19 shows the processed results of simulating Glare 3-4/3-0.4 with different loading conditions. These simulation results are overlaid on Alderliesten’s test and simulation results [1]. The generalized model of this paper predicts these test results as well as the Glare model of Alderliesten. The effects of different stress ratios and applied peak stresses are accurately captured.

Figure 7.20 shows the simulation and test results for a thicker laminate, Glare 3-4/3-0.4, with different starter notch sizes. The generalized model captures the behavior of the two laminates with larger notches well, but the model predicts the $a_0 = 1.5$ mm laminate’s growth rate increases faster over the length of the test than actually occurred. However, the initial growth rate predicted by the generalized model does match the test data.

Figure 7.21 compares the growth rates of two Glare 3-6/5 laminates with different metal sheet thicknesses, 0.4 mm and 0.5 mm. The 0.5 mm laminate’s

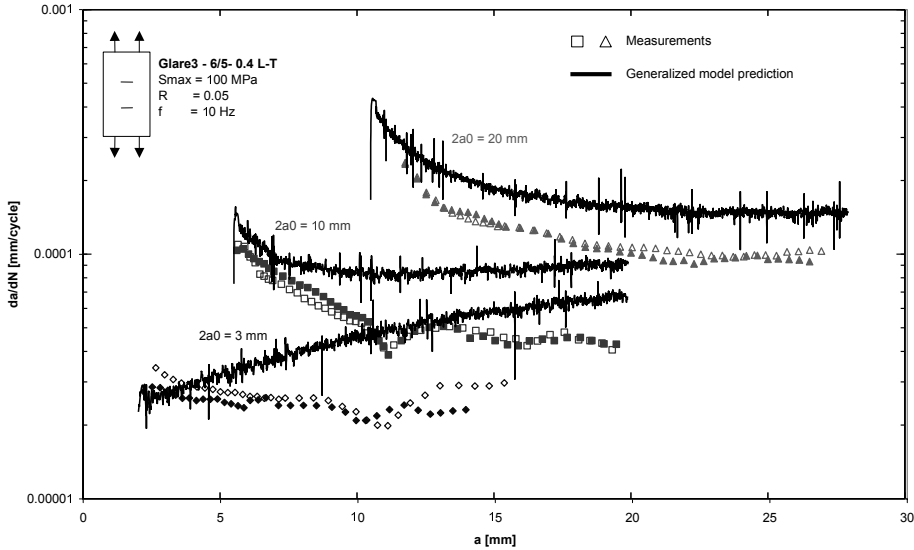


Figure 7.20 – Glare data from Alderliesten [1] with generalized model predictions

cracks grew similarly faster than the 0.4 mm laminate’s cracks in both the test and the model. However, the increasing growth rate over the length of the tests does not match the test data. This is the same error that occurred in the other short starter notch specimen in Figure 7.20. The initial crack growth rates are well predicted by the model, indicating that the error results from an over-prediction of delamination growth.

Figure 7.22 compares simulation results for Glare4B-4/3-.5 laminates with different maximum cyclic stresses and stress ratios to test results. The generalized model predicted higher crack growth rates than occurred in the tests, but the relative differences between each loading regime are captured by the model.

Figure 7.23 shows that the model overpredicts the growth rates of Glare 4B in the L-T and T-L orientations by a factor of 2, while accurately modeling Glare 3. A difference in the level of noise in the model is evident. The Glare 3 predictions have much more noise, which may result from the presence of metal sheets bounded by 90° fiber layers on one side and 0° on the other. The Glare 3 predictions of the data of Alderliesten are the only model results that show this noise, and they are the only ones with that sort of fiber layer configuration. The 90° plies were treated as bondpreg for the purposes of shear

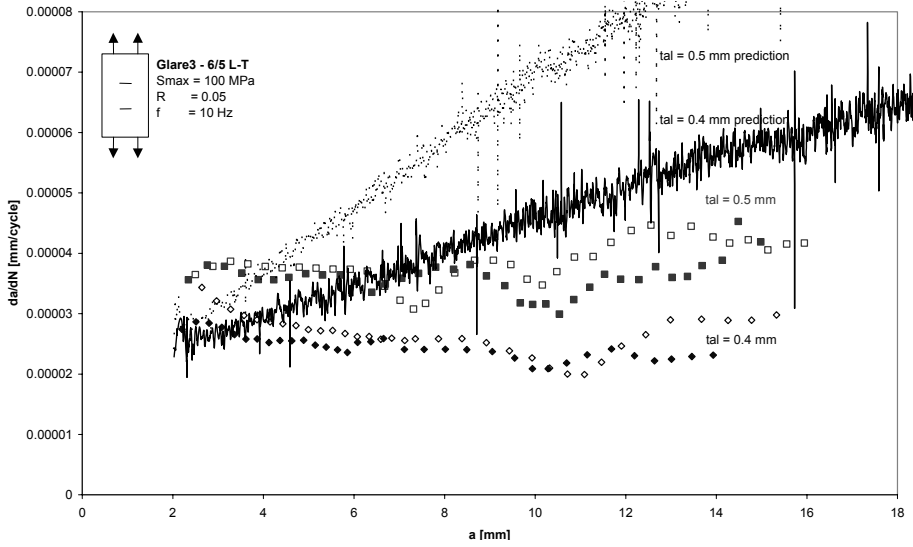


Figure 7.21 – Glare data from Alderliesten [1] with generalized model predictions

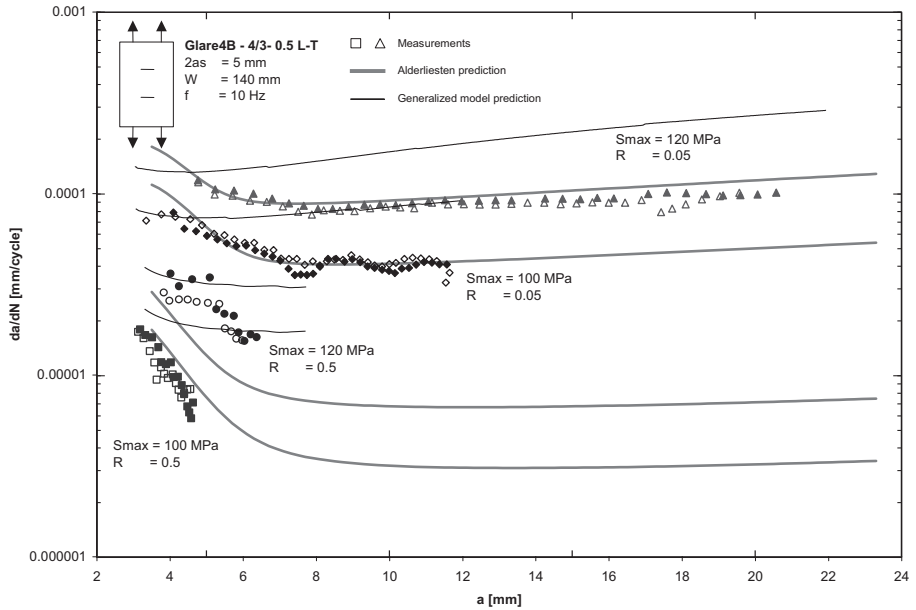


Figure 7.22 – Glare data from Alderliesten [1] with generalized model predictions

deformation and delamination location. The mismatch in ply configuration on either side of a metal layer may have exacerbated leapfrogging or errors due to the simplified SERR formulation, with no secondary bending, used in the model.

In Figure 7.24, test data and simulation results for Glare 3 laminates with different numbers of metal and fiber layers are compared. In this case, the modeled crack growth rates increase with the addition of layers, while the test results show a decrease in growth rates. The source of this error is likely related to the tendency of delaminations to grow together (discussed in Section 8.3) or additional delamination growth due to leapfrogging (discussed in Section 3.3.4). The increasing number of interfaces as more layers are added may increase the effect of either of these problems of the model.

7.3.2 Bending data of Randell

To model the tension-bending and four point bend tests of Randell, the bending moment was applied in the model as a line moment, M_x in classical laminate theory. The moment was set so that the ratio of the maximum strain in the outer layer to the strain in the neutral line of the laminate, both calculated with CLT, was equal to the bending ratio, k_b , listed by Randell for a given specimen. The applied moment in the four point bend specimen was set to achieve a strain in the outermost layer consistent with a stress of 200 MPa in the laminate ². The strain due to residual stress was first removed from these calculations, since the *in situ* measurements by Randell were necessarily zeroed with the residual stress already in place.

In the data of Randell, the initiation point of each layer through the thickness was recorded through visual inspection of the hole bore. For simplicity, the simulation in this work started all cracks together with initial lengths of 0.2 mm, in those layers where cracks were observed during the test. This may have the effect of increasing the crack growth rates of the outer layer cracks compared to what they would be with the additional bridging effects of intact inner layers for some number of cycles.

To remain consistent with the data presentation of Randell, crack lengths in the plots in this section are the distance from the edge of the hole to the

²Randell states that a strain gage was employed to achieve a stress of 200 MPa in the outer surface of the laminate, but does not make clear if that stress is calculated based on the Young's modulus of the aluminum outer sheet or the average Young's modulus of the laminate as a whole [2]. Based on the results of the simulation with the generalized model, the laminate stiffness was assumed but could not be confirmed.

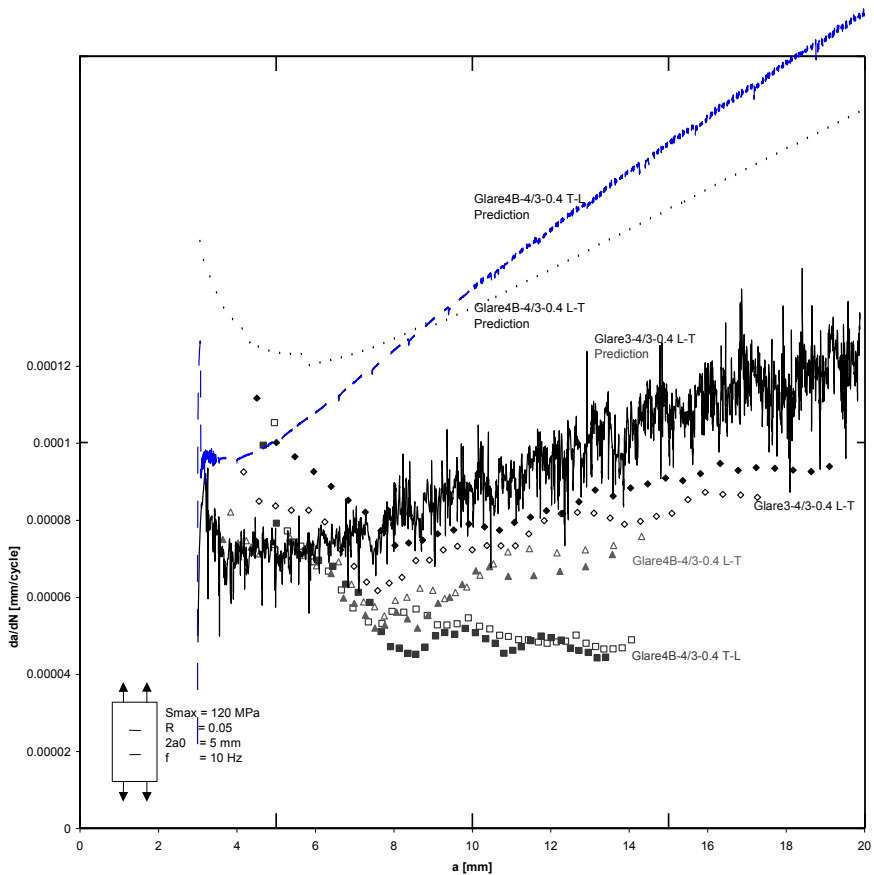


Figure 7.23 – Glare data from Alderliesten [1] with generalized model predictions

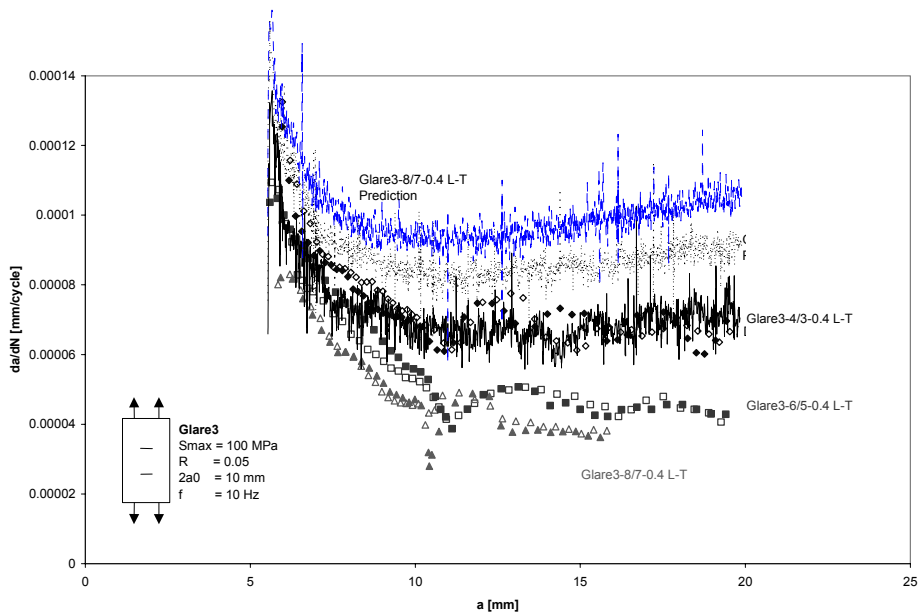


Figure 7.24 – Glare data from Alderliesten [1] with generalized model predictions

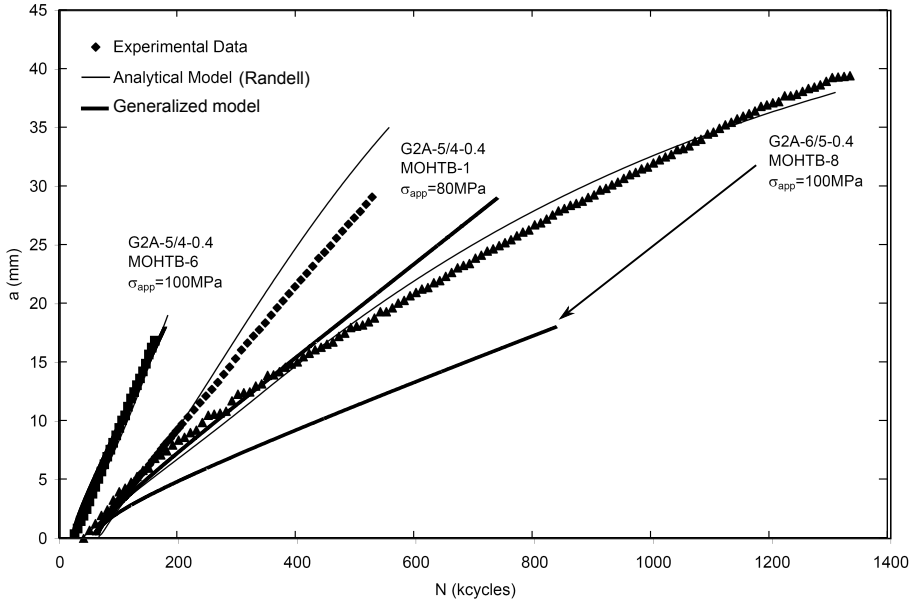


Figure 7.25 – Outer sheet crack growth data from MOHTB specimens of Randell [2] with generalized model predictions

crack tip.

Figure 7.25 compares the visually measured outer layer crack growth of three Glare 2 MOHTB specimens with the model-predicted outer layer crack growth. The model matches the test results of the Glare2-5/4-0.4 specimen with a tensile load of 100 MPa nearly exactly and underpredicts the crack growth rates of the other two specimens. Figures 7.26 through 7.28 include the post-test internal crack length measurements for these three specimens and the model-predicted internal crack growth curves. Figure 7.26 shows that the model underpredicts the final crack lengths of the two internal cracks; however, the difference in the final lengths of the two internal cracks predicted by the model, 0.46 mm, is closer to the approximately 1.5 mm difference in the experiment than the original model of Randell, approximately 5 mm.

In Figure 7.27, the underprediction of crack growth in the external layer is matched by underprediction of the crack growth rates of the internal cracks. In this case, the original prediction by the model of Randell more closely matches the experimental results. The underprediction of internal crack growth in the

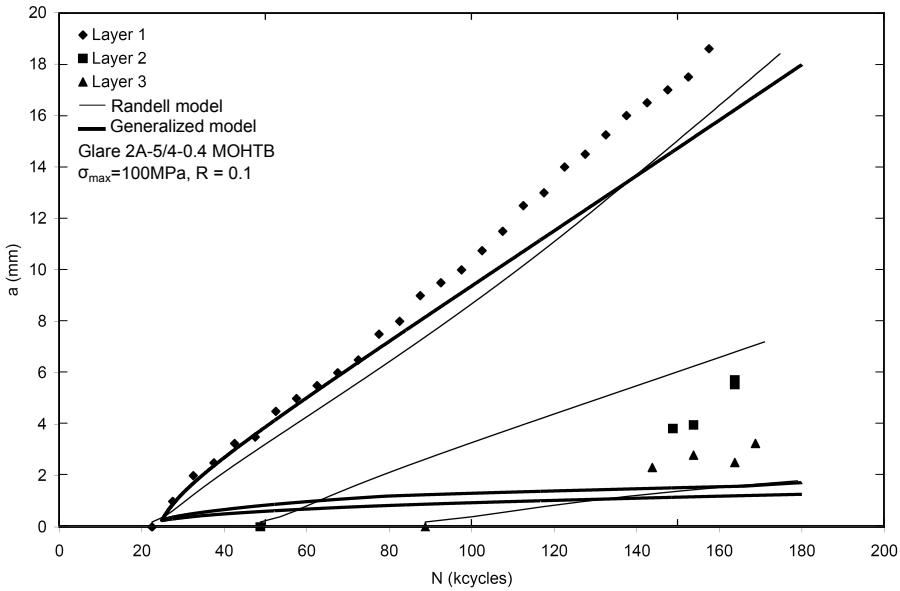


Figure 7.26 – Crack growth results from MOHTB specimen of Randell [2] with generalized model predictions for external and internal cracks

6/5 laminate of Figure 7.28 is even more pronounced. This may account in part for the observed underprediction of the growth rate of the outer layer crack, since the bridging of this crack would have been more effective in the model than in the test.

Figure 7.29 shows the external and internal crack growth results of the test and prediction for a Glare3-7/6-0.3 MOHTB specimen with a 100 MPa applied tensile stress. The generalized model slightly underpredicts the crack growth curve of the outermost layer, while more significantly underpredicting the growth of the internal cracks.

The crack growth of the four-point bend specimen’s outermost layer, shown in Figure 7.30, was twice as fast in the test as predicted by the model. Likewise, the internal crack lengths were also underpredicted by the generalized model.

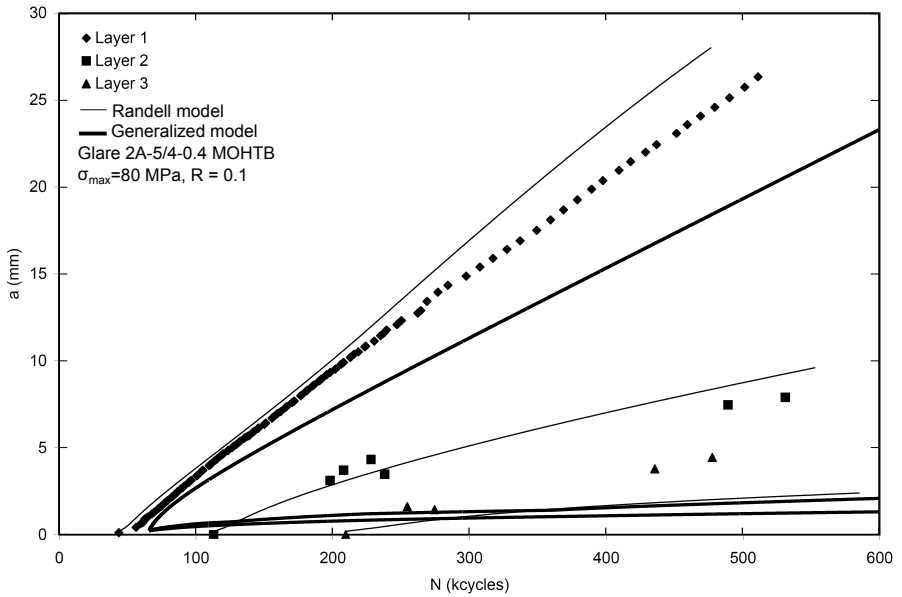


Figure 7.27 – Crack growth results from MOHTB specimen of Randell [2] with generalized model predictions for external and internal cracks

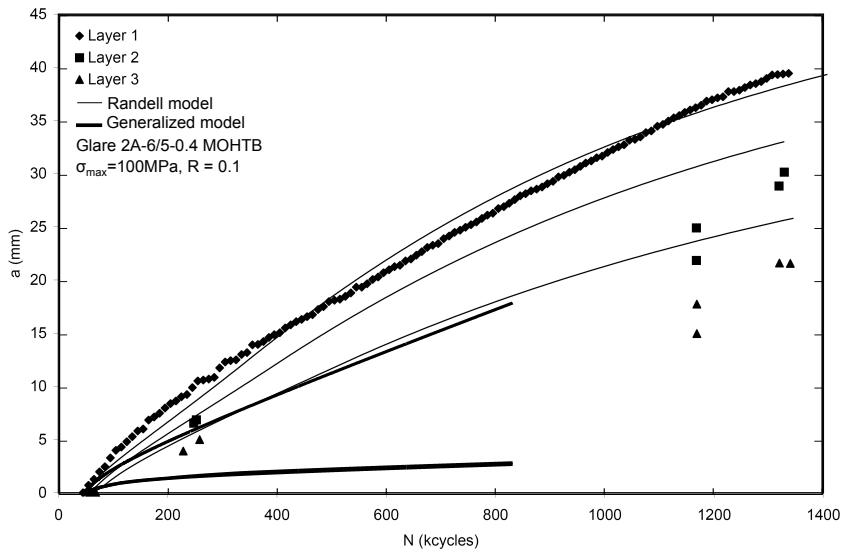


Figure 7.28 – Crack growth results from MOHTB specimen of Randell [2] with generalized model predictions for external and internal cracks

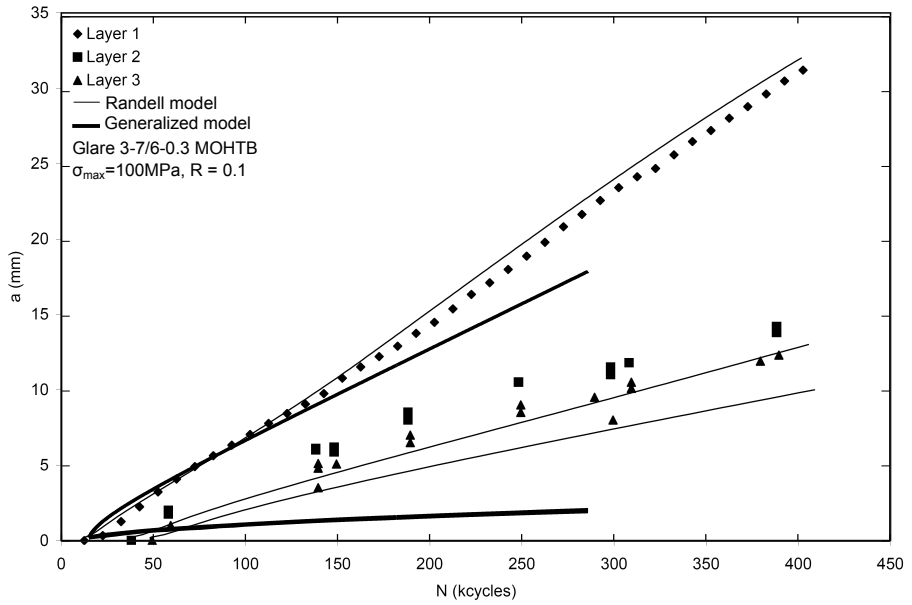


Figure 7.29 – Crack growth results from MOHTB specimen of Randell [2] with generalized model predictions for external and internal cracks

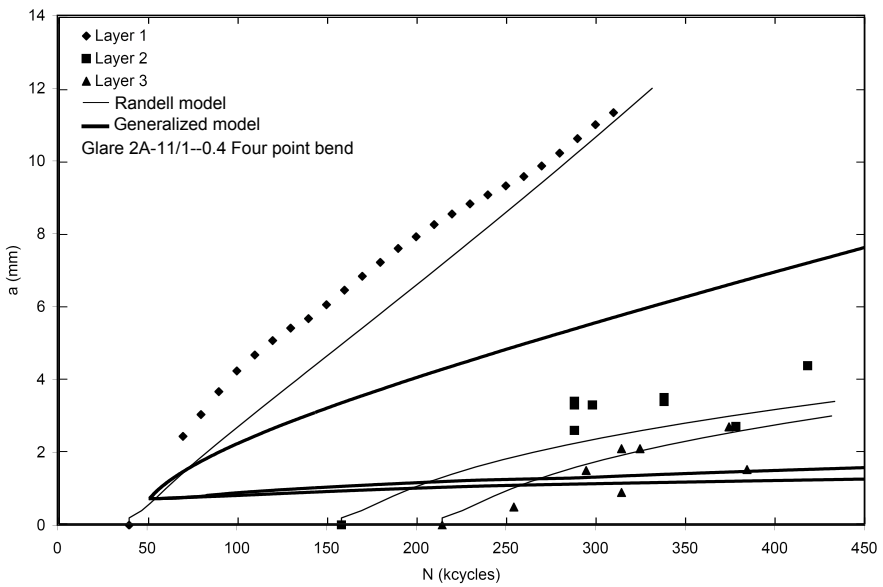


Figure 7.30 – Crack growth results from four-point bend specimen of Randell [2] with generalized model predictions for external and internal cracks

7.4 Alternate model assumptions

Two possible variations on the main generalized model were noted in Chapter 3.

First, the bridging stress calculation may be improved for laminates in which some bridging is provided by cracked metal layers with short cracks by incorporating the unique deformation of these layers, due to the stress concentration at their crack tips, into the bridging compliance. This metal bridging layer correction, referred to as δ_K , was described in detail in Chapter 4 (See Equation (4.31)). It was incorporated in the bridging stress calculation module of the model with iteration. First, a stress intensity factor of zero was assumed for each cracked metal layer. At the end of the bridging stress calculation, the calculated stress intensities were compared to the assumed value. When they differed by more than a small percentage, the calculated stress intensities became the assumed values in a subsequent iteration. Usually within two or three iterations, the values would converge. The final bridging load distribution from the iterations was used in subsequent parts of the model.

Some representative comparisons of crack growth predictions with and without this correction included are given in this section. Figure 7.31 shows such a comparison for specimen 1-1, a CentrAl laminate with 2524-T3 outer layers. While the test result was characterized by shorter cracks in the internal Glare layers leading to more effective bridging of the outer cracks, the generalized model did not capture this feature. Unfortunately, as shown in the comparison figure, neither does the model with the δ_K correction, whose results are plotted with dashed lines. This may result from the tendency of all of the delaminations through the thickness of the model to grow together, which occurs independently of the δ_K correction.

In Chapter 4, the cracked bridging layer correction was found to work best for a 3/2 laminate. Figure 7.32 shows a comparison of model predictions for a 3/2 laminate with and without the correction. The correction leads to a slight decrease in the crack growth rate. Considering that the standard model already accurately predicted the growth rate of this laminate (Figure 7.4), the addition of this correction does not seem to improve the performance of the model in any meaningful way.

The second assumption included in the model, as developed in Chapter 3, was that the SERR did not vary with delamination height, with no bending effects included in the SERR calculation. Chapter 5 developed a method of calculating SERR that incorporated the effects of asymmetry and bending with the neutral line model, NLM. For comparison to the standard generalized

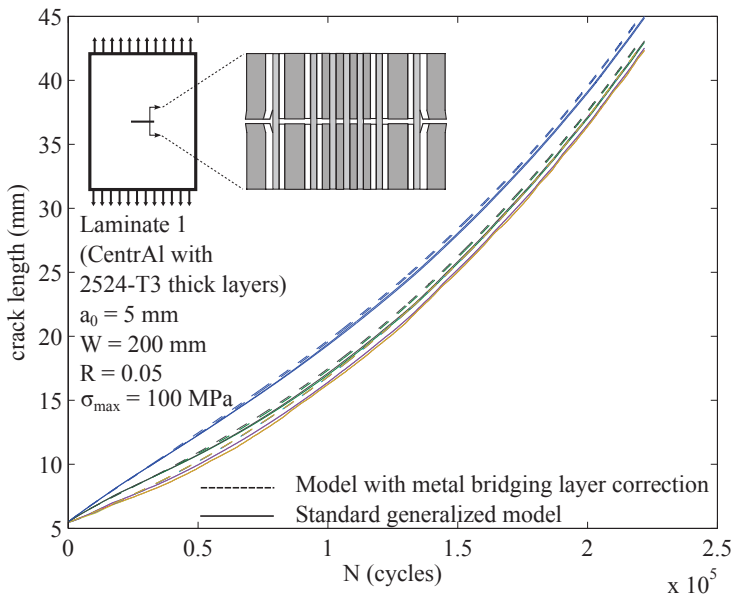


Figure 7.31 – Comparison of model predictions for a CentraI specimen with and without the δ_K cracked bridging layer correction.

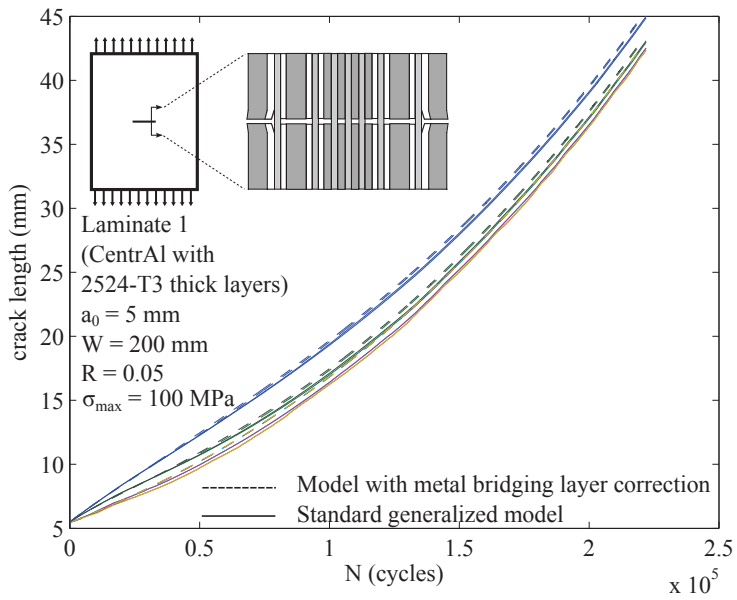


Figure 7.32 – Comparison of model predictions for Laminate 9 specimen with and without the δ_K cracked bridging layer correction.

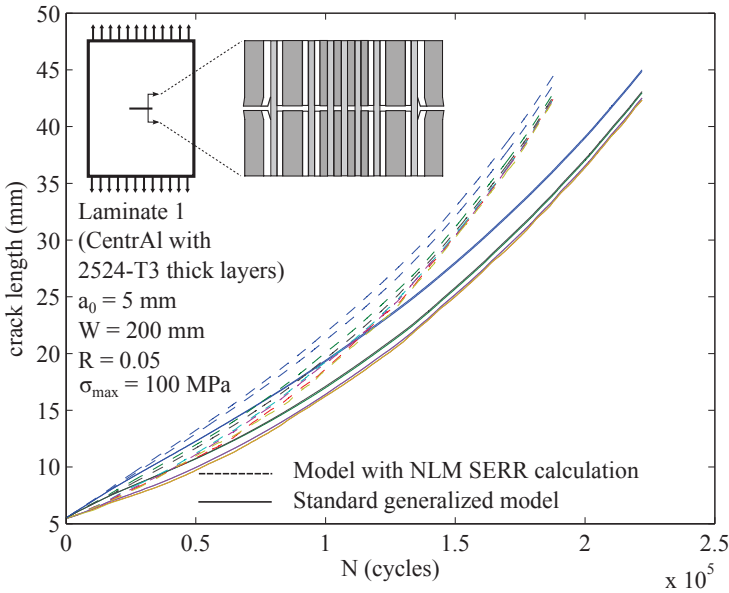


Figure 7.33 – Comparison of model predictions for a CentraI specimen with and without the full neutral line model strain energy release rate calculation.

model, several crack growth predictions with the NLM SERR calculation were performed.

Figure 7.33 shows a comparison of these NLM model results with the standard generalized model results for a CentraI laminate. The NLM model leads to a slight increase in the predicted crack growth rate of all the cracks, and does not capture the key quality of the test results for this specimen, significantly shorter cracks in the inner thin metal layers. Many other simulations with the NLM model similarly resulted in only slight differences from the original simulations. The computational cost of including the NLM calculation is high. The original simulation required 10,344 seconds of CPU time on a single CPU, while the simulation including the NLM model took 129,954 seconds, an order of magnitude longer.

One of the specimens for which the NLM approach could have been most appropriate was specimen 8-1, the results of which included drastically asymmetric delaminations on opposite sides of the single prepreg layer. The generalized model with standard assumptions successfully predicted the growth rates of this specimen, but did not predict any difference in the two delami-

nation shapes. In contrast, the model with NLM included did predict a large difference in the delaminations, as shown in Figure 7.34. The portion of the larger delamination in the region ahead of the short crack very closely matches the test result, but behind the short crack tip, this delamination is drastically over-predicted. The size of the smaller delamination is underpredicted. These differences with the test results suggest an overestimation of the out of plane bending, possibly due to the lack of constraint applied between adjacent bar elements. The crack growth curves resulting from this prediction are compared to those of the standard generalized model in Figure 7.35. The NLM model predicts a significant difference in the crack growth rates on opposite sides of the laminate, which did not occur in the test. The NLM in this case actually decreased the computational cost of this prediction, with a single CPU time of 1,946 seconds, compared to 19,800 seconds for the standard generalized model. By more accurately separating the delaminations, the NLM version of the model avoided the computationally costly effects of leapfrogging³ that occurred in the standard version of the model.

Another interesting difference with the generalized model occurred when including secondary bending for the predictions of the specimens of Randell (Section 7.3.2). A typical example is given in Figure 7.36. The NLM leads to an increase in the separation of the two inner crack lengths, which is more like the test results than the standard generalized model. However, the use of the NLM also leads to an underprediction of the crack growth in the outer metal layer, which the standard generalized model already matched well.

7.5 Summary

This chapter has presented a number of test results compared alongside predictions for those same tests made with the generalized FML crack growth model developed in previous chapters. In many cases the model accurately captures the behavior of the laminate, and in others, particularly those in which separation of the different interfaces is pronounced, the model misses the mark. These discrepancies, the limits of the models ability to predict crack growth results accurately, and the versatility of the model in its capability to model a

³See section 3.3.4 for an explanation of leapfrogging. It becomes computationally costly when the volatile SERRs associated with the constantly changing relative delamination heights in a given bar element lead to smaller intervals of cycle count for each iteration of the model as a means of limiting the delamination growth occurring in a given increment. This could be fixed in future development of the model by adjusting the interval after the correction for leapfrogging is made.

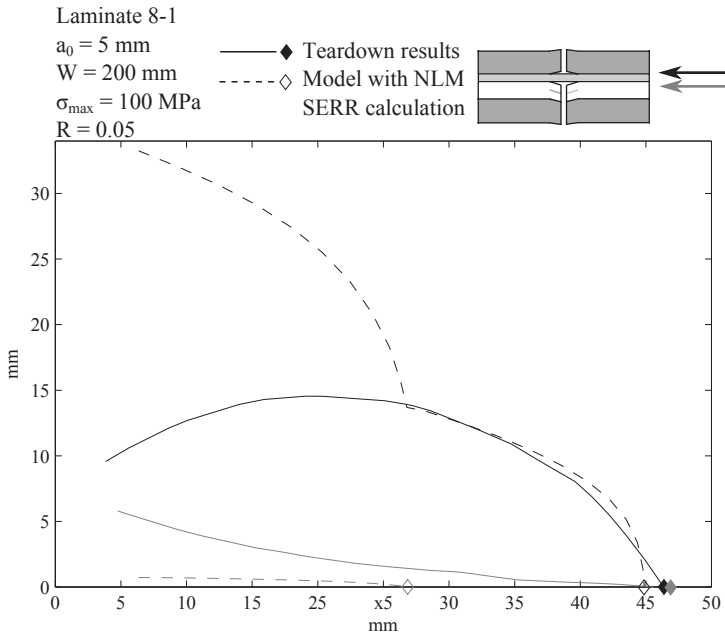


Figure 7.34 – Delamination predictions of the model including the full neutral line model strain energy release rate calculation compared to the final measured delamination shapes from the test.

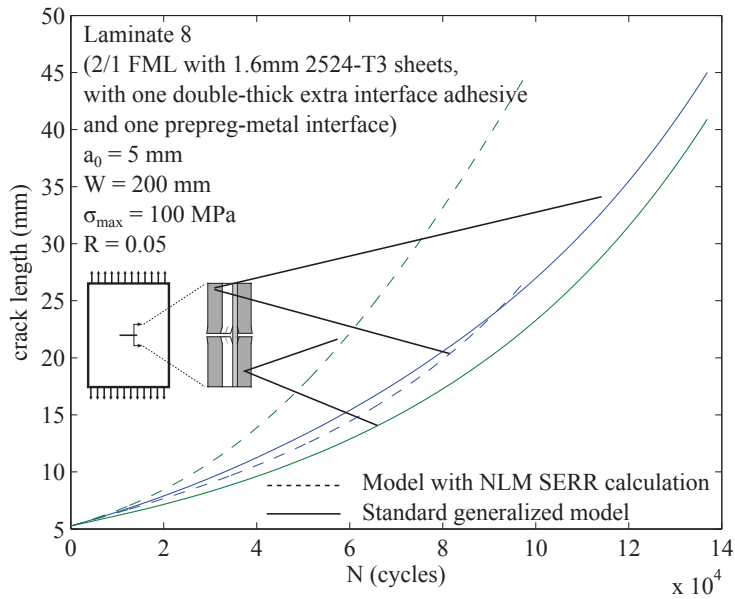


Figure 7.35 – Comparison of model predictions for a laminate 8 specimen with and without the full neutral line model strain energy release rate calculation.

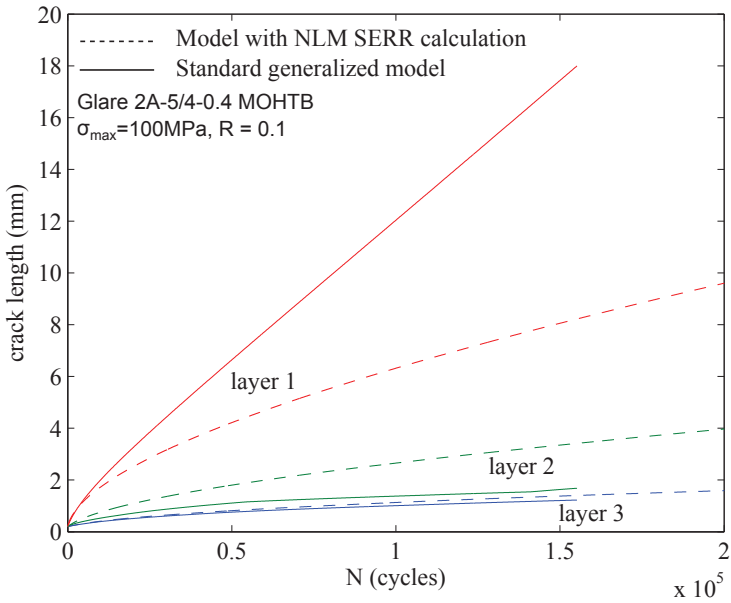


Figure 7.36 – Comparison of model predictions for a Glare 2 modified open hole bending specimen with and without the full neutral line model strain energy release rate calculation.

variety of different laminates in different loading conditions are all discussed in the following chapter.

Bibliography

- [1] Alderliesten, R. C. (2005) *Fatigue crack propagation and delamination growth in Glare*. Ph.D. thesis, Delft University of Technology, Delft, The Netherlands.
- [2] Randell, C. E. (2005) *Subsurface Fatigue Crack Growth in Glare Fibre Metal Laminates*. Ph.D. thesis, Delft University of Technology, Delft, The Netherlands.
- [3] ASTM Standard E647, 2008e1 (2008), Standard test method for measurement of fatigue crack growth rates. ASTM International.

Chapter 8

Discussion

8.1 Introduction

This chapter will assess the generalized model in light of the objectives of its development, explaining for each how it meets them or falls short. To add additional context to the model, several example applications and a discussion of the way forward for moving the model beyond constant amplitude crack growth of center-cracked flat panels are included.

8.2 Overview of the model

The model developed in this work was intended to address the following goals, repeated from Chapter 2:

Develop a crack growth model for fiber metal laminates that can account for the following:

- Arbitrary lay-up subject to arbitrary loading
- Independent crack lengths in each cracked layer
- Independent growth of delaminations at each interface

This model should predict crack and delamination growth as accurately as possible; be derived solely from first principles of

mechanics as much as possible; and take as input only material properties, laminate configuration and geometry, and loading conditions.

In Chapters 3-7, such a model was derived and described. In this section, the model itself will be reviewed in the context of how its characteristics meet the objectives above relating to the nature of the model. The subsequent section will address how the model fared in meeting the objective of accurately predicting crack and delamination growth.

The model is set up modularly. A unified laminate and damage definition is the basis for the model, and the components operate in a defined sequence. Once the laminate is defined, the stresses in the undamaged laminate are calculated. These stresses are passed to the bridging load calculation module, in which the load transfer occurring around the delaminations is determined. These bridging loads, along with the rest of the laminate definitions and stresses, are passed to the strain energy release rate (SERR) module, which calculates the driving parameters of delamination growth in the laminate. The laminate stresses, bridging loads, stress intensity factors, and SERRS are used by the damage growth module to extend the cracks and delaminations, and prepare the damage geometry for the subsequent iteration, which starts again with the bridging load module.

Each of these modules has a basis in well-understood principles of mechanics. Where new assumptions have been made to accommodate the specifics of the generalized FML problem or to facilitate computation, these assumptions have been noted in the preceding chapters.

The laminate stress calculation module is based on a standard implementation of Classical Laminate Theory [1], which in turn is an extension of plate theory. This module outputs the stress of each lamina, strain and curvature of the laminate, and the components of each of these due to residual thermal stress.

The bridging load calculation module depends on the mechanics principle of compatibility: the displacement of each layer must be equal at the delamination boundaries where they are in contact. The displacements calculated in satisfying the compatibility criterion are calculated with various mechanics approaches. The cracked metal layer displacement is determined with fracture mechanics. Westergaard stress functions that take into account the farfield and point loading of the metal layers and their damage geometry are used to calculate the displacement at any point of interest. The displacement of the bridging material was calculated with CLT, including a modification to account for the

effect of the delaminated and cracked layers on the stiffness of each bridging segment.

To ensure that its combination of methods resulted in accurate calculations of the bridging loads, the bridging load module was verified independent of the entire laminate crack growth model. This verification, discussed in detail in Section 4.2 of Chapter 4, consisted of direct comparisons between model-calculated bridging loads and finite element model-derived bridging loads for a number of test cases designed to include the novel aspects of this bridging load calculation, such as bending, asymmetrical damage, and asymmetrical layups.

Calculating SERR in its module relied on a standard definition of the energy release rate as the difference between the work done by an applied force and the change in strain energy when damage grows in a structure [2, 3]. The components of this calculation were determined with conventional mechanics approaches. The displacements and stresses were determined with the same modified CLT approach used in the bridging load module. This approach was augmented with a non-linear treatment of bending, the neutral line model, though as concluded in Section 3.3.2, the main model has been finalized without it. The neutral line model provided better results in the simple asymmetric delamination test cases in Chapter 7, but in the complete FML fatigue crack growth model, it provided no major improvement in the results, while contributing to the computational cost. Instead an assumption that ignores secondary bending, while still including stress due to applied bending moments, was used. Verification of the SERR calculations, independent of the complete laminate crack growth model, occurred through comparison to finite element model results, as described in Section 5.3.

The growth of cracks in the aluminum layers was calculated in the damage growth module with the well-established principle that cyclic crack growth rates are functions of the cyclic stress intensity factor [4]. While this concept is not a fundamental principle of mechanics, the relationship between stress intensity factors and crack growth rates is commonly treated as a material property. Likewise, the relationship between energy release rates and delamination growth rates, used by the damage growth module to calculate delamination extension, is treated as a property of a particular interface. This relationship is generally treated as an experimentally derived property (see for example [5, 6]).

The only concession in achieving a fully mechanics-derived model is in aspects necessary to make computation possible or efficient, including discretization of the laminate into nodes and incrementalization of the damage growth processes. As noted in Section 3.2.3, the nature of the bridging problem necessitates discretization of the bridging stress distribution. The displacement of a

cracked layer due to bridging stresses is found by integrating the effect of the bridging loads along the length of the delamination. Since these bridging loads are allowed to be an arbitrary and unknown distribution in the model, the compatibility relationship that forms the basis of the bridging load calculation cannot be solved without taking a step away from a purely analytical model and resorting to numerical methods.

The crack growth problem is a natural fit for an iterative calculation method, since damage accumulates cycle-by-cycle. However, performing all of the calculations of the model every cycle would be computationally expensive, requiring hundreds of thousands of iterations per simulation. Since the change in load redistribution and crack tip stress intensity is small from one cycle to the next, given the slow rates of cyclic damage growth of the specimens simulated in this work, negligible fidelity is lost by incrementing the simulation in steps of multiple cycles per iteration. Further, crack and delamination growth are stochastic processes highly dependent on local microstructural details. The degree of variation in damage growth from one cycle to the next renders cycle-by-cycle data meaningless for structural applications [7].

Given that discretization and incrementation of the model are not in-line with the goal of every component of the model being derived directly from first principles, and rather are approximations of the true behavior of the damaged FMLs, additional consideration is needed to ensure that the model accurately captures the behavior of the material. The principle of convergence is used to validate these components of the model. In Section 3.3.6 it was shown that given sufficiently small distances between nodes and small increments of crack and delamination extension, the results of the model converge to a stable value. Since the limit of decreasing the distances between bridging load nodes to zero is a continuous load distribution, and the limit of decreasing cycle increments is cycle-by-cycle incrementation¹, demonstrating stable convergence as these parameters are decreased is sufficient to demonstrate that the model's results converge to the solution that would be obtained with actual continuous delamination fronts and cycle-by-cycle incrementation. This is analogous to convergence in finite element simulations, in which the spatially discretized elements are decreased in size, and the time increments between steps of model analysis are

¹No lower bound on cycle step size per iteration was used in the model. Due to transient high strain energy release rate values occurring in the early stages of the simulation and occasionally throughout the simulation in the nodes nearest the crack tips and where delaminations interact through the thickness of the laminate, occasional sub-cycle increments are required when setting step size in accordance with per-iteration limits on crack and delamination growth.

decreased, until convergence is obtained².

The goal of using no input apart from material properties, laminate configuration, and loading conditions was met. Below is a sample section of code that initializes and runs a laminate simulation. The listed code includes all of the options and inputs that are necessary to establish the simulation of a particular laminate subject to a given set of loads and initial conditions. Only the `wmax0` does not fall into one of the three categories. It controls the increment interval and node density, allowing the user to find a balance between computational efficiency and convergence, as noted in the previous paragraph. None of the inputs could be described as fitting parameters or “fudge factors.”

```

%% Central with 2524 + Bondpreg, Smax = 100 MPa, R = -.3
clear all
starttime=cputime;
plotting = 0;
5 %Initialize run: laminate def, a0, s, stresses, etc.
global t E1 E2 nu12 G12 CTE1 CTE2 angles ismetal iscracked Cd nd
      Ccg ncg isBondpreg t1BP t2BP is2524 SkyV1 SkyV2 SkyV3

BP_t = 0.12;
props = [1.6 72400 72400 .33 26900 .000022 .000022 0 1 1 1.27E
10      -11 2.94 NaN NaN 0 NaN NaN 0 .55 .33 .12; %metal
        BP_t 5500 5500 .33 5550 .0000262 .0000262 0 0 0 NaN
          NaN 0.0005645 7.166 1 BP_t BP_t 0 NaN NaN NaN; %
          adhesive
        .26 48900 5500 .33 5550 .0000061 .0000262 0 0 0 NaN
          NaN 0.0005645 7.166 0 .12 .12 0 NaN NaN NaN; %fiber
          0
        BP_t 5500 5500 .33 5550 .0000262 .0000262 0 0 0 NaN
          NaN 0.0005645 7.166 1 BP_t BP_t 0 NaN NaN NaN; %
          adhesive
        1.6 72400 72400 .33 26900 .000022 .000022 0 1 1 1.27
          E-11 2.94 NaN NaN 0 NaN NaN 0 .55 .33 .12; %metal
15      BP_t 5500 5500 .33 5550 .0000262 .0000262 0 0 0 NaN NaN
          0.0005645 7.166 1 BP_t BP_t 0 NaN NaN NaN; %adhesive
        .26 48900 5500 .33 5550 .0000061 .0000262 0 0 0 NaN
          NaN 0.0005645 7.166 0 .12 .12 0 NaN NaN NaN; %fiber
          0

```

²More specifically, this is analogous to h -type finite element refinement. An analog to p type refinement, in which convergence is demonstrated by increasing the order of the element shape functions, can be created using this generalized model. Instead of discretizing the bridging load distributions and using nodes, approximate the bridging load distribution as a polynomial of order p with unknown coefficients. With such a function, the integral of metal layer displacement due to bridging may be solved implicitly, and the bridging problem solved by solving the compatibility equations for the coefficients of bridging (such a solution would likely require iterative methods due to the complexity of the terms of the equations). Convergence would be demonstrated by simulation with increasing order, p .

```

BP_t 5500 5500 .33 5550 .0000262 .0000262 0 0 0 NaN NaN
    0.0005645 7.166 1 BP_t BP_t 0 NaN NaN NaN; %adhesive

    .4 72400 72400 .33 26900 .000022 .000022 0 1 1 1.27E
      -11 2.94 NaN NaN 0 NaN NaN 0 .55 .33 .12; %metal
0.26 48900 5500 .33 5550 .0000061 .0000262 0 0 0 NaN
      NaN 0.05 7.5 0 NaN NaN 0 NaN NaN NaN; %fiber 0
20  .4 72400 72400 .33 26900 .000022 .000022 0 1 1 1.27E
      -11 2.94 NaN NaN 0 NaN NaN 0 .55 .33 .12; %metal
0.26 48900 5500 .33 5550 .0000061 .0000262 0 0 0 NaN
      NaN 0.05 7.5 0 NaN NaN 0 NaN NaN NaN; %fiber 0
    .4 72400 72400 .33 26900 .000022 .000022 0 1 1 1.27E
      -11 2.94 NaN NaN 0 NaN NaN 0 .55 .33 .12; %metal
0.26 48900 5500 .33 5550 .0000061 .0000262 0 0 0 NaN
      NaN 0.05 7.5 0 NaN NaN 0 NaN NaN NaN; %fiber 0
    .4 72400 72400 .33 26900 .000022 .000022 0 1 1 1.27E
      -11 2.94 NaN NaN 0 NaN NaN 0 .55 .33 .12; %metal

25 BP_t 5500 5500 .33 5550 .0000262 .0000262 0 0 0 NaN NaN
    0.0005645 7.166 1 BP_t BP_t 0 NaN NaN NaN; %adhesive
    .26 48900 5500 .33 5550 .0000061 .0000262 0 0 0 NaN
      NaN 0.0005645 7.166 0 .12 .12 0 NaN NaN NaN; %fiber
      0
BP_t 5500 5500 .33 5550 .0000262 .0000262 0 0 0 NaN NaN
    0.0005645 7.166 1 BP_t BP_t 0 NaN NaN NaN; %adhesive
    1.6 72400 72400 .33 26900 .000022 .000022 0 1 1 1.27
      E-11 2.94 NaN NaN 0 NaN NaN 0 .55 .33 .12; %metal
30 BP_t 5500 5500 .33 5550 .0000262 .0000262 0 0 0 NaN NaN
    0.0005645 7.166 1 BP_t BP_t 0 NaN NaN NaN; %adhesive
    .26 48900 5500 .33 5550 .0000061 .0000262 0 0 0 NaN
      NaN 0.0005645 7.166 0 .12 .12 0 NaN NaN NaN; %fiber
      0
BP_t 5500 5500 .33 5550 .0000262 .0000262 0 0 0 NaN NaN
    0.0005645 7.166 1 BP_t BP_t 0 NaN NaN NaN; %adhesive
    1.6 72400 72400 .33 26900 .000022 .000022 0 1 1 1.27E
      -11 2.94 NaN NaN 0 NaN NaN 0 .55 .33 .12]; %metal

35 t = props(:,1);
E1 = props(:,2);
E2 = props(:,3);
nu12 = props(:,4);
G12 = props(:,5);
40 CTE1 = props(:,6);
CTE2 = props(:,7);
angles = props(:,8);
ismetal = props(:,9);
iscracked = props(:,10);
45 Ccg = props(:,11);
ncg = props(:,12);
Cd = props(:,13);

```

```

nd = props(:,14);
isBondpreg = props(:,15);
50 t1BP = props(:,16);
t2BP = props(:,17);
is2524 = props(:,18);
SkyV1 = props(:,19);
SkyV2 = props(:,20);
55 SkyV3 = props(:,21);

s=5.025; % Initial half-saw cut length [mm]
]
W=200; % Coupon width [mm]
60 a=[s+.5;NaN;NaN;NaN;s+.5;NaN;NaN;NaN;s+.5;NaN;s+.5;NaN;s
+.5;NaN;NaN;NaN;s+.5;NaN;NaN;NaN;s+.5];% Initial crack lengths

a0=a;
wmax0 = .25; % Maximum width of 1-D delamination
zone at crack tip
65 wmax = wmax0;
b0=0.25*(a-s); % Initial delamination size scaling
factor

%----- Define Loading Parameters
-----
% Variable Description
70 Tcur=120; % zero-stress curing temperature [C]
T=20; % operating temperature [C]
Slam=[100,0,0,0,0,0]; % applied laminate stress [Sx,Sy,Sz,Mx,My,
Mz] [MPa,MPa*mm]
R=-.3; % applied R-ratio
theta=0; % laminate off-axis loading angle
75 %-----
-----

%----- Initial Conditions
-----
Ntotal=0; % Total cycle count
%numloops=1500; % number of calculation loops performed
80 a_limit = 45; % mm
%-----
-----

%name output file
datafilename = '7.dat';
85 avsnfilename = '7_avsN.dat';
%call code
single_block_analysis

```

```

endtime = cputime;
elapsed_cputime = endtime-starttime;
90 fprintf(fcg,'CPU runtime is %f seconds\n\n',elapsed_cputime)
closeDataFiles % calls script to close the output data files
avN = fopen(avNfilename, 'wt');
for ii = 1:length(Nrecord)
95 fprintf(avN,'%10.1f \t',Nrecord(ii));
fprintf(avN,'%g \t',arecord(ii,:));
fprintf(avN,'\n');
end
fclose(avN)
100 %close output file

```

Lines 9 through 33 list the laminae, in order from bottom to top, along with their thicknesses, orientations, and material properties. Other relevant information included in these lines is used by the model to determine how it treats each layer. For example, by declaring a given layer to be “BondPreg,” the model will use the shear deformation formulation derived for an additional adhesive layer when calculating the shear compliance of this layer’s interface, and the model will consider this layer to be delaminated along with the adjoining cracked metal layer in SERR calculations. This portion of the model initialization also informs the model which metal layers are cracked. The variable indicating that a given layer is metal is not currently used in the model, but serves as a placeholder for use in simulations that include plasticity, to which this variable will be relevant.

The damage is initialized on line 60 with a vector containing the initial crack length of each cracked layer, and NaN used as a placeholder in all non-cracked layers. Line 66 initializes the delamination heights at the notch tip as a function of the initial crack lengths. In principle, this could also be a vector, so that the delamination height at each interface could be initialized arbitrarily.

A small number of inputs in the above code example represent placeholders for further generalization. The terms dealing with ply orientation in the laminate definition section are used in the laminate stress calculation module of the model, but the effect of changing angles on the properties used in calculating the strain energy release rate or on the effective shear stiffness in the adhesive and prepreg shear compliance calculations have not been fully incorporated into the model. Likewise, the laminate off-axis angle, θ , and the other loading components, besides N_x and M_x , are not fully accounted for throughout the model.

8.3 Lessons of validation

The previous section discussed all but one of the requirements initially laid out, and how the model satisfies them. Remaining to be addressed is the goal that the “model should predict crack and delamination growth as accurately as possible.” The value of the model ultimately hinges on the question of how effectively the model meets this goal.

Unfortunately, there is no universally accepted objective standard for deciding whether or not a crack growth simulation successfully predicted the results of a particular test. One reason is that the need for accuracy is largely application-dependent. Factors such as component type, primary *vs.* secondary structure, acceptable margin on crack growth, and if the crack growth performance of a given component the constraining parameter of its design all play a role in deciding if a simulation is acceptably accurate. A second reason is the variability inherent in fatigue crack growth. When test results of crack growth rates can vary by factors of 50% or more (for example, see [8]), whether a prediction matches a given test result within 5% or 10% or 20% becomes less important.

For purposes of this discussion, prediction results referred to as “good” will be those in which the predicted crack growth rate falls within 50% of the test results for at least 75% of the crack length in a da/dN *vs.* crack length chart. Additionally, where teardown inspections occurred, the predicted delaminations and internal crack lengths must not qualitatively differ significantly from those observed in the tested specimens.

Overall, one factor tends to differentiate the successful predictions from those that poorly capture the test results. Those tests in which the non-uniform delamination shapes and sizes through the thickness affect the crack growth rates were poorly predicted by the generalized model. Those model predictions included delaminations that grew together through the thickness, in contrast to the test results. The SERR of smaller delaminations was high, and they grew until they caught up to the larger ones — the delaminations were sticky.

Those test results that were well predicted include those in which the delaminations did grow together, so that the delamination stickiness in the model did not lead to errors. Examples of such good results include the 2/1 and 3/2 thick FMLs, laminates 6 and 9, as defined in Tables 6.1 and 6.2 in Chapter 6. With two different loading regimes applied to each laminate, the crack growth and delamination predictions of the generalized model were in excellent agreement with the test and destructive delamination measurement results.

In the case of laminate 7, a 2/1 laminate with different thickness metal layers, the generalized model matched the tested crack growth rates within 1×10^{-4} mm/cycle. But, where the delaminations in the tested article were different through the thickness, with the delamination adjacent the thick layer being larger, the delaminations predicted by the model were stuck together, with a size that roughly averaged the delaminations measured after testing. Likewise, for laminate 8, with its asymmetric additional adhesive, the predicted crack growth rates very nearly matched those of the test, despite a drastic difference between the large and small delaminations in each interface of the tested laminate and the equal delaminations predicted by the model. The same is true of laminates 11 and 12, with similarly asymmetric additional adhesive. Though the delaminations in these laminates differ through the thickness, the effect on the crack growth rates is limited.

For the CentrAl laminates tested in this study, the difference in delamination size through the laminate thickness seemed to be a significant factor in their crack growth rates. As evidenced by the teardown inspection of two tested CentrAl specimens, the internal cracks and delaminations are much smaller than the cracks and delaminations in the outer portion of the laminate. This difference means that the thicker, outer layers are more effectively bridged, thanks to the contribution of the intact internal metal layers, slowing crack growth. The sticky delaminations of the generalized model's simulation, in contrast, remove this effect. The result is that for short crack lengths, before the through-thickness differences in crack and delamination size have fully developed, the generalized model predicts the crack growth rates of the outer sheets quite well. As the cracks lengthen, the model underestimates the bridging effectiveness of the CentrAl laminates and predicts increasing crack growth rates, whereas the tested specimens continued to grow at a slow, steady rate.

In comparing the model results to the Glare 3 and Glare 4 data of Alderliesten, similar observations can be made. The model predicts the crack growth rates of thinner Glare 3 laminates well, and for all of the laminate variations, effects of changing parameters like stress, starter notch length, and metal layer thickness are captured by the model. However, for the Glare 4 laminates and some of the Glare 3 laminates with more layers (such as 6/5), a clear divergence occurs. For short cracks, the predicted crack growth rates match the test data, but as crack lengths increase, the predicted rates increase much faster than the test results. This could be explained by the delamination stickiness problem of the model. These laminates may have shorter internal cracks and smaller delaminations, thanks to the increased number of layers of the 6/5 Glare 3 or the lower metal volume fractions of Glare4, which may reduce the influence of

a given crack on the growth of cracks and delaminations in other metal layers. Unfortunately, post-test measurements of delamination size and crack lengths from these tests are not available.

Comparisons of model predictions to the combined tension-bending results of Randell show that the generalized model predicts the crack growth rates of the outer-most layers accurately, but tends to underpredict the growth rates of the inner layer cracks. This is true for the several Glare 2 test results compared, as well as one with Glare 3, and one with Glare 2 subject to four-point bending. The assumption used in making these predictions — that all of the cracks begin at the same length, rather than initiating in sequence — may have contributed to the underpredicted crack growth rates of the internal cracks. The poorer bridging that would occur for a short crack in layer two when a long crack is present in the outer-most layer would result in faster crack growth. However, the final crack lengths should still have approached those measured in the test, and the predictions for these tended to fall short. The predicted delaminations of the internal cracks tended to grow together, indicating that the delamination stickiness of the model once again explains the discrepancy with the test results.

8.3.1 Lessons learned

Conclusion of the model validation is that the model accurately models crack growth in many arbitrary FML configurations, apart from those for which the crack growth results are significantly dependent on non-uniform delamination sizes through the thickness.

8.4 Limits of validity

Ordinarily, the scenarios to which a new model can be validly applied are determined based on that model's deviation from some existing standard solution or from well-vetted finite element results. In this case, no such standards exist, and the range of validity of the model can only be inferred through comparison to test data and observations about the model itself.

The predictions and tests made to validate the model were mostly carried out to maximum crack lengths of 45 mm. Since the test specimens were 200 mm wide, the good agreement of the predictions with crack growth rates from the tests represents a demonstration of validity to at least $2a/W \leq 45\%$. No attempt was made to correct for finite specimen width in the model. The test of specimen 0-1, in which the crack growth occurred at a nearly constant rate out

to $2a/W = 93.8\%$, shows that, compared to typical monolithic crack growth specimens, a finite width correction would be relatively small. If accuracy of the model for larger crack lengths than $2a/W \leq 45\%$ is required, a finite width correction could be derived by calculating the redistribution of the extra load not carried by an infinite sheet back into the finite laminate, following the method of Dixon [9].

The model tended to best match the crack growth rates of test data at smaller crack lengths, and errors tended to increase as cracks grew longer. For very short cracks, the effect of bridging is very limited due to the small displacement of the cracked layers. In the limit, the growth of small cracks out of a notch is dependent on the farfield stress and material properties only. Thus, errors in the bridging and delamination growth portions of the model would not manifest in data for short cracks. While this means there is no effective limit on how short a crack this model can simulate, it also means that, for predicting the growth of short cracks in FMLs, the model is not really necessary. There are practical limitations for simulating short cracks, however. Since there must be at least one bar element in the wake of a crack to perform a bridging calculation, and preferably more, a very fine distribution of bar elements is required at the start of the simulation. This can become cumbersome once the simulated cracks grow, but measures such as coarsening the bar element distribution through the course of the simulation can accommodate beginning with very short cracks.

Another issue for short cracks is that there is a strong dependence of the stress intensity factor on the notch or hole geometry. In the model as presented, the stress intensity factor and Westergaard stress functions for an infinitely thin and sharp notch were used. If high fidelity is required for very small crack sizes, these must be corrected to reflect the actual geometry of interest.

The maximum metal layer thickness evaluated was 1.6 mm, and the maximum laminate thickness was 10.78 mm. In principle, the validity of the model for high thickness laminae and laminates ends where the assumptions of classical laminate theory, such as plane stress and plate bending, hold. The thinnest metal layer considered was 0.3 mm. There is no theoretical reason that a minimum thickness for which the model is valid exists, but practical limitations on the production of aerospace alloys makes a 0.3 mm minimum thickness a practical limit on the usefulness of the model. No variation in fiber prepreg layer thickness has been considered for model validation. As thickness is increased, the shear deformation calculation may have to be adjusted due to its simplifying assumption of constant shear strain through half the thickness of a given layer.

The maximum number of laminae against which the model was validated

was fifteen; however, the issue of delamination stickiness through the thickness, as discussed previously in this chapter, led to the weakest match of crack growth predictions to test data. Once that aspect of the model is fixed, the accurate modeling of laminates with even more layers may be possible.

The loading parameters included in the model validation range from maximum stresses of 80 MPa to 160 MPa and stress ratios from -0.3 to 0.5. Such parameters are broadly representative of the range of loading that may be found in aircraft lower wing skins.

8.5 Practical uses

The greatest potential usefulness of the generalized model is not in matching test data that is already available, but in providing prescriptive input to the design of new laminates and in serving as a tool for structural designers to explore the vast design space opened by new concepts for arbitrary FMLs. This section presents two examples of the kind of insight that might be obtained with this model.

8.5.1 Considering the Glare 3 lay-up

The standard configuration of Glare 3, a cross-ply laminate with equal amounts of fibers in the 0° and 90° directions with respect to the metal layers, generally also includes ensuring that the 0° plies are biased toward the outside of the laminate [10]. This gives a slight advantage in the bending stiffness for moments in the 0° direction. The 0° fibers were also thought to improve the bridging of cracks in the outer layers, which are critical since they are only bridged on one side. No test data comparing the effects of switching this — biasing the 90° plies toward the outside layers of the laminate — on crack growth in Glare 3 is known by the author to exist.

The generalized crack growth model allows the distinction between the interface properties and shear behavior of the different ply orientations to be made, allowing the consequences of choosing a particular stacking sequence for Glare 3 to be considered. Table 8.1 lists six Glare 3 layups, the crack and delamination growth of which have been simulated with the generalized model.

Figure 8.1 shows the results of predicting all of these laminates. In each case, the use of 0° fibers as the outermost layers resulted in a 10%–30% decrease in crack growth rates, suggesting that the standard layup of Glare 3 is indeed the best choice from a perspective of fatigue crack growth.

Table 8.1 – *Layups of Glare 3 used to explore the effect of changing the prepreg stacking sequence*

Laminate	Layup (layer thickness in mm)
Glare3-3/2-0.4 0° out	2024-T3 (.4) / prepreg 0° (.13) / prepreg 90° (.13) / 2024-T3 (.4) / prepreg 90° (.26) / prepreg 0° (.13) / 2024-T3 (.4)
Glare3-3/2-0.4 90° out	2024-T3 (.4) / prepreg 90° (.13) / prepreg 0° (.13) / 2024-T3 (.4) / prepreg 0° (.26) / prepreg 90° (.13) / 2024-T3 (.4)
Glare3-4/3-0.4 0° out	2024-T3 (.4) / prepreg 0° (.13) / prepreg 90° (.13) / 2024-T3 (.4) / prepreg 0° (.13) / prepreg 90° (.13) / 2024-T3 (.4) / prepreg 90° (.26) / prepreg 0° (.13) / 2024-T3 (.4)
Glare3-4/3-0.4 90° out	2024-T3 (.4) / prepreg 90° (.13) / prepreg 0° (.13) / 2024-T3 (.4) / prepreg 90° (.13) / prepreg 0° (.13) / 2024-T3 (.4) / prepreg 0° (.26) / prepreg 90° (.13) / 2024-T3 (.4)
Glare3-5/4-0.4 0° out	2024-T3 (.4) / prepreg 0° (.13) / prepreg 90° (.13) / 2024-T3 (.4) / prepreg 0° (.13) / prepreg 90° (.13) / 2024-T3 (.4) / prepreg 90° (.26) / prepreg 0° (.13) / 2024-T3 (.4) / prepreg 90° (.26) / prepreg 0° (.13) / 2024-T3 (.4)
Glare3-5/4-0.4 90° out	2024-T3 (.4) / prepreg 90° (.13) / prepreg 0° (.13) / 2024-T3 (.4) / prepreg 90° (.13) / prepreg 0° (.13) / 2024-T3 (.4) / prepreg 0° (.26) / prepreg 90° (.13) / 2024-T3 (.4) / prepreg 0° (.26) / prepreg 90° (.13) / 2024-T3 (.4)

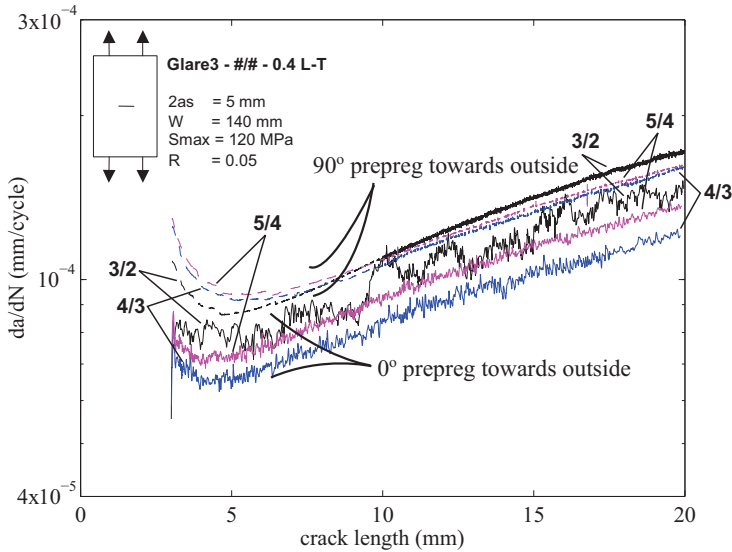


Figure 8.1 – Results of three different layups of Glare 3, comparing the opposite orientation of the glass fiber prepreg layers.

8.5.2 Directed crack growth subject to combined tension-bending

As noted in Section 2.2.1, an asymmetric laminate may be useful for improving the inspectability of aircraft structure. The damage scenario tested in [11], and discussed in Section 2.3, is an example of where such tailoring would be extremely useful. The lower wing skin of a large transport aircraft is expected to maintain its structural integrity with a severed stringer and cracked skin underneath that stringer. The stringer must be assumed to be cracked in such a scenario because the wing's stringers, located inside the wing, often in a region where fuel is stored, are difficult to inspect outside of major depot inspections. In a monolithic metal wing, a severed stringer leads to higher than normal loading in the skin near the damage, and a fatigue crack may develop in the skin. As it grows, it will become a complete through-thickness crack, inspectable from the underside of the wing. With an FML skin, the bridging layers may delay the growth of the crack through the thickness, and the secondary bending induced by the severed stringer may encourage significantly longer crack growth on the stringer side of the skin compared to that on the

exterior of the wing. With such a damage configuration, an exterior inspection of the wing skin may no longer be relied upon to ensure the continued integrity of the wing structure. It would be extremely desirable to design a laminate in which the exterior crack is assured to grow at the same rate as, or faster than, the crack on the stringer side of the skin.

The generalized FML crack growth model allows laminate configurations to be manipulated, and analyzed in combined tension-bending loading, in an attempt to achieve this valuable property. In this section, an example is presented in which a baseline CentraAl laminate in such an attempt. The applied loading will consist of a maximum cyclic load of $\sigma_{max} = 120$ MPa with a stress ratio of $R = -0.3$, as well as a moment of $M = 30$ MPa-mm with the same stress ratio.

The baseline laminate is Laminate 0 from Table 6.2, and its simulation results are shown in Figure 8.2. The crack in the “stringer side” of the laminate, which receives a tensile contribution from the bending moment, is predicted to grow around 4 mm ahead of the crack on the “skin side.” This means an outer skin-only inspection could underestimate the real size of damage in the laminate, or even miss it entirely.

Three strategies for altering the laminate will be evaluated for their ability to change the difference in crack lengths on opposite sides of the laminate. The goal is to ensure that, subject to the assumed loading, the crack in the outermost layer of the skin side of the laminate is longer than the stringer side crack or any internal damage. The laminate will be altered subject to the constraint that the overall thickness and metal volume fraction of the laminate are maintained. By leaving these parameters constant, the laminate stiffness and static strength will remain largely unchanged.

The first approach will be to increase the thickness of the thick metal layers on the skin side and decrease it on the stringer side. The thinner layers will be more effectively bridged, since the same bridging load results in a greater K_{br} the thinner the metal layer is. Likewise the thicker layers will be less effectively bridged, and their cracks will grow faster. The results of several different combinations of metal layer thickness are plotted in Figure 8.3 as the difference between the crack lengths on the stringer and skin sides of the laminate. The bigger the thickness difference, the more the difference in crack lengths is reduced, until the skin side actually becomes the longer crack. This strategy is successful. It is interesting to note that the laminate with bigger thicknesses also are predicted to sustain more load cycles before the maximum crack length of 45 mm is reached. The location of the end of each curve with respect to the horizontal axis of the figure gives this life.

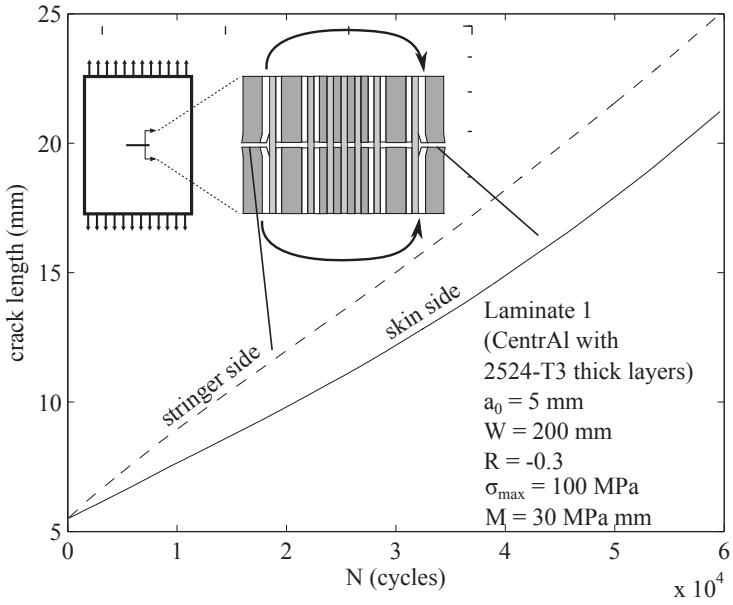


Figure 8.2 – Crack growth prediction for a CentAl laminate with applied tension and bending moment.

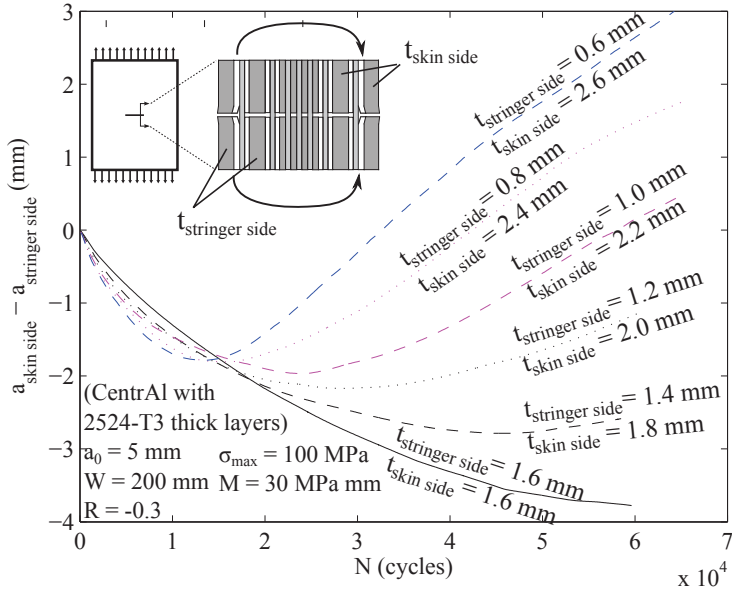


Figure 8.3 – Difference in crack lengths on opposite sides of a CentrAl laminate subject to combined tension-bending loading due to varying the metal layer thicknesses. Positive values are preferred for inspection purposes.

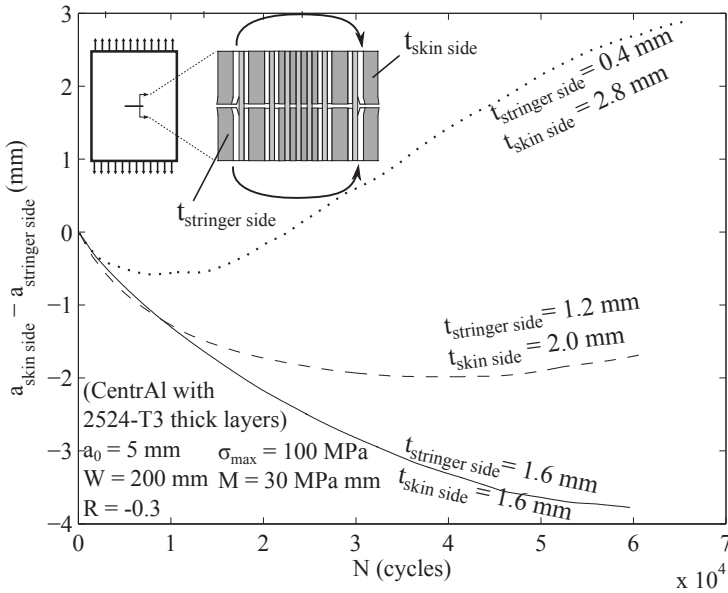


Figure 8.4 – Difference in crack lengths on opposite sides of a CentrAl laminate subject to combined tension-bending loading due to varying the outside metal layer thicknesses. Positive values are preferred for inspection purposes.

Perhaps it is necessary to only change the thickness of the outside layers, leaving the internal thick metal layers at their original thicknesses. The results of doing so are plotted in Figure 8.4, and the results show that this, too, is a successful strategy for ensuring that the skin side crack is the longest crack in the laminate.

Rather than changing thicknesses, a third option is to change the stacking sequence of the laminate. By moving the internal Glare reinforcement toward the stringer side of the laminate, the stringer side should be better reinforced. This also has the effect, as does the examples in which the thickness is changed, of changing the stress distribution through the laminate thickness. With the thick metal layers concentrated toward one side, the neutral line of the laminate shifts toward that side, and the layers toward the stiffer side carry more of the load. As can be seen in Figure 8.5, shifting the Glare one step toward the stringer side leads to a small improvement. The second shift leads to a drastic improvement, since the outermost layer of the stringer side is now 0.4 mm thick.

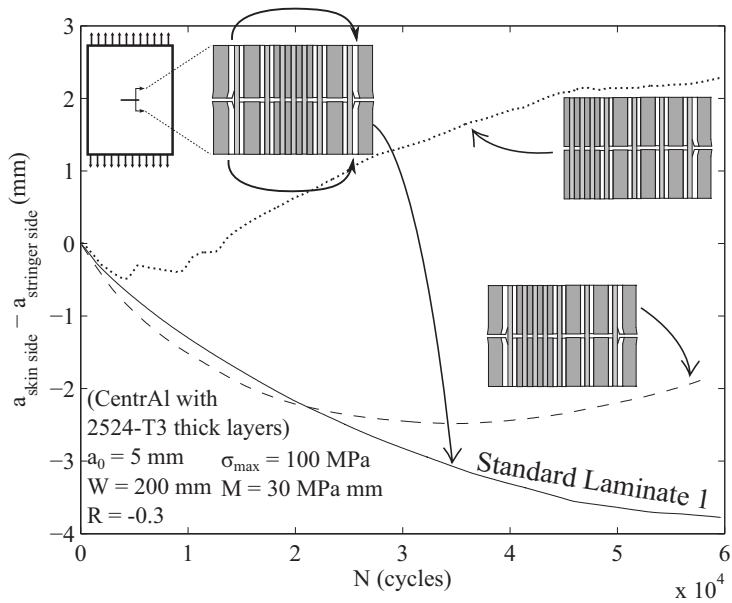


Figure 8.5 – Difference in crack lengths on opposite sides of a CentraAl laminate subject to combined tension-bending loading due to varying the outside metal layer thicknesses. Positive values are preferred for inspection purposes.

Some combination of these three difference approaches, along with potential variations in the metal alloys used, would allow for an even better solution to this problem and would be a very interesting subject for a constrained optimization of the layup.

8.6 Extensibility

8.6.1 Alternate geometries and structural configurations

The model presented in this thesis calculates crack and delamination growth for center-cracked rectangular specimen geometry. While few aeronautical structures correspond exactly to such a geometry, model results should be broadly applicable to portions of large sheets with shallow curvature, such as wing skins.

For structures in which more complex structural elements effect the damage tolerance properties, such as stiffeners, cutouts, and edges, alterations to the model will enable accurate predictions that take the structural realities into account. The modular approach taken to the development of this model assists in this task.

For alternate crack configurations, such as edge cracks, cracks growing out of or near holes, cracks in lugs, and multiple in-plane cracks, stress functions for the metal sheets are available in [12]. By substituting the geometry-appropriate stress functions in Equations (4.9) and (4.11), the correct relationship between the bridging loads applied to each layer and that layer's displacement can be used to determine the bridging loads through the compatibility constraint, Equation (4.26). Appropriate stress intensity factors are also available for a variety of configurations. If Westergaard stress functions are not available for a given configuration, alternative approaches to relating farfield and point loading to displacement will work just as well. Such alternatives include Green's functions or approximate numerical solutions based on finite element analysis results.

When stress concentrations are present, such as cracks growing out of holes, the increased elongation of bridging material in the vicinity may need to be considered, since it could reduce the bridging effectiveness. However, when the bridging material is unidirectional fibers, the low shear stiffness of the fibers limits the area in which effects of the stress concentration are felt. Further, the effects of the stress concentration due to the presence of a starter notch are ignored in this model and previous FML crack growth models, with negligible impact.

The presence of stringers, bonded doublers, or fasteners can be accounted for by displacement compatibility. The models of Poe [13, 14] are derived from applying displacement compatibility in the case of a cracked sheet with broken and intact fastened stringers. By treating the point load transferred at each fastener as an additional bridging force in the compatibility relationship of the model. The compatibility can then be applied at each rivet location. An extra term to account for stringer elongation would have to be included. Open questions in doing so involve the distribution of load from the rivet into the laminate. Is the load evenly distributed through the thickness of the laminate, or is the load distribution determined by the properties and thickness of each layer? How does one account for the portion of the loading transferred from the rivet to the fiber layers?

The same approach, adding additional points at which compatibility is to be maintained and solving for the additional load transferred at these locations, can be used with bonded stiffeners or straps, as well. Previous work by Rodi explored adding bonded straps to the Alderliesten model [15] in this way. The additional challenge to doing so for a generalized laminate is accounting for the distribution of load from the strap or doubler through the thickness of the laminate.

8.6.2 Variable amplitude fatigue crack growth

The model described in this thesis only concerned itself with constant-amplitude applied loads. Significant load-history effects are known to occur in metals when drastically different loads are applied from one cycle to the next [16, 17]. In short, high load excursions cause retardation in subsequent crack growth, and exceedingly low cyclic minima result in subsequently accelerated crack growth. Crack closure phenomena are generally cited as the cause of this behavior. Closure occurs as a result of crack tip plasticity, roughness, and corrosive build-up.

Numerous models exist to model the effects of closure on crack growth in metals. Khan has explored the integration of many available closure models in the Alderliesten Glare crack growth model [18]. Since the bridging effect of the fibers in FMLs reduces the stress intensity factor of the cracks in the metal layers, the size of the crack tip plastic zone resulting from high peak loads is reduced. The effect of load history on the crack growth rates of FMLs is thus muted compared to the effect seen in monolithic metals. Khan found that different retardation calculation methodologies work better for different

loading spectra, depending on the particularities of each given spectrum. In some cases, ignoring retardation altogether best matched experimental results.

The loading sequence can also affect the delamination behavior of FMLs. Peak loads can cause rapid delamination growth, especially around the crack tip, where bridging loads are highest. In subsequent cycles, this larger delamination makes the fibers less effective at bridging the crack. However, Khan showed that in the Glare laminate system, there is no retardation effect on the delamination growth rate with respect to the SERR of subsequent loading cycles [19, 20]. This means that a simple summation of cyclic crack growth increments is sufficient to model delamination growth in FMLs subject to variable amplitude loading, and the crack retardation effects are the only addition needed for the model.

The same retardation calculation schemes implemented by Khan for Glare, applied to all crack tips together in the Alderliesten model, can be applied to each crack tip independently in the generalized model of this thesis. Additionally complexity results from the potential for through-the thickness interaction of plasticity when cracks are different sizes. If the plastic zone size in a given metal layer is significant, it would cause additional stress in the adjacent fiber layers, reducing their bridging effectiveness. Also, the size of the plastic zone may be reduced by offloading stress to adjacent layers. In the extreme, a large plastic zone in a layer with a long crack may induce plasticity in other metal layers, with shorter cracks, affecting the rate of crack propagation through the yielded material.

In reality the impacts of these through-the-thickness effects could be negligible in terms of impact on crack growth rates. Experiments can shed light on whether more detailed through-the-thickness plasticity considerations are necessary. For instance, from an initial condition of one long and one short crack in a 2/1 laminate, the application of an overload would result in some plasticity ahead of the longer crack. Subsequent crack growth results would answer two questions: does the presence of the additional bridging metal limit the retardation of the longer crack growth, and does is the growth of the shorter crack retarded as it passes the longer crack's location from the time of the overload, indicating that the plastic deformation spread through the thickness?

8.6.3 Residual strength

Rodi has used the bridging and damage growth model of Alderliesten as a basis for calculating the residual strength of damaged Glare sheets [21]. The damage scenarios considered includes sharp notches through the entire thickness of the

laminate and fatigue cracks, and their attendant delaminations, having grown some distance from a notch or hole.

Whereas the Alderliesten model for Glare dealt with cyclic damage growth, the model of Rodi focuses on quasi-static damage growth when the laminate is subject to monotonically increasing loading. Cracks are extended according to a crack tip opening angle (CTOA) criterion [21]. Delaminations are extended according to a static delamination criterion based on the G_{IIC} of the interface. The CTOA can be readily calculated from the generalized FML crack growth model by using the expressions for cracked layer displacement in Equations (4.9) and (4.11) to calculate the opening at a defined distance behind the crack tip and determine the angle of opening. For delamination growth, an SERR calculation identical to that of the generalized model can be used.

Two new damage modes are introduced in the residual strength model of Rodi: fiber breakage and crack tip plasticity. Experimental observations found that as stable tearing of the cracked metal layers occurred, the fibers in the tearing regions broke as the cracks extended by them. Fibers in the pre-tearing wake of the crack, that served as bridging fibers during fatigue crack growth, tend to remain intact during some portion of the stable tearing. Modeling this phenomenon in a generalized FML will require several questions to be addressed. When static failure begins with cracks of unequal lengths throughout the laminate, which fibers ahead of extending crack tips will break? It may be that only those directly bonded to the extending crack will break along with it, the peak stress associated with the failure may extend through the thickness, or perhaps the reinforcement of adjacent intact metal layers relieves the stress on all of the fibers. How will this behavior change when initially equal cracks extend quasi-statically at different rates? Careful performance, observation, and post-test inspection of residual strength tests on FMLs with initially varied crack lengths, or with significant differences in properties and thicknesses of laminae can inform modeling assumptions about fiber behavior. Rodi has demonstrated the value of making careful observations *in situ* while increasing the applied load or displacement in small increments [21–23]. Tear-down inspections like those conducted in this study and described in Section 6.2.1, performed on specimens where some stable tearing crack extension, could be added to the testing regimen to allow a full understanding of fiber failure and crack extension in more complex laminates.

The residual strength model of Rodi accounts for crack tip plasticity with a strip yield model. The effective crack length is used as the crack length in Westergaard stress function calculations of cracked metal layer displacement, and closure is imposed with a distributed crack face loading in the plastic zone,

between the physical and effective crack tips. The same means of including plasticity could be employed in the generalized model. The only additional challenges would center on how plasticity affects the results when it is not uniform through the thickness. How does the plastic displacement of a short-cracked metal layer affect the bridging of longer cracks? And how is plasticity distributed to other layers in the thickness when crack lengths or material properties differ?

8.7 Summary

By evaluating the model, developed and validated over the course of several chapters, against the originally-stated goals of its development, this chapter has shown that the result is a model capable of adapting to any arbitrary fiber metal laminate and providing a reasonably accurate prediction of fatigue crack and delamination growth. The key weakness of the model, the problem of delamination stickiness, was discussed identified as an important area for improvement. Other notions of future improvement to the model were discussed, such as adaptations for new geometries, variable amplitude loading, and residual strength. Additionally, two examples of the model itself being used to find new insight into the design of FMLs were presented.

Bibliography

- [1] Gay, D. (2002) *Composite Materials: Design and Applications*. CRC Press.
- [2] Irwin, G. R. (1948) Fracture dynamics. *Fracturing of metals: a seminar on the fracturing of metals held during the Twenty-ninth National Metal Congress and Exposition, Chicago, October 18 to 24, 1947*, American Society for Metals.
- [3] Irwin, G. R. and Kies, J. A. (1954) Critical energy rate analysis of fracture strength of large welded structures. *Welding Journal*, **33**, 193s–198s.
- [4] Paris, P. C., Gomez, M. P., and Anderson, W. E. (1961) A rational analytic theory of fatigue. *Trend in Engineering (University of Washington)*, **13**, 9.
- [5] Alderliesten, R. C. (2009) Damage tolerance of bonded aircraft structures. *International Journal of Fatigue*, **31**, 1024–1030.

- [6] Rans, C., Alderliesten, R., and Benedictus, R. (2011) Misinterpreting the results: How similitude can improve our understanding of fatigue delamination growth. *Composites Science and Technology*, **71**, 230–238.
- [7] Strauss, B., Putatunda, S., on Fatigue, A. C. E.-, and on Fracture Testing, A. C. E.-. (1990) *Quantitative methods in fractography*. ASTM special technical publication 1085, ASTM.
- [8] Rosenberger, A. H. (2008) Variability in component life due to fatigue crack growth variability (preprint). Tech. Rep. AFRL-RX-WP-TP-2008-4311, AFRL.
- [9] Dixon, J. R. (1960) Stress distribution around a central crack in a plate loaded in tension: effect of finite width of plate. *Journal of the Royal Aeronautical Society*, **64**, 141–145.
- [10] Vlot, A. and Gunnink, J. (2001) *Fibre metal laminates: an introduction*. Kluwer Academic Publishers.
- [11] Heinimann, M., Kulak, M., Bucci, R., James, M., Wilson, G., Brockenbrough, J., Zonker, H., and Sklyut, H. (2007) Validation of advanced metallic hybrid concept with improved damage tolerance capabilities for next generation lower wing and fuselage applications. Lazzeri, L. and Salvetti, A. (eds.), *Proceedings of the 24th ICAF Symposium*, Naples, Italy, May.
- [12] Tada, H., Paris, P., and Irwin, G. (1973) *The Stress Analysis of Cracks Handbook*. Del Research Corporation, 1 edn.
- [13] Poe, C. C., Jr. (1971) Stress-intensity factor for a cracked sheet with riveted and uniformly spaced stringers. Tech. Rep. NASA TR R-358, NASA Langley research center.
- [14] Poe, C. C., Jr. (1973) The effect of broken stringers on the stress intensity factor for a uniformly stiffened sheet containing a crack. Tech. Rep. NASA-TM-X-71947, NASA Langley research center.
- [15] Rodi, R. (2007) *Analytical Modeling of Fiber Metal Laminate Stiffened by Bonded Straps: The effect of external stiffening elements on the fatigue crack growth in Fiber Metal Laminates*. Master's thesis, UNIVERSITA DEGLI STUDI DI PISA, Pisa, Italy.
- [16] Grandt, A. F., Jr. (2003) *Fundamentals of structural integrity: damage tolerant design and nondestructive evaluation*. Wiley-Interscience.

- [17] Schijve, J. (2009) *Fatigue of Structures and Materials*. Springer, 2 edn.
- [18] Khan, S., Alderliesten, R., Rans, C., and Benedictus, R. (2010) Application of a modified wheeler model to predict fatigue crack growth in fibre metal laminates under variable amplitude loading. *Engineering Fracture Mechanics*, **77**, 1400–1416.
- [19] Khan, S., Alderliesten, R., and Benedictus, R. (2009) Delamination growth in fibre metal laminates under variable amplitude loading. *Composites Science and Technology*, **69**, 2604–2615.
- [20] Khan, S., Alderliesten, R., and Benedictus, R. (2011) Delamination in fiber metal laminates (glare) during fatigue crack growth under variable amplitude loading. *International Journal of Fatigue*, **33**, 1292–1303.
- [21] Rodi, R., Alderliesten, R., and Benedictus, R. (2010) Experimental characterization of the crack-tip-opening angle in fibre metal laminates. *Engineering Fracture Mechanics*, **77**, 1012–1024.
- [22] Rodi, R., Wilson, G. S., Alderliesten, R. C., and Benedictus, R. (2009) The effect of bridging fibres on the entire strain field in fibre metal laminates. *17th ICCM International Conference on Composite Materials*, Edinburgh, UK.
- [23] Rodi, R., Alderliesten, R. C., and Benedictus, R. (2009) An experimental approach to investigate detailed failure mechanisms in fibre metal laminates. Bos, M. J. (ed.), *ICAF 2009, Bridging the Gap between Theory and Operational Practice: Proceedings of the 25th Symposium of the International Committee on Aeronautical Fatigue, 27-29 May 2009, Rotterdam, The Netherlands*, pp. 492–512.

This page intentionally left blank.

Chapter 9

Conclusions

This work set out to develop a generalized model for crack and delamination growth in arbitrary fiber metal laminates. The chapters of this thesis introduce the need for such a model (Chapter 2), describe the model's structure and components (Chapter 3), present the solution to the bridging stress problem of arbitrarily damaged FMLs (Chapter 4), derive a generalized method of calculating strain energy release rates (Chapter 5), describe the experimental work carried out in support of the model validation (Chapter 6), compare model predictions to experimental data (Chapter 7), and evaluate the model while providing context for its future development and use (Chapter 8). The following key conclusions are supported by the content of these chapters:

- A generalized crack growth model was developed that is derived entirely from first principles of mechanics or material properties, excepting assumptions relating to out-of-plane deformation in the context of strain energy release rates and certain accommodations made to account for the numerical aspects of the model.
- The model is organized in a modular way, so that each aspect of the calculation can be modified and improved separately.
- The two most computationally intensive modules of the model, the bridging load distribution and strain energy release rate calculations, were validated, independent of the entire model, by comparison to finite element simulations.

- The model subdivides the damage of the laminate into nodes, discrete locations along every single delamination front, for tracking the damage in the laminate and discrete calculation of the bridging loads and strain energy release rates.
- The model is stable with respect to initial conditions, and convergence with increasing bar element density was demonstrated.
- User input to the model consists only of material properties, laminate stacking sequence, initial damage configuration, and one parameter that determines bar element density — no “fudge factors.”
- The model is more generalized than any other existing analytical model.
- The model accurately predicts the crack and delamination growth of generalized FMLs in most cases.
- The cases in which the model poorly predicts damage growth are those in which growth of delaminations through the thickness to drastically different sizes strongly influences crack growth. The delamination stickiness in the model is the main aspect of the model in need of improvement.
- The modularity of the model makes it extensible to problems of varying geometry, variable amplitude crack growth, and residual strength.
- The effective use of the model for guiding design choices has been demonstrated.

Appendix A

Effect of adhesive layer thickness on Fiber Metal Laminate delamination growth rate

This appendix is a reproduction of [1].

A.1 Introduction

Fiber metal laminates (FMLs) consist of alternating layers of metals and fiber-reinforced composites. One variant, Glare, a combination of thin aluminum sheets and fiberglass-epoxy composite, is currently in use as a fuselage skin material on the Airbus A380 [2-4]. The properties of the adhesive bonds between the metal and fiber layers of FMLs are critical to these materials' structural performance. The bonds must be strong enough to withstand shear and peel loads under static conditions and they must be durable enough to maintain their integrity over the life of the FML structure. Their durability is particularly important when the metal layers develop fatigue cracks. The bonded fiber layers are much more resistant to fatigue and some of the load of the cracked metal layers is redistributed into the intact fibers. This redistribution occurs

in the form of high shear load transfer over the adhesively bonded interface between the layers. This high load transfer leads to the growth of delaminations in the interfaces. Various models of fatigue crack growth in FMLs consider the effects of delamination size on the bridging loads transferred from metal to fiber layers, and incrementally grow the delaminations based on the strain energy release rate (SERR) associated with the amount of load transferred [5–9]. A larger delamination leads to lower bridging load transfer, which in turn causes the cracks in the metal layers to grow faster. It is therefore desirable to have a durable bond in which delaminations grow slowly.

Recent developments in FMLs include laminate concepts that rely on thicker metal layers to increase stiffness in tension and shear and decrease the number of layers required in a laminate, thereby aiming to reduce manufacturing costs for thicker laminates [10–12]. Initial crack growth tests on such laminates, with the thick layers bonded to internal Glare reinforcement directly with pure adhesive, resulted in no delamination in the adhesive-only bonds and unacceptably large delaminations in the first fiber-metal interface of the internal Glare. The addition of two fiber prepreg layers to the interface between thick and thin metals, along with the layer of adhesive film, allowed this interface to delaminate and improved the crack growth performance of the entire laminate. This resulted from a reduction in the delamination size at the first Glare metal-fiber interface, and the improved bridging stiffness thanks to the additional fibers. Further investigation of the concept of combining fiber prepreg and adhesive film layers, sometimes referred to as Bondpreg, was carried out, showing that laminates with thicker metal sheets and additional adhesive had better crack growth performance than those same laminates with fibers but not the added adhesive layers [10]. This investigation also showed that so-called symmetric Bondpreg, having two thinner layers of adhesive on either side of the fiber prepreg, each with half the thickness of the adhesive film in the non-symmetric, single-sided Bondpreg, provided an improvement in crack growth performance over the single-sided Bondpreg concept.

Similar concepts have been used in other composite materials to toughen interfaces where delamination occurs. Interleaving adhesive plies between the prepreg layers of carbon fiber reinforced composites has been shown to significantly increase the load at which free edge delamination occurs [13] and decrease the growth rate of such delaminations in test specimens subject to cyclic loading [14]. Interleaving adhesive plies also reduces the amount of delamination damage that occurs at a given impact energy [15, 16]; however, as the ply interfaces were toughened, the impact energy was dissipated through other failure modes, such as through-thickness cracking. Sela *et al.* [17] studied

the effect of varying the thickness of the interleaved adhesive and found that the Mode I and Mode II fracture toughness of interfaces with additional adhesive increased with increasing adhesive layer thickness. However, the Mode II fracture toughness did decrease when the adhesive thickness increased from 0.68 mm to 1.1 mm.

Other proposed methods of improving interface toughness in interfaces between polymer composites and metal include increasing the surface roughness of the metal [18] and increasing the flexibility of the adhesive in a lap-shear joint between aluminum and a polymer composite [19]. While the surface treatment of the aluminum layers in Glare, chromic acid anodizing followed by application of a primer, was optimized for laminate fatigue crack growth performance [3], it is possible that a different surface treatment could yield improved properties in an interface with additional adhesive. Likewise, using an adhesive with a different stiffness than the Cytec-produced FM94 used in Glare and Bondpreg, provides further space for improving the interface.

Though the extra adhesive layer of the Bondpreg concept leads to significant improvement in crack growth performance of FMLs, it degrades many static properties. The adhesive has such a low stiffness and strength compared to the other FML constituents that adding adhesive to the laminate provides virtually no increase in the amount of load a given laminate can carry while increasing the laminate's thickness and weight, effectively reducing the strength and stiffness of the laminate.

A trade-off is required: since additional adhesive layers are good for crack growth and bad for static properties, the best-designed interface (the amount of adhesive in addition to the prepreg) will be different depending on the requirements of a given structure. In order to optimally make this trade-off, an understanding of the effect of adhesive layer thickness on laminate properties is required.

For static properties, the metal volume fraction method [20, 21] provides a means of estimating the effects of adhesive thickness. The fatigue crack growth of regular FMLs such as Glare can currently be modeled based solely on material properties [8], and current research is ongoing to extend modeling capability to general laminates with non-uniform constituents and cracks/delaminations through the thickness. One of the important properties needed for such analysis is the delamination growth rate of the adhesive bond between the fiber and metal.

Previous testing has shown that the adhesive thickness used for Bondpreg does have a slower delamination growth rate than a traditional Glare interface [22], but has only addressed that one specific adhesive layer thickness.

The layup used was 0.12 mm adhesive, 0.26 mm fiberglass, and another 0.12 mm adhesive layer. This is the same layup used in a number of crack growth experiments [10, 11]. Such a layup was in common use due to the ready availability of adhesive sheets in that particular thickness rather than any specific consideration for the “right” thickness.

Data on that particular configuration is certainly useful, but for future design work it is preferable to know the delamination growth rate of interfaces for any possible adhesive thickness, or even if changing the thickness makes a difference, so the best design can be selected. A good understanding of the effects of adhesive layer thickness could provide justification for manufacturing of adhesive film in a previously non-standard thickness, or even provide guidance for manufacturing of a specialized prepreg with extra adhesive layers. Data on the change in delamination growth resistance as a function of adhesive layer thickness is needed to understand the effects of laminate design choices and to develop the best interface for the job at hand.

A.1.1 Theory

The rate of delamination growth in FMLs has been shown to be characterized by the cyclic range of strain energy release rate (SERR) [5, 8, 9]:

$$\frac{db}{dN} = C_d (\Delta G)^{n_d} \quad (\text{A.1})$$

where C_d and n_d are treated as material properties, measured with testing, and ΔG is defined [23]:

$$\Delta G = \sqrt{G_{max}} - \sqrt{G_{min}} \quad (\text{A.2})$$

With G_{max} and G_{min} the cyclic maximum and minimum SERRs of delamination growth, respectively.

The definition of G is given by:

$$G = \frac{\sigma_{lam}^2}{2jE_{al}} \left[\gamma^2 (n_{al} - n_{cr}) t_{al} - \lambda^2 n_{al} t_{al} + \frac{E_{f,0}}{E_{al}} n_{f,0} t_{f,0} (\gamma^2 - \lambda^2) + \gamma^2 \frac{E_{ad}}{E_{al}} (n_{ad} - n_{cr,ad}) t_{ad} - \lambda^2 \frac{E_{ad}}{E_{al}} n_{ad} t_{ad} \right] \quad (\text{A.3})$$

Table A.1 – *Test Matrix*

Laminate	t_{al} [mm]	$t_{f,0}$ [mm]	t_{ad} [mm]	Cure Pressure [bar]	Measured t_{lam} [mm]	Estimated t_{ad} [mm]
A	0.3	0.26	0	6	0.875	0.008
B	1.6	0.26	0	6	3.455	-0.002
C	1.6	0.26	0	4	3.480	0.010
D	1.6	0.26	0.12	4	3.715	0.128
E	1.6	0.26	0.24	4	3.905	0.223
F	1.6	0.26	0.36	4	4.065	0.303
G	1.6	0.26	0.06	4	3.655	0.098
H	1.6	0.26	0.03	4	3.563	0.051

where

$$\gamma = \frac{t_{lam}}{(n_{al} - n_{cr})t_{al} + \frac{E_{f,0}}{E_{al}}n_{f,0}t_{f,0} + \frac{E_{ad}}{E_{al}}(n_{ad} - n_{cr,ad})t_{ad}} \quad (\text{A.4})$$

and

$$\lambda = \frac{t_{lam}}{n_{al}t_{al} + \frac{E_{f,0}}{E_{al}}n_{f,0}t_{f,0} + \frac{E_{ad}}{E_{al}}n_{ad}t_{ad}} \quad (\text{A.5})$$

This is adapted from [24], where the terms for the adhesive layer replace those of the 90 degree fiber layer, taking into account that experimental observations show that in ply interrupt specimens the adhesive cracks where the metal plies are interrupted, and the delaminations grow at the interface between the adhesive layer and the fiber layer [22].

A.2 Material and Methods

Ply interrupt specimens with different interface configurations were produced according to Table A.1.

Laminate A is a standard Glare 2 configuration [2], making it possible to compare the test results to previous tests of Glare delamination.

Laminate B used thicker metal sheets to show that the effect of sheet thickness is properly accounted for in the SERR calculation, with the expectation that in a ΔG basis, B specimens will have the same delamination growth rates as the A specimens.

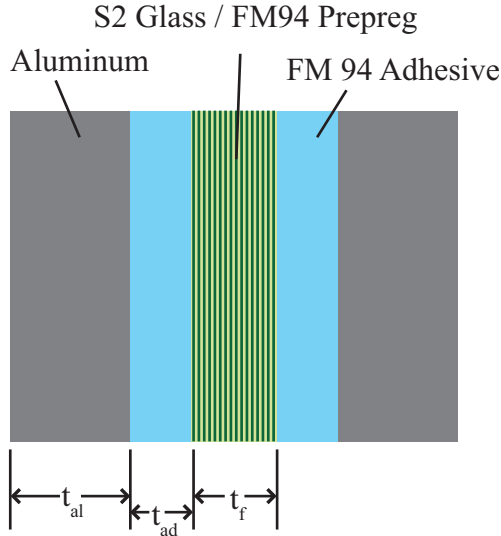


Figure A.1 – Depiction of Bondpreg and definition of layup parameters

The difference between Laminates B and C is the cure pressure. The standard cure cycle for Glare calls for a 6 bar pressure cycle, while the Bondpreg in [10] had been cured with a slightly lower 4 bar cycle to avoid squeezing out too much of the additional adhesive. Laminates with both normal Glare and Bondpreg interfaces, such as CentrAl, have often been manufactured in two cycles: first the Glare core at 6 bar, then the entire laminate at 4 bar. Testing Laminate C - a Glare interface with a Bondpreg cure cycle - allows a more complete picture of the differences in delamination between Bondpreg and Glare to be drawn.

Laminates D through H all have additional adhesive layers of differing thickness. Laminate D is the same configuration as the symmetric Bondpreg of [11].

The metal sheets were 2024-T3 for Laminate A and 2524-T3 for all other specimens. All sheets were chromic acid anodized and primed with BR127 in preparation for bonding.

A.2.1 Manufacturing

The specimens were manufactured as sheets of 350 mm x 450 mm. The metal layers were composed of two sheets of 350 mm x 225 mm butted along the long edge, forming the ply interrupt from which delaminations would initiate. The butting edges of the metal sheets were carefully deburred to prevent localized damage to the fiber layers. Care was taken to ensure that the interrupts in both metal layers of the laminate lined up directly through the thickness, though some sliding of these layers did occur during cure. The maximum offset of the gaps was 1 mm, in Laminate G, while the other laminates had offsets less than 0.5 mm.

Fiber layers were composed of two layers of S2 glass fibers preimpregnated with FM94 adhesive at a fiber volume fraction of approximately 59%.

For Laminates D, E, and F, the adhesive layers were produced by one, two, or three layers of FM94 film adhesive with a knit carrier, such that the nominal thickness of one layer is 0.12 mm.

Since no thinner FM94 film was available, Laminates G and H were produced by cutting an unsupported FM94 film into strips, and laying those strips, perpendicular to the fiber/loading direction, at regular intervals to achieve the desired quantity of adhesive (Figure A.2). Laminate G had strips 10 mm wide with 10 mm gaps, to reduce the thickness by half, and Laminate H had strips 5 mm wide with 15 mm gaps, to achieve one quarter of the thickness.

After lay-up, the laminates were vacuum-bagged and cured at 120°C and either 4 or 6 bar pressure, as per Table A.1.

Specimens were cut from the laminates to sizes of 30 mm wide by 400 mm long, yielding 10 specimens per laminate, plus over 2 cm scrap edge on all sides. The long sides of each specimen were milled to enhance viewing of the delamination tips. The specimen geometry is shown in Figure A.3.

The bonded interfaces from several specimens, having been tested and destructively inspected, are shown in Figure A.4. The amount of adhesive remaining on these metal surfaces after delamination — the test delamination zones are the bottom portion of each metal strip — illustrates the thickness distribution of the adhesive layer, as well as the path of the delamination between the prepreg and adhesive layers, consistent with that depicted in Figure A.3. Laminate C, on the left of Figure A.4, has no additional adhesive, which results in a smooth, nearly adhesive-free surface in the cyclic delamination growth zone. Laminates H and G, had thin adhesive layers produced by distributing strips of carrier-free adhesive. The locations of these strips are visible, having more

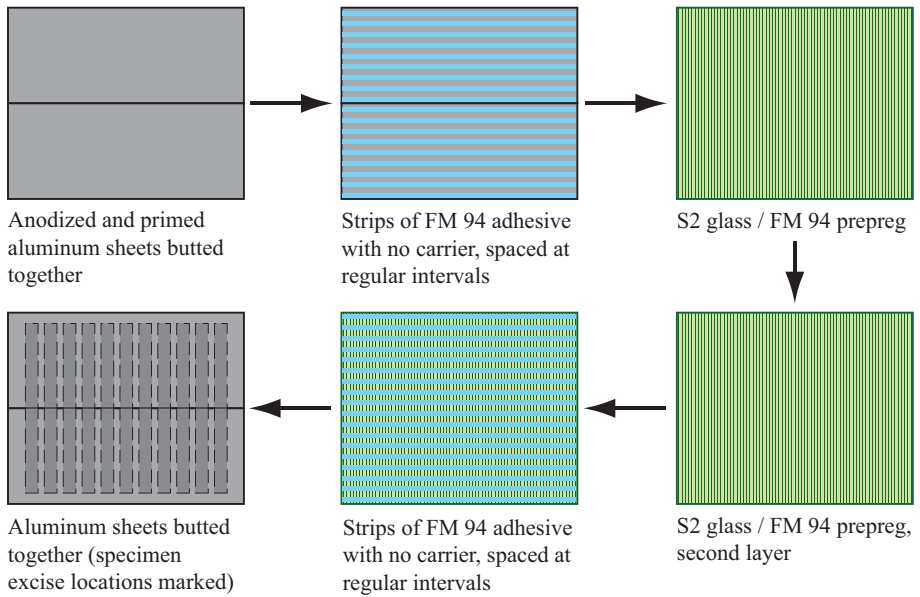


Figure A.2 – Lay-up process for Laminates G and H. Lay-up of Laminates A–F used full FM 94 sheets (with carrier) in place of strips

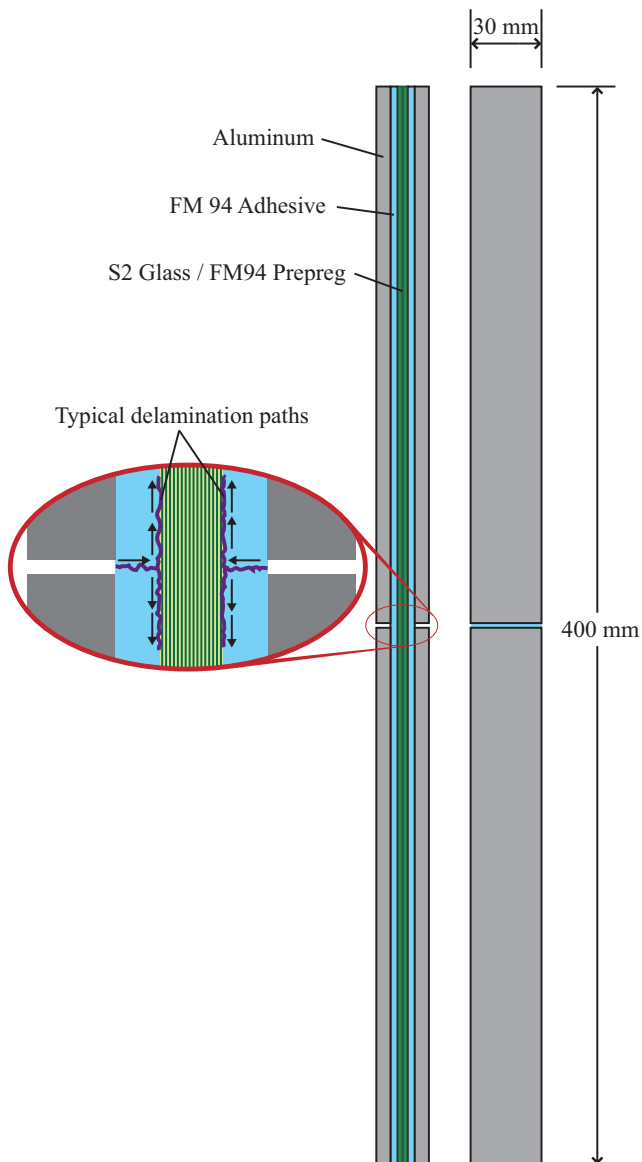


Figure A.3 – Specimen dimensions and delamination growth example

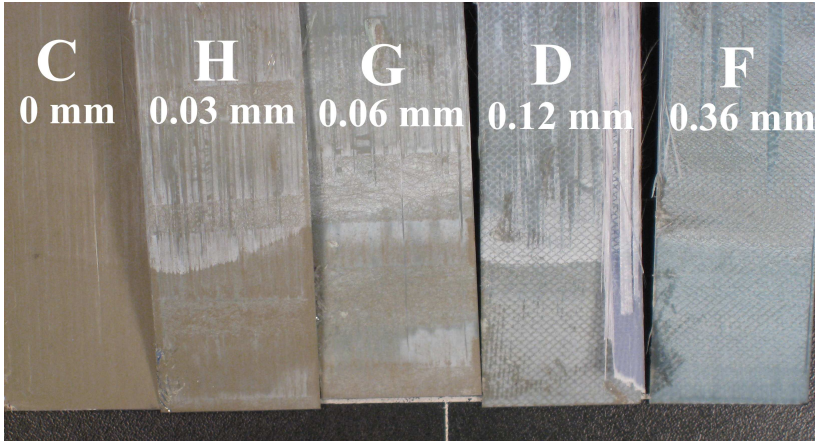


Figure A.4 – Post-test image of surface of metal layers of several specimens. The bottom 30 mm of each surface are the delamination surfaces created during testing. The rougher surfaces above are a result of manual disassembly of the specimens.

adhesive than the surrounding areas. On Laminate H, a small amount of adhesive remains on the metal surface. Laminate G, having a thicker adhesive layer, has more adhesive remaining on the metal surface. Laminates D and F were produced with one and three layers of woven-carrier adhesive, respectively, in the interface. The carrier pattern is visible, as well as the significant thickness of adhesive remaining on the surface.

Difficulty in polishing the milled specimen edges limited the ability to directly measure the adhesive layer thickness. However, thickness measurement of the manufactured laminates allows the adhesive layer thickness to be estimated. Thickness measurements of each specimen, made prior to testing, were averaged for each laminate, and are listed in Table A.1. Adhesive layer thicknesses were estimated by subtracting the nominal metal and fiber layer thicknesses, and are listed in the same table. The inferred t_{ad} for all the laminates with no additional adhesive are all 0.01 mm or less. Taking this to be the level of accuracy of the measured adhesive thickness, Laminate D, with one standard adhesive layer at each interface, had the expected thickness. Laminates E and F, with additional adhesive, had lower-than-expected thicknesses, indicating possible loss to squeeze-out. Laminates G and H had greater-than-expected adhesive thickness. Uneven adhesive distribution, consistent with that shown in Figure A.4, could account for this greater laminate thickness.

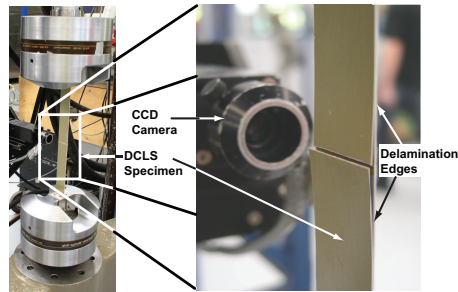


Figure A.5 – Test setup with specimen in hydraulic grips, showing camera location [9]

A.2.2 Testing

Specimens were installed in a 10 kN MTS servo-hydraulic load frame and clamped in the hydraulic grips as shown in Figure A.5. A CCD camera was used to measure the extent of the delamination from one edge. The camera was mounted on a 3-axis positioning system which allowed a close-in view of the delamination tips, while maintaining precise measurements over long lengths.

The measured side of the specimen was painted with a layer of correction fluid, diluted with isopropanol, to aid in the visualization of the delamination tips.

Specimens were cyclically loaded at a frequency of 10 Hz and a stress ratio of $R = 0.05$. Since load history effects are known to be minimal in ply interrupt tests of S2 glass / FM94 prepreg [9], each specimen was tested at several different stress ranges to maximize the amount of data acquired.

At regular intervals the specimens were held at the maximum cyclic load to allow measurement of the delamination lengths. At least nine measurements were taken at each load level, and the first one or two measurements from each set were excluded from the delamination growth rate calculation due to transient fast or slow growth after the load change.

Measurements of delamination length were taken at each of the four delamination fronts visible to the camera. The growth rates of these delaminations between each measurement were averaged together, giving one growth rate at that applied stress for that specimen. Further, most combinations of specimen and stress level were tested twice, so the reported growth rates represent the average from two separate tests.

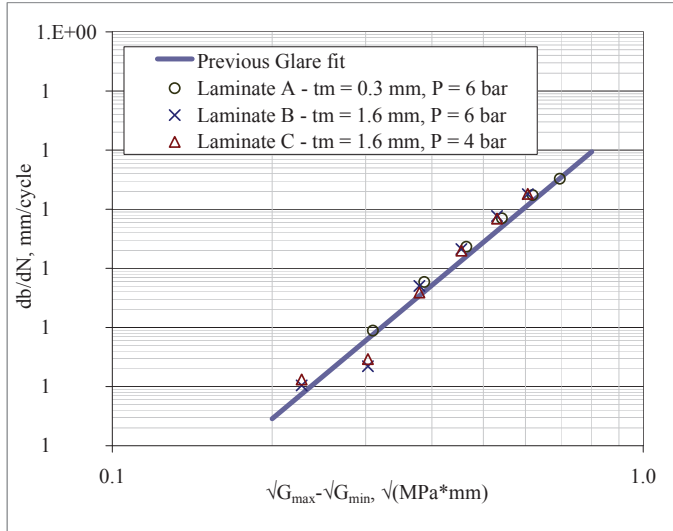


Figure A.6 – Test results of fiberglass-metal interfaces with different metal thickness and cure pressure

Inconsistent results were obtained for Specimen H by testing with multiple stresses per specimen. Since uneven distribution of adhesive from the 5 mm strips, spaced 20 mm apart, was of concern, a second set of tests was done using one stress for each specimen, with delaminations grown to as long as 35 mm.

A.3 Results

The average delamination growth rates of specimens A, B, and C are plotted in Figure A.6 against the cyclic ΔG . A power law curve representing the average delamination growth rate of Glare from previous tests [8] is also shown. All three specimens, which have the same prepreg-metal interface but different metal thicknesses and cure pressures, show the same delamination growth rate properties as each other and as the reference Glare curve.

In Figure A.7 the delamination growth rates of two individual H specimens are shown. Compared with the two individual D specimen results, which are in agreement with each other, the two H specimens had different growth rates at every ΔG at which they were tested. Further, the results do not exhibit

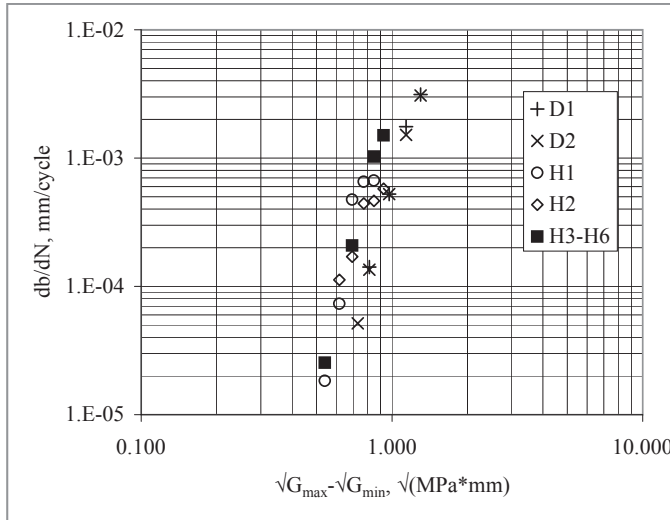


Figure A.7 – Specimens H1 and H2 ($t_{ad} = 0.03$ mm) showed inconsistent results. The two Laminate D specimens are shown to demonstrate the good agreement in results seen in the other laminates. Specimens H3–H6 were each tested at a single cyclic loading for the duration of the test.

the power law behavior seen in other specimens. The sparse placement of adhesive strips in Laminate H may have led to uneven adhesive distribution, with the measured growth rate at a given ΔG depending on the 5 mm range over which the growth at that range was measured. Data from four additional tests of Laminate H, in which the ΔG was kept constant through the entire test (H3–H6), are also plotted in Figure A.7. These data exhibit the characteristic power law relationship with ΔG and are used subsequently in this paper as the representative data from laminate H. The average delamination growth rate data from these four tests are plotted as a function of average delamination length in Figure A.8. When normalized against the average growth rate for each test, all four specimens show the same relationship between delamination length and growth rate. The growth rates tend to be faster than average at lengths below 10 mm and between 17 and 22 mm. This correlates to the 20 mm spacing of 5 mm wide adhesive strips used to achieve the desired thickness, indicating that uneven adhesive distribution could have contributed to the high variability of Laminate H.

In Figure A.9, the delamination growth rate curves of the specimens with

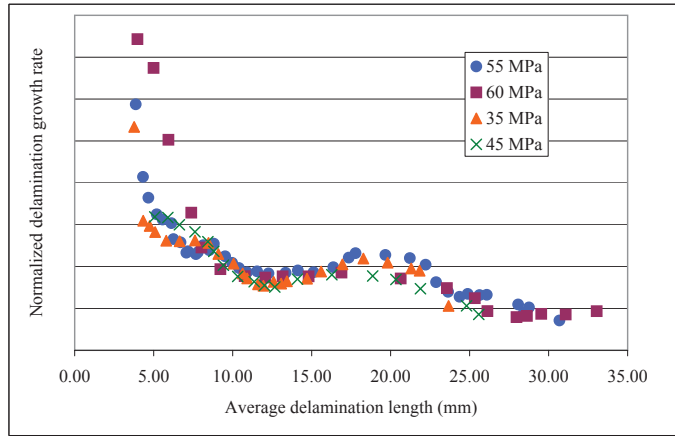


Figure A.8 – Average delamination growth rates of specimens H3–H6, all with $t_{ad} = 0.03$ mm, plotted against the average delamination length. The rates are normalized by dividing the rate by the mean rate of each specimen in order to make the trends in growth rate with respect to delamination more directly comparable.

different adhesive thicknesses are plotted, along with the reference Glare curve, which represents a zero adhesive thickness. All of the data are fit well by power laws, apart from Laminate H, the thinnest laminate. Further testing of this laminate is recommended, taking care to grow the delaminations over long distances to avoid local variations in the adhesive layer due to the production technique used.

To illustrate the variability of the measured delamination growth rates, the average growth rates of each of the four delamination fronts in each specimen were treated separately. A log normal distribution was fit to the four or eight data points for each adhesive layer thickness at each SERR range tested. Figure A.10 shows error bars on the data points representing the standard deviation of the log normal distribution of each set of measured rates. Generally, there was more variability at lower growth rates, and each of the laminates, apart from Laminate H, have comparable levels of variability. The variability of Laminate H is low as a result of measuring a much longer period of growth, with each specimen used to test only one stress level.

Power law fits to the delamination growth rate data from each specimen are given in Table A.2. The C_d and n_d terms are based on ΔG in units of $\sqrt{\text{MPa mm}}$ and $\frac{db}{dN}$ in units of mm/cycle.

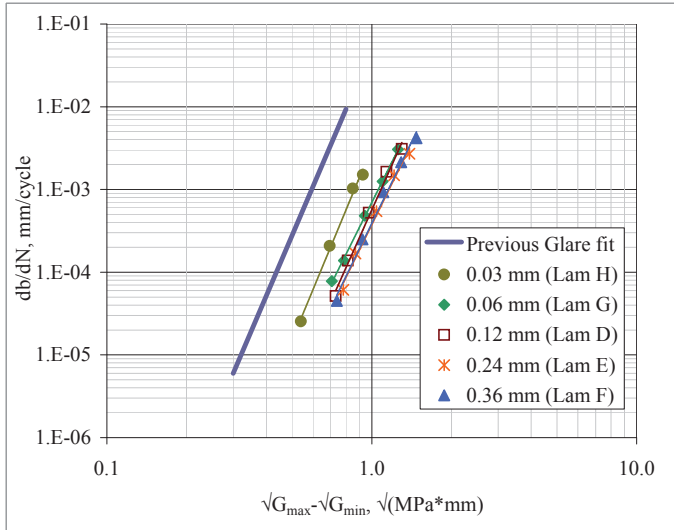


Figure A.9 – Effect of adhesive layer thickness on delamination growth rate

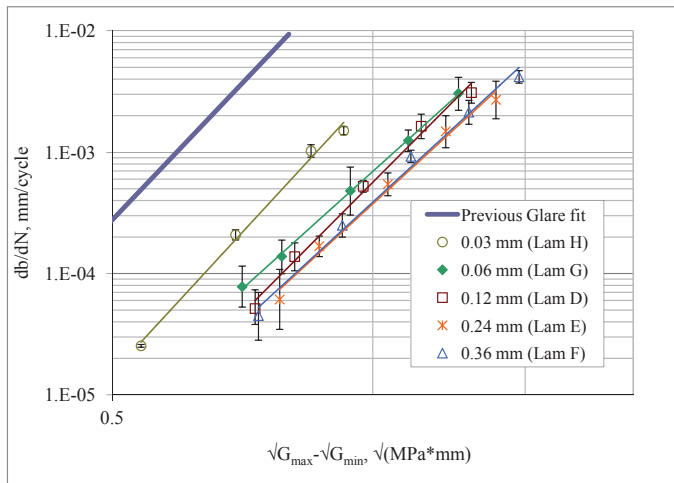


Figure A.10 – Results from Figure A.9 replotted with error bars representing one standard deviation above and below the average growth rate based on a log normal fit of the growth rate of each of the four or eight delamination fronts measured for each SERR range.

Table A.2 – Power law fits for Equation (A.1) for each adhesive layer thickness

t_{ad} (mm)	C_d	n_d
0.03	3.196×10^{-3}	7.731
0.06	6.941×10^{-4}	6.422
0.12	5.646×10^{-4}	7.166
0.24	3.742×10^{-4}	6.541
0.36	3.875×10^{-4}	6.565

A.4 Discussion

The similar delamination growth rates of Laminate A, Laminate B, and the historical Glare curve are as expected. The results show that the thickness of the metal sheets does not affect the durability of the metal-to-prepreg bond and that the use of the appropriately defined ΔG captures the effects of the constituent thickness.

That the results of Laminate C are similar to that of Laminates A and B suggests that changing the cure pressure from 6 bar to 4 bar has little effect on the bond's resistance to delamination. The 6 bar cure for Glare was developed by studying the porosity of laminates, as measured by ultrasonic C-scan, and finding a 6 bar cure cycle eliminated any measurable porosity. Because this cure pressure was developed to ensure good bonding for laminates with curvature, the results of these tests on flat laminates can not be taken to suggest that the properties of the bonds produced in lower pressure cures as good in real, curved structures.

The results of testing interface configurations with varying adhesive thicknesses show that adding a small amount of adhesive (0.3 mm) leads to a drastic reduction in the delamination growth rate, compared to that of a conventional Glare laminate. Additional adhesive beyond this amount up to a thickness of 0.12 to 0.24 mm leads to a small additional decrease in growth rate, and further increase in adhesive thickness provides no additional benefit. Figure A.11 demonstrates this relationship by taking the delamination growth rate from the power law fits of each adhesive thickness at a number of different SERR ranges.

The results suggest that the improvement in delamination growth performance due to an additional adhesive layer results from strengthening the bond line at which delamination occurs. The delaminations were observed to occur at the adhesive-prepreg interface, indicating that this interface is weaker in delamination than the adhesive-metal interface. Yet the slower rates of delamination

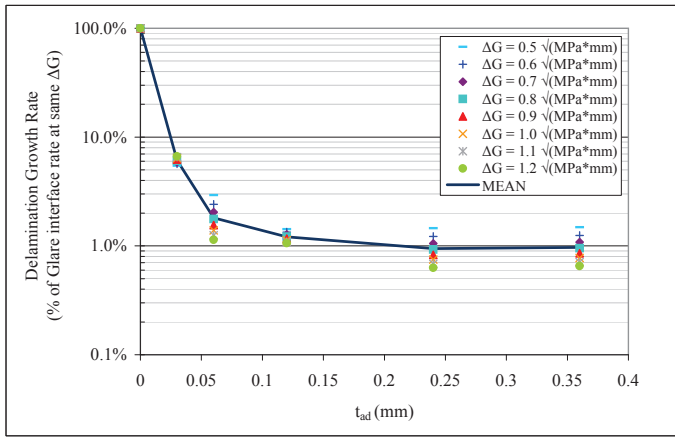


Figure A.11 – Relative decrease in delamination growth rates with addition of adhesive in the bondline

growth in Bondpreg compared with Glare show that the adhesive-prepreg interface is significantly more resistant to delamination than the metal-prepreg interface of Glare.

If the improvement resulted rather from changing the severity of load transfer around the delamination through increased prepreg shear deformation, one would expect to see further improvement with increasing adhesive thickness, though detailed finite element analysis would be required to confirm just how the stress distribution changes with changing adhesive thickness.

It is possible that the slightly higher rates of delamination growth of the 0.03 mm and 0.06 mm adhesive thickness specimens results not from the thickness of the adhesive itself, but from the differences in production of these thickness samples. The two differences were the use of an adhesive film with no carrier and spacing strips of the film at regular intervals to achieve the thickness. The non-uniform distribution of adhesive in the 0.03 mm and 0.06 mm adhesive thickness specimens, as can be seen in the failure surfaces in Figure A.4, leads to additional uncertainty in directly comparing the rates measured in these specimens to those with thicker, uniformly distributed adhesive. The normalized rates plotted against delamination length in Figure A.8 show that the growth rate is affected by this uneven distribution. It would be advisable to source an adhesive film made for a thickness less than 0.12 mm with a carrier to see if its delamination growth resistance is in line with the trend found in this

study, or if the improved manufacturing quality leads to improved delamination performance. Alternatively, a 0.12 mm thick adhesive specimen could be produced with carrier-free adhesive and compared to the results with a carrier. However, production of such a specimen could be complicated by the tendency of thick adhesive to squeeze out during cure in the absence of a carrier. This is why such a specimen was not originally considered for this study.

The implications of these test results for the design of FMLs are that with thinner adhesive layers at the interface than applied in previous studies most of the benefits in terms of increased delamination resistance can be retained while mitigating much of the reduction in static properties. Prepreg and adhesive film systems that enable adhesive layers as thin as 0.03 mm on either side of the fiber layers to be reliably and easily produced should be pursued. Doing so will enable FMLs with metal layers much thicker than those in use today to be utilized as high performance structural solutions, with a good balance of damage tolerance and static properties. Though this thickness recommendation applies specifically to the FM94 adhesive system that was tested, similar studies could be undertaken for FMLs with other materials to optimize the interface.

A.5 Conclusion

Ply-interrupt delamination growth rate tests were conducted on a number of fiber metal laminate configurations with additional FM94 adhesive layers between the fiber and metal layers of varying thickness. Additional tests in the test matrix allow comparison of these test results to historical data.

The results of testing indicate that adding adhesive to the interface improves the delamination growth rate of FMLs, and that this improvement is not in proportion to the adhesive layer thickness but reaches a horizontal asymptote as the thickness is increased. The adhesive thickness of most symmetric Bondpreg previously studied, 0.12 mm, is sufficiently thick to achieve the full benefit of added adhesive. This research suggests that much of that benefit can be retained with adhesive that is one fourth of that thickness, enabling the design of laminates with thick metal layers with good damage tolerance and static properties. However, the differences in manufacturing required to achieve the thinner adhesive layers in these tests introduce additional uncertainty, which should be addressed by repeating the tests in this study with adhesive sheets produced with the decreased thickness.

Bibliography

- [1] Wilson, G. S., Fassih, Y., Alderliesten, R. C., and Benedictus, R. (2011) Effect of adhesive layer thickness on fiber metal laminate delamination growth rate. Submitted for journal publication July 2011.
- [2] Vlot, A. and Gunnink, J. (2001) *Fibre metal laminates: an introduction*. Kluwer Academic Publishers.
- [3] Vlot, A. (2001) *Glare: history of the development of a new aircraft material*. Kluwer Academic Publishers.
- [4] Beumler, T. (2008) MoC for A380 hybrid structure. *ASIP 2008: the 2008 aircraft structural integrity program conference, Dec 2 – 4, 2008. San Antonio, Texas*.
- [5] Marissen, R. (1988) *Fatigue crack growth in ARALL. A hybrid aluminium-aramid composite material: Crack growth mechanisms and quantitative predictions of the crack growth rates*. Ph.D. thesis, Delft University of Technology, Delft, The Netherlands.
- [6] Guo, Y. J. and Wu, X. R. (1998) A theoretical model for predicting crack growth rates in fiber-reinforced metal laminates. *Fatigue & Fracture of Engineering Materials and Structures*, **21**, 1133–1145.
- [7] Guo, Y.-J. and Wu, X.-R. (1999) Bridging stress distribution in center-cracked fiber reinforced metal laminates: modeling and experiment. *Engineering Fracture Mechanics*, **63**, 147 – 163.
- [8] Alderliesten, R. C. (2007) Analytical prediction model for fatigue crack propagation and delamination growth in glare. *International Journal of Fatigue*, **29**, 628–646.
- [9] Khan, S., Alderliesten, R., and Benedictus, R. (2009) Delamination growth in fibre metal laminates under variable amplitude loading. *Composites Science and Technology*, **69**, 2604–2615.
- [10] Roebroeks, G. H. J. J., Hooijmeijer, P. A., Kroon, E. J., and Heinimann, M. B. (2007) The development of CentrAl. *First International Conference on Damage Tolerance of Aircraft Structures*, Delft, The Netherlands.
- [11] Heinimann, M., Kulak, M., Bucci, R., James, M., Wilson, G., Brockenbrough, J., Zonker, H., and Sklyut, H. (2007) Validation of advanced metallic hybrid concept with improved damage tolerance capabilities for

- next generation lower wing and fuselage applications. Lazzeri, L. and Salvetti, A. (eds.), *Proceedings of the 24th ICAF Symposium*, Naples, Italy, May.
- [12] Miller, D. and Phelps, H. (2010) A finite element based stress intensity solution for cracks in fiber metal laminates. *ASIP 2010: the 2010 aircraft structural integrity program conference, Nov 30 – Dec 2, 2010. San Antonio, Texas.*
- [13] Chan, W. S., Rogers, C., and Aker, S. (1986) Improvement of edge delamination strength of composite laminates using adhesive layers. Whitney, J. M. (ed.), *Composite Materials: Testing and Design (Seventh Conference)*, ASTM STP 893, pp. 266–285, ASTM, Philadelphia.
- [14] Chan, W. S. (1986) Delamination arrester — an adhesive inner layer in laminated composites. Hahn, H. T. (ed.), *Composite Materials: Fatigue and Fracture*, ASTM STP 907, pp. 176–196, ASTM, Philadelphia.
- [15] Sun, C.-T. and Rechak, S. (1988) Effect of adhesive layers on impact damage in composite laminates. Whitcomb, J. D. (ed.), *Composite Materials: Testing and Design (Eighth Conference)*, ASTM STP 972, pp. 97–123, ASTM, Philadelphia.
- [16] Norman, T. L. and Sun, C.-T. (1993) Delamination growth in composite laminates with adhesive strips subjected to static and impact loading. *Composites Science and Technology*, **46**, 203–211.
- [17] Sela, N., Ishai, O., and Banks-Sills, L. (1989) The effect of adhesive thickness on interlaminar fracture toughness of interleaved CFRP specimens. *Composites*, **20**, 257–264.
- [18] Lee, H. Y. and Qu, J. (2003) Microstructure, adhesion strength and failure path at a polymer/roughened metal interface. *Journal of Adhesion Science and Technology*, **17**, 195–213.
- [19] Owens, J. F. P. and Lee-Sullivan, P. (2000) Stiffness behaviour due to fracture in adhesively bonded composite-to-aluminum joints ii. experimental. *International Journal of Adhesion and Adhesives*, **20**, 47–58.
- [20] Hagenbeek, M., van Hengel, C., Bosker, O. J., and Vermeeren, C. A. J. R. (2003) Static properties of fiber metal laminates. *Applied Composite Materials*, **10**, 207–222.

- [21] Rickerd, G. (2010) Considering fiber metal laminate aircraft wings — what should we know? *ASIP 2010: the 2010 aircraft structural integrity program conference, Nov 30 – Dec 2, 2010. San Antonio, Texas.*
- [22] Doevendans, L. P. (2007) Report b2v-07-03 - delamination behaviour of adhesive films. Tech. rep., Delft University of Technology.
- [23] Rans, C., Alderliesten, R., and Benedictus, R. (2011) Misinterpreting the results: How similitude can improve our understanding of fatigue delamination growth. *Composites Science and Technology*, **71**, 230–238.
- [24] Alderliesten, R. C. (2009) Damage tolerance of bonded aircraft structures. *International Journal of Fatigue*, **31**, 1024–1030.

This page intentionally left blank.

Appendix B

Steady-state crack growth in hybrid fiber metal laminates as a tool for design

This appendix is a reproduction of [1].

B.1 Introduction

Fiber metal laminates (FMLs) are known for having exceptional damage tolerance, in particular having slow crack growth and high residual strength with cracks, and they have been used in several recent aeronautical structures in damage tolerant critical areas. These applications have been limited to thin structure; however, there are a number of thicker structural components for which a high degree of damage tolerance is desired, for example, the lower wing skins of transport-class aircraft. Using FMLs with increasing thickness affords greater tailorability of laminate properties to the designer of such structure, though with this increased freedom to design comes a greater burden to understand and characterize the laminates' behavior. An empirical observation of FMLs, that cracks tend to grow at approximately constant rates, may greatly simplify analysis of FML crack growth behavior. In this paper, a method for

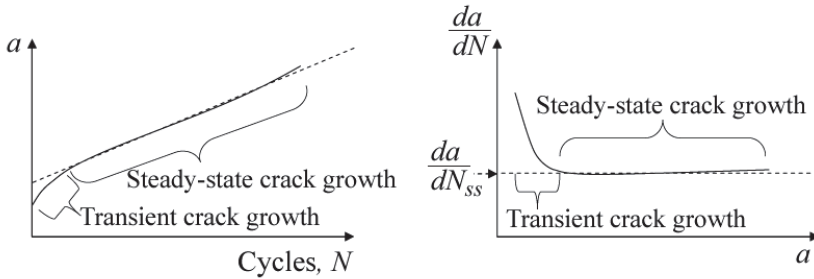


Figure B.1 – a vs. N (left) and crack growth rate vs. crack length (right) plots representing the results of a typical fatigue crack growth rate test in a typical FML [2]

performing crack growth analysis of thick FMLs by exploiting this constant crack growth rate phenomenon will be explored and assessed experimentally.

FMLs commonly exhibit crack growth behavior as shown in Figure B.1 [2]. After an initial transient period, in which the crack grows quickly, the growth rate slows and remains roughly constant, regardless of crack length. The mechanism responsible for the slow crack growth of FMLs is that while the metal layers crack, the fibers remain intact, bridging the cracks. This bridging mechanism offloads the cracked layers, reducing the crack driving force. Because the cracks encountered in FMLs are typically growing from a hole or notch, it takes some amount of crack growth for a sufficient amount of fibers to be in the wake of the crack providing bridging. This is the reason for the initial faster growth in the transient period.

The steady-state crack growth (SSCG) has been observed in a variety of FMLs, such as Glare, ARALL and CentAl [3–5]. SSCG has occurred in a variety of test configurations, from simple coupons, to stiffened panels, to full fuselage barrel tests [6]. SSCG occurs whether constant-amplitude or flight spectrum loading is applied, and over a range of positive and negative stress ratios [2, 5].

Figure B.2 shows the crack length measured over the course of a test of a CentAl laminate in a prior study by the authors [2]. The laminate is referred to as Central because it has several thick layers of aluminum bonded around a central Glare core with Bondpreg, an adhesive-rich glass-fiber composite layer. The SSCG behavior of the laminate is clearly visible in this chart, with the cracks grown to within 10 mm of the edges of the 200 mm wide specimen at an approximately constant rate.

Figure B.3 shows the crack growth rate vs. crack length results from four

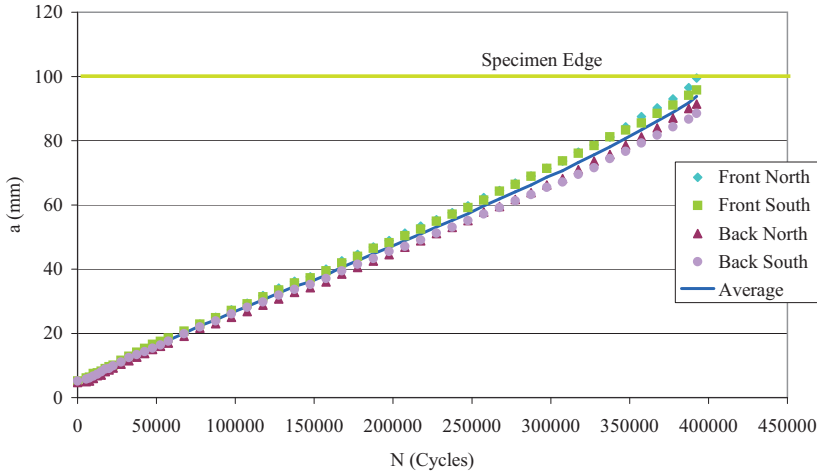


Figure B.2 – Test results from [2] showing constant crack growth rate for cracks up to 90% of specimen width. Loaded with $\sigma_{max} = 100$ MPa, $R = 0.05$

tests on the same laminate at the same stress ratio, R , with the rates derived with the 7-point polynomial method from [7]. This figure demonstrates that the constant crack growth rate, da/dN_{SS} , increases with increasing stress amplitude. Figure B.4 shows that these crack growth rates increase as a power-law function of the stress amplitude and that at different stress ratios, the power law shifts but retains the same slope, for this laminate.

In [2], a method of exploiting the SSCG behavior of this laminate was proposed, and it is depicted in Figure B.5. If the crack growth rate of the laminate can be characterized in terms of the stress in the laminate, a static analysis of the stress in a structural component provides sufficient information to predict the growth of a crack by integrating the crack growth rate, which is given as a function of the stress along a given crack path. For this method to work, the following assumptions must hold: the crack growth in the outer metal layers is driven by the stress at the location of the crack tip, and the stress at the location of the crack can be accurately estimated by a static analysis of the uncracked structure, or in other words, that the stress redistribution due to cracking can be neglected.

The experiments discussed in this paper are aimed at validating the proposed method and confirming or rejecting its underlying assumptions.

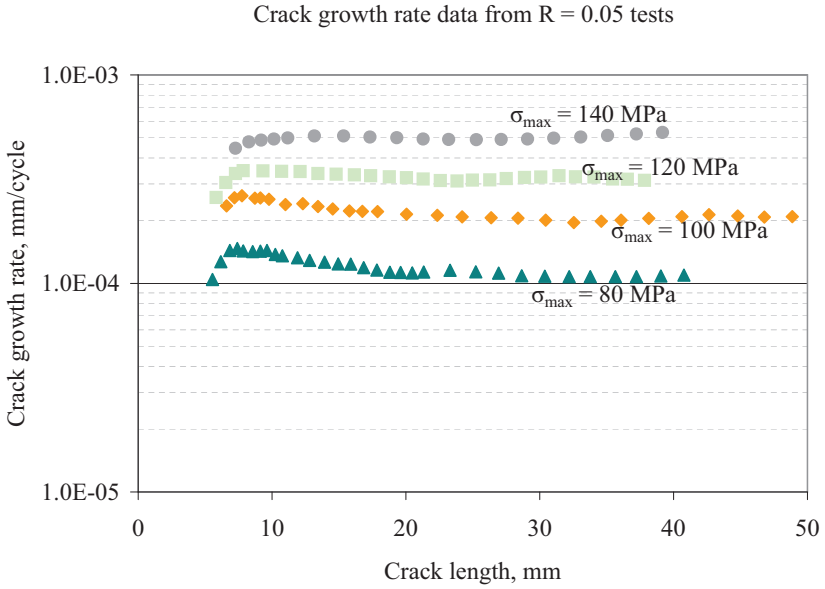


Figure B.3 – Results from crack growth rate tests on CentrAl with 2024-T3 thick sheets [2]

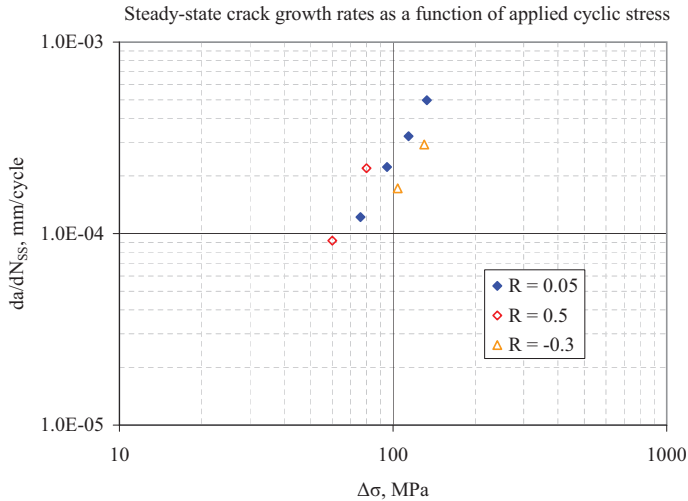


Figure B.4 – Results from crack growth rate tests on CentrAl with 2024-T3 thick sheets [2]

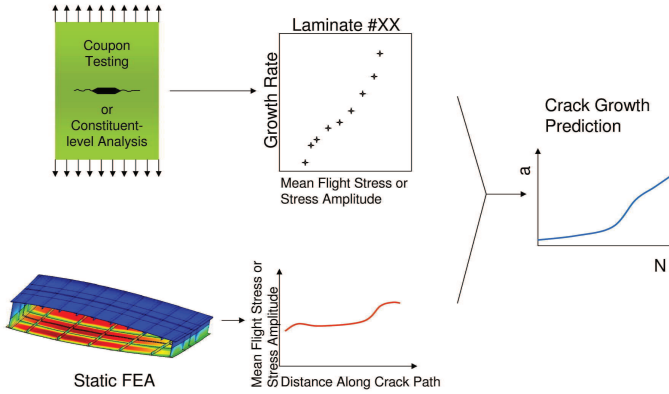


Figure B.5 – Method for crack growth prediction using SSCG of FMLs

B.2 Property assessment, prediction, and validation

B.2.1 Testing of laminates with 2524 thick sheets

The data presented in Section B.1 were collected from thick laminates with only 2024-T3 aluminum as the metal constituent, for both the thick outer layers and the thin inner Glare layers. The work presented in this paper is on laminates in which the thick layers (1.6 mm) are comprised of 2524-T3, with the thinner metal layers of the inner Glare still of 2024-T3. The laminate configuration is given in Table B.1.

Testing was done to compare the new 2524-T3 laminate to the previous study with 2024-T3, as well as to establish baseline crack growth rate vs. stress properties to be used in subsequent prediction steps using the SSCG method. Fatigue crack growth tests were carried out on center cracked tension specimens with a width of 200 mm and a starting notch width of $2a = 10$ mm, matching the specimens from [2]. The tests were conducted at room temperature in a lab air environment, with loading at a frequency of 10 Hz. Periodic measurements of crack length were made visually, with the aid of a loupe. Tests were allowed to continue until an average crack length of around 45 mm was reached.

Figure B.6 shows the results of the test conducted with a maximum applied cyclic stress of 100 MPa. The plot includes the lengths of every surface crack, the average crack length, and the average crack length of the test made at the

Table B.1 – *Laminate definitions*

Material	Thickness (mm)
Al 2524-T3	1.6
Bondpreg	0.5
Al 2524-T3	1.6
Bondpreg	0.5
Al 2024-T3	0.4
FM94 S2 Glass Prepreg	0.26
Al 2024-T3	0.4
FM94 S2 Glass Prepreg	0.26
Al 2024-T3	0.4
FM94 S2 Glass Prepreg	0.26
Al 2024-T3	0.4
Bondpreg	0.5
Al 2524-T3	1.6
Bondpreg	0.5
Al 2524-T3	1.6
Bondpreg Definition	
FM94 Adhesive	0.12
FM94 S2 Glass Prepreg	0.26
FM94 Adhesive	0.12

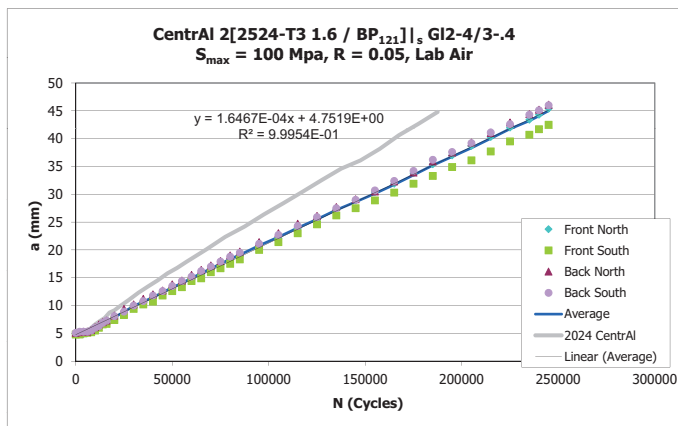


Figure B.6 – Crack growth results from the FML with 2524-T3 thick sheets compared with the average results of the FML with 2024-T3 from [2]. The front and back terms refer to which face of the laminate the crack was located, while the North and South terms refer to the two ends of the central notch.

same loads with the FML from [2], which had 2024-T3 for thick metal layers. The chart shows the typical SSCG behavior of this laminate. Initially, the crack growth occurs slowly, as the cracks initiate from the starter notch, followed by a period of relatively fast crack growth before fiber bridging slows the crack to the steady state rate, at which it grows for the remainder of the test. The 2524 laminate clearly grew at a slower rate than the equivalent laminate with 2024 thick sheets. This is to be expected, as monolithic 2524-T3 sheet has better crack growth properties than 2024-T3 sheet [8].

The crack growth rate vs. crack length plots, based on the average crack length of each test, are given for three tests at different stress levels in Figure B.7. Crack growth rates of the tests with starter notch lengths of 5 mm. The same, typical, SSCG behavior is observable in all three tests, as is the expected trend that increasing stress increases the steady-state crack growth rate. In Figure B.8, the three da/dN_{SS} data points from the current study are put in context with the 2024-T3 laminate data from [2]. As with the previous laminate, the laminate in this study exhibits a power law relationship between the cyclic stress range and the da/dN_{SS} , though the laminates data is shifted right, since the crack growth of the 2524 laminate is slower. A regression analysis of the present data gives a power law fit of:

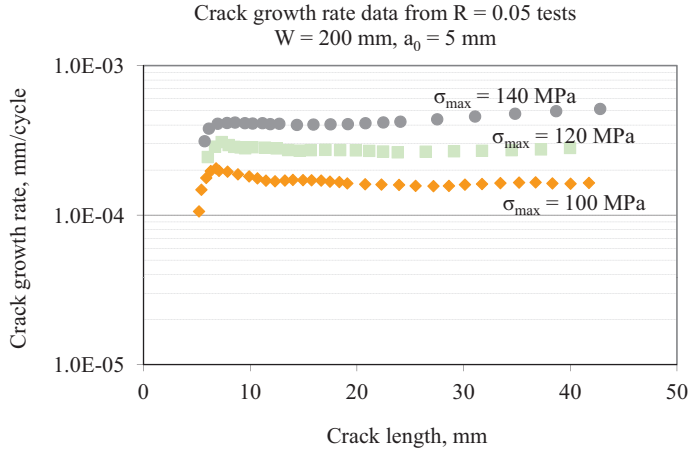


Figure B.7 – Crack growth rates of the tests with starter notch lengths of 5 mm

$$\frac{da}{dN}_{SS} = 4.424 \times 10^{-10} \Delta\sigma_{app}^{2.814} \quad (\text{B.1})$$

The 2524 specimens tested at 120 and 140 MPa have comparable final crack lengths to the 2024 hybrid laminates from reference [2] tested at the same stresses. It is therefore possible to compare the delaminations in each specimen, as measured via through-transmission ultrasonic C-scan. Note that the C-scan does not reveal any information about specific delaminations in individual interfaces, rather it shows the combination of all the delaminations through the thickness. However, it is often the case that the outermost delaminations on the front and back are the largest throughout the thickness [5], and the C-scan can be quite informative. Destructive investigation of these specimens, with the aim of measuring all the internal delaminations, will occur at a later time. It is clear in Figure B.9 that the two 2524 laminates have larger delaminated regions than the 2024 laminates.

This delamination difference is a result of the slower crack growth of 2524 with respect to 2024. Consider two laminates, one with 2524-T3 thick layers and one with 2024-T3 thick layers, each with identical crack lengths and delaminations already present. Because the stiffness of the two alloys is virtually identical, the bridging forces between the fiber layers and metal layers are the same in the two laminates, and likewise the resultant stress intensity factor of the equivalent metal layers in each laminate. The crack will progress more

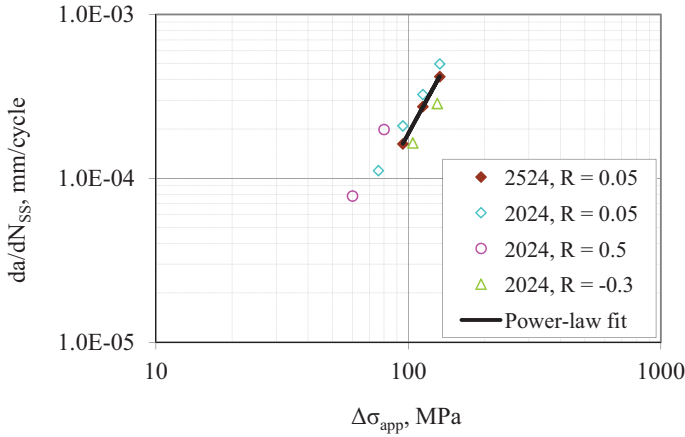


Figure B.8 – Steady-state crack growth rates plotted against applied cyclic stress range

slowly in the 2524 laminate, but the delaminations will grow at equal rates in both laminates. The ratio of delamination growth to crack growth is thus higher in the 2524 laminate, and when cracks in the two laminates are grown to equal lengths, the delamination in the 2524 laminate is greater than that in the 2024 laminate.

B.2.2 Tests to Evaluate Net Stress as the Driving Parameter

The tests described in Section B.2.1 all used starting notches in the center of the specimens with length $a = 5$ mm. It is known from previous studies of crack growth in FMLs that increasing the starter notch size increased the crack growth rates [3]. Since there are a variety of hole sizes used in aircraft structures, as well as varying sizes of cutouts, corners, or accidental damage scenarios, it would not be feasible to produce curves of the sort in Figure B.8 for a sufficient range of load cases and a sufficient range of notch or hole sizes. Therefore, it is highly desirable to find some way of relating the crack growth rate of samples with different geometries. In [2], it was suggested that the net section stress of the specimens may be such a unifying parameter.

Three crack growth tests with different starting notch sizes were performed in order to investigate net stress as a potential crack growth-characterizing

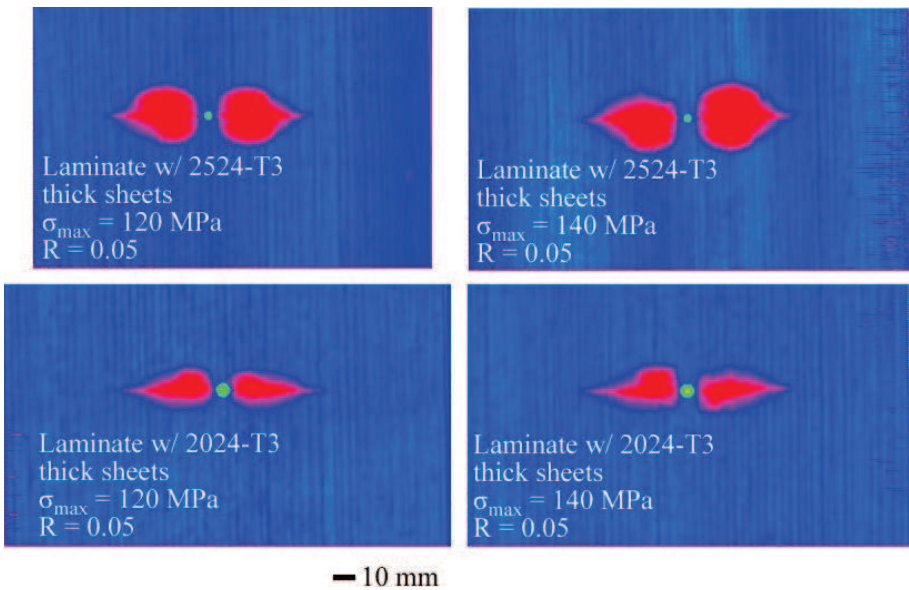


Figure B.9 – Ultrasonic C-Scan images comparing delamination (red region) in the laminates from the current study with those from [2]

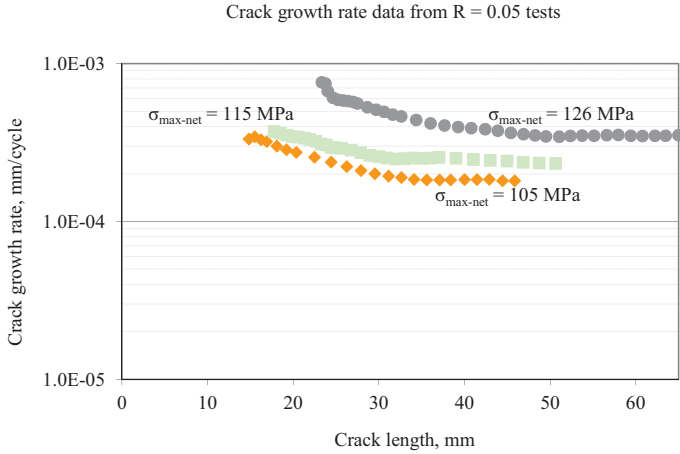


Figure B.10 – Crack growth rates determined for the specimens with long starter notches, determined from 7-point polynomial method with average crack lengths

parameter.

The first had a starter notch of $a = 20.7$ mm and an applied maximum cyclic stress of 100 MPa, resulting in a net cross-sectional maximum cyclic stress of 126 MPa, equal to that of the $a = 5$ mm test with applied max loading of 120 MPa. The second had a starter notch of $a = 12.95$ mm and an applied maximum cyclic stress of 100 MPa, resulting in a net-section stress of 115 MPa, in between the net stresses of the original 100 MPa and 120 MPa tests. The third had a starter notch of $a = 13.05$ mm and an applied maximum cyclic stress of 91.5 MPa, resulting in a net cross-sectional maximum cyclic stress of 105 MPa, equal to that of the $a = 5$ mm test with applied max loading of 100 MPa.

The crack growth rates from these tests, derived from the average crack length results using the 7-point polynomial method [7], are given in Figure B.10. Most noticeable, in comparison with the results of the 5 mm starter notch tests from Figure B.7, is that the larger starter notches result in more pronounced and longer-lasting transient periods of faster crack growth. This is likely a result of having fewer bridging fibers in the wake of the crack, requiring longer crack growth before the crack is sufficiently bridged to achieve an approximately constant crack growth rate.

The steady state crack growth rates are plotted in Figure B.11 along with those from Section B.2.1 in terms of the net cyclic stress range. The long

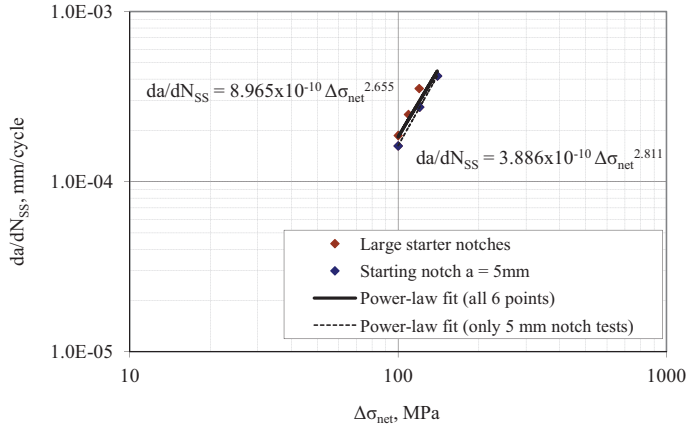


Figure B.11 – By changing the notch size, different net stresses were achieved. The data nearly coalesce into a power law function of net applied stress range. All tests used the laminate in Table 1 at a stress ratio of $R = 0.05$

starter notch results fall near but slightly above the power law fit of the earlier results. Whether or not they are sufficiently close to conclude that the net stress accurately describes da/dN_{SS} is dependent on the level of accuracy required of predictions made with this data. For subsequent sections, the curve fit from all six data points in Figure B.11 will be used to predict the crack growth rates:

$$\frac{da}{dN_{SS}} = 8.965 \times 10^{-10} \Delta\sigma_{net}^{2.655} \quad (\text{B.2})$$

B.2.3 Evaluation of the SSCG Method for Predicting Crack Growth Through Stress Gradients

The proposed method of crack growth prediction by applying the relationship between the local stress and steady-state crack growth rate for FMLs was examined by performing two sets of trial predictions. Two different specimen configurations were produced with an eye towards creating a stress gradient in the crack path that is unusual for a center-cracked tension specimen.

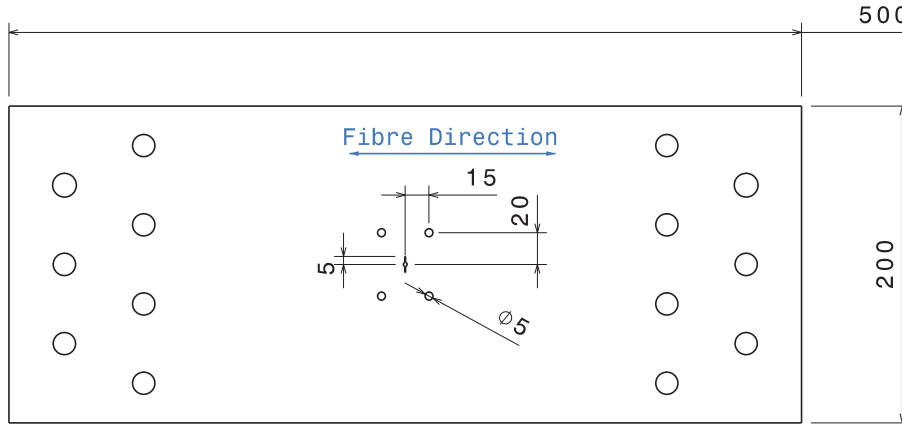


Figure B.12 – 4-hole specimen design. The second 4-hole specimen had holes placed 25 mm from the center, rather than 20 mm. All dimensions in mm

4-hole Configuration

The 4-hole configuration is as pictured in Figure B.12. The extraneous holes, which are left unfilled in the test, reduce the stress directly between them on the crack path. A quarter-symmetric finite element simulation of this specimen is pictured in Figure B.13, where this effect can be seen. Two different configurations were used, one where the holes were located 20 mm horizontally from the center of the specimen, depicted in the figure, and one where the holes were located 25 mm horizontally from the center. This change in hole location changes the stress distribution in the crack plane.

The finite element analysis was conducted using two-dimensional shell elements with composite laminate material section. In order to derive the laminate stress from the results, the strain was output and multiplied by the laminate modulus, as calculated with classical laminate theory. The stress results were then used in conjunction with Equation (B.2) to predict the growth rate of the crack at each point along its path.

The predictions and results from the two tests are given in Figures 14 and 15. In both cases, the results are predicted well, but not perfectly. The measured rates follow the same trend as the predictions, first decreasing until approximately the crack length that corresponds to the horizontal location of the holes, then increasing as the cracks leave the reduced stress fields, and finally settling into a nearly constant rate. However, in neither specimen is the dip in

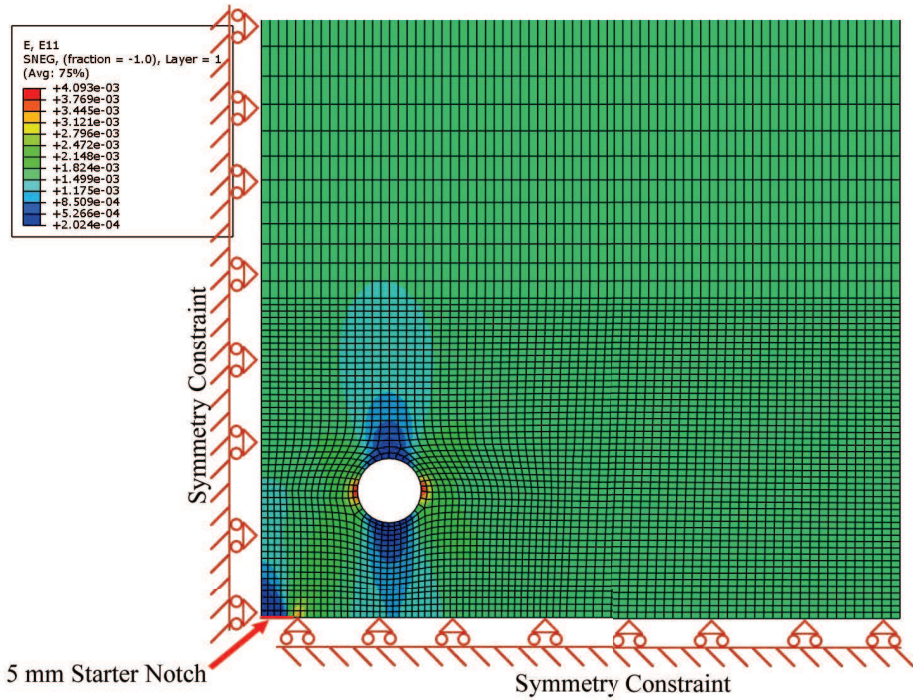


Figure B.13 – ABAQUS results for fiber-direction strain in 4-hole specimen. Line load equivalent to 100 MPa applied at top of specimen, cut off in image

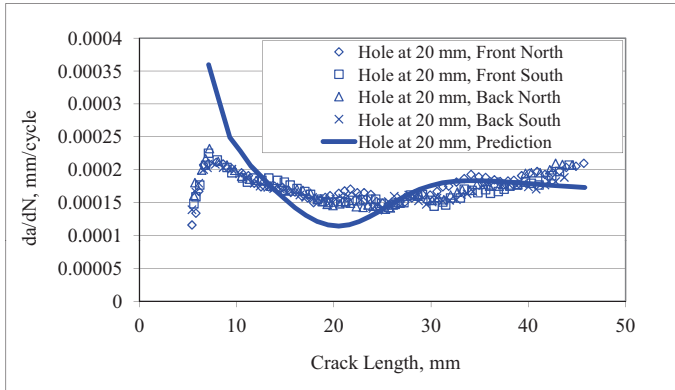


Figure B.14 – Results of the 4-hole specimen with holes at 20 mm from the center, tested at $\sigma_{app,max} = 100$ MPa and $R = 0.05$

growth rates quite as deep as predicted.

Broken-stiffener Configuration

The broken-stiffener configuration employs severed straps along the length of the specimen to alter the stress distribution in the laminate, in much the same way that a broken stringer would shed load into the skin underneath. Straps were placed on the front and back sides of the specimen in order to avoid bending effects.

The specimen design is depicted in Figure B.16. The straps were 2024-T3 aluminum with thicknesses of 3 mm in the first specimen, and the straps were doubled on the second specimen to act as 6 mm thick straps. Neat fit bolts were used in the holes along the center of the straps.

A finite element analysis was performed to estimate the stress distribution in the crack paths. Just as for the 4-hole design, two-dimensional shell elements were used for the laminate, and additional two-dimensional shells were used for the straps. The bolts were approximated using rigid multi-point constraints (MPCs) in the hole radii. The model, with contour results for strain in the loading direction, is depicted in Figure B.17. Results were processed in the same manner at the 4-hole finite element results in order to obtain the stress of the laminate along the crack path.

The results of both tests, depicted in Figure B.18, show that the crack

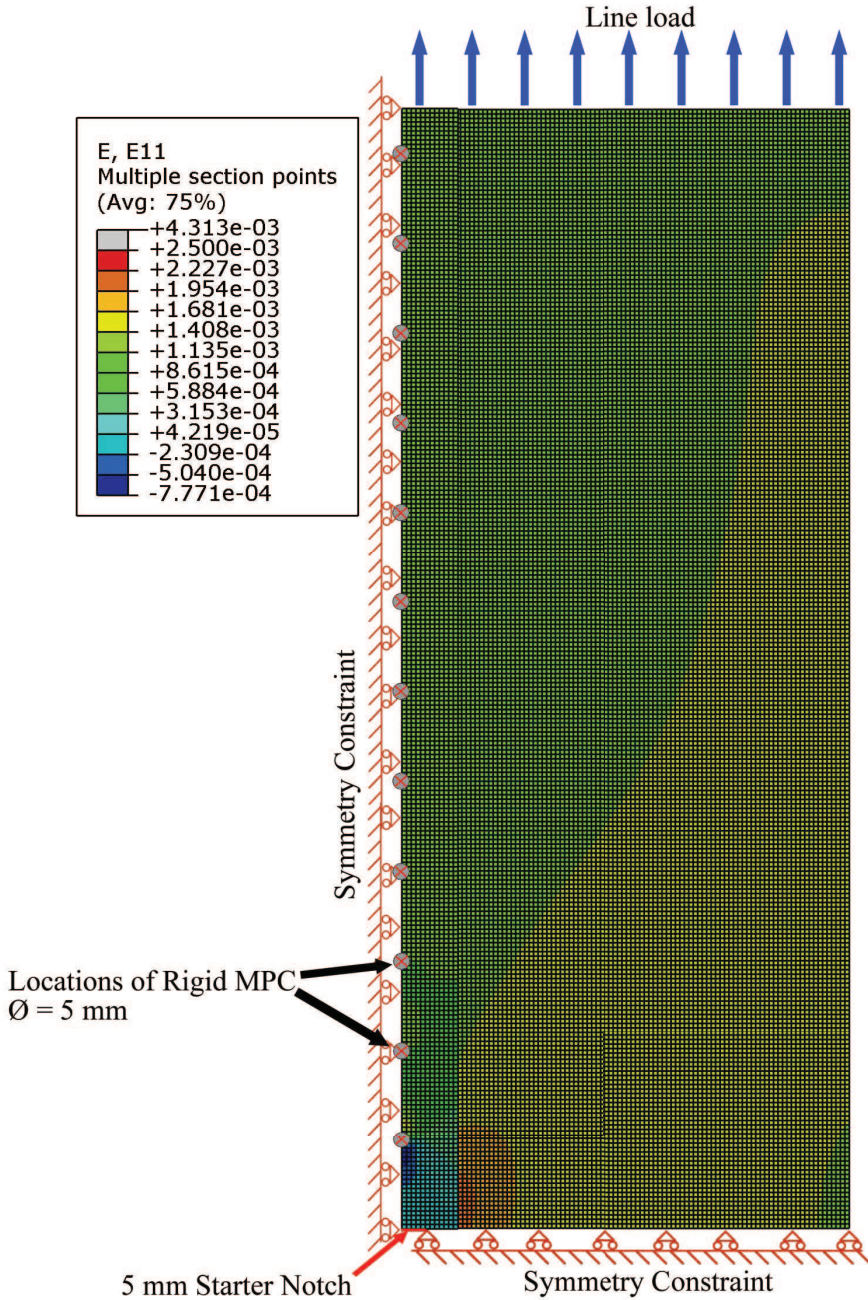


Figure B.17 – FEA output for broken strap model

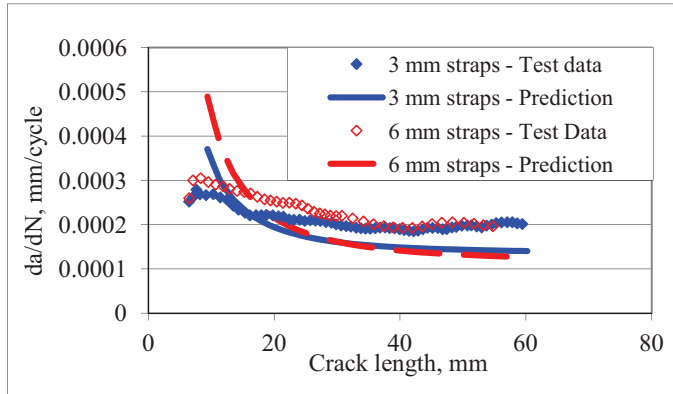


Figure B.18 – Comparison of prediction with test results for the broken-stiffener tests. Both tests were conducted at $\sigma_{app,max} = 100$ MPa and $R = 0.05$

growth rates decreased continuously from the beginning of crack growth to crack lengths of 40 mm. This is in agreement with the prediction, since the load shed into the laminate from the broken straps increases the stress in the region of the strap, an effect that decreases with distance from the specimen center. Where the predictions fail to match the results is in the specific crack growth rates achieved. Starting at crack lengths around 16 mm, the predicted crack growth rates are significantly less than those observed in the test. It is important to also consider the efficacy of the method in predicting the size of the cracks over the life of the test specimens. This is done by integrating the crack growth rate with respect to crack length. The results of such a prediction are compared to the test data in Figure B.19, and it is clear that even though the predicted rates seem poor, the resulting crack growth prediction is reasonably accurate, and would be suitable for preliminary design calculations.

B.3 Conclusions

The results of this study on a thick FML with 2524-T3 thick sheets provide insight into the nature of crack growth in FMLs with respect to composition, thanks to direct comparisons to previous data on similar laminates with 2024-T3, and with respect to the empirical SSCG method for analyzing crack growth.

By substituting an alloy with improved crack growth properties in the laminate, the overall crack growth properties of the laminate were improved. This

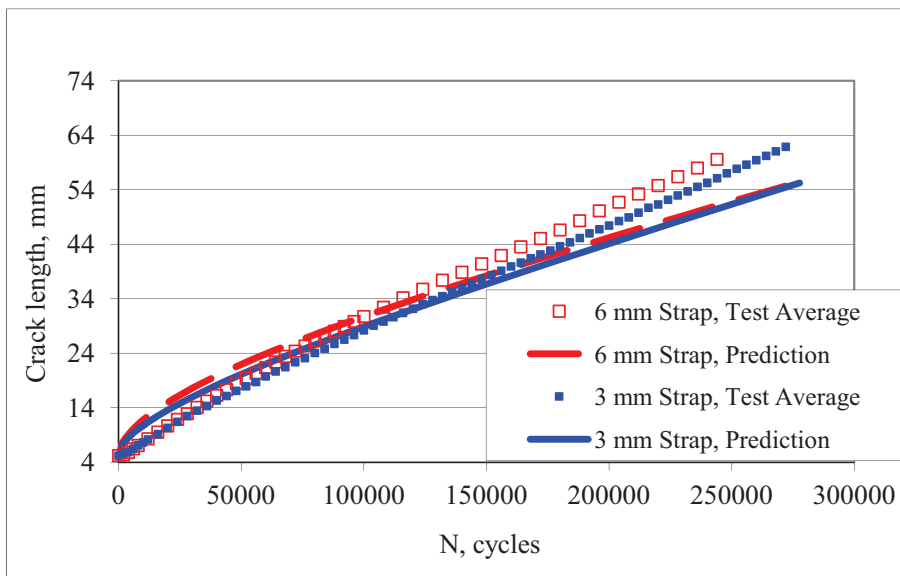


Figure B.19 – Comparison of predicted crack growth to the broken-stiffener tests data

result is intuitive, yet it is still useful to have direct confirmation of the effects of different metal constituent properties. Such results may be useful in assessing techniques for calculating the crack growth properties of laminates based on constituent properties.

One less intuitive result of comparing the 2524-T3 and 2024-T3 laminates is that the 2524-T3 laminates from this study had larger delaminations around the cracks. However, the explanation provided in Section B.2.1 - that the slower crack growth of the 2524-T3 means that the ratio of delamination growth to crack growth should be higher - is adequate to describe this phenomenon. The larger delamination size is not necessarily a disadvantage of the laminate, since it is still a stable delamination that grows in proportion to the crack size. This result does suggest that consideration of the consequences of changing constituent properties should be made with regard to the laminate as a system, where unintended negative effects are possible when individual constituent properties are improved. In the case of crack growth, improved metal crack growth resistance should be balanced with improved delamination resistance in order to maintain the best laminate crack growth possible.

The investigation of crack growth in laminates with differing notch size showed that net stress is practical, but not perfect, for characterizing the steady state crack growth rate, da/dN_{SS} . It is incumbent upon the user of the SSCG approach to take into consideration that the greater the difference between the notch or hole size of the specimen from which laminate property data was obtained and the structure being analyzed, the greater the inaccuracy introduced in the prediction of structural performance.

In the stress gradients tested in this study, the SSCG prediction method predicts the correct trend in the crack growth behavior, but not exactly the correct rates. However, the impact of the prediction error on the overall crack growth prediction is fairly small, and such predictions would be useful in preliminary structural sizing calculations. The advantage of the SSCG method in this case is its simplicity and ease of implementation. Only a static, crack-free, finite element analysis of the structure is necessary, along with the characterization of the SSCG behavior of the laminate of interest subject to the given load history. Methods that are more precise, but more costly, may still be required for analysis of fatigue-critical regions of structure.

Bibliography

- [1] Wilson, G. S., Alderliesten, R. C., and Benedictus, R. (2010) Steady-state crack growth in hybrid fiber metal laminates as a tool for design. *International SAMPE Symposium and Exhibition (Proceedings)*, May.
- [2] Wilson, G. and Alderliesten, R. (2009) Steady state crack growth prediction method for glare and advanced FMLs. *Proceedings of the 50th AIAA/ASME/ASCE/AHS/ASC Structures, Structural Dynamics, and Materials Conference*, May.
- [3] Alderliesten, R. C. (2007) Analytical prediction model for fatigue crack propagation and delamination growth in glare. *International Journal of Fatigue*, **29**, 628–646.
- [4] Marissen, R. (1988) *Fatigue crack growth in ARALL. A hybrid aluminium-aramid composite material: Crack growth mechanisms and quantitative predictions of the crack growth rates*. Ph.D. thesis, Delft University of Technology, Delft, The Netherlands.
- [5] Roebroeks, G. H. J. J., Hooijmeijer, P. A., Kroon, E. J., and Heinimann, M. B. (2007) The development of CentrAl. *First International Conference on Damage Tolerance of Aircraft Structures*, Delft, The Netherlands.
- [6] Wanhill, R. J. H., Platenkamp, D. J., Hattenburg, T., Bosch, A. F., and de Haan, P. H. (2009) Glare teardowns from the megaliner barrel (mlb) fatigue test. Bos, M. J. (ed.), *ICAF 2009, Bridging the Gap between Theory and Operational Practice: Proceedings of the 25th Symposium of the International Committee on Aeronautical Fatigue, 27-29 May 2009, Rotterdam, The Netherlands*.
- [7] ASTM Standard E647, 2008e1 (2008), Standard test method for measurement of fatigue crack growth rates. ASTM International.
- [8] Bray, G. H., Bucci, R. J., Colvin, E. L., and Kulak, M. (1997) Effect of prior corrosion on the s/n fatigue performance of aluminum sheet alloys 2024-t3 and 2524-t3. van der Sluys, W. A., Piascik, R. S., and Zawierucha, R. (eds.), *Effects of the Environment on the Initiation of Crack Growth, ASTM STP 1298*, ASTM, Philadelphia.

This page intentionally left blank.

Summary

This thesis presents the derivation, structure, and validation of a generalized model for crack growth in fiber-metal laminates (FMLs). FMLs, such as Glare and ARALL, have historically been composed of many thin layers, with uniform composition through the thickness. Crack growth in such laminates has been adequately modeled with approaches that take advantage of their through-thickness uniformity in structure and damage evolution. Newer concepts for thick FMLs, intended for structures such as aircraft wing skins, employ metal layers of variable thickness and alloy, as well as fiber reinforcing layers of different composition. The damage behavior of such laminates has been observed to be nonuniform, necessitating the development of this generalized model, which is intended to account for the interaction of differing crack lengths and delamination shapes in each metal layer and interface, respectively, in predicting damage evolution in FMLs.

The model is based on an iterative concept, in which the current damage state is used to calculate damage growth rates, which are used to update the damage state for the subsequent step. Compatibility between each metal layer and its adjoining fiber layers is used as the basis for the simultaneous solution of the bridging load transfer at each delamination. The stress intensity factors of the metal layers are determined by superposition of the stress intensity due to the far field layer stress and the reduction in stress intensity due to bridging load transfer. The cyclic stress intensity factor — the calculation must be performed at both the maximum and minimum applied loading since the stress ratio seen at the crack tip may differ from the applied stress ratio due to residual stress within the laminate — is used to predict the metal layer crack growth rates. The laminate stresses and bridging loads are also used to calculate the strain energy release rate along each delamination boundary, which in turn is used to calculate delamination growth.

The generalized bridging load and strain energy release rate formulations

were validated by comparison to finite element models of FML with non-uniform, arbitrary crack and delamination configurations. The overall model predictions of crack and delamination growth were validated through a series of fatigue crack growth tests on a variety of thick FML configurations, including some with non-uniform thickness layers, asymmetry, differing metal alloys, and different arrangements of composite prepreg and adhesive plies. After a period of crack growth, the tested laminates were destructively inspected to determine the delamination dimensions at each interface. Many of the crack growth rate predictions differed from the experimental results within the acceptable window of 50%; however, poor prediction results were obtained for laminates where the crack growth rates were dependent on drastically different delamination sizes through the thickness. The tendency of short delaminations to catch up to longer delaminations in an exaggerated way due to the strain energy release rate formulation used was the major area identified as needing improvement.

Several examples of the use of the model for informing improved material design decisions are presented. The major advantages of the model are that it is derived from first principles of mechanics, takes as material parameters only independently testable material properties, and is formulated in a modular way such that it can be adapted to different geometries or different failure modes such as FML residual strength or spectrum fatigue crack growth.

Samenvatting

Dit proefschrift beschrijft de derivatie, structuur en validatie van een generaliseerd model voor scheurgroei in vezel-metaallaminaten (FMLs). FMLs, zoals Glare en ARALL, zijn gewoonlijk gemaakt van vele dunne lagen, en hebben een uniforme samenstelling in de dikterichting. Scheurgroei in deze laminaten wordt reeds adequaat gemodelleerd met methoden die profiteren van deze uniformiteit in zowel materiaalcompositie als schade-evolutie. Nieuwere concepten echter voor dikke FMLs bestemd bijvoorbeeld als huid op vliegtuigvleugels, gebruiken metaallagen variërend in dikte en materiaal, alsmede vezellagen van verschillende typen vezel. De schade-eigenschappen van dergelijke laminaten is als niet-uniform waargenomen en dus is een model benodigd dat met niet-uniforme schade kan omgaan. Een dergelijk model moet rekening houden met de interactie van verschillende scheurlengten in de metaallagen enerzijds en de delaminaties van verschillende grootte tussen de aanwezige lagen anderzijds, om een goede voorspelling te kunnen maken.

Het model is gebaseerd op een iteratief concept, waarbij de omvang van de huidige schade wordt gebruikt voor de berekening van scheur- en delaminatiegroeisnelheden, welke vervolgens worden gebruikt om de schadegrootte in de volgende stap te bepalen. Compatibiliteit van de verplaatsing tussen elke laag vormt de basis van de gelijktijdige oplossing van de drukverdeling aan de rand van elke delaminatie in het laminaat. De spanningsintensiteitsfactor van elke gescheurde metaallaag wordt bepaald door de superpositie van de intensiteit door de verre spanning en de vermindering van de intensiteit door de overheveling van last door de overbruggende vezels. De cyclische spanningsintensiteitsfactor — het is belangrijk om de berekening op zowel de minimum en maximum externe belasting te doen, omdat de lokale spanningsverhouding kan afwijken van de toegepaste spanningsverhouding als gevolg van restspanning — bepaalt de scheurgroeisnelheid in de metaallagen. De delaminatiegroeisnelheid wordt berekend aan de hand van de afgiftesnelheid van vervormingsenergie, wat

op haar beurt bepaald is doormiddel van de eerder genoemde laminaatspanningen en lastoverhevelingen.

De wijzen van berekening van de spanningsintensiteitsfactor en de vervormingsenergieafgiftesnelheid werden gevalideerd door vergelijking met eindigelement modellen van FMLs met niet-uniforme en willekeurige scheur- en delaminatieconfiguraties. Voorspellingen voor scheur- en delaminatiegroei van het algemene model werden gevalideerd doormiddel van een reeks van scheurgroeitesten op een verscheidenheid van dikke FML-configuraties, waaronder enkele met lagen van niet-uniforme dikte, asymmetrie, verschillende metaallegeringen en verschillende arrangementen van prepreg en lijmlagen. Na een periode van scheurgroei werden de proefstukken destructief geïnspecteerd om de delaminatieafmetingen op elk raakvlak te meten. Veel van de scheurgroeisnelheidsvoorspellingen verschilden van de experimentele resultaten binnen het aanvaardbare interval van 50%. Slechte voorspellingsresultaten werden echter verkregen voor laminaten waar de scheurgroeisnelheden afhankelijk waren van delaminatiegroottes die door de dikte drastisch verschilden. De neiging van korte delaminaties om langere delaminaties op een bovenmatige manier in te halen, te wijten aan de formulering van het model voor de vervormingsenergieafgiftesnelheid, was geïdentificeerd als het belangrijkste gebied voor verdere verbetering.

Enkele voorbeelden van het gebruik van het model voor het informeren van verbeterde materiaalontwerpkeuzen zijn gepresenteerd. De belangrijkste voordelen van het model zijn dat het is afgeleid uit de eerste principes van mechanica, dat het als materiaalparameters slechts onafhankelijk testbare materiaaleigenschappen gebruikt, en het is zodanig op modulaire wijze geformuleerd, dat deze kan worden aangepast aan verschillende geometrieën en verschillende faalwijzen zoals FML residuaalsterkte of spectrumvermoeiingsscheurgroei.

Acknowledgments

The work described in this thesis, and its assembly into a coherent document, was only possible through the support and helpful input of many others. I would like to express my sincere gratitude to this great community of people.

The Structural Integrity Chair in Delft's Aerospace Faculty fosters an engaging and creative environment. Many great ideas have been hatched at on- and off-topic discussions around the chair's *koffietafel* and in its outstanding laboratories. My supervisors in this endeavor, Rinze Benedictus and René Alderliesten were most welcoming in establishing my studies at the university. Rinze's encouragement to engage in extra projects and teaching responsibilities greatly enhanced the value of my experience. René's work provided an excellent foundation from which to begin attacking the problems posed by thicker generalized fiber metal laminates. His approach to mechanics and pushing the boundaries of what analytical methods can do, and what insights can be gained, opened my eyes to what was possible. Analytical methods unfortunately receive too little credit in the modern engineering world, and René's continuing innovation should serve as an example. It certainly did to me.

Dr. Calvin Rans also provided a great deal of technical back-and-forth and unsticking of problems. That he and René shared an office was fortunate for everyone doing FML research at the time, as there was a one-stop-shop for deep and detailed discussion of technical questions. Similarly, the community of researchers in the Structural Integrity chair working on FMLs created a great collaborative environment, including Riccardo Rodi, Sharif Khan, Greg Rickerd, Cory Cooper, Ilhan Sen, and Guillaume Delgrange. Guillaume's clever FML disbond modeling script was crucial in generating FEA results for validation in Chapter 5. Youssef Fassih provided valuable test data in carrying out many of the delamination growth rate experiments described in Appendix A. The contribution of my other PhD researcher colleagues to the generally high-level yet fun environment around the vliegtuighal was also most appreciated.

In particular I'd like to thank all of those with whom I shared *the office at the end of the hall*: Sandra, Ligeia, Patricio, Konstantin, and Ilhan. I am also very appreciative of the efforts of Gemma van der Windt, who holds the whole place together. Thanks to Siebe Spronk, who, in the course of using my model in his master's work, has gone through my code with a fine-toothed comb, helping me re-examine my assumptions and refine my thinking.

The ability to conduct all the experimental work for this thesis is owed to the fantastic quality of the laboratory in the *vliegtuighal* and to the many people who have built that facility up over the years. The technicians Berthil, Frans, Hans, Niels, and Serge all gave huge amounts of help and made the experiments "doable."

I would like to thank the team at the Alcoa Technical Center for their support and advocacy in getting me to Delft and the provision of most of the material used in the experimental work. I am grateful for the expert guidance of the very experienced veterans of the FML world, Geert Roebroeks, Peter Hooijmeijer, and Erik Kroon. I was also most pleased to be supported in the latter period of my stay at Delft thanks to a research program funded by the Dutch government and GTM Advanced Products.

Most of all, I am grateful for the support of my wife, Leah, who put her own career on pause to join me in Delft, making my time there so much richer, who was a big advocate of my going to Delft in the first place, and who was always encouraging and stabilizing. Thank you.

Propositions
accompanying the thesis

**Fatigue Crack Growth Prediction
for generalized fiber metal laminates and hybrid materials**

by Gregory Scott Wilson

The greater tortuosity of cracks in monolithic 2524-T3 compared with those in FMLs with 2524-T3 means predictions of crack growth in FMLs based on monolithic data will be non-conservative.

The clamping force of a rivet or fastener enhances crack bridging and slows delamination growth of an FML.

Considering FMLs are prized for their outstanding crack growth performance, an inordinate amount of research is conducted on crack growth of FMLs.

The model developed in this thesis is a finite element model.

Destructive inspections should be performed on all FML crack growth tests specimens.

Developing an intuition for handling uncertainty in material response, calculation of material allowables, and comparison of designs based on average properties and allowables should be part of a structural designer's education.

By changing the bridging material displacement formulation to reflect slip and shear at the fiber-matrix interface, the Alderliesten model of Glare crack growth is applicable to metal-matrix composites of simple laminate architecture.

In science and engineering, a proposition formulated to be opposable and defensible can always be reformulated as a hypothesis-testing experiment.

Scholarly publications which derive quantitative results from test data do a disservice to the scientific community when they do not cite or describe in detail the method used to calculate those results.

Patents should be granted for useful new computable algorithms, but not for the software that implements an algorithm.

These propositions are regarded as opposable and defensible, and have been approved as such by the supervisor, Prof.dr.ir R. Benedictus

Stellingen

behorende bij het proefschrift

Fatigue Crack Growth Prediction for generalized fiber metal laminates and hybrid materials

door Gregory Scott Wilson

De grotere grilligheid van scheuren in monolithische 2524-T3 vergeleken met FMLs met 2524-T3 betekent dat voorspellingen van scheurgroei in FMLs gebaseerd op monolithische gegevens niet-conservatief worden.

De klemkracht van een klinknagel of bout verbetert scheuroverbrugging en vertraagt delaminatiegroei van een FML.

Gezien het feit dat FMLs worden gewaardeerd voor hun uitstekende scheurgroei-prestaties, is er een buitensporige hoeveelheid onderzoek verricht naar scheurgroei van FMLs.

Het model dat werd ontwikkeld in dit proefschrift is een eindige elementen model.

Destructieve inspecties moeten worden uitgevoerd op alle FML scheurgroei proefstukken.

Het ontwikkelen van een intuïtie voor de behandeling van onzekerheid in materiaal respons, berekening van materiaal allowables, en vergelijking van modellen gebaseerd op de gemiddelde eigenschappen en allowables moet deel uitmaken van het onderwijs van een constructief ontwerper.

Door de verplaatsingsformulering van het overbruggingsmateriaal te veranderen om slip en afschuiving op de vezel-matrix-interface weer te geven, is het Alderliesten model van Glare scheurgroei van toepassing op metaal-matrix composieten van eenvoudige laminaat architectuur.

In wetenschap en techniek kan een stelling geformuleerd om opponeerbaar en verdedigbaar te zijn altijd worden geherformuleerd als een hypothese-testbaar experiment.

Wetenschappelijke publicaties die kwantitatieve resultaten ontlenen aan testgegevens bewijzen een slechte dienst aan de wetenschappelijke gemeenschap als ze niet verwijzen naar of in detail de gebruikte methode om die resultaten te berekenen uitleggen.

Octrooien moeten worden verleend voor nuttige nieuwe berekenbare algoritmes, maar niet voor de software die een algoritme implementeert.

Deze stellingen worden opponeerbaar en verdedigbaar geacht en zijn als zodanig goedgekeurd door de promotor, Prof.dr.ir R. Benedictus



The excellent durability performance of Glare, a thin fiber metal laminate (FML) material system, is now being proven in service. This has motivated work towards the application of FMLs to thicker structures driven by damage tolerance. In order to fully characterize the crack growth life of such materials, models are necessary that can account for the unique aspects of material systems under consideration, including non-uniformity of composition and stress states, and the resulting complex damage state involved in fatigue crack growth. This thesis presents a generalized analytical model for the prediction of fatigue crack and delamination growth in FMLs of arbitrary lay-up, including differing metal alloys, different thickness layers, and different combinations of reinforcing composite layers. Cracks in each layer, and delaminations in each interface, are allowed to grow separately, with the interactions of the damage throughout the laminate taken into account. The model is structured in a modular and iterative fashion. Modules for determining the load redistribution around damage and the strain energy release rate of delamination have been derived and independently validated through comparison to finite element analyses. A series of tests with thick fiber metal laminates of varied construction was carried out to verify the overall crack growth predictions of the model. While some discrepancies between the results and predictions for the most complex laminates suggest that refinement of the delamination strain energy release rate formulation is needed, many of the test results were accurately predicted, demonstrating the suitability of this model for use in design and analysis of thick FML structures.